Bridging first principles modelling with nanodevice TCAD simulations

Palsgaard, Mattias

Publication date:
2018

Document Version
Publisher's PDF, also known as Version of record

Bridging first principles modelling with nanodevice TCAD simulations

Mattias Palsgaard
PhD Thesis August 2018

DTU Nanotech
Department of Micro- and Nanotechnology

TECHNICAL UNIVERSITY OF DENMARK

DOCTORAL THESIS

Bridging first principles modelling with nanodevice TCAD simulations

Author:
Mattias PALSGAARD

Supervisors:
Prof. Mads BRANDBYGE
Dr. Troels MARKUSSEN
Dr. Tue GUNST
Dr. Kurt STOKBRO

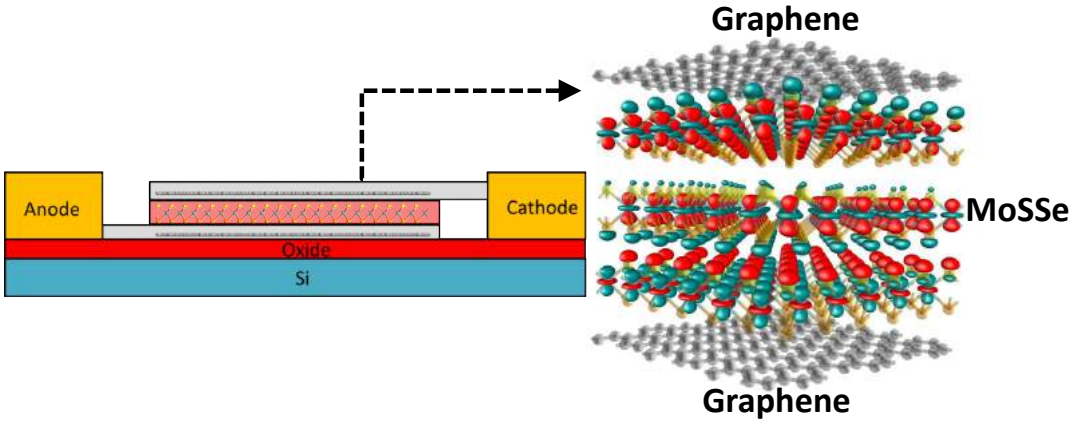

A thesis submitted in fulfillment of the requirements for the degree of Doctor of Philosophy

in the

Theoretical Nanoelectronics group
Department of Micro- and Nanotechnology

August 30, 2018

Preface

This thesis is submitted in candidacy for the Ph.D. degree at the Technical University of Denmark (DTU). The work was carried out between September 2015 and August 2018 at the Department of Micro- and Nanotechnology (DTU Nanotech) and at Synopsys-QuantumWise under the supervision of Prof. Mads Brandbyge, Dr. Troels Markussen, Dr. Tue Gunst and Dr. Kurt Stokbro. The project was financed by Innovation Fund Denmark.

I would like to thank my dream team of supervisors. Working with all of you has been a great experience! I would like to thank Mads for always having the door open and taking time to ponder over new ideas. I would like to thank Troels for his enthusiasm and many inspiring ideas during the project and for guiding me safely through the development of commercial software. I would like to thank Tue for being an awesome office-mate, and for listening to and answering countless questions without ever being (visibly) annoyed. I would also like to thank Kurt for his great overview and support during the project and for giving me the opportunity to work in a great place like QuantumWise where you actually get to do quantum transport calculations for work!

Big thanks also to Andrea Crovetto, Ole Hansen and Kristian Sommer Thygesen for collaborations which breathed new life into my project and taught me many new things. I would also like to thank Lee Smith and Geoffrey Pourtois for their great hospitality during my stays at Synopsys in Santa Clara, CA, USA and at IMEC in Leuven, Belgium.

I would like to thank my co-workers in the Theoretical Nanoelectronics and Theoretical Nanotechnology groups and at Synopys-QuantumWise for providing awesome working environments. Whether it has been playing foosball or boardgames, eating countless cakes or going on boat rides I have enjoyed every minute of it! Additional thanks to Nick Rübner Papior and Susanne Leitherer for helping with reading through this report and to Thomas Aktor for keeping me company during the first month of writing.

Finally I would like to thank my family and friends for their support and especially my girlfriend for tolerating me during this last period.

Abstract

This thesis is concerned with calculating the properties of electronic devices using first principles atomic scale methods. For this purpose, we develop new methods to extract important information from these calculations that can be included in device level simulations tools. The design of electronic devices is often supported by technology computer aided design (TCAD) tools. At the device level, TCAD models typically use continuum descriptions defining the constituent materials by parameters like effective masses and mobility. These parameters are typically measured in experiments or obtained from atomic-scale calculations of bulk crystals when no experiments are available.

Atomic-scale phenomena like surface effects or interfaces are becoming more important than ever due to the continued miniaturization of electronics. As a result the bulk parameters used in device level TCAD simulations, in many cases, fail to accurately describe the properties of the electronic devices. In this thesis we use density functional theory (DFT) together with nonequilibrium Green's function (NEGF) theory to accurately calculate transport at the atomic level. These calcualtions are non-emperical and can therefore be used to make prediction about devices using new promising materials. New methods to extract mobility and effective masses are developed including effects such as quantum confinement and coupling between electrons and quantized vibrations of the crystal lattice (phonons). The methods are tested against the current state-of-the-art and the resulting parameters are compared to those measured in experiments.

We also carry out studies of several different thin-film solar cells including at the same time light-matter interactions and electron-phonon coupling. The current due to sunlight illumination is calculated either from device level TCAD simulations, including details from the atomic scale parametrically, or directly from atomic-scale DFT-NEGF transport calculations. Both methods show excellent agreement when compared to relevant experiments and offer new information useful for the optimization of these solar cells. We also find that an exciting, newly discovered two-dimensional material opens up for the fabrication of atomically thin solar cells generating a substantial out-of-plane current. Several other promising device applications using this material are also found, including a record high homogeneous simultaneous p and n-type doping of graphene layers in close proximity.

Resumé

Denne afhandling omhandler beregningen af elektroniske komponenters egenskaber fra parameterfrie atomarskala metoder. Til dette formål udvikler vi nye metoder til at udtrække vigtig information fra disse atomarskala beregninger, der kan inkluderes i komponentskala simulations værktøjer. Design af elektroniske komponenter bliver ofte understøttet af teknologi computerbaserede design (TCAD) værktøjer. På komponentskala bruger TCAD modeller typisk kontinuum beskrivelser hvor parametre så som effektive masser og mobilitet definerer de materialer der udgør komponenterne. Disse parametre bliver typisk målt i eksperimenter eller ekstraheret fra atomarskala beregninger når der ikke er eksperimenter til rådighed.

Atomarskala effekter så som overflade effekter og grænseflader bliver stadigt mere vigtige grundet den fortsatte nedskalering af elektroniske komponenter. Dette resulterer i at komponentskala TCAD simuleringer baseret på parametre fra perfekte krystaller ofte fejler, da de ikke beskriver disse atomarskala effekter præcist nok. I denne afhandling bruger vi tætheds funktional teori (DFT) sammen med ikkeligevægts Green's funktions (NEGF) teori til at beregne atomarskala transport nøjagtigt. Disse beregninger er ikke-empiriske og kan derfor benyttes til at lave forudsigelser om elektroniske komponenter baserede på nye lovende materialer. I denne afhandling bliver nye metoder til at ekstrahere mobilitet og effektive masser udviklet hvor effekter som f.eks. kvanteindsnævring (quantum confinement) og kobling mellem elektroner og kvantiserede vibrationer i krystalgitteret (fononer) er inkluderet. Metoderne bliver sammenlignet med allerede eksisterende metoder og de beregnede parametre bliver sammenlignet med dem der er målt i eksperimenter.

Vi udfører også studier af flere forskellige tyndfilms solceller, hvor både interaktion med sollys og elektron-fonon kobling inkluderes på samme tid. Strømmen genereret i disse solceller bliver beregnet, enten direkte fra atomarskala DFT-NEGF transport beregninger, eller fra komponentskala TCAD simuleringer hvor atomarskala effekter er inkluderet ved hjælp af parametre. Begge metoder giver god overensstemmelse med bl.a. tomgangspændingen målt i eksperimenter og forsyner os med vigtig ny information der kan bruges til at optimere de studerede solceller. Ydermere finder vi at et spændende nyt todimensionelt materiale gør det muligt at fabrikere ultratynde solceller der generere en signifikant ude-af-plan strøm. Flere andre lovende applikationer af dette materialer bliver også fundet, inklusiv en rekordhøj homogen p og n-type dotering af grafen lag adskilt af få nanometer.

List of publications

Included papers

Paper 1

Semiconductor band alignment from first principles: A new nonequilibrium Green's function method applied to the CZTSe/CdS interface for photovoltaics
Mattias Palsgaard, Andrea Crovetto, Tue Gunst, Troels Markussen, Ole Hansen, Kurt Stokbro, and Mads Brandbyge
2016 International Conference on Simulation of Semiconductor Processes and Devices (SISPAD), pp. 377–380

Paper 2

Interface band gap narrowing behind open circuit voltage losses in Cu_2ZnSnS_4 solar cells
Andrea Crovetto, *Mattias Palsgaard*, Tue Gunst, Troels Markussen, Kurt Stokbro, Mads Brandbyge, and Ole Hansen
Applied Physics Letters. **110**, 083903, (2017)

Paper 3

Electron-phonon scattering from Green's function transport combined with molecular dynamics: Applications to mobility predictions
Troels Markussen, *Mattias Palsgaard*, Daniele Stradi, Tue Gunst, Mads Brandbyge, and Kurt Stokbro
Physical Review B **95**, 245210 (2017)

Paper 4

First-principles electron transport with phonon coupling: Large scale at low cost
Tue Gunst, Troels Markussen, *Mattias Palsgaard*, Kurt Stokbro, and Mads Brandbyge
Physical Review B **96**, 161404(R) (2017)

Paper 5

New approaches for first-principles modelling of inelastic transport in nanoscale semiconductor devices with thousands of atoms
Tue Gunst, Mads Brandbyge, *Mattias Palsgaard*, Troels Markussen and Kurt Stokbro
2017 International Conference on Simulation of Semiconductor Processes and Devices (SISPAD), pp. 13-16

Paper 6

Efficient First-Principles Calculation of Phonon-Assisted Photocurrent in Large-Scale Solar-Cell Devices
Mattias Palsgaard, Troels Markussen, Tue Gunst, Mads Brandbyge, and Kurt Stokbro
Physical Review Applied **10**, 014026 (2017)

Paper 7

Stacked Janus device concepts: abrupt pn-junctions and cross-plane channels
Mattias Palsgaard, Tue Gunst, Troels Markussen, Kristian Sommer Thygesen, and Mads Brandbyge
Submitted to Nanoletters

Other papers

Unravelling the role of inelastic tunneling into pristine and defected graphene
Mattias Palsgaard, Nick Rübner, and Mads Brandbyge
Physical Review B **91**, 121403(R) (2015)

Giant tunnel-electron injection in nitrogen-doped graphene
Jérôme Lagoute, Frédéric Joucken, Vincent Repain, Yann Tison, Cyril Chacon, Amandine Bellec, Yann Girard, Robert Sporken, Edward H. Conrad, François Ducastelle, *Mattias Palsgaard*, Nick Papior Andersen, Mads Brandbyge, and Sylvie Rousset
Physical Review B **91**, 125442 (2015)

Patent application

Systems and methods for providing approximate electronic-structure models from calculated band structure data
Kurt Stokbro, and *Mattias Palsgaard*
PCT Patent Application No. PCT/EP2016/064628

Conference oral presentations

Semiconductor band alignment from first principles: A new nonequilibrium Green's function method applied to the CZTSe/CdS interface for photovoltaics
Mattias Palsgaard, Andrea Crovetto, Tue Gunst, Troels Markussen, Ole Hansen, Kurt Stokbro, and Mads Brandbyge
2016 International Conference on Simulation of Semiconductor Processes and Devices (SISPAD), 6-8 September 2016, Nuremberg, Germany

Atomistic modeling of semiconductors and their interfaces
Mattias Palsgaard
Emerging Technologies 2017 (ETCMOS), 28-30 May 2017, Warsaw, Poland

List of Abbreviations

IC	**I**ntegrated **C**ircuit
TCAD	**T**echnology **C**omputer **A**ided **D**esign
BTE	**B**oltzmann **T**ransport **E**quation
DFT	**D**ensity **F**unctional **T**heory
NEGF	**N**on**E**quilibrium **G**reen's **F**unction
ITRS	**I**nternational **T**echnology **R**oadmap for **S**emiconductors
TEM	**T**ransmission **E**lectron **M**icroscopy
TMD	**T**ransition **M**etal **D**ichalcogenide
PV	**P**hoto**V**oltaics
ITRPV	**I**nternational **T**echnology **R**oadmap for **P**hoto**V**oltaics
FET	**F**ield-**E**ffect **T**ransistor
EMA	**E**ffective **M**ass **A**pproximation
EPC	**E**lectron-**P**honon **C**oupling
MD	**M**olecular **D**ynamics
KS	**K**ohn-**S**ham
LDA	**L**ocal **D**ensity **A**pproximation
GGA	**G**eneral **G**radient **A**pproximation
PW	**P**lane **W**ave
LCAO	**L**inear **C**ombination of **A**tomic **O**rbitals
SCBA	**S**elf-**C**onsistent **B**orn **A**pproximation
LOE	**L**owest **O**rder **E**xpansion
DOS	**D**ensity **O**f **S**tates
WBA	**W**ide **B**and **A**pproximation
MC	**M**onte **C**arlo
STD	**S**pecial **T**hermal **D**isplacement
CBO	**C**onduction **B**and **O**ffset
VBO	**V**alence **B**and **O**ffset
PBC	**P**eriodic **B**oundary **C**ondiction
DZP	**D**ouble **Z**eta **P**olarized
BZ	**B**rillouin **Z**one
LDOS	**L**ocal **D**ensity **O**f **S**tates
CBM	**C**onduction **B**and **M**inimum
VBM	**V**alence **B**and **M**aximum
STM	**S**canning **T**unneling **M**icroscopy
SRH	**S**hockley-**R**ead-**H**all
SiNW	**Si**licon **N**ano**W**ire
DFTB	**D**ensity **F**unctional **T**ight **B**inding
EAM	**E**mbedded **A**toms **M**odel
CNT	**C**arbon **N**ano**T**ube
hBN	**h**exagonal **B**oron **N**itride
cp	**c**ross-**p**lane

Physical Constants

Speed of Light	$c = 2.997\,924\,58 \times 10^{8}\,\mathrm{m\,s^{-1}}$
Planck's constant	$h = 6.626\,070\,04 \times 10^{-34}\,\mathrm{J\,s}$
Reduced Planck's constant	$\hbar = 1.054\,571\,80 \times 10^{-34}\,\mathrm{J\,s}$
Boltzmann constant	$k_B = 1.380\,648\,52 \times 10^{-23}\,\mathrm{J\,K^{-1}}$
Conductance quantum	$G_0 = 7.748\,091\,73 \times 10^{-5}\,\mathrm{S}$
Electron rest mass	$m_0 = 9.109\,383\,56 \times 10^{-31}\,\mathrm{kg}$
Elementary charge	$e = 1.602\,176\,62 \times 10^{-19}\,\mathrm{C}$

Contents

Preface iii

Abstract v

Resumé vii

List of publications ix

1 Introduction 1
1.1 Technology computer aided design tools . . . 1
1.2 Nanoelectronics . . . 2
1.2.1 Miniaturization in Photovoltaics . . . 5
1.3 Challenges for TCAD . . . 5
1.3.1 Bridging first principles modelling with TCAD simulations . . . 6
1.4 Outline of the thesis . . . 7

2 Methods 9
2.1 Electronic structure methods . . . 9
2.1.1 Density Functional Theory . . . 9
2.1.2 Effective Mass Approximation . . . 12
2.2 NEGF transport . . . 12
2.2.1 Interacting current . . . 13
2.2.2 Noninteracting current . . . 14
2.3 Electron-phonon coupling . . . 15
2.3.1 Calculating phonons . . . 15
2.3.2 Lowest Order Expansion . . . 15
2.3.3 Special Thermal Displacement . . . 17
2.4 Summary . . . 18

3 Multiscale study of the CZTS(e) thin-film solar cell 21
3.1 The CZTS(e) solar cell . . . 21
3.2 Multiscale modeling approach . . . 23
3.3 First principles band alignment calculation . . . 23
3.3.1 Bulk approach . . . 24
3.3.2 DFT-NEGF approach . . . 25
3.3.3 Band gap correction with DFT + U . . . 25
3.3.4 Setting up the interface . . . 25
3.4 Results for the CZTSe/CdS interface . . . 27
3.4.1 Dealing with residual potential slope . . . 27
3.4.2 Extracted CBOs . . . 29
3.5 Results for the CZTS/CdS interface . . . 29
3.5.1 Localized interface state . . . 31
3.5.2 Inclusion of interface state in the TCAD model . . . 32

3.5.3 Temperature dependence of open-circuit voltage . . . 34
3.6 Summary . . . 34

4 Calculating phonon limited mobilities from Landauer transport 37
4.1 EPC coupling from atomistic device calculations . . . 37
4.2 MD-Landauer approach . . . 38
4.2.1 Independent variables . . . 40
4.3 Comparison with experiments and Boltzmann . . . 42
4.3.1 Gold nanowire . . . 44
4.3.2 Bulk gold . . . 44
4.3.3 Semiconducting and metallic carbon nanotube . . . 46
4.3.4 Limitations of MD-Landauer approach compared to BTE . . . 47
4.4 LOE-Landauer approach . . . 49
4.5 STD-Landauer approach . . . 50
4.6 Summary . . . 52
4.6.1 Outlook . . . 52

5 Modeling phonon-assisted photocurrent 53
5.1 Simulating the silicon solar cell . . . 53
5.2 First principles photocurrent calculation . . . 54
5.2.1 EPC through special thermal displacement . . . 56
5.2.2 Modelling sunlight illumination . . . 56
5.2.3 Band gap correction with DFT-1/2 . . . 57
5.3 Results and discussion . . . 57
5.3.1 Photocurrent . . . 58
5.3.2 Total current . . . 59
5.3.3 Temperature dependence . . . 61
5.3.4 Solar irradiance dependence . . . 62
5.3.5 Solar cell efficiency . . . 62
5.4 Summary . . . 64
5.4.1 Outlook . . . 64

6 Devices in Janus MoSSe 65
6.1 Discovery of Janus MoSSe . . . 65
6.2 Monolayer Janus MoSSe . . . 66
6.3 Stacked Janus MoSSe . . . 68
6.4 Graphene as electrodes for Janus MoSSe devices . . . 68
6.4.1 Graphene doping . . . 69
6.4.2 Cross-plane transport calculations . . . 71
6.5 Janus MoSSe solar cell . . . 71
6.6 Summary . . . 74
6.6.1 Outlook . . . 74

7 Calibrating TCAD simulations with confined DFT bandstructure 77
7.1 The band structure of confined systems . . . 77
7.2 Description of the multiband fitting approach . . . 79
7.3 Sorting algorithm . . . 79
7.3.1 Effective mass model . . . 81
7.3.2 Results . . . 82
7.3.3 Checking the quality of the match . . . 83
7.4 Fitting to the sorted bands . . . 85

7.5 Results and discussion 85
7.6 Summary 87

8 Summary **89**
8.1 Outlook 90

A Boltzmann transport equation calculation parameters
A.1 Silicon nanowire . . . . .
A.2 Bulk silicon . . . . .
A.3 (8,0) carbon nanotube . . . . .
A.4 (4,4) carbon nanotube . . . . .

B Publications

Chapter 1

Introduction

Since the origins of the integrated circuit (IC) in the early 1960s and late 1950s, electronics have penetrated every aspect of human life to the point where every human living in the developed world interacts with ICs many times a day, every day. The fundamental building block of the IC, enabling mathematical operations, is the transistor. The transistor utilizes semiconductors and logic gates to facilitate switching between on and off states. Optimizing processing and design of transistors through engineering is important in order to improve performance and achieve higher yields.

1.1 Technology computer aided design tools

The use of technology computer aided design (TCAD) tools, in the design phase of IC production, has become commonplace in the industry. TCAD tools are for example used for optimization of yields during processing and for engineering of devices. Many simulation tools exist, with different approximations and uses. Generally these tools can be separated into three perspectives or levels of abstraction as shown in Fig. 1.1. Lowest in the hierarchy of Fig. 1.1 is the circuit level. At the circuit level compact models are typically used to test ICs using inputs like current voltage characteristics fitted to analytical equations. The large number of inputs (sometimes over 100) used for compact models leads to a high level of complexity and very little transparency[1, 2]. Compact models can handle large circuits in milliseconds, but do not explicitly account for detailed transport physics.

The inputs for the compact models can be obtained experimentally from measurements on isolated devices. Alternatively, as indicated in Fig. 1.1, device level TCAD models can be used to generate parameters for the compact models. At the device level approaches like drift-diffusion and Monte Carlo sampling of the Boltzmann transport equation (BTE) are used to simulate transport properties including various scattering effects parametrically. These models employ a continuum description of the included materials defining them by parameters such as effective masses and mobilities or relaxation times in the case of BTE.

Highest in the hierarchy in Fig. 1.1 is the atomic level. Here models, including explicitly the atomic make-up and quantum nature of materials, are used to predict material properties. Some methods like the popular density functional theory (DFT) are first principles, meaning no fitting parameters are used, leading to a high predictive power. First principles calculations can be very computationally demanding, and are most commonly used to extract material bulk properties like crystal structure, Young's modulus, or effective masses that can be used in device level simulations. However, using nonequilibrium Green's function (NEGF) formalism, it is also possible to do transport simulations directly from first principles, on systems of limited

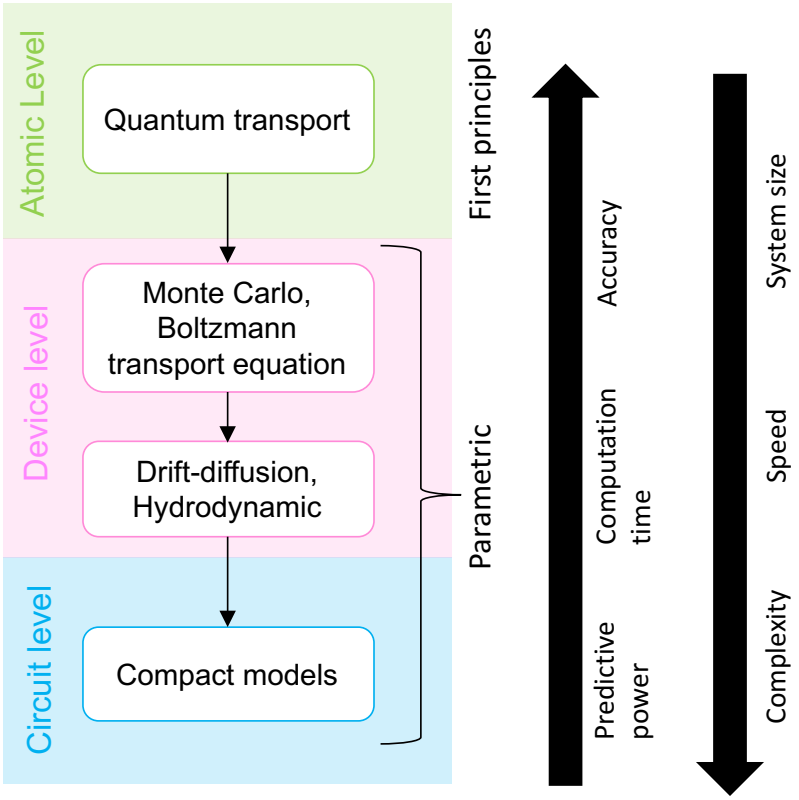

FIGURE 1.1: Jacobs ladder of TCAD tools. Flow diagram showing the hierarchy of methods used within TCAD and the level at which they are used. The small arrows drawn between methods indicate the feeding of parameters typically used within TCAD. The large arrows highlight some of the advantages and disadvantages of the different methods.

size[3, 4].

Ideally these methods are used in tandem, as indicated in Fig. 1.1, where the higher level methods are used to calibrate the lower level methods, continuously providing parameters and deeper understanding of the underlying physical effects[1, 2]. In this thesis we will study the coupling between the atomic level and the lower levels.

1.2 Nanoelectronics

The rapid downscaling of electronic devices, driven by the need for faster CPUs and more memory, was predicted in 1965 by Gordon Moore who stated that the number of components in integrated circuits would double every year[6]. Ten years later he predicted the rate of development to fall to a doubling every *two* years[7]. This has since become known as Moore's Law within the electronics community, and the rapid development has continued ever since. Perhaps the most impressive feature of this extreme downscaling of devices, is the average transistor price, which has dropped by an order of magnitude every few years since the first commercial transistor hit the market. In fact, in 2010 the the average price of a transistor fell below

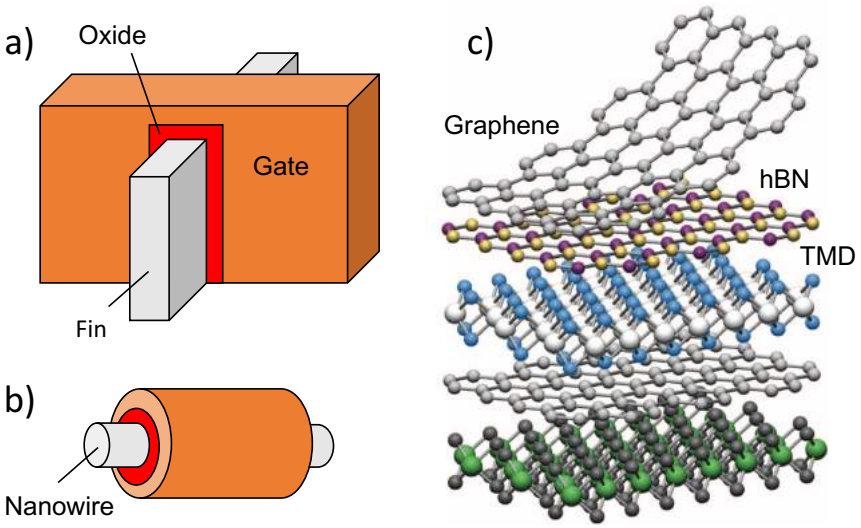

FIGURE 1.2: Ultrascaled electronics. a) Sketch of a tri-gate FinFET device. b) Sketch of an all-around-gate nanowire-FET. c) A drawing of stacked two-dimensional materials taken from [5].

the price of ink for a single letter of print[8][1].

The 2015 version of the International Technology Roadmap for Semiconductors (ITRS), put together by leading experts within the field of electronics, states that sub 7 nm technology nodes are expected to be available by 2021[10]. Some examples of ultrascaled systems relevant for electronics are shown in Fig. 1.2. The Fin field-effect transistor (FinFET) with tri-gate, sketched in Fig. 1.2a, can be found in many chips of today and is confined heavily in one direction. Figure 1.3(top) shows a transmission electron microscopy (TEM) image of a Intel Xeon E3-1230V2 Server CPU[11]. The tri-gate silicon Finfet geometry is clearly visible, and zooming in on the top part of the Fin in 1.3(bottom) one can actually see the crystal structure of the [110] direction and count the number of silicon atoms across the Fin. Confining along two directions we get the nanowire-FET (shown in Fig. 1.2b) where an all-around-gate is used to increase the natural length and avoid short channel effects which reduce performance. In this thesis we will calculate the properties of both nanowires and Fins made of different semiconducting and metallic materials. In our calculations we will include explicitly the effects of nanoscaling on the transport properties.

Scaling materials down to single layers of atoms we arrive at more exotic system, like the two-dimensional graphene and monolayers of transition metal dichalcogenides (TMDs) like molybdenum disulfide (MoS_2) shown in Fig. 1.2c. These materials have, due to their remarkable electronic and thermoelectric properties, received a huge amount of interest from the scientific community as possible replacements for the current technology in many fields, including electronics in the coming decades. We will consider, in this thesis, a particular TMD with a built-in cross plane dipole, which opens up for new interesting phenomena. In summary, nanoelectronics is truly becoming part of the business and replacement may be needed to fulfill Moore's law in the near future.

[1]The listed price is for a letter of print in the publication *Tape Up*. The average price of transistors is now comparable to the price of one cubic millimeter of dirt $\sim 10^{-9}$\$[9], bringing new meaning to the expression *dirt cheap*.

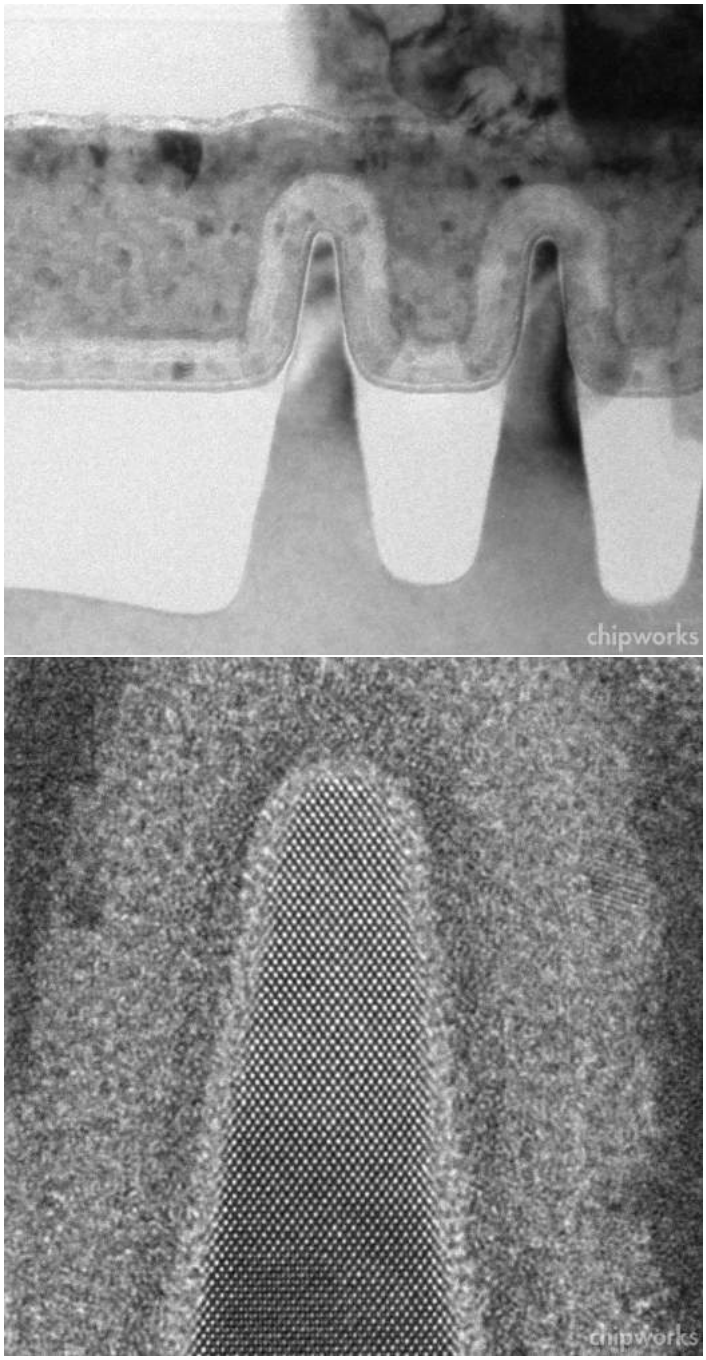

FIGURE 1.3: TEM images of the Intel Xeon E3-1230V2 Server CPU taken from [11]. Top: The cross-section of two tri-gate FinFETs. Bottom: Zoom-in on one Fin, showing the atomic crystal lattice of the silicon.

1.2.1 Miniaturization in Photovoltaics

Solar cells are thought to be one of the most promising solutions to the ever growing problem of rising greenhouse gas levels and their dire consequences. Although not nearly as rapid as in the field of electronics, miniaturization is also a challenge in the field of photovoltaics (PV), driven mainly by the need for reducing PV cell prices and increasing their efficiency. According to the 2018 International Roadmap for Photovoltaics (ITRPV)[12] and the 2017 Fraunhofer Photovoltaics report[13], material cost makes up the majority of the cost of a silicon PV cell and reducing this cost by e.g. downscaling is critical in order to compete in the energy market. A result of this need for cost reduction, can be seen in the growing market share taken up by the cheap thin-film solar cells based on alternatives to silicon absorbers like cadmium telluride (CdTe) and CIGS ($CuInGASe_2$)[13]. In the thesis we will consider thin-film solar cells made of Cu_2ZnSnS_4, $Cu_2ZnSnSe_4$, silicon and the two-dimensional material Janus MoSSe. Increased conversion efficiency in todays PV cells is often facilitated by the precise tailoring of device properties through introduction of new thin layers of material. An extreme case of this could be the stacking of 2D materials shown in Fig. 1.2c facilitating ultrathin absorbers with precisely controlled properties. As such, the size of individual components of PV cells is decreasing, in order to enhance efficiency, even if the total size of a cell is kept the same[14].

1.3 Challenges for TCAD

The continued miniaturization also presents a challenge for the field of TCAD, since the effects directly related to the atomic scale crystal lattice of the materials are impacting devices more and more: Coupling between electrons and the vibrations of the crystal lattice (phonons) is increasingly important, as dissipation of heat away from devices becomes a bottleneck. The nanostructuring of devices leads to confinement effects that change the band structure of both electrons and phonons. The detailed effects of edges and interfaces begin to play a major role, and have even been suggested as a method for tailoring properties in nanowires[15]. Moreover, the quantum mechanical nature of electronics can no longer be ignored. This is seen in the form of new challenges like leakage currents due to tunneling and in the form of new opportunities like the tunneling-field-effect-transistor (TFET) with reduced power consumption[16].

All of the above effects are difficult to treat properly using traditional device level TCAD models fitted to bulk parameters. However, using quantum transport based on DFT-NEGF calculations these effects can be captured accurately. This has lead to increased interest in research related to first principles transport, as indicated by the steady increase in publications shown in Fig. 1.4(top). As suggested above the precise treatment of quantum transport effects comes with a significant computational burden, and historically DFT-NEGF calculation have been used mainly to consider systems for molecular electronics such as the extreme case shown in Fig. 1.4(middle) of a H_2 molecule connected to two 1D gold chains.

Interestingly the downscaling of electronics and resulting increase in computational power, together with major development in computational science over the last decade, has permitted the treatment of transistor level devices directly from first principles calculations as shown in Fig. 1.4(bottom). Improvements made in the field of first principles transport calculations, and increased interest shown by the

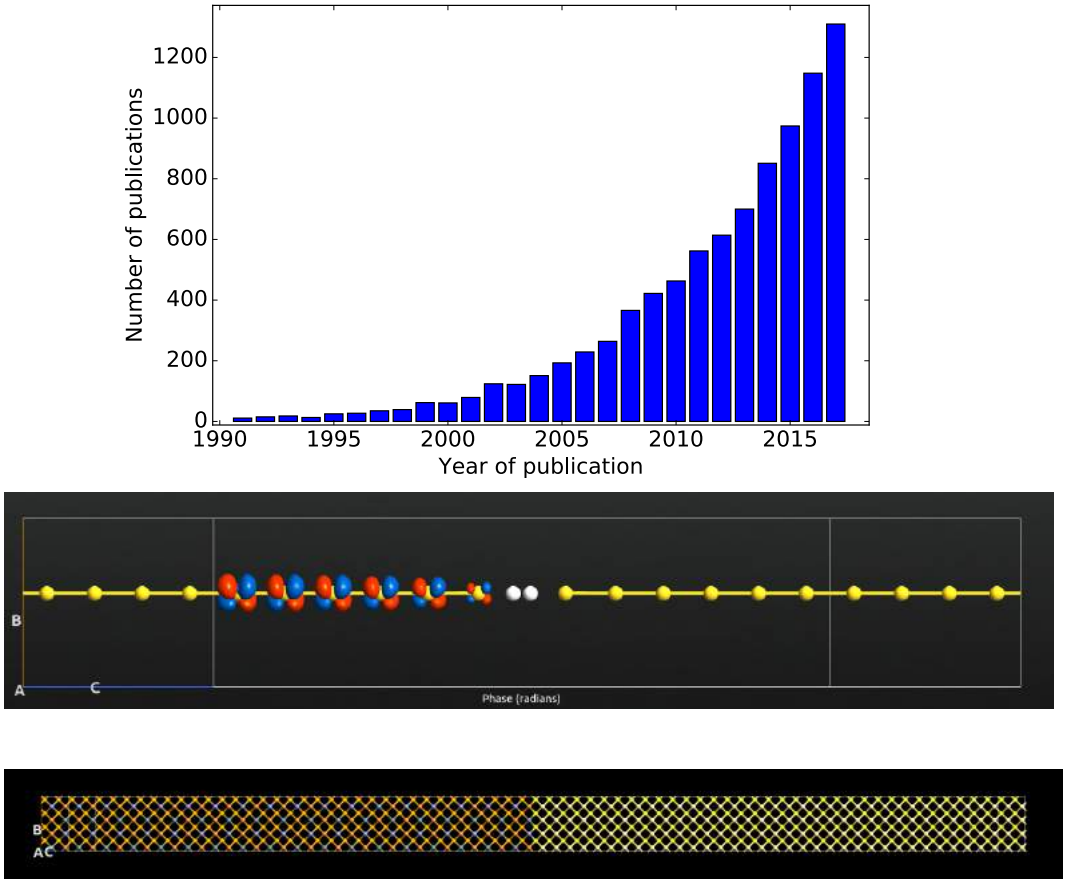

FIGURE 1.4: Evolution of first principles transport calculations. Top: Number of publication with the topic listed as "DFT(or first principles) transport" per year (Data from ISI Web of Knowledge). Middle: Molecular electronics device consisting of a H_2 molecule between two 1D gold chains, taken from[17]. Bottom: Device structure of a CZTSe/CdS interface studied in Paper 1.

industry, has spawned several companies providing software enabling atomic scale transport simulation. The market leader QuantumWise, whose costumers include the biggest names in the semiconductor industry such as Intel, Samsung, Global foundries and many more, is a danish company which recently became part of the major TCAD software provider Synopsys. The success of this company is a symptom of the growing demand for precise treatment of transport properties at the atomic level.

1.3.1 Bridging first principles modelling with TCAD simulations

The interplay between device level transport simulation and circuit level design tools is an established and well understood field of electronics, with some TCAD software providers selling full device-to-circuit-level solutions[1, 2]. However, the connection between atomic level transport calculations and device level methods is still very much in its infancy. First principles simulations are mostly used on bulk materials to extract parameters for lower level methods, for materials where experimental values do not exist. This approach is however insufficient in ultrascaled devices, where the bulk properties are no longer a fair representation of the components of the device.

In this thesis we complete theoretical studies, in an effort to establish reliable approaches to extract information obtained from first principles calculation, to improve TCAD modeling.

1.4 Outline of the thesis

- In **Chapter 2:**
  We first describe the electronic structure methods applied: Density functional theory (DFT) and effective mass approximation (EMA). NEGF theory for electronic transport including interactions is then introduced, before addressing various methods of including electron-phonon coupling (EPC) in NEGF and how the phonon properties are calculated.

- In **Chapter 3 (Paper 1, 2):**
  We introduce a multiscale simulation approach where details of interfaces, calculated from first principles atomic scale simulations, are included in device level TCAD simulations of a thin film CZTS(e) solar cell. We show how the interplay between atomic level and device level simulation improves agreement with experiments and provides, so far, unobtained insight into the device properties. With this new information at hand, we suggest routes for optimization of the solar cell performance.

- In **Chapter 4 (Paper 3, 4, 5):**
  A new method for treating electron-phonon coupling using NEGF transport calculations combined with Molecular dynamics (MD) is described. The method is then applied to extract the phonon-limited mobility of one-, two-, and three-dimensional semiconducting, and metallic systems. The results are compared to experimental values and calculations using other methods. Lastly the advantages and disadvantages of using the different methods to account for EPC are discussed.

- In **Chapter 5 (Paper 6):**
  We present DFT-NEGF calculations of a 19.6 nm silicon solar cell including at the same time electron-phonon and electron-photon interaction under working conditions. The calculated solar cell open-circuit voltage under sunlight illumination shows nice agreement with experimental values and the temperature, and intensity dependence is also captured. We include a short discussion of the massive potential of the method used, for the benchmarking of future PV devices.

- In **Chapter 6 (Paper 7):**
  The exciting electronic and optical properties of a newly discovered 2D material, with a built-in out-of-plane dipole, are studied. Based on the findings we suggest applications of this material in optoelectronic devices.

- In **Chapter 7 (Patent application, Manuscript in preparation):**
  We first describe the effect of confinement on the band structure of a semiconductor, and the challenges faced by conventional EMA models in describing confined systems properly. Secondly, we develop a new automated approach to sorting the DFT band structure of confined systems into ladders of subbands for subsequent fitting. As a proof of concept, the method is used to generate effective mass models of various confined silicon and InAs systems.

- In **Chapter 7:**
  We summarize the main results of the thesis and give an overall outlook.

Chapter 2

Methods

This chapter describes the methods applied throughout this thesis and serves as a reference point for basic equations and concepts discussed in the coming chapters. The chapter is divided into three sections. The first section details the methods used to describe the electronic structure of the systems investigated. In the second section the non-equilibrium Green's function (NEGF) method for quantum transport is introduced. In the third section we consider the different approaches used in this thesis to calculate the effect of lattice vibrations (phonons) on the electronic current.

2.1 Electronic structure methods

The majority of this thesis concerns the calculation of electronic transport of atomic-scale systems under a variation of influences. In order to calculate electronic transport, one must first choose an appropriate model for the electrons. Here we introduce the electronic structure methods applied in this thesis.

2.1.1 Density Functional Theory

Density Functional Theory (DFT) is an extremely popular approach to model electronic structure within materials science. It is a first principles model, which means no fitting parameters are used. Many variations of DFT with different levels of approximations have been developed, some of which are shown in Fig. 2.1. As indicated in Fig. 2.1 most DFT methods allow the treatment of systems with up to $\sim 10^3$ atoms included.

DFT takes advantage of the fact that the electronic many-body problem can be written as a functional of the total electron density $n(\mathbf{r})$. This idea was first put forward by Hohenberg and Kohn[18, 19] who proved that the total energy is a unique functional of the electronic density and that the density that minimizes the total energy is the exact ground state density, reducing the many body problem of considering a solid state system with N particles from a 3N-dimensional problem to a 3-dimensional one. As a result, the total energy E can be written as a functional of the electronic density and separated into terms of varying complexity:

$$E[n] = T[n] + \int d\mathbf{r}\, n(\mathbf{r}) v_{\text{ext}}(\mathbf{r}) + \frac{1}{2}\int\int d\mathbf{r} d\mathbf{r}' \frac{n(\mathbf{r})n(\mathbf{r}')}{|\mathbf{r}-\mathbf{r}'|} + E_{XC}[n]. \tag{2.1}$$

The first term is the kinetic energy, the second term is the interaction of the electron with an external field and the last two terms, describing different parts of the interaction of particles within the electron gas are called the Hartree and exchange-correlation energy respectively. The object is now to minimize Eq. (2.1) to obtain the

ground state density. Expressions for the kinetic and interaction energy functionals are however not known and approximations must be made. To evaluate the kinetic energy the vast majority of DFT codes uses some variation of the Kohn-Sham (KS) equations[19, 20]. The KS equations approach relies on the idea that the ground state density of an interacting system is the same as the ground state of an non-interacting system with an effective external potential. To evaluate the kinetic energy one constructs a fictional non-interacting reference system with the same electronic density as that of the interacting system subjected to the effective potential

$$v_{\mathbf{eff}}(\mathbf{r}) = v_{\mathbf{ext}}(\mathbf{r}) + \int \frac{n(\mathbf{r}')}{|\mathbf{r}-\mathbf{r}'|} d\mathbf{r}' + \frac{\delta \tilde{E}_{XC}[n]}{\delta n(\mathbf{r})}. \tag{2.2}$$

The electron density $n(\mathbf{r})$ and associated total energy is evaluated self-consistently; First the effective potential of the non-interacting reference system is evaluated using an initial guess of electron density, the effective potential is then used to solve the non-interacting single particle Schröedinger equation to obtain a new electron density, and this cycle is repeated until convergence is reached. A fraction of the kinetic energy is not captured using the KS equations and is subsequently absorbed in the exchange-correlation potential[19].

The exchange-correlation energy is a sum of two corrections to the Hartree interaction term. The exchange energy describes the repulsion that occurs due to the Pauli exclusion principle. Correlation describes the mutual avoidance of particles that lowers the coulomb repulsion energy. These two terms are treated at the same level of approximation as an exchange-correlation potential.

The two most popular approximations to the exchange-correlation are the Local Density Approximation (LDA) and the General Gradient Approximation (GGA) (see also Fig. 2.1). The LDA energy functional is given by [19]

$$E_{XC}^{\mathrm{LDA}} = \int d\mathbf{r}\, n(\mathbf{r}) \epsilon_{XC}^{\mathrm{hom}}[n(\mathbf{r})], \tag{2.3}$$

and describes the exchange-correlation interaction as an interaction with a homogeneous electron gas with exchange-correlation energy $\epsilon_{XC}^{\mathrm{hom}}$ and the same density of the real electron gas at the position $\mathbf{r}$.
The GGA functional is an improvement of the LDA expressions, including first order dependence on the electron density, and as a result it is more computationally costly.

In order to simplify treatment of the electron wave function close to the nuclei, many DFT codes replace the actual coulomb potential which is large and negative with a more smooth pseudo-potential including closely bound core electronic states in the description of the core. This is done to avoid rapidly varying electron wave functions near the core[19]. The available choices of pseudo-potentials varies from code to code. Codes that consider all electronic states rigorously are often referred to as all-electron codes and calculations using them are typically very computationally demanding.

The available basis set chosen to represent the single particle Kohn-Sham wavefunctions also depends on the program chosen. Most DFT codes are implemented using

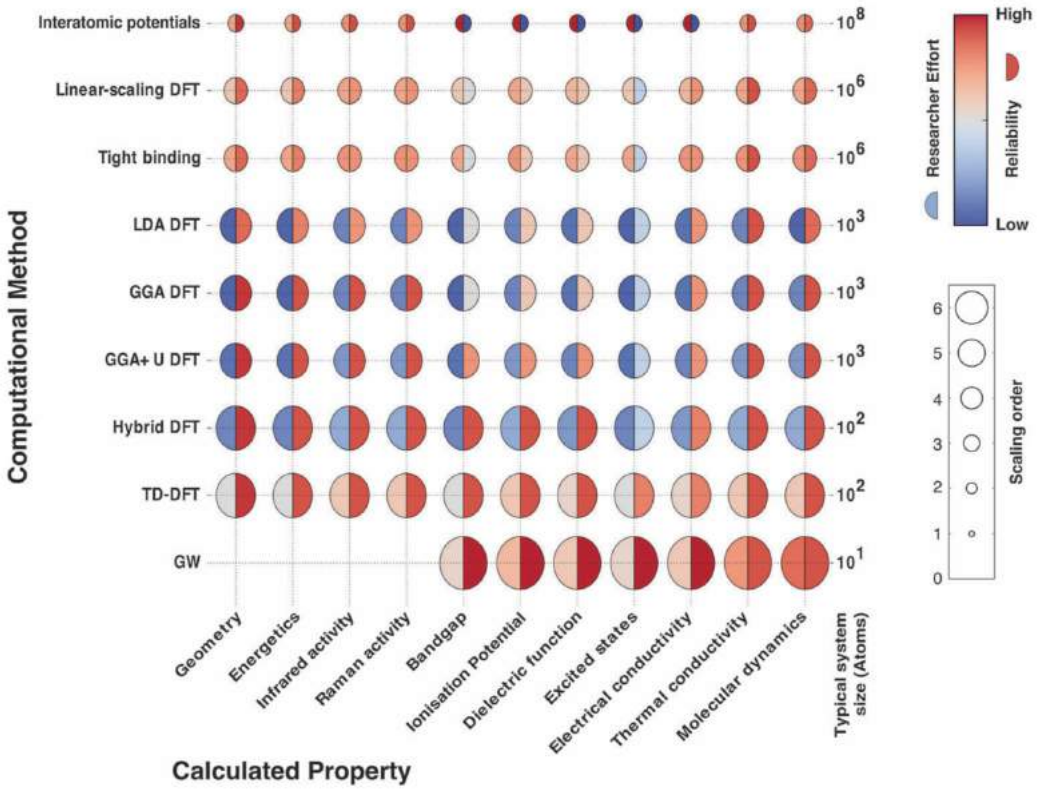

FIGURE 2.1: Map of different computational methods commonly used to calculate material properties. The circle size represents the scaling order of the computational effort with system size. The color on the left side of the circles represent the effort needed to calculate the material property indicated in the bottom row. The color on the right side represents the reliability of using the method for calculating the material property indicated in the bottom row. Adapted from [21]

a plane wave (PW) description, which is exact in the limit of using an infinite number of PWs. The flavor of DFT used throughout this thesis from the QuantumATK code uses a Linear Combination of Atomic Orbitals (LCAO) localized on the atom nucleus with a real space cutoff and pseudo-potentials to describe the core[3, 4, 22]. LCAO is typically a less computationally heavy approach than PW, at the expense of some precision. The LCAO basis we use is non-orthogonal, and as a result the usual Schrödinger equation is replaced with the following eigenvalue problem

$$\mathbf{H}\psi_k(\mathbf{r}) = \epsilon\mathbf{S}\psi_k(\mathbf{r}), \tag{2.4}$$

where $\mathbf{H}_{i,j} = \langle\phi_i|H|\phi_j\rangle$ is the Kohn-Sham Hamiltonian expanded in the LCAO basis $\{\phi_i\}$ and $\mathbf{S}_{i,j} = \langle\phi_i|\phi_j\rangle$ is the overlap matrix. As discussed in the following chapter, this choice of basis set is particularly convenient for investigating transport properties using NEGF, since the atomically localized basis set makes the separation of the Hamiltonian into leads and an interacting device region straightforward.

As an output of a ground state theory, the single particle Kohn-Sham eigenstates and energies do not provide a strictly accurate description of excited states. A famous consequence of this is the general underestimation of band gaps using standard LDA and GGA level DFT calculations. Many approaches to improve the description of

excited states from DFT have been developed. In Fig. 2.1 some of these are listed in order from low to high complexity. In hybrid functionals a fraction of exact exchange is included in the exchange-correlation potential to improve the band gap. In chapter 3 we will descrcibe the GGA + U method, which is a computationally cheap method to correct the band gap error. In spite of their apparent shortcomings, the Kohn-Sham wavefunctions have been successfully used for numerous studies of quantum transport problems[23, 24].

2.1.2 Effective Mass Approximation

A common simple model for the electronic structure is the effective mass approximation, where the band structure is described by a second order polynomial around the band minimum

$$\epsilon_{nk} = \frac{\hbar^2(k_x - k_{x0})^2}{2m_x^*} + \frac{\hbar^2(k_y - k_{y0})^2}{2m_y^*} + \frac{\hbar^2(k_z - k_{z0})^2}{2m_z^*} + \epsilon_{nk_0}, \tag{2.5}$$

where ϵ_{nk} is the electron energy of band number n, (k_x, k_y, k_z) is the electron wave vector, ϵ_{nk_0} is the energy of the band minimum, (k_{x0}, k_{y0}, k_{z0}) is the wave vector at the band minimum, and (m_x^*, m_y^*, m_z^*) are the anisotropic effective masses. Some versions of the effective mass approximation go beyond the second order polynomial description and include non-parabolicity effects we will discuss this further in chapter 7. Most commonly, the effective mass model for a system is obtained by fitting the parameters of the model (the effective masses) to the band structure of an infinite periodic crystal of the considered material. This band structure can either be calculated using first principles methods such as DFT, or measured experimentally from e.g. photoemission or inverse photoemission.

2.2 NEGF transport

The real-space representation of the Hamiltonian in DFT using a LCAO basis set allows for the straightforward separation of the system into an interacting device region (D) and noninteracting left (L) and right (R) electrode regions (leads) as illustrated in Fig. 2.2. The Hamiltonian and overlap matrix of the partitioned system then become

$$\mathbf{H} = \begin{bmatrix} \mathbf{H}_L & \mathbf{V}_{LD} & 0 \\ \mathbf{V}_{DL} & \mathbf{H}_D & \mathbf{V}_{DR} \\ 0 & \mathbf{V}_{RD} & \mathbf{H}_R \end{bmatrix}, \tag{2.6}$$

$$\mathbf{S} = \begin{bmatrix} \mathbf{S}_L & \mathbf{S}_{LD} & 0 \\ \mathbf{S}_{DL} & \mathbf{S}_D & \mathbf{S}_{DR} \\ 0 & \mathbf{S}_{RD} & \mathbf{S}_R \end{bmatrix}, \tag{2.7}$$

where the V matrices describes hopping between the left/right region and the device region, and we have assumed a device region large enough that no coupling directly between the electrodes occurs. We can now express our single particle Kohn-Sham Hamiltonian in terms of the unperturbed single particle retarded Green's functions defined as

$$\mathbf{G}_0 = [(\epsilon + i\eta)\mathbf{S} - \mathbf{H}]^{-1}, \tag{2.8}$$

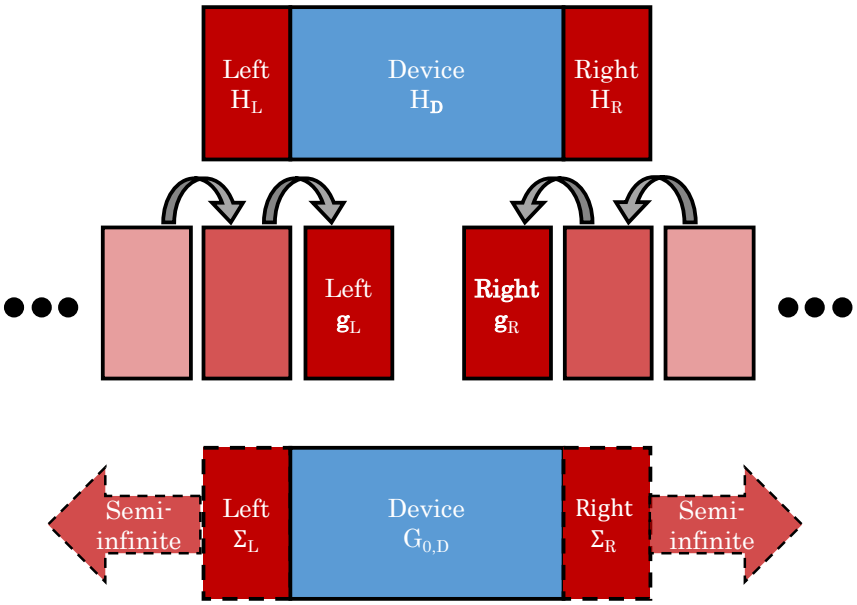

FIGURE 2.2: Sketch of the NEGF procedure. Top: First the system is partitioned into a central device (D) region and left (L) and right (R) electrode regions. Middle: The retarded surface Green's functions are calculated recursively from the left and right unit cells. Bottom: The self-energies of the left and right electrodes are connected to the device region through the expression Eq. (2.9) replacing the left and right region with semi-infinite leads.

where η is a positive infinitesimal. Combining Eq. (2.6),Eq. (2.7) and Eq. (2.8) and solving for the central part of the retarded Green's function matrix we recover the Green's function for the device region

$$\mathbf{G}_{0,D} = [(\epsilon + i\eta)\mathbf{S} - \mathbf{H} - \mathbf{\Sigma}_L - \mathbf{\Sigma}_R]^{-1}, \tag{2.9}$$

where $\mathbf{\Sigma}_L$ and $\mathbf{\Sigma}_R$ are the left and right self-energies describing the coupling of the device region to semi-infinite electrodes. The self-energies are given by the expression

$$\mathbf{\Sigma}_R = (\mathbf{V}_{D,\alpha} - \epsilon\mathbf{S}_{D,\alpha})\mathbf{g}^r_\alpha(\epsilon)(\mathbf{V}_{\alpha,D} - \epsilon\mathbf{S}_{\alpha,D}), \tag{2.10}$$

where $\mathbf{g}^r_\alpha$ is the surface Green's function of the electrode α which can be calculated using a recursive method in the case of a periodic electrode structure[25].

This entire procedure, illustrated in Fig. 2.2 is carried out using the commercial software QuantumATK[4]. In the case of a finite applied bias between the two electrodes the device Green's function is recalculated taking into account the effects of the potential drop on the electronic density. The electronic properties of the considered system are extracted from the Green's functions introduced above.

2.2.1 Interacting current

One property that we will extract several times throughout this thesis is the electronic current since it is the observable most relevant for electronic applications. The current flowing into lead α including interactions in the device region is given by the

Meir-Wingreen equation [26, 27]

$$\begin{aligned} I_\alpha =& \frac{G_0}{e}\int_{-\infty}^{\infty} d\epsilon\, \mathcal{T}_\alpha, \\ \mathcal{T}_\alpha =& \mathrm{Tr}\{\mathbf{\Sigma}_\alpha^<(\epsilon)\mathbf{G}_D^>(\epsilon) - \mathbf{\Sigma}_\alpha^>(\epsilon)\mathbf{G}_D^<(\epsilon)\}, \end{aligned} \tag{2.11}$$

where $G_0 = \frac{2e^2}{h}$ is the conductance quanta, $\mathbf{G}_D^{\gtrless}(\epsilon)$ is the lesser/greater device Green's function including interactions in the device region and $\mathbf{\Sigma}_\alpha^{\gtrless}(\epsilon)$ is the lesser/greater self-energy of lead α giving the rate of electrons/holes coming from the lead into the device region. The lesser and greater self-energies are given by

$$\mathbf{\Sigma}_\alpha^< = i\mathbf{\Gamma}_\alpha f_\alpha, \quad \mathbf{\Sigma}_\alpha^> = -i\mathbf{\Gamma}_\alpha(1-f_\alpha), \tag{2.12}$$

where $f_\alpha = 1/(e^{(\epsilon-\mu_\alpha)/k_BT}+1)$ is the Fermi Dirac distribution function with chemical potential μ_α and $\mathbf{\Gamma}_\alpha$ is the broadening of device states due to the coupling with the semi-infinite states of lead α. We can express the broadening in terms of the lead self-energies as follows

$$\mathbf{\Gamma}_\alpha = i(\mathbf{\Sigma}_\alpha - \mathbf{\Sigma}_\alpha^\dagger). \tag{2.13}$$

The lesser and greater Green's function are given by the steady state Keldysh equations [27–30]

$$\mathbf{G}_D^{\gtrless} = \mathbf{G}_D\left[\sum_\alpha \mathbf{\Sigma}_\alpha^{\gtrless} + \mathbf{\Sigma}_{\mathrm{int}}^{\gtrless}\right]\mathbf{G}_D^\dagger, \tag{2.14}$$

and the full retarded Green's function $\mathbf{G}$ is given by Dysons equation[27–30]

$$\mathbf{G}_D = \mathbf{G}_{0,D} + \mathbf{G}_{0,D}\mathbf{\Sigma}_{\mathrm{int}}\mathbf{G}_D, \tag{2.15}$$

where we have introduced the lesser/greater $\mathbf{\Sigma}_{\mathrm{int}}^{\gtrless}$ and retarded $\mathbf{\Sigma}_{\mathrm{int}}$ interaction self-energies, accounting explicitly for additional interactions that occur inside the device region. In this thesis we will calculate the current due to light-matter interaction (derived in chapter 5) and due to electron-phonon coupling which we will describe in the following section.

2.2.2 Noninteracting current

We can consider a non-interacting device region by setting $\mathbf{\Sigma}_{\mathrm{int}} = \mathbf{\Sigma}_{\mathrm{int}}^{\gtrless} = 0$, and after some rewriting we recover from Eq. (2.11) the well known Landauer-Büttiker formula

$$I_0 = \frac{G_0}{e}\int_{-\infty}^{\infty} d\epsilon\, \mathcal{T}_0(\epsilon)[f_L(\epsilon) - f_R(\epsilon)] \tag{2.16}$$

$$\mathcal{T}_0 = \mathrm{Tr}\{\mathbf{\Gamma}_L\mathbf{G}_{0,D}\mathbf{\Gamma}_R\mathbf{G}_{0,D}^\dagger\} \tag{2.17}$$

giving the non-interacting current.

2.3 Electron-phonon coupling

One type of interaction, which will be considered in chapters 4 and 5, is the interaction between the current carrying charges and the vibrations of the lattice at finite temperature also known as electron-phonon coupling (EPC). In this section we will introduce basic concepts of the different methods used in the thesis to include electron-phonon coupling.

2.3.1 Calculating phonons

To obtain the eigenvectors $\mathbf{e}_\lambda$ and frequencies Ω_λ of the phonon modes λ we use the frozen phonon method[31–33]. The dynamical matrix is given by

$$\mathbf{D}_{i\mu,j\nu} = \frac{1}{\sqrt{M_i M_j}}\mathbf{K}_{i\mu,j\nu}, \tag{2.18}$$

where M_i are the atomic masses of the ions in the system and $\mathbf{K}_{i\mu,j\nu}$ is the Hessian matrix obtained by displacing each atom i away from its relaxed position along direction μ and evaluating the force F on the atom j in direction ν. Using finite difference $\mathbf{K}$ is obtained from

$$\mathbf{K}_{i\mu,j\nu} = \frac{\partial^2 E}{\partial r_{i,\mu}\partial r_{j,\nu}} = \frac{F_{j,\nu}(\Delta_{i,\mu}) - F_{j,\nu}(-\Delta_{i,\mu})}{2\Delta_{i,\mu}}, \tag{2.19}$$

where Δ is a small displacement. The phonon eigenvectors and energies are then obtained from the dynamical matrix by solving the equation

$$\mathbf{D}\mathbf{e}_\lambda = \Omega_\lambda^2 \mathbf{e}_\lambda. \tag{2.20}$$

The force F can be evaluated directly from DFT or, when applicable, using classical inter-atomic potentials.

In practice, when calculating the Hessian matrix, the dynamical part of the system is repeated a few times along periodic directions before performing the displacements of atoms. These repetitions can make the evaluation of the dynamical matrix from DFT extremely computationally demanding, especially in bulk systems where all directions are periodic.

2.3.2 Lowest Order Expansion

One way to derive an expression for the current due to EPC in the device region, is to start from the Meir-Wingreen equation Eq. (2.11) introducing a phonon self-energy $\mathbf{\Sigma}_{ph}$ as the interaction self-energy. Assuming free uncoupled phonons one can derive the following expressions for the phonon self-energies

$$\mathbf{\Sigma}^{\gtrless}_{ph}(\epsilon) = \sum_\lambda i \int_{-\infty}^{\infty} \frac{d\Omega_\lambda}{2\pi} \mathbf{M}_\lambda \mathbf{D}_0^{\gtrless}(\Omega_\lambda)\lambda \mathbf{G}^{\gtrless}(\epsilon - \Omega_\lambda)\mathbf{M}_\lambda, \tag{2.21}$$

$$\mathbf{\Sigma}_{ph} = \frac{1}{2}(\mathbf{\Sigma}^{>}_{ph} - \mathbf{\Sigma}^{<}_{ph}) - \frac{i}{2}\mathcal{H}(\mathbf{\Sigma}^{>}_{ph} - \mathbf{\Sigma}^{<}_{ph}), \tag{2.22}$$

where $\mathbf{D}_0^{\gtrless}$ are the free greater/lesser bosonic phonon Green's functions, $\mathbf{M}_\lambda$ is the electron-phonon coupling matrix and $\mathcal{H}$ is the Hilbert transform. This is known as the self-consistent Born approximation (SCBA) and can be solved iteratively to

evaluate the current including EPC. However, the computational time needed for this evaluation means it is only a viable approach for systems containing a handful of atoms. In the case of weak EPC the SCBA current expression can be expanded to lowest (second) order in $\mathbf{M}$ arriving at the Lowest Order Expansion (LOE) current expression

$$I_{LOE} = \sum_{\lambda} \frac{G_0}{e} \int_{-\infty}^{\infty} d\epsilon [\mathcal{T}_{\lambda}^{ems}(\epsilon) F_{\lambda}^{ems}(\epsilon) + \mathcal{T}_{\lambda}^{abs}(\epsilon) F_{\lambda}^{abs}(\epsilon)], \tag{2.23}$$

where the transmission due to emission/absorption of a phonon is given by

$$\begin{aligned} \mathcal{T}_{\lambda}^{ems/abs} =& \mathrm{Tr}\{\mathbf{M}_{\lambda} \tilde{\mathbf{A}}_L^{\pm} \mathbf{M}_{\lambda} \mathbf{A}_R^{\mp}\} + \mathrm{Im}[\mathrm{Tr}\{\mathbf{M}_{\lambda} \mathbf{A}_R^{\pm} \mathbf{\Gamma}_L^{\pm} \mathbf{G}_0^{\pm} \mathbf{M}_{\lambda} \mathbf{A}_R^{\mp}\}] \\ &+ \mathrm{Tr}\{\mathbf{M}_{\lambda} \mathbf{A}_R^{\mp} \mathbf{\Gamma}_L^{\mp} \mathbf{G}_0^{\mp} \mathbf{M}_{\lambda} \mathbf{A}_L^{\pm}\}, \end{aligned} \tag{2.24}$$

where $\mathbf{A}_{\alpha} = \mathbf{G}_0 \mathbf{\Gamma}_{\alpha} \mathbf{G}_0^{\dagger}$ is the spectral function of lead α and $\tilde{\mathbf{A}}_{\alpha} = \mathbf{G}_0^{\dagger} \mathbf{\Gamma}_{\alpha} \mathbf{G}_0$ is the time-reversed spectral function of lead α and we have introduced the shorthand $\mathbf{G}_0^{\pm} = \mathbf{G}_0(\epsilon \pm \hbar\Omega_{\lambda}/2)$. The universal prefactors are given by

$$\begin{aligned} F_{\lambda}^{ems} =& f_L(1 - f_R^{+})(f_{\lambda} + 1) - f_R^{-}(1 - f_L) f_{\lambda}, \\ F_{\lambda}^{abs} =& f_L(1 - f_R^{-}) f_{\lambda} - f_R^{+}(1 - f_L)(f_{\lambda} + 1), \end{aligned} \tag{2.25}$$

where $f_{\lambda} = 1/(e^{\hbar\Omega_{\lambda}/k_B T} - 1)$ is the Bose-Einstein distribution function. In Eq. (2.24) and Eq. (2.25) we have assumed Γ-point phonons with zero momentum ($q = 0$).
Here we simply state the current equations, while the rigorous derivation of these equations can be found elsewhere[34, 35][*Paper 5*].
In the case of finite q, special care must be taken to ensure momentum conservation[*Paper 5*].

The electron-phonon coupling matrix $\mathbf{M}_{\lambda}$ is to lowest order given by the Hamiltonian derivative with respect to coordinate position $\nabla_{\mathbf{r}}\mathbf{H}$[34, 35][*Paper 5*]. In the harmonic approximation $\nabla_{\mathbf{r}}\mathbf{H}$ can be calculated from finite difference as in Sec. 2.3.1 and the electron-phonon coupling is given by

$$\mathbf{M}_{\lambda,ij} = \sum_{I\nu} \langle \phi_i | \frac{\partial \mathbf{H}}{\partial r_{I\nu}} | \phi_j \rangle \, \mathbf{e}_{\lambda,I\nu} \sqrt{\frac{\hbar}{2M_I \Omega_{\lambda}}}. \tag{2.26}$$

The dynamical matrix, $\mathbf{D}$, and Hamiltonian derivative, $\nabla_{\mathbf{r}}\mathbf{H}$ in particular, are computationally demanding to calculate from first principles, and are often out of reach for systems with large device regions. In *repeated two-probe systems* the device region is simply a repetition of the electrode unit-cell along the transport direction and as such $\mathbf{D}$ and $\nabla_{\mathbf{r}}\mathbf{H}$ can be obtained from the electrode unit-cell, reducing the calculation time drastically[Paper 5].

Calculating the inelastic LOE current in Eq. (2.23) involves, for each phonon mode, the energy integral over traces, which becomes a daunting computational task for large systems with many phonon modes. The energy dependent left/right spectral functions included in the traces are related to the density of states (DOS) coming from left/right moving states in the leads. E.g. for metallic systems where the DOS is approximately constant on the scale of the phonon energy $\hbar\Omega_{\lambda}$, one can assume that the spectral functions are constant with respect to energy. This approximation, known as the Wide Band Approximation (WBA), reduces the LOE current problem

to calculating the traces in Eq. (2.23) only once per phonon mode.

An alternative to the perturbation theory approach that has been used previously to estimate the impact of EPC on the current, is stochastic sampling of lattice vibrations using Monte Carlo (MC) or configuration sampling using Molecular Dynamics (MD) simulations[36–42][*Paper 3*]. These methods, which go beyond the harmonic approximation, often yield good results and are much more direct, conceptually simple and memory efficient compared to LOE. The memory efficiency comes from the fact that only the non-interacting Landauer-Büttiker transmission in Eq. (2.17) needs to be evaluated. The inclusion of EPC through sampling of configuration using MD, will be discussed in more detail in chapter 4.

2.3.3 Special Thermal Displacement

In order to properly sample all the atomic displacements of the investigated system when performing the stochastic sampling many transmission calculations must be performed at an additional computational cost. In the case of MC sampling of displacements along eigenvectors of the phonon-modes[36, 37] this computational cost scales linearly with the number of atoms, making the analysis of large systems difficult.

Recently a new method for calculating the thermally averaged current for sufficiently large structurally periodic systems was developed[*Paper 4*]. Here the inclusion of electron-phonon coupling is reduced to the evaluation of the non-interacting Landauer-Büttiker transmission $\mathcal{T}_0$ of the system under a single, cleverly chosen, displacement of atoms named the Special Thermal Displacement (STD). The work was inspired by a previous paper introducing a similar approach for the calculation of thermally renormalized bulk properties[43]. The starting point for the derivation of the STD is the expression for the thermally averaged current in the adiabatic limit

$$I(V,T) = \frac{G_0}{e}\int_{-\infty}^{\infty} d\epsilon \langle \mathcal{T}(\epsilon,T)\rangle [f_L - f_R], \tag{2.27}$$

$$\langle \mathcal{T}(\epsilon,T)\rangle = \Pi_\lambda \int_{-\infty}^{\infty} du_\lambda \frac{1}{\sqrt{2\pi}\sigma_\lambda} e^{-u_\lambda^2/2\sigma_\lambda^2} \mathcal{T}(\epsilon,\{\mathbf{u}_\lambda\}), \tag{2.28}$$

where $\mathbf{u}_\lambda$ represents a displacement of atoms in the device region along the phonon eigenvector $\mathbf{e}_\lambda$ with root mean square given by the Gaussian width

$$\sigma_\lambda = l_\lambda\sqrt{2f_\lambda + 1} = \sqrt{\langle \mathbf{u}_\lambda^2\rangle}, \tag{2.29}$$

and $l_\lambda = \sqrt{\hbar/2M_I}$ is the characteristic length of the phonon mode λ. In previous approaches the integral in Eq. (2.28) is evaluated numerically using e.g. Monte Carlo sampling. If we consider the Taylor expansion of the transmission in Eq. (2.28) around the relaxed atomic positions with respect to the displacements $\mathbf{u}_\lambda$ we have

$$\mathcal{T}(\epsilon,\{\mathbf{u}_\lambda\}) = \mathcal{T}_0(\epsilon) + \sum_\lambda \frac{\partial \mathcal{T}(\epsilon,\{\mathbf{u}_\lambda\})}{\partial \mathbf{u}_\lambda}\mathbf{u}_\lambda + \sum_\lambda \frac{\partial^2 \mathcal{T}(\epsilon,\{\mathbf{u}_\lambda\})}{\partial \mathbf{u}_\lambda^2}\frac{\mathbf{u}_\lambda^2}{2} + \mathcal{O}(\sigma^3). \tag{2.30}$$

What was shown in [43] for the case of the dielectric function of bulk systems is that the sampling of displacements can be replaced by a single displacement given by

$$\mathbf{u}_{\mathrm{STD}}(T) = \sum_{\lambda} s_\lambda (-1)^{\lambda-1} \sigma_\lambda(T) \mathbf{e}_\lambda, \tag{2.31}$$

where s_λ is the sign of the first finite element of the eigenvector $\mathbf{e}_\lambda$, included to avoid canceling between phonon modes with similar eigenvectors. If we consider now the expansion of the transmission in Eq. (2.28) with respect to the single displacement $\mathbf{u}_{\mathrm{STD}}$ we have

$$\begin{aligned}\mathcal{T}(\epsilon, \mathbf{u}_{STD}) =& \mathcal{T}_0(\epsilon) - \sum_{\lambda} \frac{\partial \mathcal{T}(\epsilon, \mathbf{u}_\lambda)}{\partial \mathbf{u}_\lambda} s_\lambda (-1)^{\lambda-1} \sigma_\lambda(T) \\ &+ \sum_{\lambda,\lambda'} \frac{\partial^2 \mathcal{T}(\epsilon, \mathbf{u}_\lambda)}{\partial \mathbf{u}_\lambda \partial \mathbf{u}_{\lambda'}} s_\lambda s_{\lambda'} (-1)^{\lambda+\lambda'-2} \frac{\sigma_\lambda(T)\sigma_{\lambda'}(T)}{2} + \mathcal{O}(\sigma^3).\end{aligned} \tag{2.32}$$

For very large systems, phonon modes λ and $\lambda+1$ are nearly degenerate, making the partial derivatives in Eq. (2.32) coincide. As a result, subsequent terms in the first order part of Eq. (2.32) cancel, as do the second order terms where $\lambda \neq \lambda'$. In the limit of very large systems we therefore have

$$\lim_{N\to\infty} \mathcal{T}(\epsilon, \mathbf{u}_{STD}) = \mathcal{T}_0(\epsilon) + \sum_{\lambda} \frac{\partial^2 \mathcal{T}(\epsilon, \mathbf{u}_\lambda)}{\partial \mathbf{u}_\lambda^2} \frac{\sigma_\lambda^2(T)}{2} + \mathcal{O}(\sigma^4) = \langle \mathcal{T}_0(\epsilon, T) \rangle, \tag{2.33}$$

where the final equality can be obtained by combining Eq. (2.30) and Eq. (2.28).
In summary, it is possible to obtain the thermally averaged current Eq. (2.27), for large systems with many repetitions of the same unit cell, by performing a single displacement of the atomic coordinates along the vector $\mathbf{u}_{\mathrm{STD}}(T)$, and calculating the non-interacting Landauer-Büttiker current. This represents a huge improvement in computational time for large systems, since the bottleneck is reduced to evaluating the dynamical matrix.

Close to a gap in the phonon band structure, it is possible to have a contribution from the first-order term in Eq. (2.32) for the modes that have energies right at the edge of the gap, since the subsequent mode will not have the same energy and consequently the term is not canceled[43]. However in the limit of large N, with 3N phonon modes, the contribution from a single mode will be insignificant and can be ignored.

Fig. 2.3 shows the calculated on and off current of a silicon *n-i-n* junction including ∼2000 atoms calculated using the STD-approach and compared to the same calculation using the LOE approach outlined in Sec. 2.3.2. The results compare nicely even though the STD calculation is at least 6000 times less expensive than LOE for this system if including the full finite bias potential.

2.4 Summary

In this chapter we have introduced the electronic structure and transport methods used throughout the thesis. We also accounted for several different ways to include electron-phonon coupling discussing only briefly their strengths and weaknesses. More detailed comparisons of these methods will be provided in chapter 4. In the

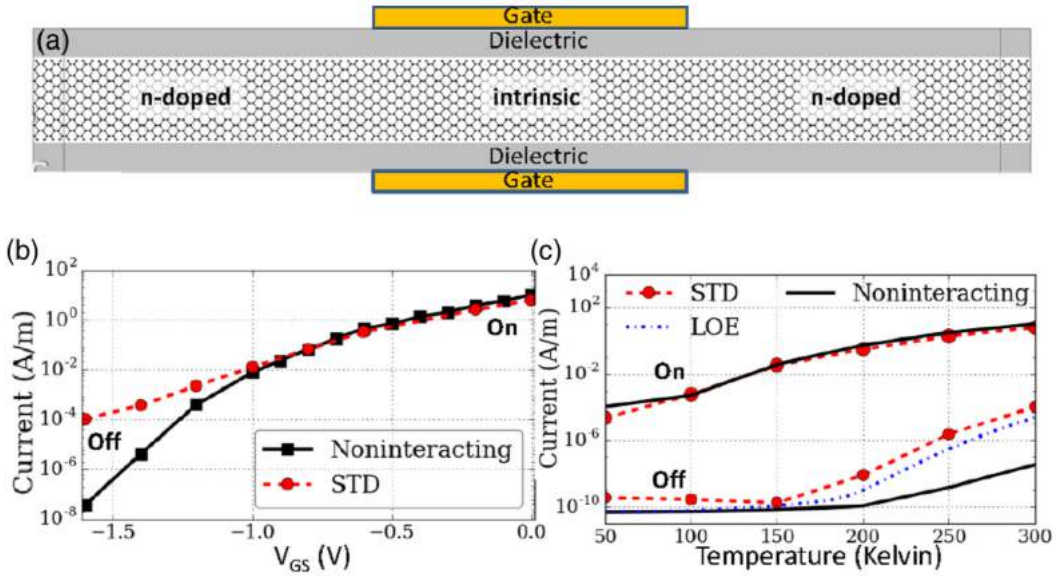

FIGURE 2.3: (a) silicon *n-i-n* juntion device setup including ∼2000 atoms. (b) Source-drain current as a function of gate voltage V_G with a source-drain voltage of $V_{SD} = 0.1\,\mathrm{V}$ calculated using the non-interacting Landauer-Büttiker expression. (c) On/off current as a function of temperature with $V_G = -1.6\mathrm{V}$ (on) and $V_G = -0\mathrm{V}$ (off). Taken from *Paper 4*

following chapter we begin our investigation of ways to improve TCAD tools by bridging them with the first principles methods introduced in this chapter.

Chapter 3

Multiscale study of the CZTS(e) thin-film solar cell

In continuum TCAD device models, material parameters are typically based on experimental measurements or first principles calculations performed on bulk materials[44]. As a result, they often fail to properly describes systems that are inherently "un-bulk-like". Later in this thesis we will study, for instance, the effect of confinement on the electronic structure in nanowire systems and how well the continuum approach to confinement works when the nanowire diameter becomes just a few nanometers.

Another important, un-bulk-like component of any semiconductor device, that can impact performance, is the interface between layers of materials. This could for example be the interconnects between semiconductors and metallic leads, where the Schottky barrier could impede transport across the interface[45] or interfaces between semiconductors, where for instance band bending or rough non-epitaxial surfaces can lead to unwanted electronic resistances in the device[46]. These heterointerfaces play an increasingly important role in optical and electronic devices due to miniaturization and to the continuing trend of introducing new materials to tailor the desired device properties[14].

In this chapter, which provides a review of results in paper 1 and 2, we will account for a multiscale approach to simulating semiconductor devices including explicitly from first principles the atomic-scale details of important material interfaces. The suggested approach could in principle be applied to any layered device where the interfaces are often known to impact the device, but not well understood. We choose, as our case study, two materials which have gained much interest in the photovoltaics community as potential new candidates for the absorber layer in thin-film solarcells.

3.1 The CZTS(e) solar cell

Solar cell technology based on silicon absorbers still makes up over 90% of the solar cell market[13]. This is in spite of the fact that silicon is only a weakly absorbing material. The indirect band gap of silicon means that absorption of a photon must be accompanied by the emission or absorption of a phonon. Such a two-excitation process is of lower probability than absorption in a direct band gap semiconductor and consequently it happens at a slower rate.

The success of a solar cell technology is based primarily on the relation between

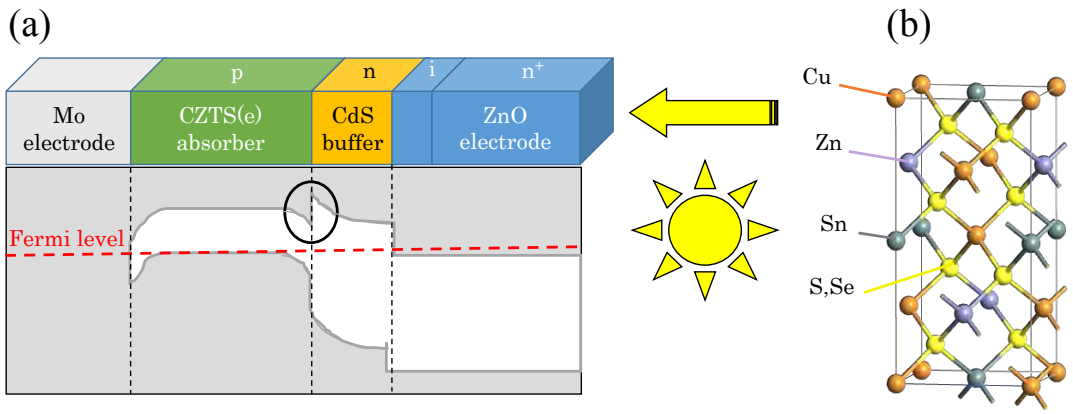

FIGURE 3.1: (a) Typical CZTS(e) solar cell device and related device band structure. (b) CZTS unit-cell in the zinc-blende crystal phase.

the efficiency of converting solar energy into electrical current and the cost of producing the solar cell. As a result, much research throughout the years has gone into technologically improving the efficiency of the silicon absorber layer[13]. One example is the addition of a reflective back layer to keep photons inside the silicon for longer, improving the chances that they get absorbed[47, 48].

Even with the improvements to silicon absorption, thick slabs of silicon of several hundred micron are still typically used in conventional wafer based solar cells[13]. The materials contributes up to 50% of the total cost of producing todays silicon solar cells, so reducing the absorber layer thickness without loosing efficiency could greatly improve the cost/efficiency relation[13, 48].

Thin-film solar cells using direct band gap absorber materials, could potentially improve the efficiency and reduce cost compared to their silicon based counterparts since high absorption of photons can be obtained using only hundreds of nanometer thick absorber layers. Thin-film solar cells based on CdTe and $CuIn_xGa_{1-x}Se_2$ (CIGS) absorber layers are already commercially successful and have carved out a part of the market for themselves[13]. However both of these absorber materials include scarce elements (Te,In,Ga) increasing production cost and making them unfit for the large scale production needed to replace the burning of fossil fuels. Replacing then the rare elements in CIGS with the earth abundant elements Zn and Sn in adjacent groups in the periodic table you get $Cu_2ZnSnSe_4$ (CZTSe, band gap 1.0 eV), Cu_2ZnSnS_4 (CZTS, band gap 1.5 eV) and their alloy $Cu_2ZnSnS_xSe_{4-x}$ (CZTSSe, tunable band gap 1.0-1.5 eV) which are direct band gap absorbers consisting only of earth abundant materials[13, 49–51]. To indicate all three materials in general terms we use the notation CZTS(e).

Fig. 3.1a shows a typical CZTS(e) solar cell device band diagram with a p-type CZTS(e) absorber layer where electron/hole-pairs are created. The electrons travel along the conduction band towards the transparent metal-oxide top electrode while holes are picked up by the bottom electrode creating a current across the device. A thin layer of n-type CdS is typically included as the n-type heterojunction partner of CZTS(e), with which the best conversion efficiencies reported so far have been achieved [52, 53]. Fig. 3.1b shows the crystal structure of CZTS and CZTSe.

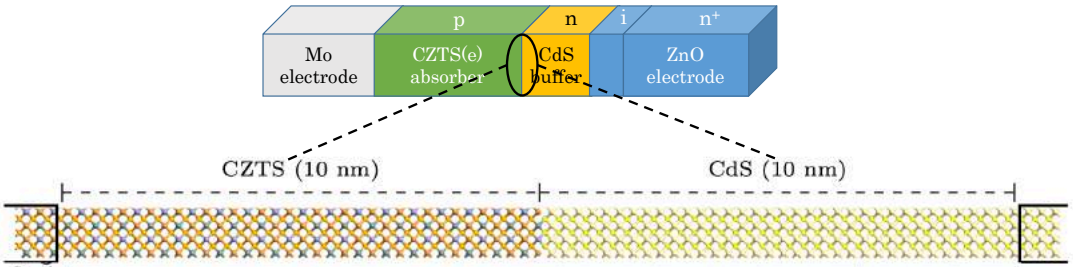

FIGURE 3.2: Illustration of multi scale approach. Continuum TCAD model is used to describe the full solar cell device while critical "un-bulk-like" component (in this case the CZTS(e)/CdS interface) is modeled using first principles calculations. The structure shown is used to simulate the 100/100 interface of CZTSe (left) and CdS (right). The supercell is more than five times larger than that used in previous work[54] and are based on device calculations that ensure converged band adjustment. Partly adapted from Paper 1.

3.2 Multiscale modeling approach

So far efficiency has been lacking in solar cells based on CZTS(e). As noted in a number of review papers [55–57], loss mechanisms at the CZTS(e)/CdS interface (Highlighted by a black circle in Fig. 3.1) due to unfavorable band alignment is believed to be one of the reasons why laboratory-scale CZTS(e) solar cells still lag far behind their theoretical maximum efficiency. In Fig. 3.1a we have drawn what is known as a "spike" in the conduction band offset (CBO) between CZTS(e) and CdS. The sign convention of the CBO and valence band offset (VBO) is such that a positive CBO means that the CdS conduction band lies above the CZTS(e) conduction band. A positive (negative) CBO in this case, is known as conduction band spike (cliff).

Multiscale models, where parameters of device level TCAD models are calibrated to account for properties simulated in more detail, are often used to study complex devices[58, 59]. To investigate the potentially dramatic consequences of an unfavorable band alignment of the CZTS(e)/CdS interface on solar cell efficiency, we have performed multiscale modeling where first principles studies of the interface CBO are carried out and relevant information is extracted and used to calibrate TCAD device level simulations of the solar cell efficiency.

The workflow of this multiscale model is illustrated in Fig. 3.2. Device level modeling is performed by a finite element drift-diffusion calculation as implemented in the software SCAPS[44].

3.3 First principles band alignment calculation

At the atomic level we wish to extract the CBO and VBO using first principles calculations. Previously, methods to obtain VBO and CBO from first principles have been reviewed[60]. A modeling method based on bulk calculations with periodic boundary conditions (PBC) in all directions has gained popularity due excellent agreement with experiments[61–63]. In this section we will first account for this method based on the description in [54], and discuss its strengths and weaknesses. We will then introduce an alternative method based on DFT-NEGF calculations and review the

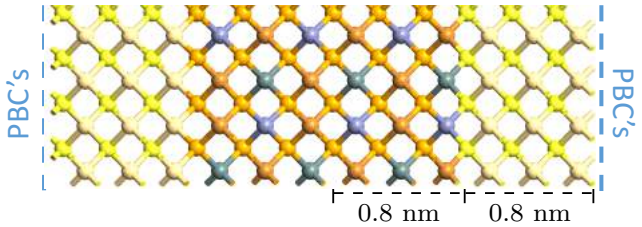

FIGURE 3.3: Periodic supercell containing the (100)/(100) interface of CZTS and CdS, dimensioned as in previously reported calculations [54]. Taken from Paper 1.

results of this method compared to experiments and the results of previous studies using the bulk approach.

3.3.1 Bulk approach

The bulk approach to calculating the CBO between two materials A and B is inspired by the photoemission measurement. In this method, the energy positions of the valence bands of materials A and B are first calculated separately in the two unstrained bulk materials with respect to a reference energy unique to each bulk calculation (for example, the position of a core level). This is done using an all electron code where the energy of deep lying states are readily available and the valence band position is often reliable. Then, an explicit interface calculation (see Fig. 3.3) is employed to align the two valence band positions to a common energy reference, which can be a core level or the averaged local potential. This interface calculation is typically done using standard GGA level DFT due to the size of the interface supercell (∼100 atoms). The CBO offset is then obtained from

$$\Delta E_C(A/B) = \Delta E^B_{VBM',C'} - \Delta E^A_{VBM,C} + \Delta E_{C',C} + \Delta E_g(A/B) \tag{3.1}$$

where $\Delta E^{A(B)}_{VBM,C(C')}$ is the valence band maximum with respect to the core level $C(C')$ calculated separately for material A(B), $\Delta E_{C',C}$ is the difference between the core levels in the two materials calculated using the interface supercell and $\Delta E_g(A/B)$ is the difference in band gap usually obtained from experiments, or from a third calculation of the separate materials, using the computationally heavy GW or hybrid functionals to obtain reasonable band gaps.

The power of this method is that it separates the problem of getting reasonable band gaps from the interface analysis. As such, you can simulate the big interface (Fig. 3.3) using a relatively computationally cheap DFT calculation as long as $\Delta E_{C',C}$ can be calculated reliably. The separation of the problem is however also the main weakness of this approach, since it ignores effects of the interface on the electronic structure near the Fermi-level. Strain, surface reconstruction and localized interface defects (e.g. dislocation) are not taken into account when evaluating the valence band position and band gap. Furthermore a setup, like the one shown in Fig. 3.3 with two interfaces separated by 1.6 nm is hardly a good representation of the real-world device shown in Fig. 3.1. With slabs of 1.6 nm thickness like those shown in Fig. 3.3, confinement effects and interaction between the interfaces could lead to errors in the calculation of the CBO.
We will see later in this chapter that tails of the CZTS(e) conduction band states penetrate ∼1 nm into the gap of CdS. As such, in the periodic cell in Fig. 3.3, states will

tunnel into the bulk of the CdS layer. In general, convergence of $\Delta E_{C',C}$ with respect to slab size is also not trivial in this approach.

3.3.2 DFT-NEGF approach

Using DFT-NEGF we will study the CZTS(e)/CdS interface directly. NEGF is ideal for interfaces, since it uses semi-infinite boundary conditions at the left and and right side of the system allowing us to setup the calculation supercell shown in Fig. 3.2[1]. In this setup we consider a single interface (with no repetitions) separated by bulk CZTS(e) and bulk CdS at the left and right side respectively. Even though these layers are not completely bulk in the actual device the thickness of the individual layers ($\sim$100 nm) ensures that the material are approximately bulk-like far from the interface. We believe such a NEGF-setup comes much closer to capturing the true nature of the interface than the previous models based on periodic boundary conditions.

3.3.3 Band gap correction with DFT + U

In order to extract the CBO directly from the interface setup in Fig. 3.2 we must assure that we get the correct band gaps of either material from the DFT calculation. It is well known that the band gaps of CZTS(e) and CdS are underestimated with the conventional LDA or GGA level approximation to the exchange-correlation functional[54]. We therefore use the semi-empirical Hubbard correction where an additional energy term is added to the usual GGA-PBE exchange-correlation functional given by

$$E_U = \frac{1}{2}\sum_{\mu} U_\mu \left(n_\mu - n_\mu^2\right). \tag{3.2}$$

In Eq. (3.2) n_μ is the projection onto an atomic shell and U is chosen to reproduce the experimental band gap in the bulk unit cell of either material. This method is a computationally cheap way to correct for the self-interaction of localized electrons in strongly correlated systems [64].

In Fig. 3.4, we compare the density of states (DOS) of bulk CZTSe and CdS calculated with and without the Hubbard correction term[2]. As expected the band gaps are opened and the valence bands of d-like character for Zn and Cd are down-shifted in energy. This is very similar to the effects seen when using hybrid functionals on CZTS, indicating a high degree of self-interaction error in these systems[65].

3.3.4 Setting up the interface

Several different interfaces can be constructed between CZTS(e) and CdS. Here we consider the CZTS(e)(100)/CdS(100) interface, which has relatively low strain of $\sim$2.5% for CZTSe but higher strain in the case of CZTS. We can justify the choice of (100)/(100) interface orientation for the case of CZTS based on reported transmission electron microscopy results, which consistently show a (100)-oriented CZTS/CdS epitaxial interface[66, 67]. This also justifies considering the CZTS(e)/CdS interface

[1] Electronic structure calcualtions were performed using double zeta polarized (DZP) basis set, and GGA-PBE exchange-correlation potential. We sampled the Brillouin Zone (BZ) using 5x3x1 and 5x3x3 Monkhorst-Pack grids for the device and the bulk systems respectively.

[2] For CZTS(e) we used $U = 5.5$ eV. For CdS we used $U = 17.4$ eV. The term was added on all d-orbitals. The DOS was calculated using a 11x11x11 Monkhorst-Pack grid to sample the BZ.

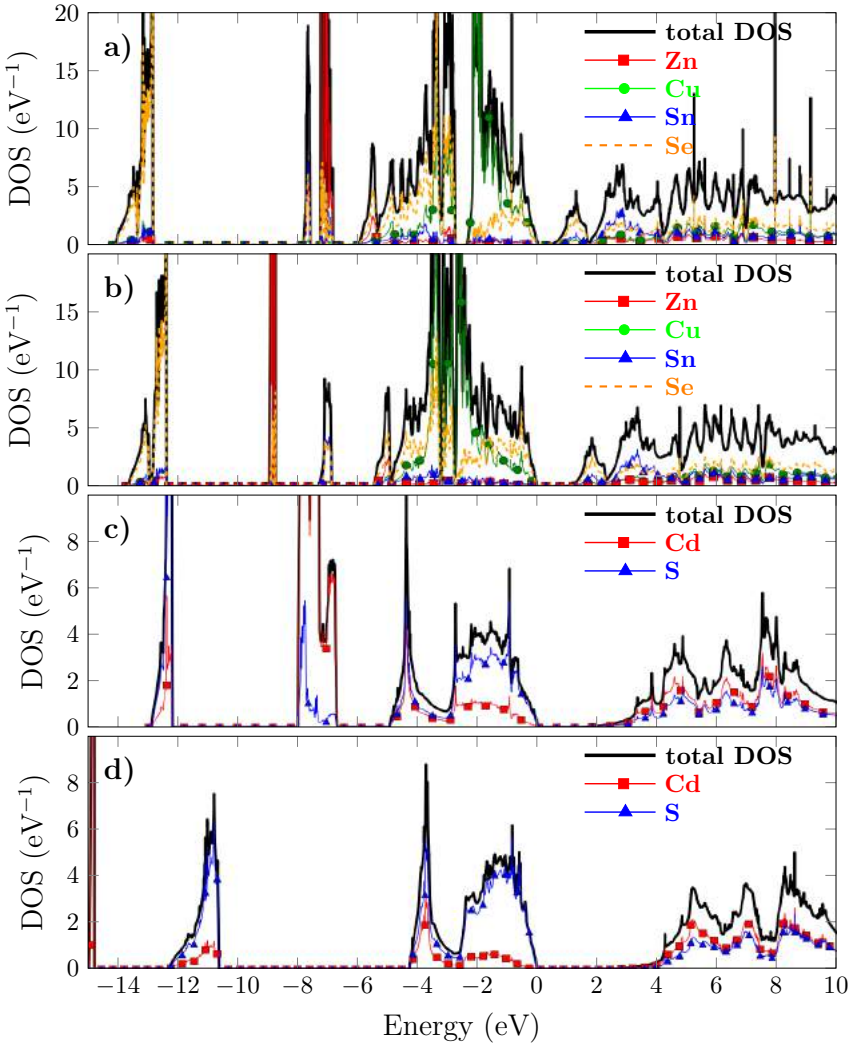

FIGURE 3.4: Total and projected density of states of bulk CZTSe calculated with GGA (a) and GGA + U (b) and for bulk CdS calculated with GGA (c) and GGA + U (d). Taken from Paper 1.

as epitaxial in our calculation.

CdS is the thinnest layer of the device shown in Fig. 3.1 and it is grown on top of CZTS(e). As a result it is typically assumed that CdS is strained to match the cell of CZTS(e). When setting up the interface, we therefore assume that the CdS bulk crystal is strained to fit that of CZTS(e) in the directions parallel to the interface. GGA + U changes lattice parameters for CZTS(e) and CdS, we therefore keep the experimental lattice parameters when choosing our U values to avoid over- or underestimating the effects of strain on the band structure of either material in the interface calculation.

The interface is set up in the following way: 1) The lattice parameter of CdS is relaxed in the direction perpendicular to the interface while keeping the other two lattice constants fixed to those of CZTS(e). 2) The two materials are brought together in a slab setup as shown in Fig. 3.5. 3) While keeping the atoms far from the interface rigid (areas indicated on Fig. 3.5) the atoms close to the interface are relaxed

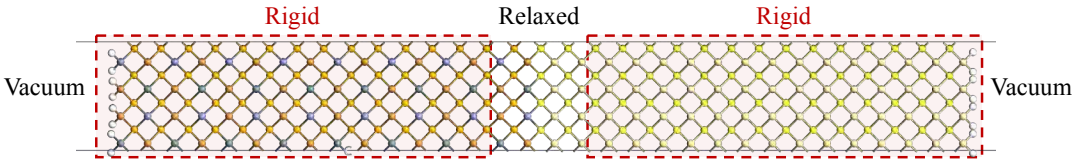

FIGURE 3.5: The slab structure used to relax the atomic positions near the interface. The marked areas(red) are where rigid constraints are employed. Rigid constraints means that the atomic positions are translated as a single body with force being evaluated on the center-of-mass.

to form an epitaxial interface[3]. 4) The vacuum shown in Fig. 3.5 is replaced with semi-infinite leads and we finally arrive at the setup shown in Fig. 3.2.

3.4 Results for the CZTSe/CdS interface

We consider first the CBO of the CZTSe/CdS, since the band alignment is relatively well established. The few existing studies for the CZTSe/CdS interface are in good agreement: Different photoemission experiments have measured 0.48 eV [68], 0.34 eV [69], and 0.3 eV offsets [70], while a theoretical study has calculated a 0.34 eV offset [54]. In the following we denote the transport direction by z.

Fig. 3.6a shows, for the intrinsic (non-doped) CZTSe/CdS interface, the local density of states (LDOS) and the effective potential, given by equation Eq. (2.2)), averaged in the (x,y)-plane[4]. The LDOS is given by the sum of contributions to the spectral function

$$\mathrm{LDOS}(\epsilon, \mathbf{r}) = \frac{1}{2\pi} \sum_{ij} A^{\mathrm{tot}}_{ij}(\epsilon) \phi_i(\mathbf{r}) \phi_j(\mathbf{r}) \tag{3.3}$$

where A^{tot}_{ij} are the matrix elements of the total spectral function $\mathbf{A}^{\mathrm{tot}} = \mathbf{A}_L + \mathbf{A}_R$. Both are plotted along the z direction perpendicular to the interface plane. The LDOS is projected onto layers of atoms with similar z-coordinates. The CBO is clearly a spike in agreement with previous theoretical and experimental studies [54, 68]. The CBO values of $\sim$0.3 eV agrees well with previous experimental data measured under equilibrium conditions [69, 70].

In Fig. 3.6a the potential shows a residual slope towards the electrodes. The potential should not be sloped at the very left or right part of the device region since the electrodes are in equilibrium and this leads to unphysical kinks in the potential. The slope indicates that the screening is not contained within the device region.

3.4.1 Dealing with residual potential slope

To address the problem of the slope in the potential near the electrodes, one can reduce the screening length of the semiconductors using doping. Doping is included in QuantumATK by adding a complementary charge fixed to the atomic sites[45].

[3] All relaxations were performed until interatomic force were below 0.02 eV/Å.

[4] For the LDOS calculation the BZ was sampled using a 11x11 Monkhorst Pack grid. To remove atomic variations, the potential is averaged in the z-direction using Gaussian kernels with a width of 3Å

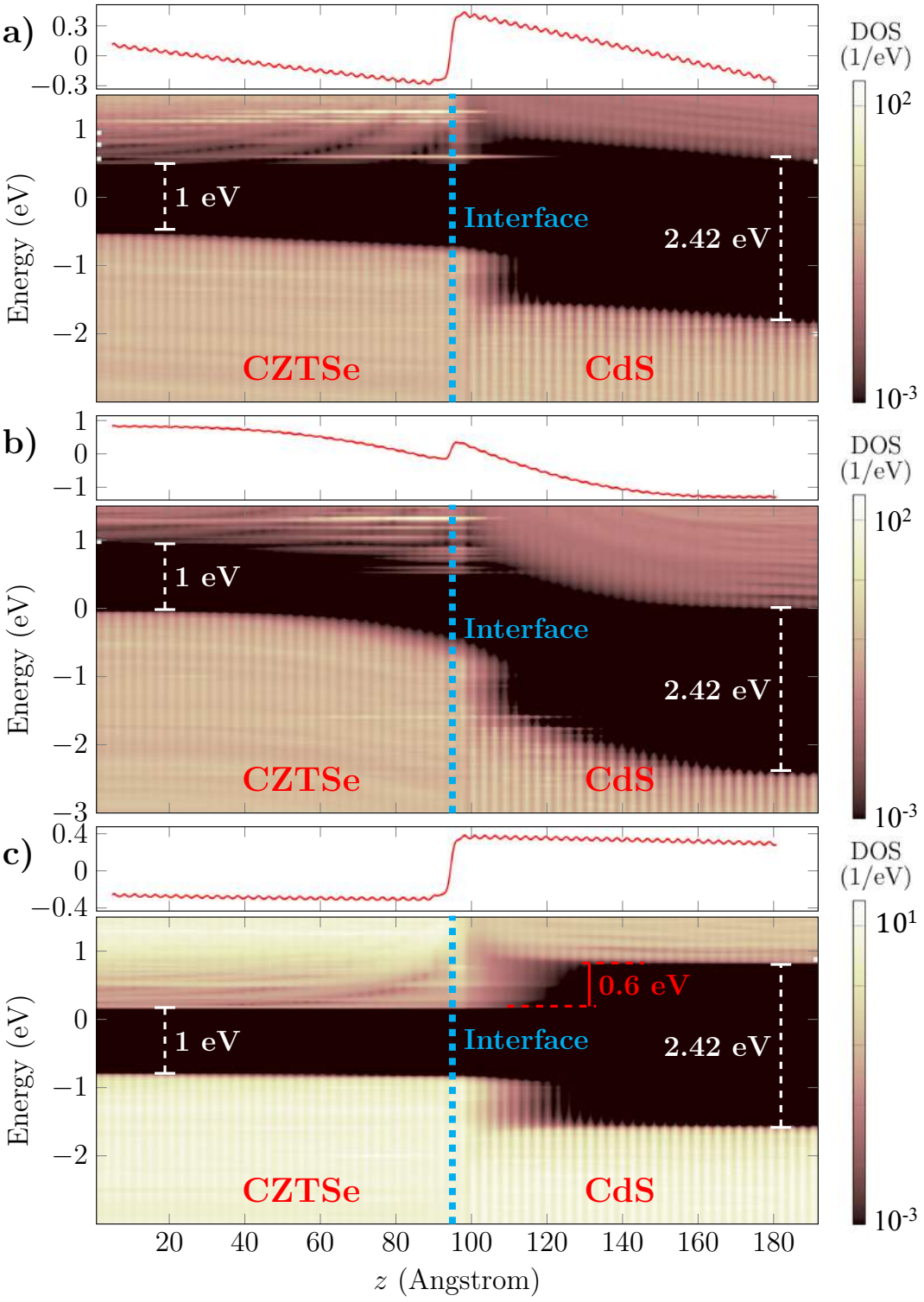

FIGURE 3.6: The local potential (top) and local density of states (bottom) of the CZTSe/CdS interface resolved along the direction perpendicular to the interface surface. (a) equilibrium conditions with zero bias and zero doping; (b) equilibrium conditions with zero bias and 10^{18} cm^{-3} doping density; (c) non-equilibrium conditions with an applied forward bias to achieve flat-band conditions and zero doping. A logarithmic scale is used for the LDOS intensity and the black areas correspond to zero DOS. Taken from Paper 1.

Fig. 3.6b shows the LDOS and local potential across the same interface where CZTSe (CdS) is doped p-type (n-type) with a charge density of 10^{18} cm^{-3}. Adding the charge removes the residual slope of the potential and the band bending near the electrode. However the large doping also changes the electronic structure of the interface. The amount of charge needed to contain the screening within our supercell is large compared to the doping density of CZTSe seen in experiments, which is on the order of 10^{15}–10^{16} cm^{-3} [52]. In fact, the experimental screening length of CZTSe ($\sim$200 nm) is about 20 times larger than the width of the CZTSe layer in our device region and consequently several hundred times larger than previous theoretical studies [52, 54].

In order to handle these weakly screened materials, where band bending occurs over distances far larger than the device region, we apply a small forward bias in the device simulations. The justification of this approach is as follows: 1) as mentioned above the electrostatic potential drop at the junction (band bending) occurs over a much larger length scale than the calculation cell length,[71–73] thus as a first approximation the bands can be assumed to be flat within the device region we consider; 2) the optimal working point of the solar cell device is indeed close to flat-band conditions (forward bias).

3.4.2 Extracted CBOs

Fig. 3.6c shows the LDOS and potential across such a system with an applied bias of 0.6 V. Clearly we have in this way achieved flat band conditions on both sides of the device and at the same time removed the residual slope of the local potential. Such a calculation is only possible due to the NEGF device setup we have used here. The obtained CBO is +0.6 eV which agrees nicely with the only reported measurement done under flat-band conditions [68]. Note that the CBO is larger in the flat-band case than in the case with band bending, which is also the case in experimental studies [68–70].

We complete our multiscale study of the CZTSe solar cell by extracting the CBO and including it in a TCAD device simulation of the entire cell. Fig. 3.7a shows the efficiency of the CZTS(e) solar cell as a function of the CZTS(e)/CdS interface CBO calculated using device level simulations. We find that a small spike (0.1-0.4 eV) is the ideal CBO giving the highest possible efficiency in agreement with similar studies on other solar cell heterointerfaces [74, 75]. Our simulation predicts a low efficiency of $\sim$1%. Using the CBO obtained in a previous first principles study ($\sim$0.34 eV) based on the bulk approach outlined above, one gets an efficiency of $\sim$11%. A CBO above 0.4 eV, such as we predict, present a high barrier for electron transport across the interface lowering the efficiency drastically. This could explain the low efficiency seen for solar cells based on CZTSe.

3.5 Results for the CZTS/CdS interface

Fig. 3.7b shows the LDOS across the CZTS/CdS interface, where the band bending has already been corrected by applying a small forward bias. The CBO extracted for the CZTS/CdS interface is 0.2 eV, which according to Fig. 3.7a should result in a

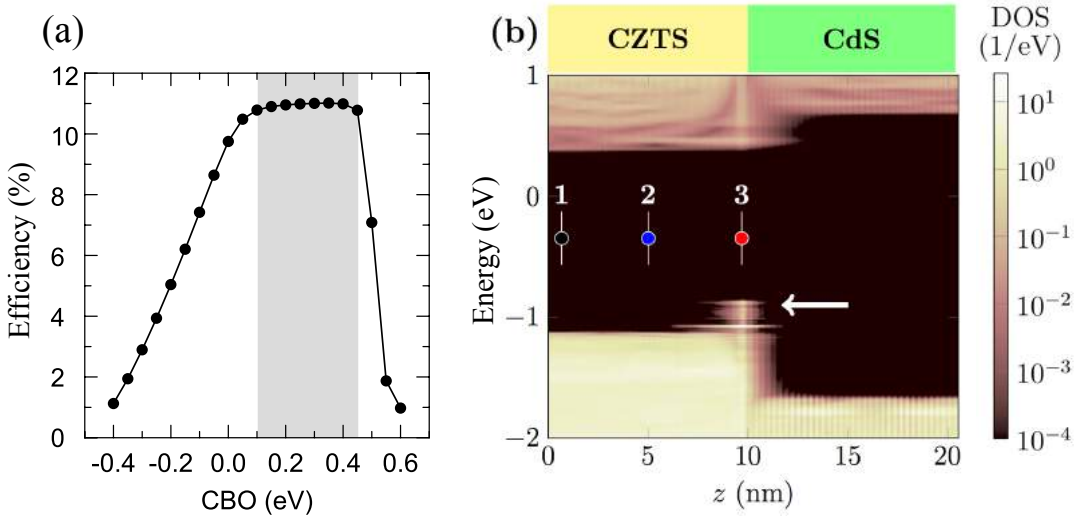

FIGURE 3.7: (a) Device simulation CZTS(e)/CdS heterojunction solar cell efficiency as a function of the conduction band offset. The shaded region is the optimal CBO range for achieving maximum efficiency. (b) Local density of states of the CZTS/CdS interface resolved along the direction perpendicular to the interface plane. Taken from Paper 1 and 2.

high efficiency. However, solar cells based on CZTS are plagued with low efficiencies. According to our result, we would not expect the CBO to be the cause of low efficiency.

To identify mechanisms of loss in solar cell devices an observable that is often extracted experimentally is the "recombination energy deficit" $\Delta\varphi$, which is the difference between the absorber band gap and the activation energy φ of the main recombination path. The activation energy φ, which is the energy distance between recombining electrons and holes in the location of the solar cell where the largest recombination current is located, can be estimated experimentally by measuring the open-circuit voltage V_{OC} at different temperatures and extrapolating to 0 K[76]. The open-circuit voltage of a photovoltaic device is the applied voltage for which zero current runs in the device. If $\Delta\varphi > 0$ the energy difference between recombining electrons and holes is smaller than the band gap of the absorber layer. Ideally, one should have $\Delta\varphi = 0$ for a good quality absorber.

In state-of-the-art CZTSe solar cell devices $\Delta\varphi$ corresponds to the penetration of bulk tail states related to "percolation" into the band gap of CZTSe[77]. As such it can be concluded that CZTSe solar cells are limited by bulk recombination. By contrast in CZTS, $\Delta\varphi$ is $\sim$0.2-0.3 eV higher than what would be expected if bulk recombination was the limiting factor[71, 73, 78–80]. A mismatch of that size implies that the energy difference between electrons and holes is reduced below the band gap of CZTS somewhere in the device leading to significant loss of efficiency. A popular explanation for this high $\Delta\varphi$ value is a negative CBO cliff of magnitude 0.2-0.3 eV at the CZTS/CdS interface. In the case of a CBO cliff the CdS conduction band minimum (CBM) would be lower than that of CZTS and recombination at the interface could occur from the CdS CBM to the CZTS VBM at an energy difference below the band gap. In Fig. 3.8 we have collected measured CBOs at the CZTS/CdS interface and the efficiency of the resulting devices. Even though many reports of a cliff-like CBO

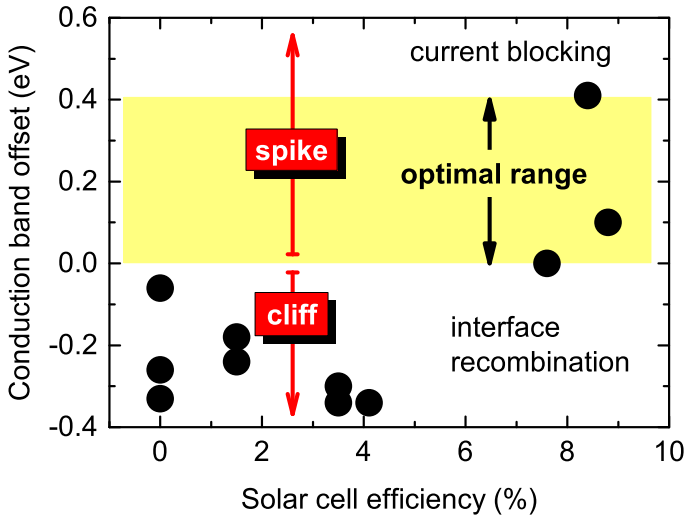

FIGURE 3.8: Correlation between measured conduction band offsets at the CZTS/CdS interface and corresponding solar cell efficiency. Data from Refs. [68, 70, 81–86]. Taken from Paper 2 supplementary.

exist for devices with low efficiency under 5%, measurements on CZTS/CdS solar cells with efficiency above 7% all yielded a spike-like or flat CBO[68, 70, 81]. Therefore, a CBO cliff cannot be used as an explanation for the high $\Delta\varphi$ of current state-of-the-art CZTS based solar cells.

3.5.1 Localized interface state

We note from the LDOS of the CZTS/CdS interface that a localized interface state appears inside the gap of CZTS (indicated by an arrow in Fig. 3.7b). Such a localized state can impact the performance electronic devices by e.g. increasing the recombination rate. In experimental measurements of band offsets a localized state can also lead to errors due to lack of sufficient resolution to distinguish an interface state from its nearest bulk band. The localized state seen in Fig. 3.7b results in an extension of the valence band maximum (VBM) near the interface up to 0.2-0.3 eV above the original VBM of CZTS (as seen in 3.9b). This interface band narrowing was also seen in calculations using the standard GGA-PBE exchange correlation potential, so it is not an artifact of the +U method. More careful relaxation of the atomic coordinates near the interface resulted in the interface state extending further into the CZTS layer, but did not remove it.

Calculations that we performed on a CZTS(100) surface, passivated with pseudo-hydrogen, also showed localized states above the VBM of CZTS. This suggests that the states are related to the CZTS(100) surface. In fact, focusing again on the CZTS/CdS interface calculation Fig. 3.7b, it is evident that the localized state is located exclusively on the CZTS side of the interface.

Here it is worthy to note, that multiple experimental results support the notion that an electrically active state exists at CZTS surfaces and not in CZTSe, as predicted by our calculation. Scanning tunneling microscopy (STM) measurements of the surface photovoltage revealed that, in CZTSe, the photocurrent scaled linearly with optical

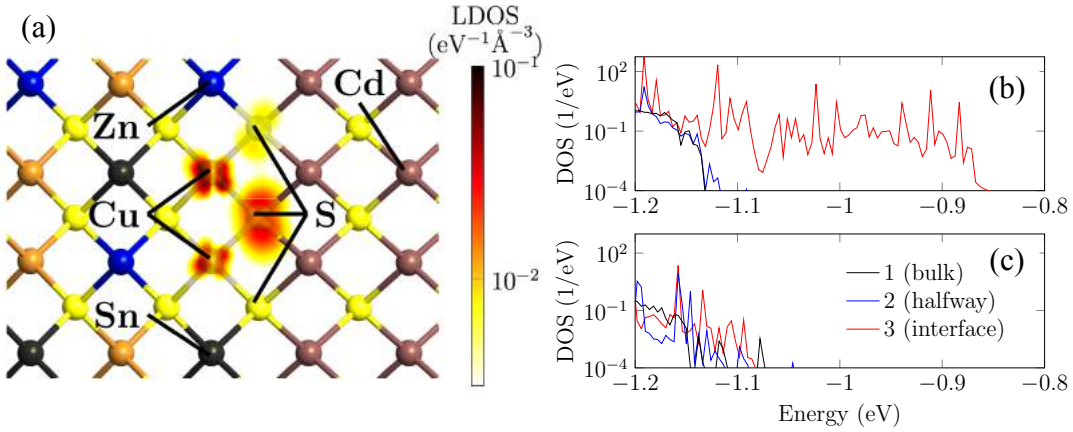

FIGURE 3.9: (a) Spatially-resolved DOS of the localized states at the CZTS/CdS interface. (b) Local density of states as a function of energy close to the VBM at the three positions indicated in Fig. 3.7b.(c) Local density of states as a function of energy close to the VBM at three positions along the CZTS/ZnS interface. Taken from Paper 2.

excitation intensity, whereas in CZTS the photocurrent saturated quickly[87]. Here the authors concluded that this was due to the "*predominance of surface states in the CZTS response but not in the CZTSe response*". Additionally, measurements of the work function on CZTSSe surfaces revealed that the Fermi level position in areas of high S content was different than expected considering the band edge positions of the bulk materials[88].

Fig. 3.9a shows the spatially resolved LDOS at the energy of the interface state. The states are highly localized on Cu sites in the first cationic layer of CZTS and on their neighboring S atoms in the interface anionic layer. In this area of the interface the difference in electronegativity between Cu and Cd could result in a local dipole across the interface capable of shifting states related to Cu, up in energy. A similar effect is seen in the two dimensional material Janus MoSSe due to the difference in electronegativity between Se and S[89–93]. We will discuss this effect further in chapter 6. Since the valence band of CZTS(e) originates from Cu and S(Se) states, (seen in Fig. 3.4 and [94]) this explains why the localized state affects the valence band but not the conduction band.

3.5.2 Inclusion of interface state in the TCAD model

Due to the potential impact on solar cell performance, we wish to include this localized interface state in our multiscale model. Fig. 3.10a shows the device band diagram near the CZTS/CdS as modeled in our device level TCAD simulation. The interface state is included as a 0.2 eV upward shift in the VBM over a 5 nm region at the CZTS side of the interface. This reduces the recombination energy barrier by 0.2 eV near the interface much like a CBO cliff as discussed above. The resulting change in hole density near the interface is shown in Fig. 3.10b. The hole density at the interface is increased by 3 orders of magnitude by the interface state reaching a value close to that of the electron density near the interface. The comparable densities of holes and electrons leads to increased Shockley-Read-Hall (SRH) recombination.

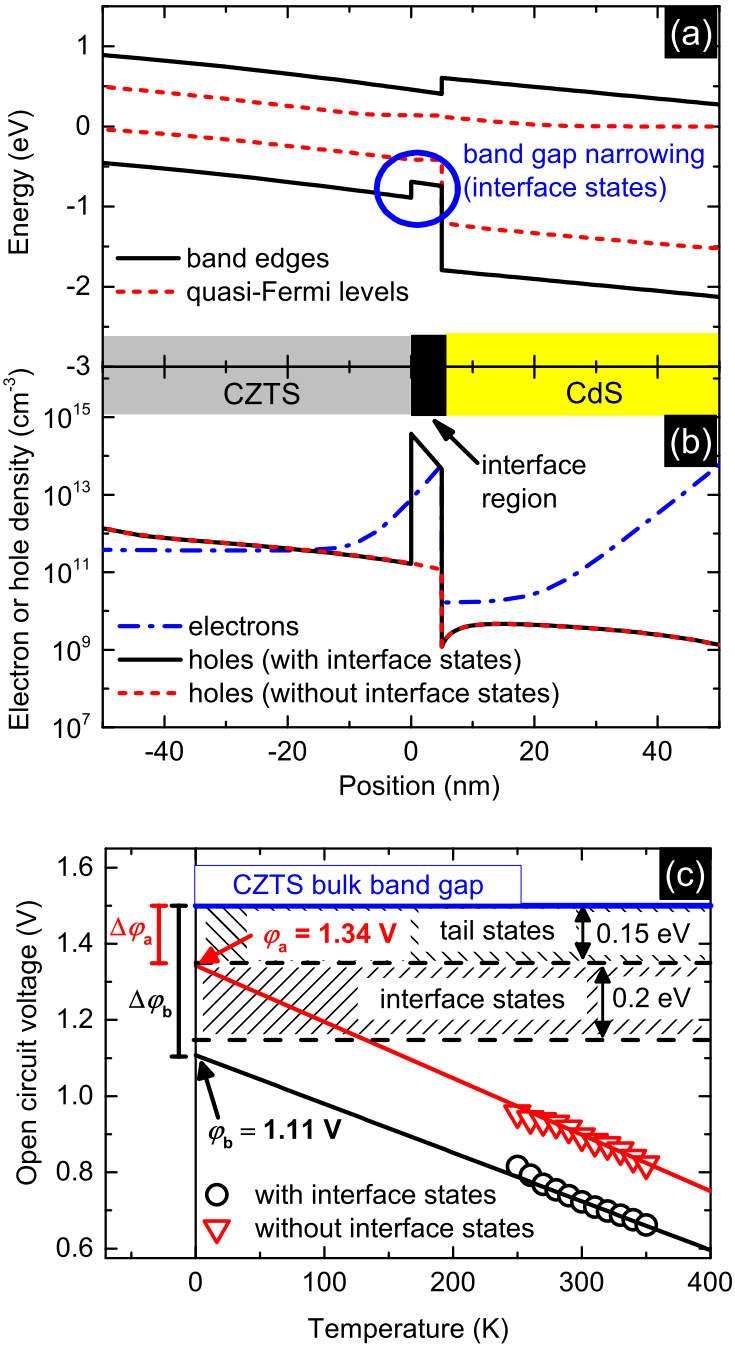

FIGURE 3.10: Simulated properties of the interface region of a CZTS/CdS solar cell under AM1.5 illumination, with the inclusion of localized states at the interface. (a) Band diagram and corresponding quasi-Fermi levels for electrons and holes. (b) Electron and hole density in the same region. The hole density increases significantly when interface states are added, whereas the electron density is the same in both scenarios. (c) Simulated open circuit voltage of CZTS/CdS solar cells as a function of temperature. The linearly extrapolated 0 K intercept of the data yields the activation energy of the dominant recombination path. Taken from Paper 2.

3.5.3 Temperature dependence of open-circuit voltage

To compare our multiscale model with real CZTS solar cell devices we calculate from drift-diffusion the temperature dependent current voltage (IV) curves and measure, as in experiments, V_{OC} extrapolating to 0 K to extract φ.

Fig. 3.10c shows the calculated V_{OC} as a function of temperature and the extrapolation to 0 K giving φ. In the TCAD model using our extracted CZTS/CdS CBO without including the interface state, the extrapolation results in $\varphi_a = 1.34$ V and $\Delta\varphi_a = 0.15$ eV, which matches the expected transport gap reduction compared to the optical gap caused by band gap variations in bulk CZTS, which were also included in the simulation. This means that the simulated device is not limited by interface recombination.

In the simulated solar cell where the interface state was included, the extrapolation results in $\varphi_b = 1.11$ V and $\Delta\varphi_b = 0.39$ eV which matches nicely the values measured experimentally ($\Delta\varphi_b = 0.3$ eV, 0.4 eV, and 0.4 eV) in the highest-efficiency CZTS/CdS solar cells[73, 78, 79]. Our multi scale simulation shows that interface recombination is the limiting factor in the device with interface states. It also demonstrates that a shift in the VBM, such as the one predicted from our DFT-NEGF calculations, can explain the temperature-dependent open circuit voltages measured in experiments on CZTS just as well as a CBO cliff does. From this simulation we have learned that optimal passivation of the CZTS(e)/CdS could potentially result in a significant enhancement of the solar cell efficiency and open-circuit voltage. This optimal passivation may be realized by replacing CdS with another suitable material.

The interface between CZTS and CdS breaks the bulk CZTS crystal structure by introducing a layer of $2Cd_{Cu} + Cd_{Zn} + Cd_{Sn}$ point defects where Cd replaces Cu,Zn and Sn. Such bulk defects of CZTS(e) have been investigated in detail before[95].
Here the authors studied the effect on the band gap of the similar defect complex called $2Zn_{Cu} + Zn_{Sn}$ and concluded that it did not narrow the band gap of CZTS. This defect resembles the effect of having a CZTS/ZnS interface. One could therefore expect that replacing CdS by ZnS could remove the interface state. To test this hypothesis, we performed a CZTS(100)/ZnS(100) interface calculation. Interestingly Fig. 3.9(c) shows that no band gap narrowing was found in this system. This indicates that one might realize an ideal interface by replacement of CdS by a Zn chalcogenide. To support this claim open-circuit voltage improvement has been achieved experimentally by Zn-based alternative buffers $Zn_{1-x}Sn_xO_x$,[80] (Zn,Cd)S,[72] and another unspecified Zn-based buffer[96]. $Zn_{1-x}Sn_xO_x$ is also the only material able to reduce $\Delta\varphi$ from the typical 0.3-0.4 eV down to 0.16 eV,[80] which suggests that bulk recombination is the limiting recombination path.

3.6 Summary

In this chapter we used a multiscale approach to study thin-film solar cells based on the earth-abundant, nontoxic absorber material CZTS(e).
In the multiscale approach we studied, using atomistic models implemented in QuantumATK[4], the details of the interface between CZTS(e) and the buffer material CdS believed to be critical for the conversion efficiency of the entire cell. The rest of the device was simulated at the continuum level using the TCAD tool SCAPS[44]. Using this approach we were able to reproduce experimental efficiencies of the CZTS(e)

based solar cells, and provide evidence suggesting a, so far, unknown loss mechanism at the CZTS/CdS interface.

Band gap narrowing at the interface, found in the DFT-NEGF calculations, were included in the continuum TCAD model allowing us to reproduce experimental measurements of the temperature dependent open-circuit voltage.
Knowledge of the scattering mechanism, obtained from the atomistic models, made it possible to suggest ways to improve performance and we concluded that Zn based buffer materials would improve the open-circuit voltage of the CZTS solar cell. The few existing experimental studies support these claims.

Chapter 4

Calculating phonon limited mobilities from Landauer transport

Electron-phonon coupling (EPC) plays a central role in the performance of most electronic devices. In continuum TCAD modeling the parameters used to describe EPC, often deformation potentials or mobilities, are extracted from bulk materials. Downscaling of electronic devices increases the impact of quantum confinement, surface effects and strain on both electrons and phonons. These effects are difficult to describe accurately with continuum models, that are parametrized to fit bulk materials.

This chapter, which covers the results reported in Paper 3 and some additional result and considerations, is concerned with developing a conceptually simple MD-Landauer approach which can be used to calculate the temperature dependent mobility and conductivity accurately for one-, two- and three-dimensional systems.

4.1 EPC coupling from atomistic device calculations

Several recent studies have investigated phonon limited transport in bulk materials by calculating the EPC from first principles and using the Boltzmann transport equation (BTE) for evaluating the electron mobility and conductivity[31, 97–103]. Integration of the coupling over both electron and phonon wavevectors (**k**- and **q**-space) makes this approach computational demanding. Furthermore precise calculation of Hamiltonian derivatives $\nabla_{\mathbf{r}}\mathbf{H}$ often requires many repetitions of the bulk cell making the evaluations very memory heavy. EPC in amorphous materials and random alloys can also only be treated approximately with the BTE approach.

Alternatively the current including EPC can be rigorously included in NEGF device calculations using perturbation theory. However, as discussed in chapter 2 this approach is also very numerically challenging and approximations such as the Lowest Order Expansion (LOE) must be applied to handle systems containing more than a handful of atoms. Furthermore, in order to save computational time, first principles methods to include EPC based on perturbation theory such as LOE and BTE, generally assume that phonons can be described within the harmonic approximation. As such anharmonic contributions are ignored, which is a very good approximation at low temperatures. However, at room temperatures and above, anharmonic contributions to the phonons are significant for many materials.

Molecular Dynamics (MD) simulations go beyond the harmonic approximation and include anharmonic contributions with no additional computational burden. MD simulations have been used in combination with Landauer transmission previously

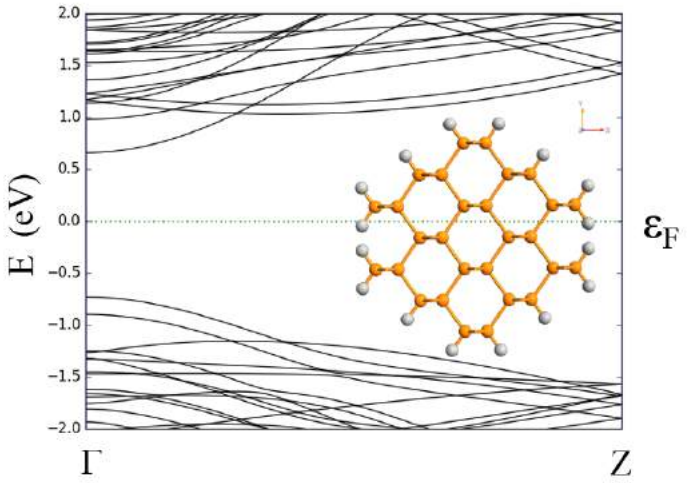

FIGURE 4.1: Electronic band structure of the SiNW. The inset shows a cross sectional view of the SiNW. Taken from Paper 3.

to sample configurations in studies of many different systems including a molecule in contact with two metallic electrodes, metallic point contacts and carbon nanotubes[37, 39–42, 104, 105]. MD has also previously been successfully used to obtain the energy dependent EPC, to estimate the effect of finite temperature on the bandstruture of silicon, and to extract mean free paths of bulk metals[38, 106, 107]. A similar approach has also been used previously to calculate mobilities of devices from NEGF transport simulations based on effective mass description of the electronic structure and deformation potentials for the EPC[108].

As an extension to these studies we develop here an MD-Landauer method to calculate the temperature dependent mobility and conductivity. This method is then applied to a broad array of systems including one, two and three dimensional versions of both metallic and semiconducting systems. As a reference, we compare our result to mobility calculations on the same systems using the well understood and widely used BTE approach as implemented in QuantumATK[31]. Where available, we also compare to experimental values. Parameters used for the BTE calculations can be found in Appendix A

4.2 MD-Landauer approach

We present here the MD-Landauer approach to calculating the temperature dependent conductance and mobility using the example of a [110] silicon nanowire (SiNW) of 1.5 nm diameter. The cross-section and electronic band structure of the SiNW used, is shown in Fig. 4.1. We see from Fig. 4.1 that the [110]-SiNW is a direct band gap semiconductor unlike bulk silicon where the band gap is indirect.

The MD-Landauer mobility calculation is performed using the NEGF device setup

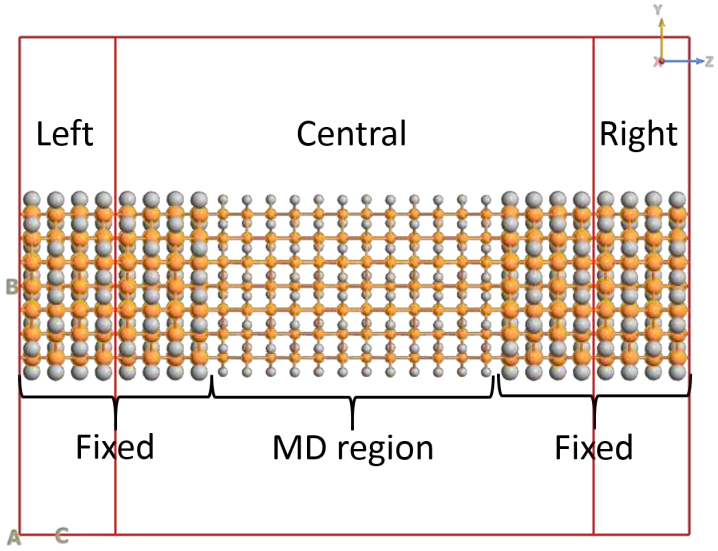

FIGURE 4.2: Device setup for the MD-Landauer approach. A central region is coupled to two semi-infinite electrodes (Left and Right). Initially the wire is periodic in the z-direction. An MD simulation is performed for the atoms in the middle part of the central region (MD region), while the electrodes as well as the first electrode copy on either side of the central region are kept fixed at their equilibrium positions. The fixed atoms are drawn as larger spheres. Taken from Paper 3.

shown in Fig. 4.2[1]. In the SiNW device setup, the Left and Right electrodes constituting semi-infinite boundary conditions are kept fixed along with the first repetition of the electrodes inside the central device region. A subset of the atoms inside the central device region labeled the *MD region*, are allowed to move according to an MD simulation. For the MD simulations in this study, classical potentials were used to evaluate the inter-atomic forces, which makes the simulations much more efficient than using DFT[109, 110].

To check the accuracy of the classical potentials used, we performed BTE calculations using both DFT and the classical potential to calculate the phonons and found that the result agreed qualitatively. Once the MD simulation has reached equilibrium at the target temperature we extract a snapshot of the final configuration and perform a self-consistent DFT-NEGF calculation on the device with atoms displaced from their relaxed position according to $\mathbf{x}\{T\}$. We then calculate the non-interacting Landauer transmission, through the configuration from

$$\mathcal{T}(\epsilon, \mathbf{x}\{T\}) = \mathrm{Tr}[\mathbf{G}(\epsilon, \mathbf{x}\{T\})\mathbf{\Gamma}_L(\epsilon)\mathbf{G}^\dagger(\epsilon, \mathbf{x}\{T\})\mathbf{\Gamma}_R(\epsilon)]. \tag{4.1}$$

The retarded Green's function depends on $\mathbf{x}\{T\}$ which in turn depends on the temperature and on the randomly distributed initial velocity used in the MD simulation. To estimate the average transmission through the system at finite temperature we perform several MD simulations and calculate the mean transmission at each energy.

[1]For the silicon systems considered, we used the LDA exchange-correlation potential and DZP basis set. For the electronic structure calculations we sampled the BZ using 1x1x11 and 11x11x11 Monkhorst-Pack grids for the SiNW and the bulk silicon systems respectively.

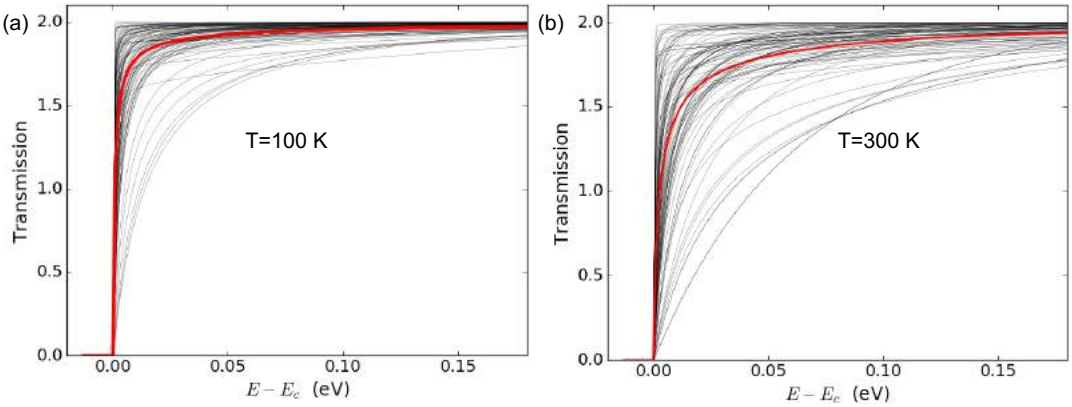

FIGURE 4.3: Transmission functions from different MD simulations (thin black lines) together with the average transmission (thick red). The length of the MD region is 2.3 nm and the temperature is (a) 100 K (b) 300 K. (a) is taken from Paper 3.

Fig. 4.3 shows the result of 100 such transmission calculations (black lines) at two different temperatures. We note that the variance of the individual transmissions in Fig. 4.3 increases as a function of temperature. After a suitable number of MD simulations have been performed the transmission mean converges to an average transmission (thick red lines in Fig. 4.3). Repeating this procedure for different lengths of the MD region $\mathcal{L}$ we get the different average transmissions $\langle \mathcal{T}_{\mathcal{L}}(\epsilon, T) \rangle$ shown in Fig. 4.4a. Using these we can calculate the length and temperature dependent conductance from the Landauer formula

$$G(\mathcal{L}, T) = G_0 \int d\epsilon \langle \mathcal{T}_{\mathcal{L}}(\epsilon, T) \rangle \left(-\frac{\partial f_\mu(\epsilon, T)}{\partial \epsilon} \right). \tag{4.2}$$

In this study we model doping by simply tuning the chemical potential μ. As such we do not account for scattering or other explicit effects induced by dopants.

4.2.1 Independent variables

Note that the average transmission in Eq. (4.2) depends only on the temperature and energy and not on the displacements $\mathbf{x}\{T\}$, after proper averaging. Instead we will represent the randomness by a standard error of the mean transmission given by

$$\sigma[\langle \mathcal{T}_{\mathcal{L}}(\epsilon, T) \rangle] = \frac{\sigma[\mathcal{T}(\epsilon, \mathbf{x}\{T\})]}{\sqrt{n_{\text{sampl}}}}, \tag{4.3}$$

where $\sigma[\mathcal{T}(\epsilon, \mathbf{x}\{T\})]$ is the standard error of the sampled transmissions and n_{sampl} is the number of sampled transmissions. By using this expression for the standard error we have assumed that $\langle \mathcal{T}_{\mathcal{L}}(\epsilon, T) \rangle$ is Gaussian distributed. In the limit of large sample sizes n_{sampl}, this assumption is supported by the central limit theorem which states that the mean of independent, identically distributed variables with finite variance tends towards a Gaussian distribution. Assuming the variance of the individual transmissions is finite, we thus only need to make sure that they are independent. In our case this condition is clearly fulfilled since every transmission is the result of a separate MD simulation with random initial velocities given by a Maxwell-Boltzmann distribution corresponding to the target temperature.

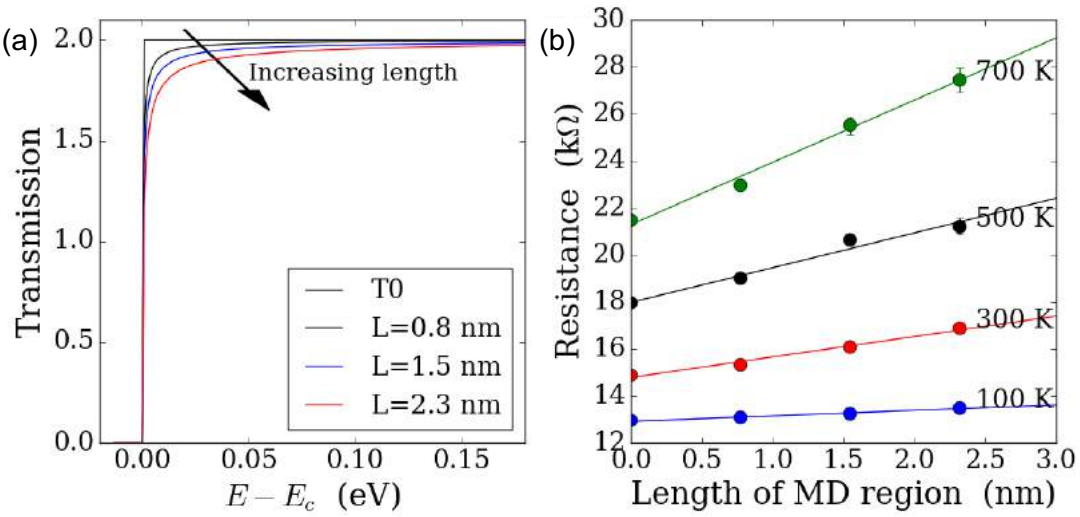

FIGURE 4.4: (a) The average transmission functions at three different lengths. (b) The resistance vs. length of the MD region for the SiNW at 100 K. Taken from Paper 3.

For complex systems where good classical potentials are not readily available, DFT can be used to perform the MD simulation. To save computational time, one could perform only one MD simulation and then sample configurations at different times. However with this sampling approach, the individual transmissions are not strictly independent and Eq. (4.3) could be a poor estimation of the standard error of the mean. To ensure independence of the individual transmissions, the configurations should therefore be sampled at reasonably separated times during the MD simulation [2].

In Fig. 4.4b we show the resistance $R(\mathcal{L}, T) = 1/G(\mathcal{L}, T)$ as a function of the MD region length. The error bars indicate the standard deviation of the average resistance calculated as $\sigma[R(\mathcal{L}, T)] = \sigma[G(\mathcal{L}, T)]/G^2(\mathcal{L}, T)$. Clearly the resistance increases linearly with length showing that the resistance is ohmic. The resistance is fitted to a linear function given by

$$R(\mathcal{L}, T) = R_0 + \rho_{1D}(T)\mathcal{L}, \tag{4.4}$$

where R_0 is independent of the MD region length and given by $R_0 = 1/G(\mathcal{L} = 0, T)$ which is the resistance in the system with no MD displacements. In Eq. (4.4) we have defined the one-dimensional resistivity $\rho_{1D}(T)$ which depends on the temperature, but not on the length of the MD region. Unlike the usual bulk resistivity which is measured in units of Ωm, $\rho_{1D}(T)$ has the unit $\Omega/$m. By multiplying $\rho_{1D}(T)$ with the wire cross sectional area A, we can recover the usual bulk resistivity i.e. $\rho_{bulk} = A\rho_{1D}$.

One should note that in calculation with a long MD region the length dependence of the resistance could become exponential due to electron localization[111]. This

[2] To test the independence, one can remove, from the set of averaged transmission, the transmissions sampled at every other time-step and recalculate the variance $\sigma[\langle \mathcal{T}_{\mathcal{L}}(\epsilon, T)\rangle]$. If the variance does not change, the data is approximately independent.

happens at shorter length for one-dimensional systems. By rewriting Eq. (4.4) as

$$R(\mathcal{L}, T) = R_c \left(1 + \frac{\mathcal{L}}{\lambda_{\text{mfp}}}\right), \tag{4.5}$$

we can obtain an estimate of the mean free path, $\lambda_{\text{mfp}} = R_c/\rho_{1D}$. Since the localization length is always longer than λ_{mfp} we can assure that the studied systems are not in the localization regime. The room temperature mean free path for the SiNW obtained from Eq. (4.5) is 17 nm, so we are safely within the ohmic regime as also indicated by the linear dependence in Fig. 4.4b. For all the systems studied here, we have checked that we are not in the localization regime.

In order to calculate the mobility $\mu = 1/qn\rho_{bulk}$ we need to obtain the carrier density n . We can calculate the carrier density per unit area from a separate calculation of the density of states, DOS(ϵ), of the bulk wire (evaluated at the equilibrium atomic structure)

$$\tilde{n}(\mu, T) = \frac{n}{A} = \int_{E_g}^{\infty} d\epsilon \, f_\mu(\epsilon, T)\text{DOS}(\epsilon), \tag{4.6}$$

where we use the undoped Fermi level (middle of the band gap), E_g, as the lower bound of the integration for the electron mobilities. To calculate the mobility of holes, we should integrate from $-\infty$, use E_g as an upper bound and replace $f_\mu \rightarrow 1 - f_\mu$. Calculating the mobility using the carrier density in Eq. (4.6) and the bulk resistivity we have

$$\mu = \frac{1}{q\, n\, \rho_{bulk}} = \frac{1}{q\, \tilde{n}\, \rho_{1D}}. \tag{4.7}$$

where we notice that the cross sectional area A, falls out of the equation making it independent of the wire area. Similarly in the two-dimensional case the slab thickness falls out of the mobility equation.

4.3 Comparison with experiments and Boltzmann

In Fig. 4.5 we show the mobility as a function of temperature for the SiNW systems calculated with the MD-Landauer approach, and compare to mobilities of the same system calculated using BTE. We see that the temperature dependent mobilities obtained with the two methods agree nicely and generally fall within a factor 2 of each other. We also show in Fig. 4.5 the calculated mobilities for bulk silicon obtained from MD-Landauer and BTE compared with values measured experimentally[112]. Also for bulk silicon, the two methods give almost identical temperature dependent mobilities. Both methods also seem to provide good estimates for the experimental values.

Interestingly the mobilities calculated for the SiNW are generally almost an order of magnitude lower than the bulk mobilities at the same temperature. This reduction in mobility for the nanowire is expected due to increased EPC caused by (i) relaxation of the strict selection rules for momentum matching in the transverse directions due to folding of the bands in the nanowire, and (ii) localization and mixing of corresponding bulk phonon modes. Previous investigations based on tight-binding modeling, agree with the reduction of mobility in nanowires observed from first principles here[113]. For the nanowire, scattering from surface modes is found to be insignificant in BTE.

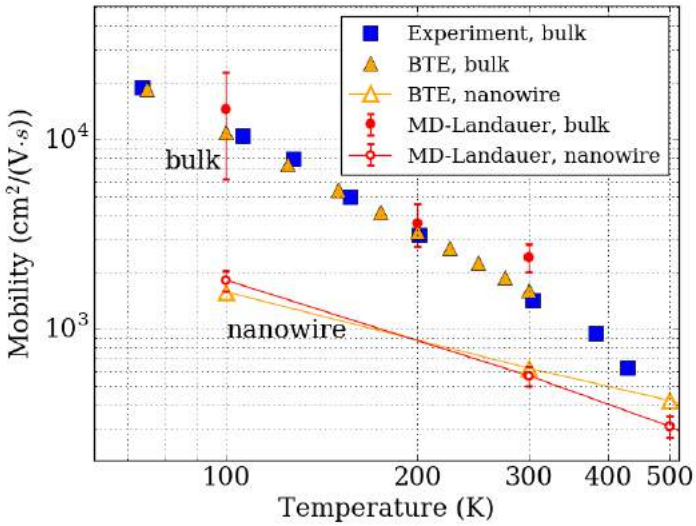

FIGURE 4.5: Phonon limited mobility vs. temperature for the SiNW (open markers with lines) and bulk silicon (filled markers) calculated with BTE and with the MD-Landauer approach using a doping level of $1 \times 10^{18}\text{cm}^{-3}$. The error bars for the MD-Landauer results indicate the standard deviations on the calculated mobilities. Experimental values for bulk silicon[112] are shown for comparison (blue dots). Taken from Paper 3.

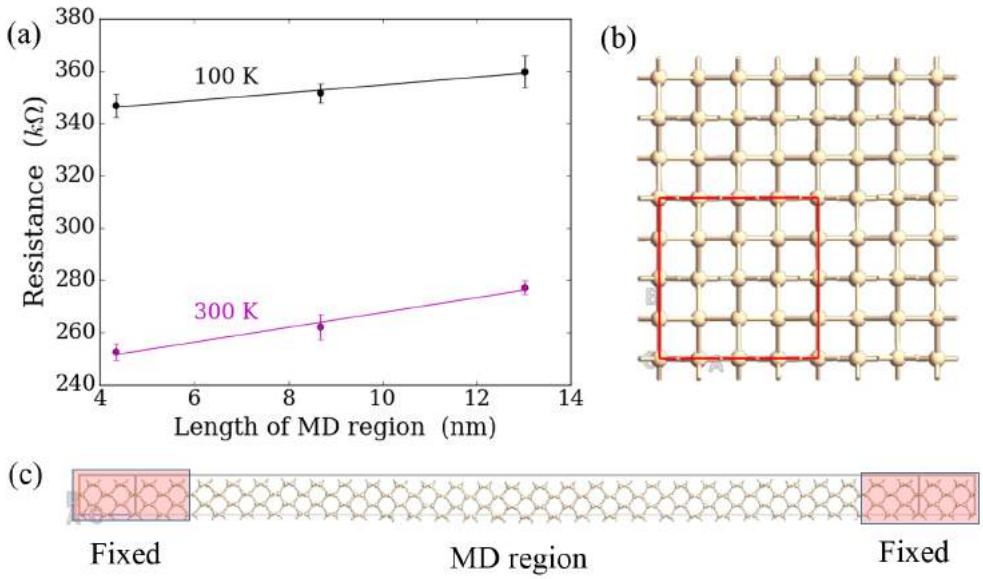

FIGURE 4.6: (a) Length dependent resistance of bulk silicon at temperatures 100 K and 300 K. Panel (b) shows the cross section of the calculation cell (red box) while the device configuration is shown in (c). The length of the MD region is 13 nm. Taken from Paper 3.

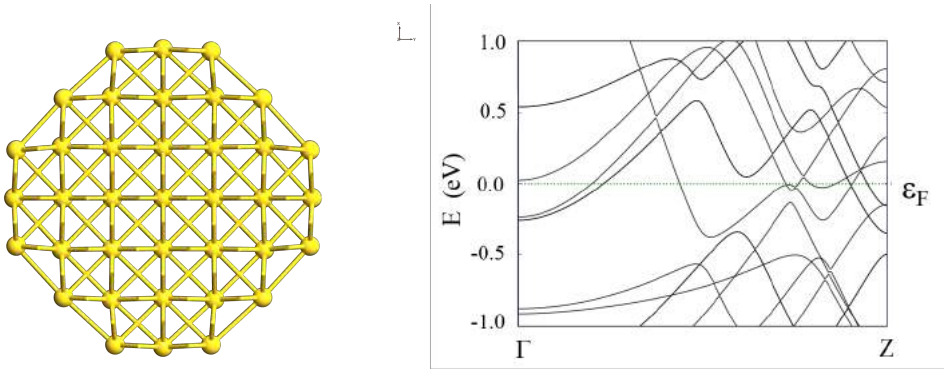

FIGURE 4.7: Cross section of the Au NW (left) and electronic band structure (right). The diameter of the wire is 1.3 nm. Taken from Paper 3.

The system used to calculate the bulk silicon mobilities with the MD-Landauer approach, shown in Fig. 4.6b-c, has transport in the [100]-direction with the length of the MD region varying from 4 to 13 nm[3]. In Fig. 4.6a the calculated resistance of bulk silicon as a function of MD region length is shown. The calculated room temperature mean free path for bulk silicon is 76 nm so we are well under the MD region lengths where electron localization would be expected. The results for bulk silicon in Fig. 4.5 and Fig. 4.6a were obtained using just 20 sampling transmissions.

4.3.1 Gold nanowire

We now move on to consider a metallic gold nanowire with a diameter of 1.3 nm. The cross sectional view and calculated band structure of the considered nanowire is shown in Fig. 4.7. Table 4.1 shows the room temperature resistivity of the gold nanowire calculated using the MD-Landauer approach and BTE. For both methods we have calculated the electronic structure and transmissions using both DFT and and density functional tight binding (DFTB). To calculate the phonons, classical potentials from the embedded atoms model (EAM) have been used[114]. To verify the use of the potentials, as with the silicon systems, we have also calculated the resistivity from BTE using DFT for the phonon calculation.
In Table 4.1 the top row shows the result where both phonons and electrons are described using DFT. All other calculations use the EAM classical potentials to describe the phonons and either DFT or DFTB for the electronic structure calculation. We see that there is an overall good agreement between the results using the different parameters.
As with the silicon systems we see that the BTE and MD-Landauer method gives similar results, within a factor two difference.

4.3.2 Bulk gold

To use the MD-Landauer approach on bulk gold, we setup a unit cell with a 0.82x0.82 nm^2 cross section and transport along the [001]-direction. The MD region length was varied from 1.2 to 2 nm[4]. To save computational time we use EAM to describe the

[3]Transmissions for bulk silicon were calculated using 11x11 transverse k-points.
[4]Transmissions for bulk gold, were calculated using 6x6 transverse k-points.

Method	Parameters	ρ ($10^{-8} \times \Omega$·m)
BTE	(DFT)	5.6
BTE	(EAM+DFT)	4.6
BTE	(EAM+DFTB)	3.8
MD-Landauer	(EAM+DFT)	7.1
MD-Landauer	(EAM+DFTB)	7.5

TABLE 4.1: Resistivities of the gold nanowire at 300 K calculated in different ways. Taken from Paper 3.

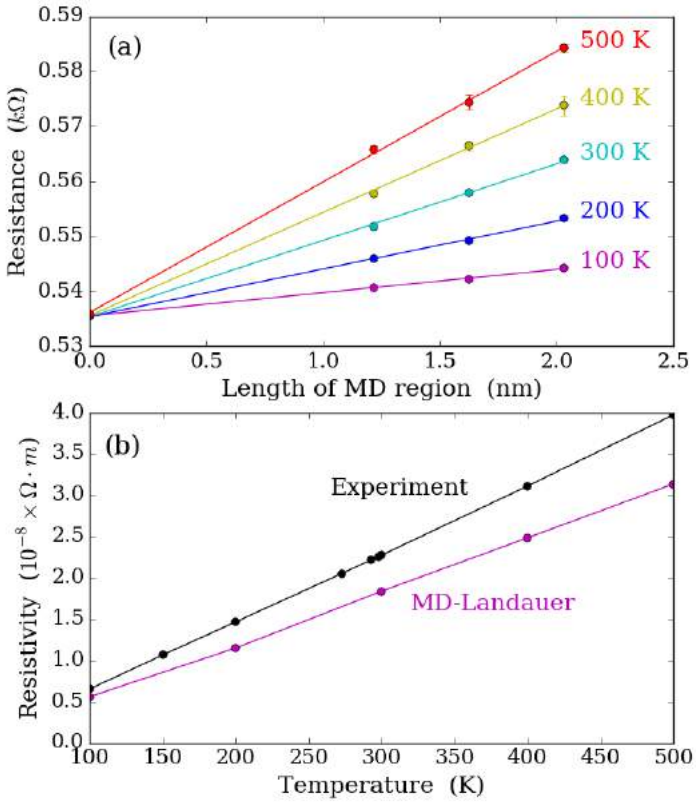

FIGURE 4.8: Length dependend resistance of bulk gold at different temperatures (a) and temperature dependent resistivity (b). The resistivity is calculated for bulk gold with the MD-Landauer method. The black points show experimental results[115]. Taken from Paper 3.

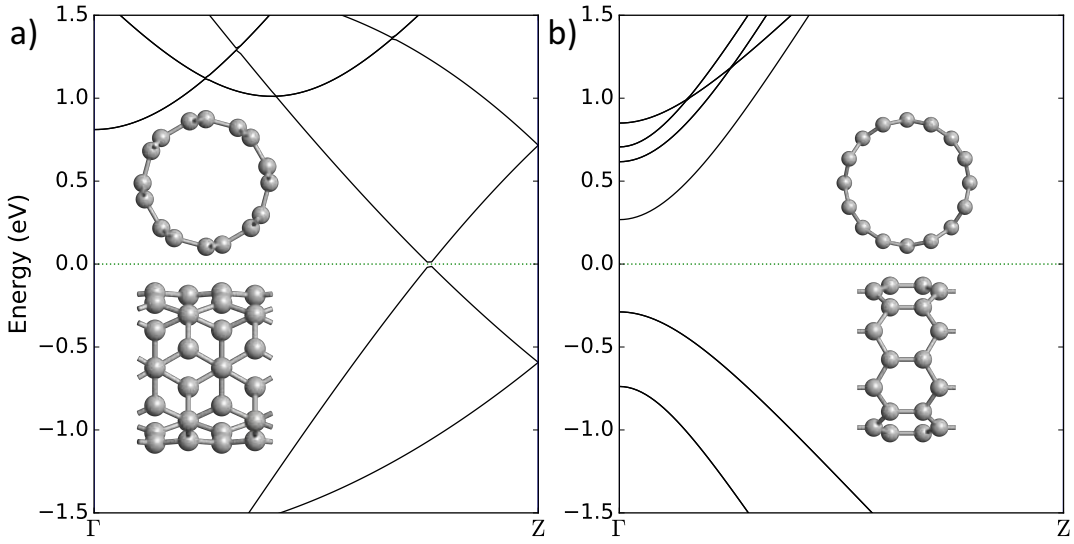

FIGURE 4.9: (a) Band structure of the armchair (4,4) CNT. Inset shows the structure of the unit cell (b) Band structure of the zigzag (8,0) CNT. Inset shows the structure of the unit cell.

phonons and DFTB for the electronic transmission calculation. The room temperature resistivity calculated with DFTB was compared to the same calculations using DFT to calculate the electronic transmission, in order to verify that the two descriptions give essentially the same results.

In Fig. 4.8a we plot the resistance as a function of MD region length for different temperatures. The resistance is clearly linearly dependent on the MD region length indicating that we are in the ohmic regime. Furthermore the calculated room temperature mean free path is 38 nm. Calculated resistivity for bulk gold is compared to experimental measurements in Fig. 4.8b. We find that both the values and their temperature dependence agrees nicely with experimental results.

4.3.3 Semiconducting and metallic carbon nanotube

Finally we use our MD-Landauer approach to calculate the temperature dependent mobility of two carbon nanotube (CNT) systems shown in Fig. 4.9[5]. The structure and band structure of a metallic (4,4) armchair CNT is shown in Fig. 4.9a. For this CNT, the length of the MD region is varied from 0.5 to 1.5 nm while the calculated mean free path at room temperature is 103 nm, so we are well below the localization regime. The structure and band structure of a semiconducting (8,0) armchair CNT is shown in Fig. 4.9b. For the semiconducting CNT the length of the MD region was varied from 0.4 to 1.3 nm while the calculated mean free path at room temperature is 24 nm, so again we are not in the localization regime and the resistance is ohmic. In addition, the calculated resistances for both of these systems show ohmic behavior as a function of MD region length.

The temperature dependent mobility, calculated with the MD-Landauer method and with BTE for the metallic and semi conducting CNT, is shown in Fig. 4.10. For the metallic armchair (4,4) CNT (Fig. 4.10a), we see that the mobilities calculated using

[5]For the CNTs we used 1x1x101 k-points to evaluate the electronic structure and the transmission and a single zeta polarized basis set with LDA as the exchange-correlation potential.

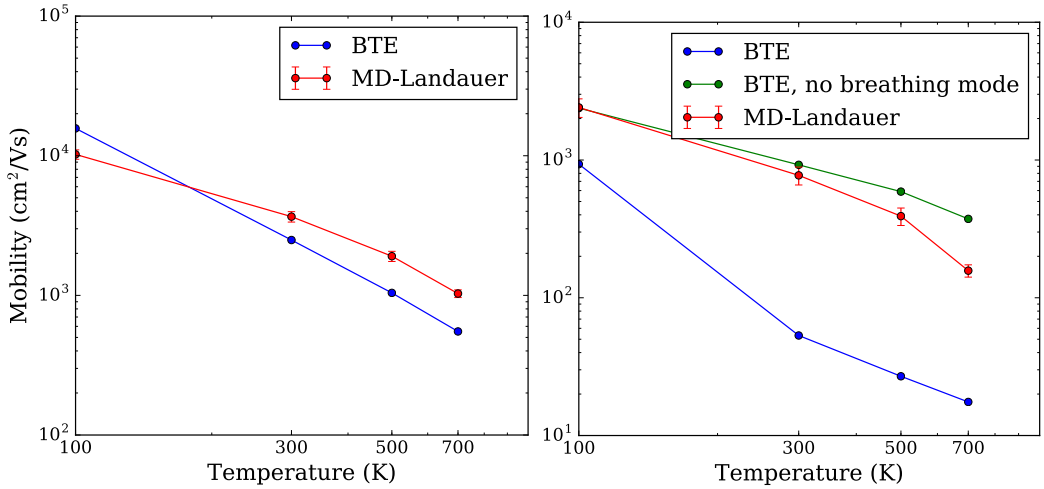

FIGURE 4.10: Temperature dependent mobility of the armchair (4,4) CNT (left) and of the zigzag (8,0) CNT (right). The mobility is calculated using the MD-Landauer method and with BTE. The green points are the BTE mobility where the contribution from the breathing mode is ignored.

MD-Landauer and BTE compare well within a factor of two. However for the zigzag (8,0) CNT (Fig. 4.10b), the mobility is over an order of magnitude lower, at room temperature and above, when calculated using BTE. Looking at the calculated EPC for the zigzag (8,0) CNT we find an unusually strong coupling for the radial breathing mode. This phonon mode is unique to nanotube systems and corresponds to increasing or reducing the radius of the nanotube. A previous first principles study also found that electron-phonon coupling of the radial breathing mode in zigzag CNTs is much stronger than for armchair CNTs[116]. BTE is only valid for phonons modes λ that couple weakly enough so that

$$\Lambda = \frac{|g|}{\hbar\Omega_\lambda} < 1 \tag{4.8}$$

where g is the scaled EPC. For the radial breathing mode $\Lambda \approx 5.9$, so perturbation theory is not well defined. A better description of the radial breathing mode could be obtained by considering e.g. polaron transport, where the renormalization of the CNT electronic structure due to the phonons is included[117, 118]. For BTE calculations, where the phonon coupling is included only to lowest (first) order, and the electronic band structure is assumed independent on phonons, this strong coupling could result in over- or underestimation the impact of the phonon on the mobility. To test this hypothesis we repeat the BTE mobility calculation including all phonon contributions except that of the radial breathing mode. As seen in Fig. 4.10 the BTE mobility is indeed over an order of magnitude higher, at room temperature and above, when ignoring the radial breathing mode indicating that the contribution is overestimated. The MD-Landauer method is not perturbative in $|g|$ and as such the strong coupling of the radial breathing mode is not a problem.

4.3.4 Limitations of MD-Landauer approach compared to BTE

Throughout this chapter we have compared the results of the MD-Landauer approach to results obtained using the BTE. We will now discuss the limitations of the two methods based on their implementation in the QuantumATK code[4].

Compared to the MD-Landauer method the BTE is definitely more rigorous and theoretically well founded. However the BTE is based on a number of approximations that we will outline here. As discussed previously EPC is only included to first order through Fermi's golden rule under an assumption of weak coupling. Furthermore since the EPC is calculated from finite displacements of individual atoms as introduced in chapter 2, the screening is assumed to be linear, so that the sum of change in Hamiltonian due to several separate single-atom displacements is the same as the change in Hamiltonian due to the summed displacements. This assumption can for example lead to incorrect inclusion of the Frölich interaction in polar materials[119]. Scattering events including multiple phonons are ignored in the BTE, as are finite temperature effect such as the lowering of the band gap of semiconductors which is captured using MD[107]. Lastly, the harmonic approximation used to calculate the phonons means that anharmonic phonon-phonon coupling is ignored.

The MD-Landauer approach, while less theoretically well founded, is based on the Born-Oppenheimer approximation that electrons move much faster than the nucleus. Considering then a short scattering MD region, an electron passing through experiences only the fixed potential landscape setup by the position of the atoms in that instance (snapshot). However, the inelastic energy transfer between electrons and phonons is not included in the MD-Landauer approach. At low temperatures MD assumes that the phonon modes are occupied according to a Boltzmann distribution rather than the Bose-Einstein distribution neglecting zero-point motion. As such the MD-Landauer approach should give incorrect results in the low temperature limit. However at temperatures above the Debye temperature of the considered materials, anharmonic effects might be important and these are inherently included in the MD-Landauer method. The MD-Landauer method also does not assume the linear screening discussed above. As such long wavelength Fröhlich scattering is included if the MD regions are long enough. Ĺastly the MD-Landauer method is not based on first order expansion of the EPC. As a result the perturbation to the Hamiltonian caused by the atomic displacements is included exactly.

Keeping in mind these fundemental differences, it is striking how similar temperature dependent mobilities are obtained for a variety of materials covering several orders of magnitude in mobility. To illustrate the qualitative agreement, we compare in Fig. 4.11 the room temperature mobility for a number of systems.

The two methods also have different advantages and disadvantages in application. The mobility at many different temperatures can be captured with very little additional computation time using the BTE, whereas separate MD simulations must be performed for each temperature in the MD-Landauer approach. BTE can be very computationally heavy due to the simultaneous sampling of k- and q-points on fine grids, especially for bulk systems with periodic boundary conditions in three directions. This is avoided in the MD-Landauer method where only convergence of the transmission with respect to k-points is necessary. An additional convergence with respect to sampled transmissions is also needed in the MD-Landauer method.

The contributions to the scattering from different phonon modes can be accessed directly from the BTE. Using the MD-Landauer approach, information about individual contributions is lost. On the other hand, not needing to store this information makes the MD-Landauer method much more memory efficient. The MD-Landauer

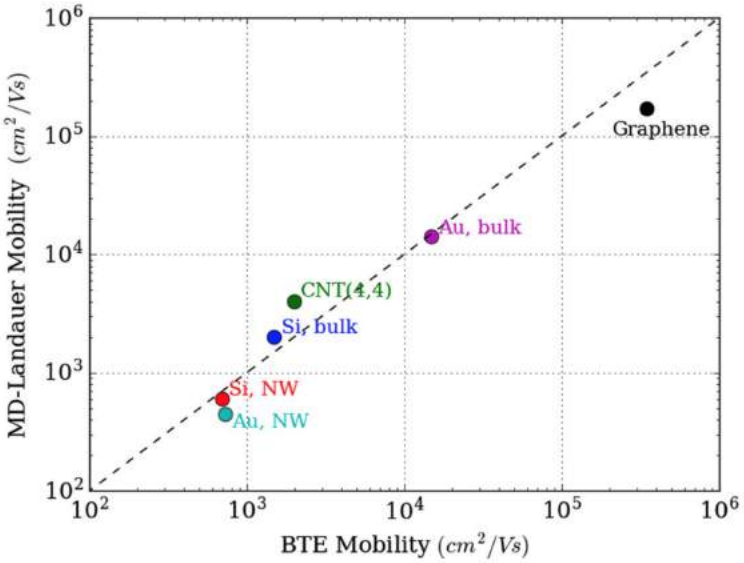

FIGURE 4.11: Comparison of room temperature (300 K) mobilities calculated with BTE and with the MD-Landauer approach. Taken from Paper 3.

approach may therefore be more appealing as a design tool for complex systems with many degrees of freedom and for bulk systems that can be very memory demanding due to the large number of k, q and phonon mode combinations needed.

For the metallic systems studied, the MD simulations have a less dramatic impact on the calculated transmissions. As a result very good estimations with low standard errors can be obtained after averaging only a few displacements. BTE for metallic systems can be very computationally demanding, since one must take into account many electronic bands and sample many k-and q-points to get reasonable results. Especially for metallic nanowire systems the MD-Landauer approach could be a powerful tool to estimate mobilities where including physical dopants, defect scattering, grain boundary scattering and studying amorphous systems is much more straightforward compared to BTE.

4.4 LOE-Landauer approach

As introduced in chapter 2, EPC can be included more rigorously in NEGF simulation by calculating the LOE inelastic current[34, 35]. Since LOE is based on many of the same assumptions as BTE, it is instructional to calculate the mobility using our MD-Landauer method but calculating instead the transmission including phonon scattering from the LOE expression.

Fig. 4.12 shows the calculated LOE transmission near the band edge for the SiNW system shown in Fig. 4.2. For the one-dimensional SiNW the DOS exhibits a van Hove singularity near the band edge. This makes the transmission sensitive towards perturbations. At high temperatures this leads to strong modifications of the current that goes beyond lowest order perturbation. In practice, this means that the inelastic LOE contribution to the transmission near the band edge explodes and results in a negative total transmission (see the blue line Fig. 4.12).

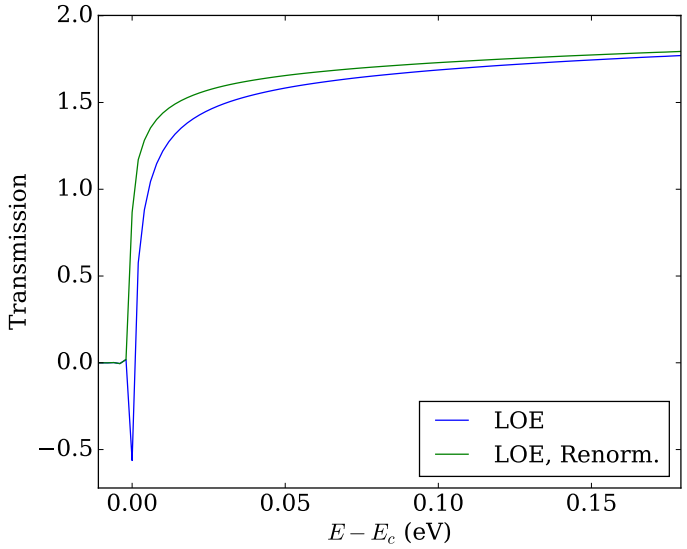

FIGURE 4.12: Inelastic transmission as calculated from LOE, for the silicon nanowire system at 500 K (blue) and the same transmission after renormalization following an analytical-continuation technique as in [120].

Recent papers have developed an analytical-continuation technique that enables a renormalization of the LOE inelastic current that improves the agreement with the current calculated from the full self-consistent Born approximation[120–122]. Using this technique the current including EPC is calculated from

$$I = \frac{I_0}{1 - I_{\mathrm{LOE}}/I_0}, \tag{4.9}$$

where I_{LOE} is the LOE current correction and I_0 is the ballistic current. Expanding Eq. (4.9) to first order in I_{LOE}/I_0 returns the usual current expression $I = I_0 + I_{\mathrm{LOE}}$. Applying the renormalization to the LOE transmission we avoid the negative transmission near the band edge, while the transmission far from the band edge is nearly unchanged as seen in Fig. 4.12. As in the MD-Landauer approach the transmission is calculated with different length of the phonon interaction region to eventually extract the mobility.

4.5 STD-Landauer approach

One of the drawbacks to the MD-Landauer approach, especially for non-metallic materials, is the need to sample many transmissions to get a sufficiently converged average transmission. As described in chapter 2 the recently developed special thermal displacement (STD) method enables the calculation of the thermally averaged transmission from a single displacement, in large systems[*Paper 4*]. Fig. 4.13a shows the STD transmission for three different scattering region lengths. The resulting transmissions for different lengths of the displaced scattering region shows similar behavior as compared to the MD averaged transmissions in Fig. 4.4a which are the average of more than 100 transmissions.

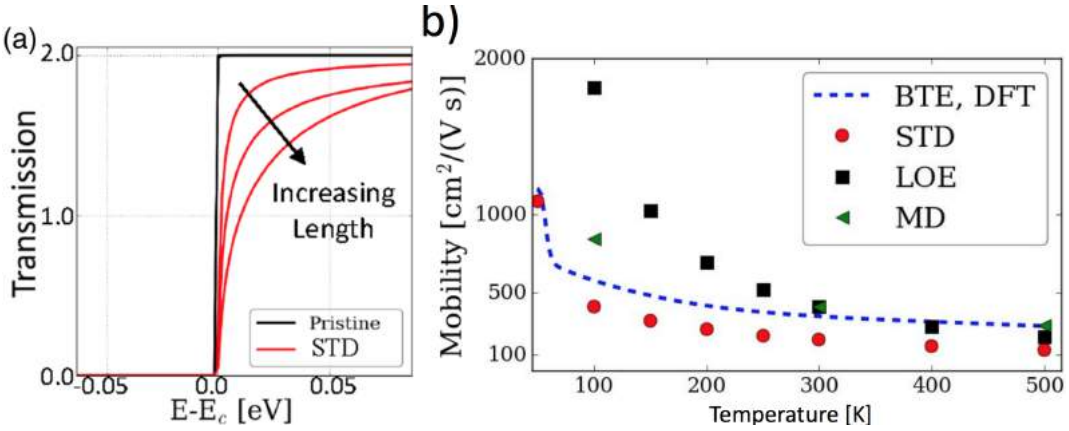

FIGURE 4.13: (a) Transmission for the pristine and STD configurations for three different lengths of a silicon nanowire. (b) Mobility as function of temperature for a silicon nanowire using the BTE, STD, MD-Landauer and LOE methods. (a) Taken from Paper 4 (b) Taken from Paper 5.

A comparison of the temperature dependent mobility for the SiNW system calculated using all of the discussed methods is shown in Fig. 4.13b. Remarkably all of the methods seem to agree nicely at room temperature and above. Above room temperature STD predicts the lowest mobility and BTE the highest. At low temperatures the LOE-Landauer approach predicts higher mobility while the other methods agree within a factor of two. One would expect the MD-Landauer method to fail in the low temperature limit, since it neglects zero-point motion.

LOE-Landauer is probably the most computationally demanding of the methods and with the added complexity of having to perform renormalization of the current according to Eq. (4.9), it is not recommended for calculating the mobility near the band edge of one-dimensional systems. However since the current at different temperatures is easily obtained from a single calculation it could be useful for studies where a high temperature resolution is needed. Furthermore contributions to the current coming from different phonon modes can be readily accessed from LOE. The limitations of the BTE approach discussed above, also apply to LOE since it relies on the same assumptions.

STD-Landauer is by far the cheapest method used, since it involves just the transmission calculation of a single displaced system. Unlike the MD-Landauer approach STD, like BTE and LOE, does however require the calculation of the dynamical matrix. For large complex systems where precise classical potentials are not yet available, this could be a limitation. Using MD in this situation would be much more memory efficient, but very time consuming. As discussed in chapter 2 the dynamical matrix calculation can be performed very cheaply, when the device region is simply a repetition of a smaller unit cell, as is the case for every system studied in this chapter. Like MD, STD does require a separate calculation for each temperature. Furthermore unlike MD, STD calculates phonons using the harmonic approximation which means that anharmonic phonon-phonon coupling effects are ignored.

STD is only a good assumption for large systems where the phonon modes are pairwise nearly degenerate. Performing the STD-Landauer analysis this could lead

to issues in keeping the scattering region short enough to avoid electron localization[111]. For three- and two-dimensional systems this issue can be avoided by repeating the structure along the transverse directions, increasing the system size, but not the length of the scattering region. The issue is particularly important for semiconducting, one-dimensional systems where not only is the localization length shorter, but repetition along transverse directions is not possible.

4.6 Summary

In summary we have presented a conceptually simple MD-Landauer method for treating EPC and phonon limited mobilities. Combining DFT-NEGF transport calculations and MD simulations, we obtained an average transmission which depends on temperature and the length of the MD region. Using the length dependence, we then evaluated the mobility. This approach was then validated by comparing to mobilities and conductivities obtained by the Boltzmann transport equation for one-, two-, and three dimensional, metallic and semiconducting materials. For bulk silicon and gold we also compared against experimental values. Similar methods to calculate the mobility based on LOE and STD were also presented and compared. Advantages and limitations of the different methods were discussed.

4.6.1 Outlook

The success seen here in estimating the phonon limited mobility using the MD-Landauer approach, opens up for the possibility of including at the same time e.g. randomly placed dopant atoms or defects in the MD snapshots to get more realistic estimates of mobilities in real devices. The computational efficiency of the STD method also enables the inclusion of EPC along with additional interactions that have so far been out of reach. The next chapter details, through the use of STD, a study of the first principles phonon-assisted photocurrent in a realistic solar cell device under operating conditions.

Chapter 5

Modeling phonon-assisted photocurrent

In chapter 3, we performed a multiscale simulation in order to characterize the performance of a CZTS(e) based thin-film solar cell, and to extract important properties such as the open-circuit voltage V_{OC}, the recombination energy deficit $\Delta\varphi$, and the efficency.

In this chapter we describe developed tools that go beyond multiscale, and calculate the photocurrent of a silicon *p-n* junction directly from first principles DFT-NEGF calculations. The open-circuit voltage dependence on temperature and light intensity is also extracted and compared to experimental results. The chapter provides a review of the results reported in Paper 6.

5.1 Simulating the silicon solar cell

A review was published recently on the design of new materials for e.g. applications in photovoltaics (PV) from first principles[21]. One of the conclusions of the authors was how the abundance of available candidate materials, like CZTS(e), together with the lack of efficient devices based on these materials, calls for precise predictive device calculations[21].

As mentioned in previous chapters it is difficult to include important effects such as confinement of electrons and phonons, surface- and strain effects in the continuum models typically used to benchmark PV cells[44]. Using DFT-NEGF calculations these effects are straightforward to include. Although in the past DFT-NEGF calculations of realistic devices was beyond reach, the massive progression in the field of computational material science means that difference between system size and complexity attainable in simulations and experiments is becoming smaller every day.

In spite of the recent influx of PV cells based on new thin-film absorbers like CdTe and CIGS, PV cells based on silicon absorber layers remains the market leader where presently around 90% of commercial solar cells are silicon based[13, 49–51].

It is well known that the indirect band gap of silicon means that absorption of a photon at the band gap energy, must be accompanied by the absorption/emission

of a phonon due to momentum conservation. In order to properly describe the silicon solar cell, it is therefore crucial that both interaction with light and EPC is accounted for. However, calculating, from first principles, the phonon-assisted photon absorption is a notoriously complex and computationally demanding problem. The difficulty comes from having to consider the complex two excitation scattering event, and calculating a double sum over fine k- and q-point grids (k and q being the wavenumber of the electrons and phonons respectively). As a result first principles calculations of phonon-assisted absorption has so far been limited to bulk crystals with periodic boundary conditions in all directions, where only a few atoms need to be considered[36, 43, 123].

As stated in chapter 2, Zacharias and Giustino[43] introduced a very efficient method (STD) for including phonon induced absorption processes using a single super cell calculation in which the atoms are displaced away from their equilibrium positions. This approach was then extended to study electron transport in silicon systems with over 1000 atoms including electron-phonon coupling (EPC) within the DFT-NEGF formalism[*Paper 4*] and to estimate the phonon limited mobility of a silicon nanowire[*Paper 5*].

A number of recent papers study the inclusion of electron-photon interaction in DFT-NEGF simulation using first order Born approximation[124–126]. In the following section we derive an expression for the current due to electron-photon interaction, as we implemented it in the QuantumATK software, and account for the inclusion of EPC through STD.[4][*Paper 6*].

5.2 First principles photocurrent calculation

The starting point is to consider the Hamiltonian of the electronic system in an electromagnetic field

$$H = \frac{1}{2m_0}(\mathbf{p} + e\mathbf{A})^2 + U + H_{\text{int}}, \tag{5.1}$$

where $\mathbf{p}$ is the momentum operator, $\mathbf{A}$ is the vector potential, U is the external potential and H_{int} accounts for additional interaction terms such as electron-electron interaction.
Assuming a field of weak intensity we can throw away second order terms in $\mathbf{A}$ and we have,

$$H \approx H_0 + H_\omega, \tag{5.2}$$

$$H_0 = \frac{\mathbf{p}^2}{2m_0} + U + H_{\text{int}}, \tag{5.3}$$

$$H_\omega = \frac{e}{m_0}\mathbf{A}\cdot\mathbf{p}, \tag{5.4}$$

where H_0 is the unperturbed electronic Hamiltonian and H_ω is the perturbation due to electron-photon interaction. For a single-mode monochromatic light source we have[126]

$$\mathbf{A} = \mathbf{e}\left(\frac{\hbar\sqrt{\tilde{\mu}_r\tilde{\varepsilon}_r}}{2N\omega\tilde{\varepsilon}c}F\right)^{\frac{1}{2}}(be^{-i\omega t} + b^\dagger e^{i\omega t}), \tag{5.5}$$

where ω is the frequency of the light, F is the photon flux, N is the number of photons, $b^\dagger$ and b are the bosonic creation and annihilation operators and $\mathbf{e}$ is a unit vector giving the polarization of the light. The relative permeability $\tilde{\mu}_r$, the relative permittivity $\tilde{\varepsilon}_r$ and the permittivity $\tilde{\varepsilon}$ are all assumed isotropic and homogeneous. Inserting Eq. (5.5) in Eq. (5.4) we can evaluate the elements of the electron-photon interaction Hamiltonian

$$\langle i|H_\omega|j\rangle = M_{i,j}(be^{-i\omega t} + b^\dagger e^{i\omega t}), \tag{5.6}$$

where we have defined the electron-photon coupling matrix given by

$$M_{i,j} = \frac{e}{m_0}\left(\frac{\hbar\sqrt{\tilde{\mu}_r\tilde{\varepsilon}_r}}{2N\omega\tilde{\varepsilon}c}F\right)^{\frac{1}{2}}\mathbf{e}\cdot\mathbf{p}_{ij}. \tag{5.7}$$

The lowest order self-energy of the electron-photon interaction based on the SCBA is

$$\boldsymbol{\Sigma}^>_\omega(\epsilon) = N\mathbf{M}^\dagger\mathbf{G}^>(\epsilon+\hbar\omega)\mathbf{M} + (N+1)\mathbf{M}\mathbf{G}^>(\epsilon-\hbar\omega)\mathbf{M}^\dagger, \tag{5.8}$$

$$\boldsymbol{\Sigma}^<_\omega(\epsilon) = N\mathbf{M}\mathbf{G}^<(\epsilon-\hbar\omega)\mathbf{M}^\dagger + (N+1)\mathbf{M}^\dagger\mathbf{G}^<(\epsilon+\hbar\omega)\mathbf{M}, \tag{5.9}$$

where N is the number of photons and the lesser/greater Green's function of the device with no electron-photon interaction can be calculated using the zero order Keldysh equation

$$\mathbf{G}^{\gtrless} = \mathbf{G}(\boldsymbol{\Sigma}^{\gtrless}_L + \boldsymbol{\Sigma}^{\gtrless}_R)\mathbf{G}^\dagger, \tag{5.10}$$

and the lead self-energies are given by

$$\boldsymbol{\Sigma}^>_\alpha = -i\boldsymbol{\Gamma}_\alpha(1-f_\alpha), \quad \boldsymbol{\Sigma}^>_\alpha = i\boldsymbol{\Gamma}_\alpha f_\alpha, \tag{5.11}$$

where $\boldsymbol{\Gamma}_\alpha$ is the broadening of lead $\alpha = L, R$ and $\mathbf{G}$ is the retarded Green's function of the device region without electron-photon interaction given by Eq. (2.9). The lesser/greater device Green's functions including electron-photon interaction are

$$\mathbf{G}^{\gtrless}_\omega = \mathbf{G}(\boldsymbol{\Sigma}^{\gtrless}_L + \boldsymbol{\Sigma}^{\gtrless}_R + \boldsymbol{\Sigma}^{\gtrless}_\omega)\mathbf{G}^\dagger. \tag{5.12}$$

When included in the Meir-Wingreen equation Eq. (2.11) the first two terms in Eq. (5.12) lead to the usual non-interacting Landauer-Büttiker current expression. The "photocurrent" in lead α due to electron-photon interaction is given by an expression very similar to the LOE current

$$I_{\omega,\alpha} = \frac{G_0}{e}\int_{-\infty}^{\infty} d\epsilon\,[\mathcal{T}^-_{\alpha,\beta}(\epsilon) - \mathcal{T}^+_{\alpha,\beta}(\epsilon)], \tag{5.13}$$

$$\begin{aligned}\mathcal{T}^-_{\alpha,\beta}(\epsilon) =& N[1-f_\alpha(\epsilon)]f_\beta(\epsilon-\hbar\omega)\mathrm{Tr}\{\mathbf{M}^\dagger\tilde{\mathbf{A}}_\alpha(\epsilon)\mathbf{M}\mathbf{A}_\beta(\epsilon-\hbar\omega)\}\\ &+ (N+1)[1-f_\alpha(\epsilon)]f_\beta(\epsilon+\hbar\omega)\mathrm{Tr}\{\mathbf{M}\tilde{\mathbf{A}}_\alpha(\epsilon)\mathbf{M}^\dagger\mathbf{A}_\beta(\epsilon+\hbar\omega)\},\end{aligned} \tag{5.14}$$

$$\begin{aligned}\mathcal{T}^+_{\alpha,\beta}(\epsilon) =& Nf_\alpha(\epsilon)[1-f_\beta(\epsilon+\hbar\omega)]\mathrm{Tr}\{\mathbf{M}\tilde{\mathbf{A}}_\alpha(\epsilon)\mathbf{M}^\dagger\mathbf{A}_\beta(\epsilon+\hbar\omega)\}\\ &+ (N+1)f_\alpha(\epsilon)[1-f_\beta(\epsilon-\hbar\omega)]\mathrm{Tr}\{\mathbf{M}^\dagger\tilde{\mathbf{A}}_\alpha(\epsilon)\mathbf{M}\mathbf{A}_\beta(\epsilon-\hbar\omega)\},\end{aligned} \tag{5.15}$$

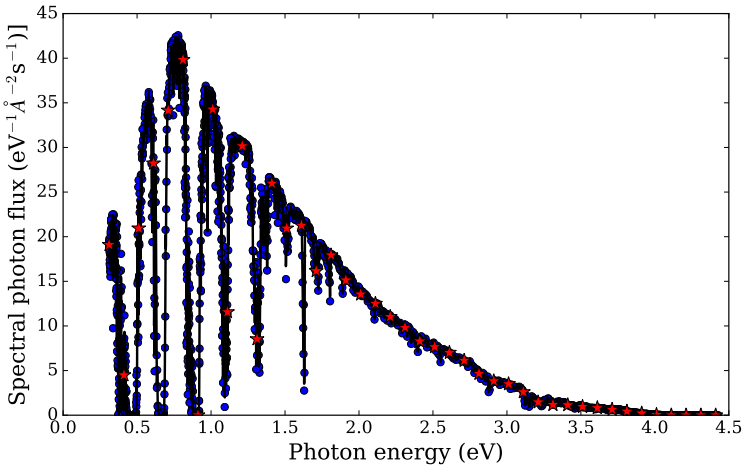

FIGURE 5.1: The AM 1.5[128] solar spectrum given in spectral photon flux as a function of photon energy (blue squares). The solid black line is an interpolation of the data points. The red stars indicate the values used to calculate the total photocurrent.

where we have reintroduced the spectral function $\mathbf{A}_\alpha$ and the time-reversed spectral function $\tilde{\mathbf{A}}_\alpha$ from chapter 2. The terms proportional to $(N+1)$, account for stimulated and spontaneous emission of photons. Since we are interested in the case with significant intensity where $N \gg 1$ we ignore spontaneous emission under the assumption $N+1 \approx N$. Furthermore, since we in this chapter consider a silicon *p-n* junction at voltages below the band gap, stimulated emission does not contribute to the current. The retarded $\mathbf{G}$ and advanced $\mathbf{G}^\dagger$ Green's functions, spectral broadening of the leads, $\mathbf{\Gamma}_\alpha$, and the dipole transition matrix $\mathbf{p}$, are calculated self-consistently from DFT-NEGF simulations of the silicon *p-n* junction device.

5.2.1 EPC through special thermal displacement

As derived in chapter 2 the configuration displaced according to $\mathbf{u}_{STD}$ gives the correct thermal average of the Landauer conductance and the optical absorption in the limit of large systems[43][*Paper 4*]. The total current including electron-photon and electron-phonon interaction at bias V and temperature T is therefore calculated as,

$$I_{\text{tot}}(V,T) = I(V, \mathbf{u}_{STD}(T)) + I_\omega(V, \mathbf{u}_{STD}(T)), \tag{5.16}$$

where $I(V,T)$ is the "dark" current due to the applied bias. By displacing the atomic coordinates once along the vector $\mathbf{u}_{STD}$, calculating and adding the two current contributions, we get the thermally averaged current under illumination of a single frequency of light[1].

5.2.2 Modelling sunlight illumination

To compare with experiments we wish to calculate the total current under sunlight illumination. For this purpose we use the AM 1.5 reference spectrum[128]. The spectrum is given for each wavelength of light in units of spectral solar irradiance

[1]Forces for the phonon calculation were calculated using Tersoff potentials[110, 127]

(unit: $Wm^{-2}nm^{-1}$) defined as

$$E_\lambda \equiv \frac{\Delta E}{\Delta \lambda_i}, \tag{5.17}$$

where ΔE is the part of the total solar irradiance coming from the spectral (wavelength) interval $\Delta\lambda_i$. For the AM 1.5 spectrum $\Delta\lambda_i$ is equal to the spectral resolution which is the distance between measured wavelengths. Integrating the spectral solar irradiance over all wavelengths gives a total solar irradiance of 1000 Wm^{-2} also known as 1 sun. The spectral solar irradiance can be converted to a spectral solar photon flux given by

$$F_\omega \equiv \frac{\Delta F}{\Delta \omega_i}, \tag{5.18}$$

where ΔF is the part of the total solar photon flux coming from the spectral (photon energy) interval $\Delta\omega_i$. The spectral solar photon flux as a function of photon energy ω is shown in Fig. 5.1.

To calculate the total current under sunlight illumination we calculate the photocurrent from Eq. (5.13) for a number of equidistant photon energies in a range from 0.0 to 5.0 eV separated by identical photon energy intervals $\Delta\omega$. The photon flux at each photon energy is then given by $F(\omega) = F_\omega \Delta\omega$ and the total photocurrent under sunlight illumination is calculated as the sum of current contributions,

$$I_{\text{sun}}(V,T) = \sum_\omega I_\omega(F(\omega),V,T). \tag{5.19}$$

Adding to this current, the "dark" current defined above we get the total current under sunlight illumination. To evaluate F_ω at values between data points, we perform an interpolation, as shown in Fig. 5.1(solid black line).

5.2.3 Band gap correction with DFT-1/2

In order to properly account for the optical properties of silicon it is important to capture the correct band gap of bulk silicon. To this end, we use the DFT-1/2 method where the self-interaction error of regular LDA or GGA DFT is corrected by adding an atomic self-energy to the DFT Hamiltonian[2]. The self-energy corresponds to the change in potential of an atom, caused by removing a fraction between 0 and 1 electrons of its charge[129]. The DFT-1/2 method is at a similar level of approximation as the DFT + U band gap correction discussed earlier in chapter 3. Using DFT-1/2 we obtain an indirect band gap of 1.135 eV for pristine silicon which agrees well with the experimental value (1.12 eV)[130].

5.3 Results and discussion

Fig. 5.2a shows the system for which we will calculate the phonon-assisted photocurrent. It is a 19.6 nm silicon *p-n* junction with the *p-n* potential along the [100] direction. The calculated local density of states of the pristine *p-n* junction is shown in Fig. 5.2b[3] and we can see the typical *p-n* profile along the device with flat bands near

[2]For the electronic structure calculation we use the GGA-1/2 exchange-correlation method with the SG15-low basis set and a 11x11 Monkhorst-Pack grid was used to sample the Brouillon zone.

[3]A 21x21 Monkhorst-Pack grid of k-points was used for the LDOS and transport calculations.

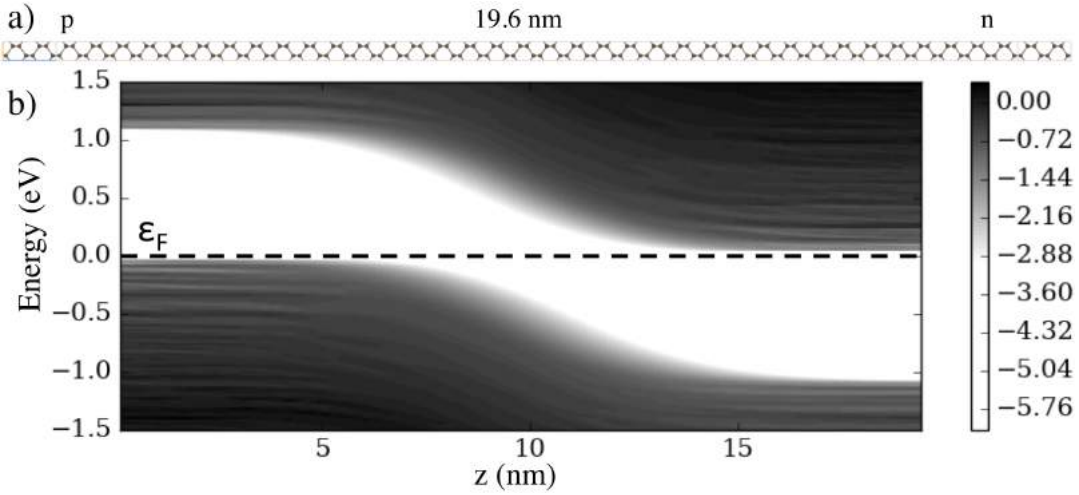

FIGURE 5.2: a) Structure and cell used in the calculation of the 19.6 nm silicon *p-n* junction with $n/p = \pm 2 \times 10^{19}\text{cm}^{-3}$. The doping is included in the same way as in chapter 3[45]. The device region includes 144 atoms. b) Local density of states along the transport direction of the silicon *p-n* junction on a logarithmic scale. Taken from Paper 6.

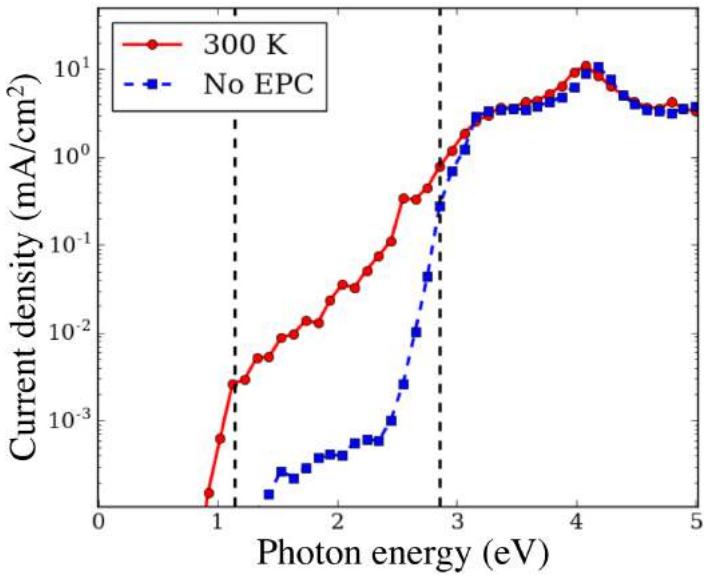

FIGURE 5.3: The calculated photocurrent density for the pristine (blue dashed) and STD displaced (red solid) system where $F = 1/\text{Å}^2 s$ and V = 50 mV. Vertical lines correspond to the calculated indirect (1.135 eV) and direct (2.853 eV) band gap of bulk silicon. Taken from Paper 6.

the electrode indicating that the screening in kept inside the device[45]. We notice also a slight narrowing of the band gap near the center of the *p-n* profile.

5.3.1 Photocurrent

In Fig. 5.3 the calculated photocurrent density of the pristine silicon *p-n* junction shown in Fig. 5.2a is compared to the photocurrent density at a temperature of 300 K where EPC is included through the displacement of atoms according to the STD.

The photocurrents in Fig. 5.3 are calculated at single photon energies using Eq. (5.13) with a constant photon flux given by $F = 1/\text{Å}^2 s$ and plotted as a function of the photon energy. The dashed vertical lines in Fig. 5.3 indicate the calculated energies of the indirect ($E_g^{\text{indirect}} = 1.135\,\text{eV}$) and direct ($E_g^{\text{direct}} = 2.853\,\text{eV}$) band gaps of bulk silicon. We observe that by including EPC using the STD we get a significant, orders of magnitude larger, contribution from the indirect transition ($1.135\,\text{eV} < \hbar\omega < 2.85\,\text{eV}$) below the direct band gap (see Fig. 5.3). We also see that the inclusion of EPC only renormalizes the current due to the direct transition ($\hbar\omega > 2.85\,\text{eV}$) slightly. Additionally, although the photocurrent due to the indirect transition is increased massively, the photocurrent coming from direct transitions is still by far the largest contribution dominating the total photocurrent. The relation between the photocurrent from the indirect and direct transitions at 300 K seen in Fig. 5.3 compares well to previous calculations of the absorption coefficients in bulk silicon where EPC was included in the same way[43]. This indicates that the difference in photocurrent is mainly due to absorption and not transport issues.

As discussed in the previous chapter the effects of finite temperature on the electronic structure is included in STD, and indeed we see in Fig. 5.3 finite photocurrent contributions at 300 K from photons below the 0 K band gap corresponding to a reduction in the band gap with temperature. In addition to the finite temperature renormalization of the band gap, we obtain the actual photocurrent of the transport setup assisted by band-to-band tunneling and including the device potential at finite bias. As such unlike the bulk silicon absorption calculations of previous studies, we find in Fig. 5.3 a small finite contribution to the photocurrent coming from the indirect transition even without EPC. Most of the photocurrent below the direct band gap in the case without EPC is related to the narrowing of the band gap at the center of the *p-n* junction seen in Fig. 5.2b and can be reduced by considering a more gradual *p-n* junction with lower doping as shown in Fig. 5.4(left). The additional much smaller photocurrent contribution at lower photon energies is traced back to symmetry breaking along the [100] direction caused by the ultrathin *p-n* junction considered here. Indeed considering the *p-n* junction along e.g. the [111]-direction reduces this small contribution (shown in Fig. 5.4(right)). In simulations on bulk silicon, which is periodic in all directions, such transitions would be strictly prohibited without EPC by the opposite symmetry of conductance and valence states. This follows from the strict selection rule due to momentum conservation, which is a consequence of the infinite translational symmetry of bulk silicon. In a *p-n* junction, silicon is not translational invariant in the direction of the *p-n* potential profile and hence the momentum in that direction is not a conserved quantity. As such the strict selection rules of the bulk case are relaxed.

5.3.2 Total current

The total current density as a function of applied bias voltage in the dark and under sunlight illumination is shown in Fig. 5.5. The lines show a least squares fit of the calculated data points to the usual analytical expression for the current of a diode under illumination

$$I = I_{\text{sun}} + I_0 \left(\exp\left(\frac{eV}{nk_BT} \right) - 1 \right), \tag{5.20}$$

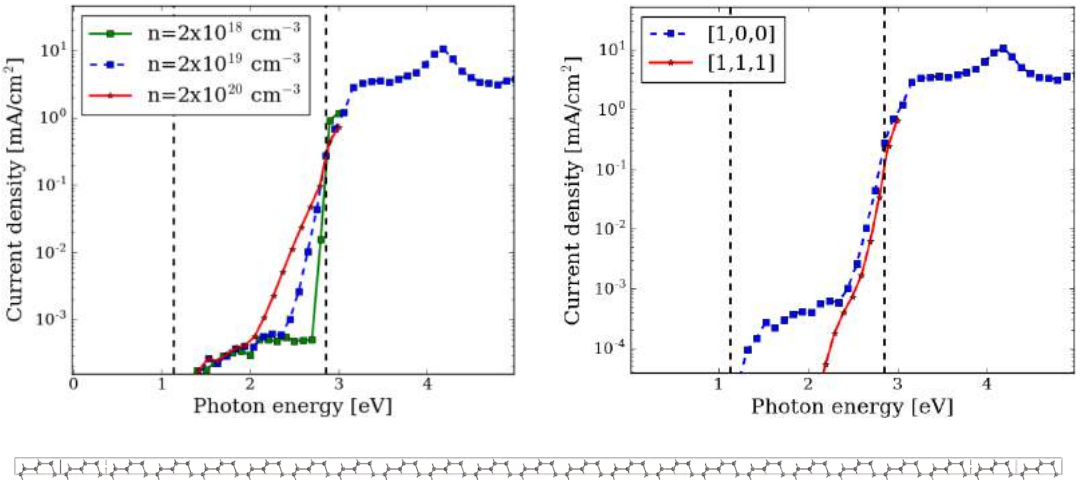

FIGURE 5.4: Left: Photocurrent density as a function of photon frequency for three different doping concentrations in pristine (undisplaced) silicon *p-n* junction. The result for $n = 2 \times 10^{18}\text{cm}^{-3}$ where obtained using a 30.4 nm system while others were 19.6 nm. Right: Photocurrent density as a function of photon frequency for a 19.6 nm pristine (undisplaced) silicon *p-n* junction along the [100] direction (blue) and along the [111] direction (red). Both calculations use $n = 2 \times 10^{19}\text{cm}^{-3}$. Bottom: Structure of the [111] silicon *p-n* junction. Taken from Paper 6 supplementary.

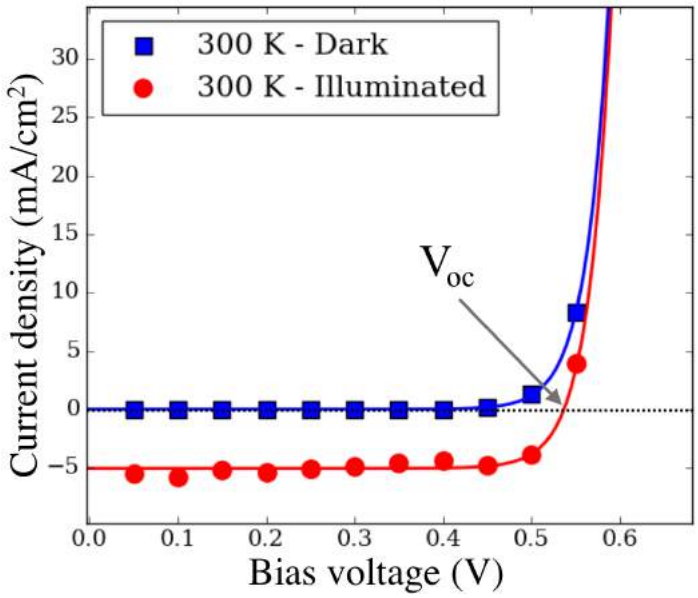

FIGURE 5.5: The calculated room temperature current density as a function of applied bias voltage for the silicon *p-n* junction in the dark ($F = 0$) and under illumination. Taken from Paper 6.

where n is the ideality factor. The IV-curve looks like expected for a diode with a photocurrent being approximately constant at all applied biases[131]. The applied bias voltage where the illuminated IV-curve crosses the zero current density line and no current is generated is the open-circuit voltage (V_{OC}). For crystalline silicon PV cells the open-circuit voltage is known to be in the range 0.55-0.60 V [132–134] at

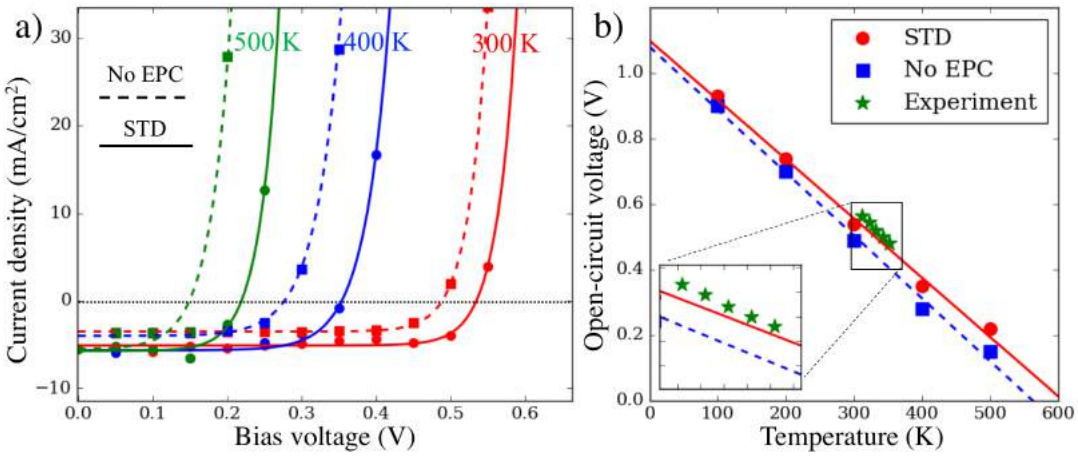

FIGURE 5.6: a) Calculated IV curves with (solid) and without (dashed) EPC for different temperatures. b) Calculated open-circuit voltage as a function of temperature with linear fits. The green star markers are experimental measurements from [132]. Inset shows a close-up near the experimental measurements. A light intensity of 1 Sun was used in all calculations and experimental values shown. Taken from Paper 6.

room temperature, in good agreement with the 0.54 V obtained from our calculation. The short-circuit current density, obtained at zero applied bias (5 mA/cm^2) is lower, but comparable to experimental values[133, 134]. It is expected that we find a lower short-circuit current density since we consider a thin-film solar cell whereas experimental values are for thick absorber layers of several hundred micron.

5.3.3 Temperature dependence

To quantify the impact of including EPC on the total current we compare in Fig. 5.6a the IV-curve for the pristine silicon system with no EPC to the IV-curve of the system displaced according to the STD to include EPC. In order to analyze also the impact of EPC on the temperature dependence, the IV-curve both with and without EPC is plotted for different temperatures. For all the temperatures plotted in Fig. 5.6a the short circuit current is underestimated by ∼25% without EPC. As we saw earlier, the biggest impact of EPC on the low bias photocurrent is the increase in photocurrent from the indirect transition (see Fig. 5.3). This indicates that ∼25% of the short circuit current is coming from the indirect transition even though indirect absorption happens at a much lower rate (see Fig. 5.3). The explanation can be found in the solar spectrum of Fig. 5.1, which shows a much higher flux of photons with energies below the direct band gap ($\hbar\omega < 2.85$ eV).

Considering again the IV-curves in Fig. 5.6a we see that also the open-circuit voltage is significantly underestimated without EPC. This underestimation is most pronounced at higher temperatures, but already at 300 K one obtains $V_{OC} = 0.49$ V which is a ∼10% underestimation. This discrepancy in open-circuit voltage is related not only to the underestimation of the photocurrent, but also to the overestimation of the "dark" current, without EPC. These results highlights the importance of including EPC to capture the temperature dependent behavior properly.

In Fig. 5.6a the short-circuit current is largely constant as a function of temperature while the open-circuit voltage is degraded for higher temperatures. This is due to increased probability of carriers tunneling through the *p-n* junction via electron-phonon scattering events at bias voltages below the band gap. In the case with no EPC the increased current at higher temperatures comes from the temperature dependence of the Fermi Dirac distribution alone.

Since we consider a thin-film silicon solar cell here, direct comparisons of the generated IV-curve to experimental measurements based on thick slabs of silicon would not be meaningful. However, the open-circuit voltage is less sensitive to slab thickness. As discussed in chapter 3, the temperature dependence of the open-circuit voltage is often measured in experiments on solar cell devices to extract the activation energy φ of the main recombination channel. In chapter 3 Fig. 3.10c, we calculated the temperature dependent open-circuit voltage for the CZTS solar cell using a continuum TCAD device model[44]. We now have the possibility of extracting these graphs directly from first principles using the results shown in Fig. 5.6a. We can therefore compare the temperature dependence of the open-circuit voltage to that reported in the literature.

The obtained open-circuit voltage as a function of temperature with and without EPC is shown in Fig. 5.6b. A least squares fit to a linear function is plotted alongside the data points. For both cases we see the expected linear temperature dependence. Extracting the activation energy φ, we get $1.1\,\mathrm{V} \pm 0.025\,\mathrm{V}$ with EPC and $1.08\,\mathrm{V} \pm 0.029\,\mathrm{V}$ without EPC both slightly below our calculated band gap. The φ value below the band gap could be related to the narrowing of the band gap in the center of the *p-n* junction seen in Fig. 5.2b. In Fig. 5.6b we also show experimental open-circuit voltage values, measured by Huang *et al.*[132] on a crystalline silicon PV module under simulated solar irradiation while controlling the cell temperature. We see a good agreement with the experimental values when including EPC. The calculated values are slightly lower than experiments, which is expected due to the ultra thin *p-n* junction considered here. Without including EPC we calculate even lower open-circuit voltages at all temperatures. Measurements of the open-circuit voltage performed at temperatures in the range 100-300 K under 1.1 sun illumination[133] (not shown) also agree nicely with the values calculated including EPC.

5.3.4 Solar irradiance dependence

We will now consider the dependence on solar irradiance, which is often measured in experiments. In Fig. 5.7 we show the calculated open-circuit voltage for different light intensities and compare with experimental values from Huang *et al.*[132]. Here we see a nice agreement between values calculated with EPC and the experimentally measured values. The best agreement is seen at the lowest intensities which is expected given the assumption of a weak field going into Eq. (5.4). The open-circuit voltages calculated with no EPC do however not agree as well with experimental values, highlighting once again the importance of EPC in this device.

5.3.5 Solar cell efficiency

Lastly we analyze how efficiently the considered silicon *p-n* junction converts solar energy into electrical power. Figure 5.8 shows the power density for the *p-n* junction

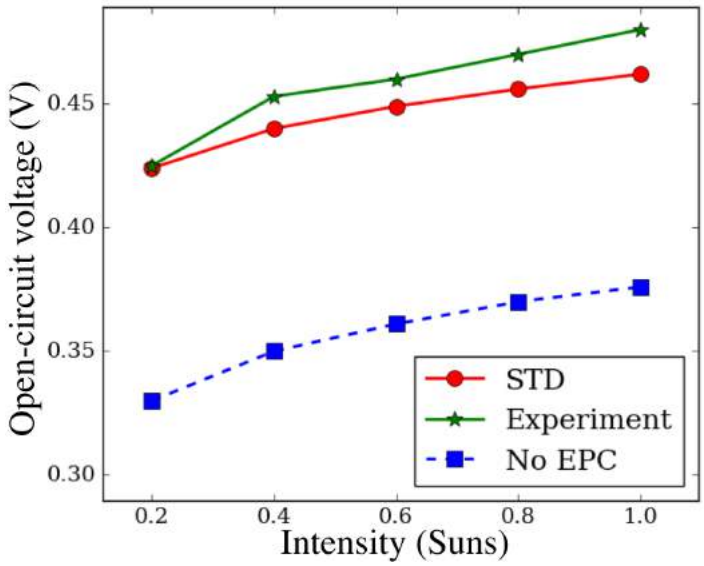

FIGURE 5.7: a) Open-circuit voltage as a function of light intensity at 352 K. The calculational results including EPC were extrapolated from the fitted line in Fig. 5.6b since we did not perform calculations at the exact temperature measured in [132]. Taken from Paper 6.

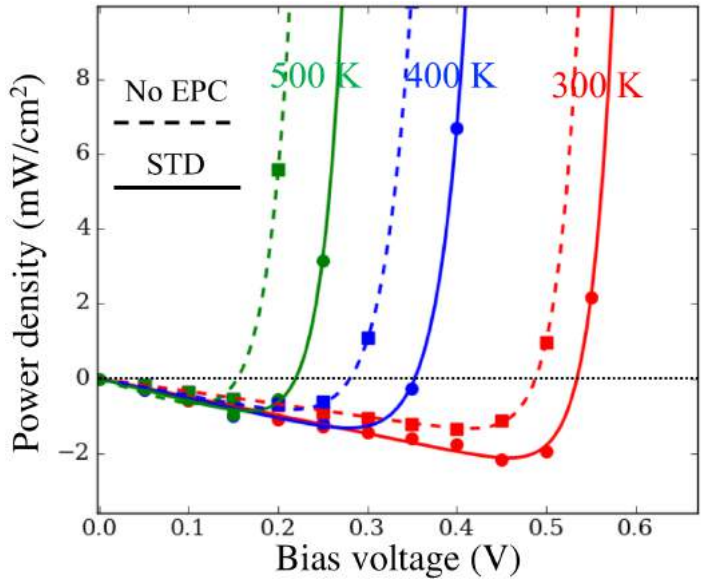

FIGURE 5.8: Calculated power density as a function of applied voltage with (solid) and without (dashed) EPC for different temperatures. Taken from Paper 6.

calculated with and without including EPC for different temperatures. The maximum power point, which is the applied bias voltage needed to generate maximum power, is lower at all considered temperatures when EPC is not included. Furthermore, the calculated room temperature maximum power density is about a factor of two higher when including EPC. Comparing the calculated maximum power of the silicon *p-n* junction with the total solar irradiance (1000 Wm^{-2}) we obtain a room temperature conversion efficiency of 2%. This low efficiency is not surprising since silicon solar cells with only a thin absorber layer, like the one considered, are known to have low efficiency. This calls for alternative materials if material cost should be

decreased by reducing absorber layer thickness. A potential ultra-thin 2D replacement will be examined in the next chapter.

Using first order perturbation to calculate the photocurrent means that we ignore all radiative recombination of photon-excited electron-hole pairs. This is because such events are second-order processes involving two photons (and two phonons in the case of an indirect transition). For the ultra-thin *p-n* junction, interacting with a low intensity field considered here, the population of photo-excited electron-hole pairs is low and this is a good approximation. Furthermore, we do not include the attenuation of the light due to absorption. In practical terms this means that the light intensity at the front and back of the solar cell is the same. For thin weakly absorbing systems like the one considered here, the light intensity is not expected to change dramatically over the device region. Both of these approximations would however lead to a slight overestimation of the solar cell efficiency.

5.4 Summary

In this chapter we presented a computationally cheap method to obtain the phonon-assisted photocurrent in large-scale devices from first-principles calculations. We applied the method to a silicon solar cell device and demonstrated, by comparing result with and without EPC, the impact of including EPC in order to properly describe the photocurrent due to an indirect transition. The temperature and intensity dependence of the calculated open-circuit voltage was successfully compared to experiments. The temperature dependence of the generated power and the solar cell efficiency could also be extracted from the results. The results illustrate the pivotal role played by EPC in photocurrent modelling to avoid underestimation of the open-circuit voltage, short-circuit current and maximum power.

5.4.1 Outlook

The developed method opens up for computational characterization of future photovoltaic devices including the combined effects of light-matter interaction, phonon-assisted tunneling and the device potential at finite bias from first-principles simulations. This method would be especially useful for the characterization of thin-film solar cells, where absorber thickness is closer to the scales obtainable for first principles calculations. For the silicon system the treatment of EPC boosted the photocurrent due to phonon-assisted absorption over the indirect band gap. For direct band gap thin-film solar cell the main role of EPC will likely be the thermal relaxation of carriers or non-radiative recombination leading to lower photocurrent. However a number of recent studies show that EPC plays a key role in the outstanding performance of PV cells based on direct band gap perovskites which have gained close to record efficiency in only a few years[135–138]. The investigation of perovskite based solar cells including EPC as described in this chapter would therefore be of great scientific value. In the following chapter we consider another promising new material, namely the two-dimensional semiconductor Janus-MoSSe.

Chapter 6

Devices in Janus MoSSe

Since the discovery of the two-dimensional (2D) material graphene by Konstantin Novoselov and Andre Geim in 2004[139], scientific research into the electrical, thermal, and mechanical properties of 2D materials has exploded and in 2010 the pair was awarded a Nobel prize for their experiments on graphene. Graphene consists of a single layer of carbon atoms arranged in a hexagonal lattice as shown in Fig. 1.2c in chapter 1. Several additional 2D materials have since then been synthesized, most notably the semiconducting transition-metal-dichalcogenide (TMD) MoS_2 and the insulating hexagonal Boron Nitride (hBN) (both also shown in Fig. 1.2c). A particularly interesting feature of these 2D materials is the possibility of stacking them in various orders creating meta-materials with new interesting properties[5, 140–142].

The recent experimental realization of a new class of 2D materials exhibiting a built in out-of-plane dipole, has received much attention for its potential usefulness for solar water splitting[89–93]. Devices including this exciting new material have yet to be fabricated in the lab or studied theoretically.

In this chapter, which covers the results of Paper 7, we present a first principles investigation of devices using monolayer and multilayer Janus MoSSe combined with monolayers of graphene. We show that the use of conventional metallic electrodes in Janus MoSSe devices presents major challenges and propose strategies to overcome said challenges. Furthermore, it is found that Janus MoSSe can be used for record high, homogenous non-destructive *p*- and *n*-doping of graphene monolayers. Finally, we calculate the cross-plane (cp) photocurrent generated by monolayer and trilayer Janus MoSSe and compare to results from the silicon *p*-*n* junction studied in the previous chapter.

6.1 Discovery of Janus MoSSe

In 2017 A.-Y. Lu et al.[89] reported the successful synthesis of a new TMD named Janus MoSSe. The synthesis process is sketched in Fig. 6.1a-b. Starting from a monolayer of MoS_2, all sulfur atoms were removed from only the top side of the monolayer, via H_2 plasma stripping, and replaced with hydrogen, creating the intermediate product MoSH, which was found to be metallic. Using thermal selenization the hydrogen was then replaced with selenium creating the Janus MoSSe layer. Using energy-dependent X-ray photoelectron spectroscopy it was verified that the sulfur had in fact only been replaced on one side. This can also be seen from the difference in contrast between the sides in an STEM image (shown in Fig. 6.1c). Using angle-resolved second harmonics generation it was discovered that the Janus MoSSe layer has a built-in dipole in the cross-plane direction. Another paper, reporting the successful synthesis of Janus MoSSe starting from $MoSe_2$ and replacing the top layer of

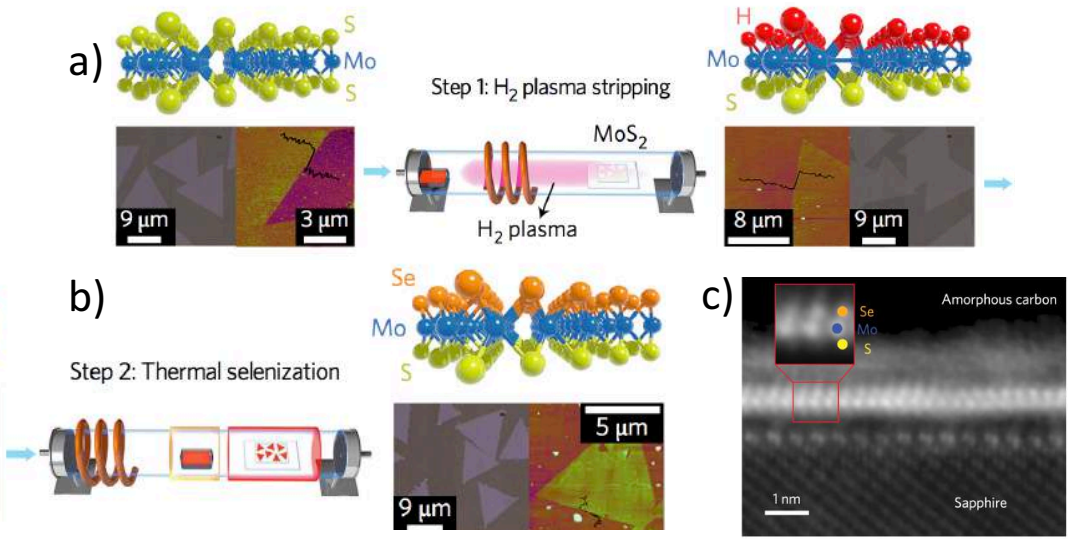

FIGURE 6.1: Synthesis of Janus MoSSe. a-b): Sketch showing the steps involved in the synthesis of Janus MoSSe. At each step optical- and atomic force microscopy images are shown at each step in the process. c): Scanning transmission electron microscopy image of the sample cross-section. The contrast in the is proportional to the square of the atomic number. These figures were adapted from [89]

Se with S, has since been published[90]. This means that the material can now be produced with either the Se or S side facing upwards.

6.2 Monolayer Janus MoSSe

The system setup and calculated band structure of a monolayer of Janus MoSSe is shown in Fig. 6.2a-b[1]. We find a direct band gap located at the K and K'-points in k-space in agreement with previous calculations[91] . The band gap is found to be 1.72 eV which corresponds nicely to the 1.77 eV optical band gap previously reported due to strong excitonic effects which are common for 2D TMDs and not included in our model[2][89, 91]. Fig. 6.2c shows the electrostatic difference potential averaged along the xy-plane as a function of the z-position and we see clearly the built-in cp dipole field. The potential difference is found to be 0.66 eV. The cp dipole field, seen in Fig. 6.2c, can be explained from the slight difference in the electronegativity of S and Se atoms, which for a full layer results in an difference in workfunction between the two sides. To accurately describe the asymmetric slab with a surface dipole, density we employ Neumann boundary conditions at the vacuum boundaries when solving the Poisson equation[141, 143]. Neumann boundary conditions allow for the system to freely adjust the dipole field self-consistently.

[1]The electronic structure calculations were performed using DZP basis set and a 51x51 Monkhorst-Pack k-point grid. LDA was used for the exchange-correlation potential. In the out of plane direction over 30 Å of vacuum is included. We chose lattice parameters as calculated previously[91]. Atomic coordinates were relaxed until all interatomic forces were below 0.02 eV / Å

[2]One could include excitonic effect through the Bethe–Salpeter equation, but this is computationally demanding and beyond the scope of our study.

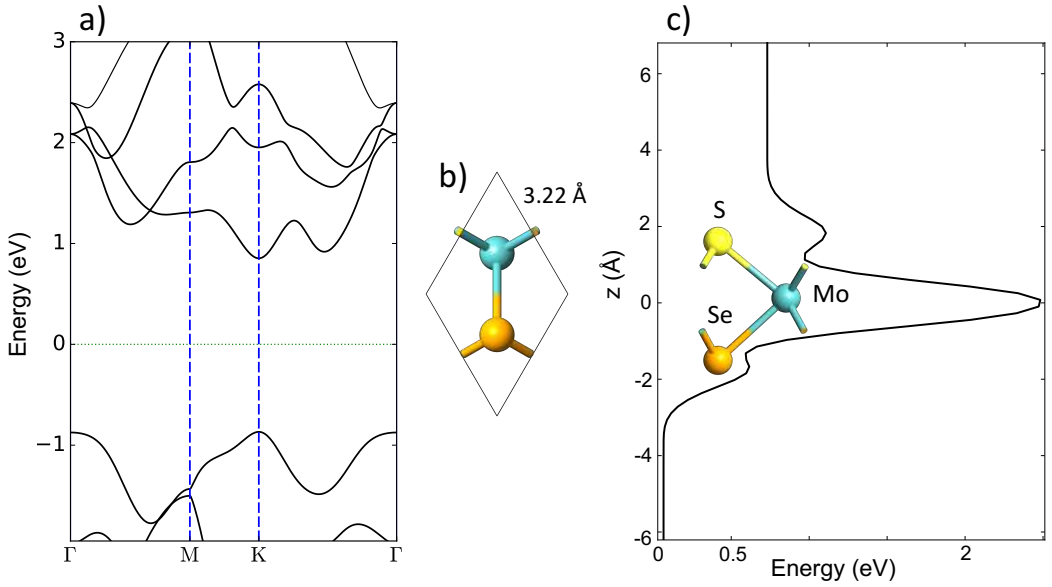

FIGURE 6.2: Janus dipole mechanism. a) Band structure and b) Top view of the unit cell of monolayer Janus MoSSe. c) Electrostatic difference potential averaged in the plane of monolayer Janus MoSSe plotted as a function of the cross-plane position, z. Taken from Paper 7.

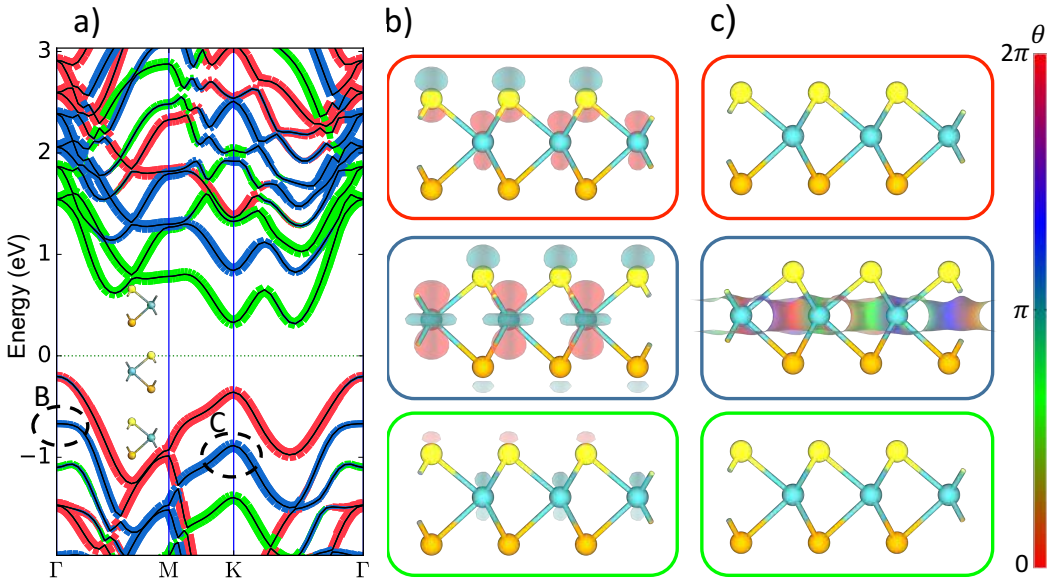

FIGURE 6.3: a) Band structure of trilayer Janus MoSSe projected onto the seperate layers. The structure is shown in the inset. Red, blue and green lines represents projections on the top, middle and bottom layers, respectively. The thickness of the lines indicates the weight of the projections. b) Cross-plane channel: Bloch state isosurface of the Γ-point state highlighted in a). c) In-plane channel: Bloch state isosurface of the K-point state highlighted in a). We chose interlayer distances as calculated previously[91]. Taken from Paper 7.

6.3 Stacked Janus MoSSe

By stacking multiple Janus MoSSe layers on top of each other it is possible to stack the dipoles of the individual layers creating a cp *p-n* junction as can be seen from the projected band structure of the trilayer Janus MoSSe shown in Fig. 6.3a. The effect of stacking Janus MoSSe layers can be summarized as follows: The local band structure of each added layer is shifted by 0.51 eV until both the conduction band minimum and valence band maximum for the Janus MoSSe layers at the outer surfaces intersect the Fermi-level, which happens after the 4th layer is added. Adding additional layers to the stack does not increase the dipole due to charge transfer between the top and bottom layers. Furthermore for stacked Janus MoSSe, the band gap becomes indirect as the valence band maximum shifts from the K, K'-points to the Γ-point. An interesting point which has not been discussed previously is the behavior of the states around the Γ-point in the valence band. From Fig. 6.3a we see that the effective mass (inverse curvature) of the valence bands around the Γ-point increases significantly for the second layer and changes sign for the third layer. This change is caused by the cp field between the layers and can be reversed by creating an external field in the opposite direction of the built-in dipole using e.g. gates of opposite polarity above and below the structure.

Another interesting feature of these Γ-point states is the mixing of projections on them. Significant contributions from all three layers are seen at these points in the projected band structure indicating that the states are delocalized in the cp direction (the blue line is thinner at the Γ-point compared to the *K*-point due to contributions from all three layers). In Fig. 6.3b we show the isosurface of the Bloch state located near the Γ-point (marked by B in 6.3a). It is clear that this state is a cp-channel distributed across all layers of the system, but exhibits molecular orbital character in the in-plane direction. In Fig. 6.3c we show the corresponding valence band state at the *K*-point (marked by C 6.3a) with the same isovalue. In contrast to the Γ-point state, the *K*-point state is an in-plane channel, very localized on the single Janus MoSSe monolayer showing no delocalization in the cp-direction. The cp-channel will be dominating the cp-transport, as shown later.

6.4 Graphene as electrodes for Janus MoSSe devices

The stacking of dipoles seen in these multilayer Janus MoSSe structures creates an unique opportunity for creating atomically thin *p-n* junctions in the cp-direction for use in photovoltaics (PV) applications. To facilitate such a device, connections to metallic electrodes are necessary, however simply adding bulk metal electrodes to the top and bottom layer would completely screen the built-in dipole ruining the *p-n* junction. A detailed investigation of this screening can be found in the supporting information of Paper 7. This screening could turn out to be a major challenge not only in simulating transport properties of Janus materials, but also in creating devices based on exploiting the built-in cp dipole.

We expect 2D materials to screen the cp fields less efficiently and therefore choose to investigate the effect of adding graphene monolayers to the top and bottom of multilayer Janus MoSSe. Fig. 6.4a-c shows the structure and projected band structure

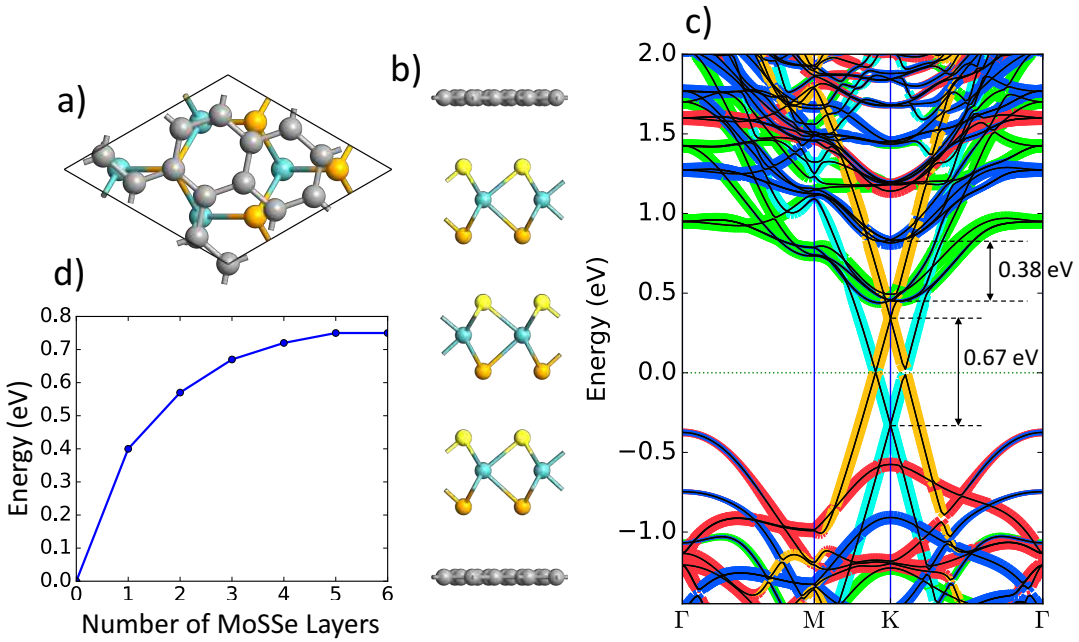

FIGURE 6.4: a) Top view of a 2D hexagonal supercell of a graphene-Janus MoSSe stack. b) Side view of trilayer Janus MoSSe sandwiched between graphene. c) Projected band structure of trilayer Janus MoSSe with graphene added on top and at the bottom. d) Energy-shift between the two graphene Dirac-points for varying number of Janus layers. Taken from Paper 7.

of trilayer Janus MoSSe with graphene (electrodes) added to the top and bottom[3]. The commensurate, hexagonal supercell of graphene on top of Janus MoSSe shown in Fig. 6.4a could be obtained with four and seven repetitions of the Janus MoSSe and graphene unit cells, respectively. Graphene is under compressive strain of ∼1% in this supercell. We choose to strain only graphene since we are interested in the details of the Janus MoSSe electronic structure while graphene is simply used as a lead. The projected band structure in Fig. 6.4c shows that while some screening occurs, the dipole mostly survives. As indicated in the band structure, the difference in energy between the states localized on adjacent Janus MoSSe layers is reduced from 0.51 eV to 0.38 eV as a result of adding graphene on either side. We therefore conclude that graphene electrodes are a promising solution to contacting Janus MoSSe without screening the cp-dipole.

6.4.1 Graphene doping

Interestingly, as seen in Fig. 6.4c the graphene layers are doped *p*- and *n*-type on the top and bottom respectively. In fact, the charge neutrality point in the graphene sheets are separated by 0.67 eV by the intense field created by the trilayer Janus MoSSe structure. Fig. 6.4d shows the difference in energy between the charge neutrality points in the top and bottom graphene layer as the number of Janus MoSSe layers is increased. The doping effect is seen to increase up to a ∼0.75 eV separation of the charge neutrality points for five layers of Janus MoSSe which is a very high homogeneous doping of graphene. This effect could be used to effectively dope graphene in a non-intrusive way, where no dopant atoms need to be implanted in the

[3]For this calculation we use a 26x26 Monkhorst-Pack k-point grid.

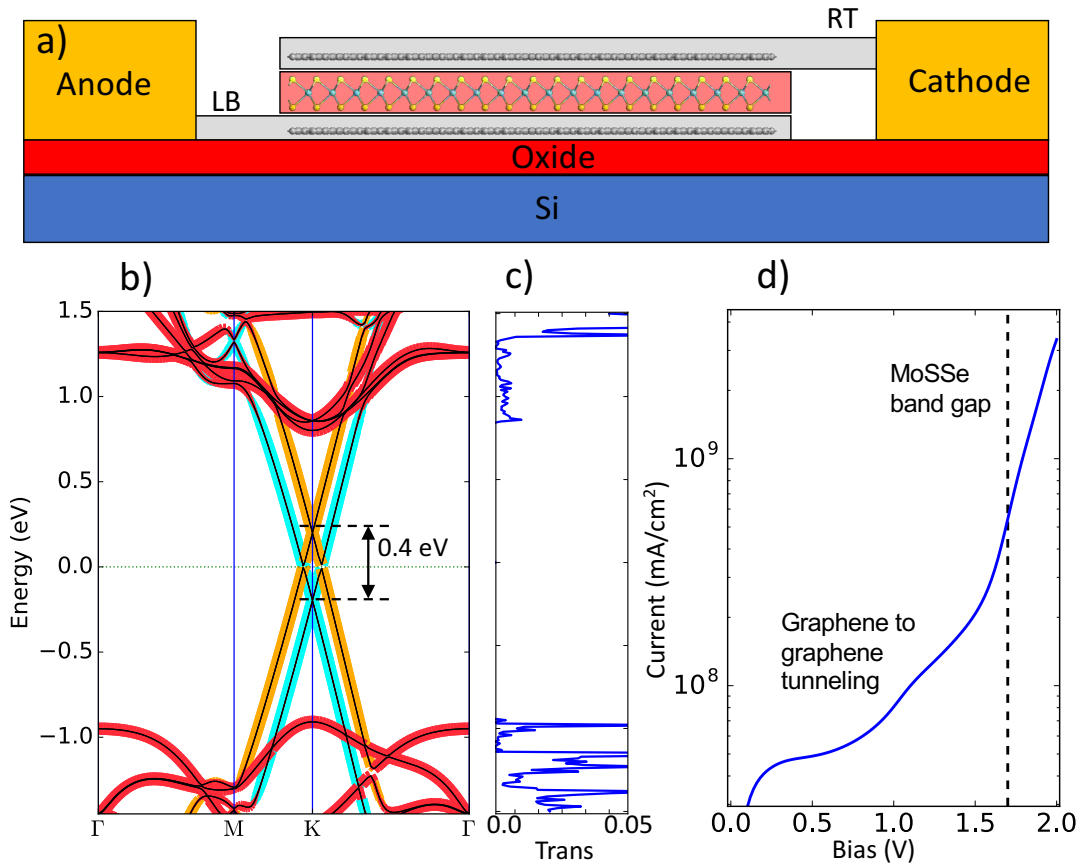

FIGURE 6.5: a) Envisioned device with graphene and Janus stacks to avoid dipole cancellation and achieve an abrupt *p-n* junction. b) Projected band structure of monolayer Janus MoSSe with graphene on top and at the bottom. Red, blue and green lines represents projections on to the first, second and third Janus MoSSe layer respectively. Yellow and cyan lines represent projection onto the top and bottom graphene layer, respectively. c) Electron transmission from the left bottom graphene electrode to the right top graphene electrode. d) IV-characteristics[144] of the graphene-Janus stacked device at 300 K. The current is evaluated from the zero bias transmission function. Taken from Paper 7.

pristine graphene sheet and the doping can be controlled by the number of stacked Janus MoSSe layers used. The maximum Fermi-level shift in either graphene layer of ∼0.4 eV corresponds to a carrier density of $1 \times 10^{13}\text{cm}^{-2}$. This is an order of magnitude higher than what can usually be achieved using molecular doping[145] or backgates[146]. It is however still lower than the ultrahigh carrier densities obtained using electrolytic gating[147, 148]. Even for a monolayer of Janus MoSSe, we see in Fig. 6.4d that a remarkable 0.4 eV shift in energy occurs between the graphene sheets, which are separated by less than 1 nm. As such, stacked Janus MoSSe structures provide a promising opportunity for creating abrupt cross-plane *p-n* junctions, which previously required complex double-gated configurations[149]. Furthermore the homogeneity of the doping far exceeds what can be expected using electrolytic or ionic gating. We also note that in the stacked configuration shown in Fig. 6.4b, the top doped graphene layer should be accessible to scanning probe measurements.

6.4.2 Cross-plane transport calculations

To check that a current can be injected from the doped graphene layers through Janus MoSSe, we imagine a device like the one shown in 6.5a where a monolayer of Janus MoSSe is contacted at the top and bottom by graphene electrodes. To calculate the cp-transmission we use a modified version of the well-known Landauer expression Eq. (2.17)

$$\mathcal{T}_{cp} = \text{Tr}\{\mathbf{\Gamma}_{BL}\mathbf{G}\mathbf{\Gamma}_{TR}\mathbf{G}^{\dagger}\}, \tag{6.1}$$

where $\mathbf{G}$ is the Green's function of the device and $\mathbf{\Gamma}_{BL/TR}$ is the broadening coming from the bottom left and top right graphene electrodes, respectively. The $\mathbf{\Gamma}_{BL/TR}$ are obtained from the full right and left spectral broadening matrices $\mathbf{\Gamma}_{L/R}$ by setting columns and rows in the matrices related to the orbital indices of the Janus MoSSe layer and the top/bottom graphene layer to zero. This procedure avoids the detailed treatment of the Janus MoSSe edges and graphene edges.

Fig. 6.5c shows $\mathcal{T}_{cp}$ for the imagined device. Fig. 6.5b shows the projected band structure of the device. Clearly transmission channels are available at energies outside the Janus MoSSe gap where states are available in all three monolayers[4]. A very small transmission due to tunneling directly from one graphene layer to the other is also seen at the Fermi-level where the graphene cones intersect (not visible in Fig. 6.5c). In Fig. 6.5d we show the cp-current calculated from the cp-transmission which has a low bias regime dominated by graphene-to-graphene tunneling and a high bias regime where the current flows through the Janus MoSSe layer.

6.5 Janus MoSSe solar cell

Now that we have shown that a connection can be made to graphene electrodes without screening the cp dipole of Janus MoSSe, we move on to consider the photocurrent due to the cp *p-n* junction in trilayer Janus MoSSe. As drawn in Fig. 6.6a we remove the graphene electrodes, and consider instead transport directly from the

[4]Transmission calculations for the graphene-MoSSe-graphene device are performed using 101 k-points in the transverse direction.

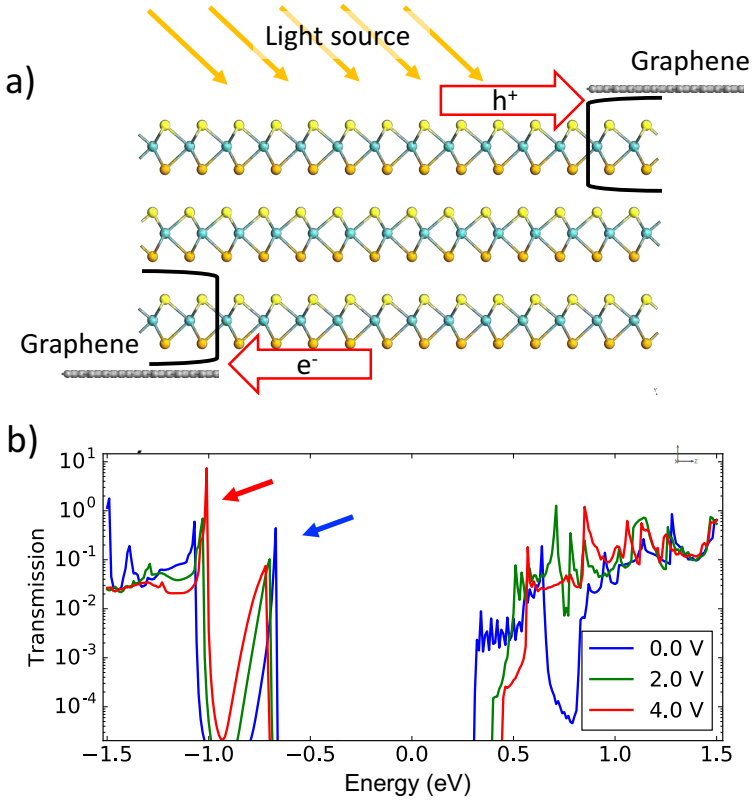

FIGURE 6.6: a) Trilayer Janus MoSSe device structure used to calculate transmission from the top to the bottom layer. b) Out-of-plane transmission for different values of the gate voltage illustrating the tunability of the cp-channel. Taken from Paper 7.

top left to the bottom right Janus MoSSe layer, to make the calculations computationally feasible[5]. This corresponds to considering a device where graphene electrodes are connected far away from the photo-active region of Janus MoSSe or considered completely transparent.

To investigate the tunability of the cp-transport, we add metallic regions (gates) above and below the device seperated by 40 Å. We applied a voltage of positive/negative polarity to the top/bottom gate to apply a field in the opposite direction of the cp-dipole in Janus MoSSe. The cp-transmission calculated using Eq. (6.1) is shown in Fig. 6.6b for three different gate voltages. For the cp-transmission with zero gate voltage, there is a peak in transmission at -0.67 eV (indicated by a blue arrow). This peak is directly related to the cp-channel identified earlier. The nearly dispersionless band of the cp-channel, leads to a Van Hove like singularity in the transmission.

As the gate voltage is increased, an electric field opposite to the built-in dipole is induced. As a result, the dispersion of the cp-channel band is increased and the related peak in the transmission is reduced (see Fig. 6.6b). As the gate is increased, an additional peak in transmission emerges at a lower energy (indicated by a red arrow in Fig. 6.6b). This peak is related to the valence state at the Γ-point with negative dispersion in Fig. 6.3a. The effective mass of this bands is tuned due to the increased

[5]Transmission calculations for the trilayer Janus MoSSe device are performed using 301 k-points in the transverse direction.

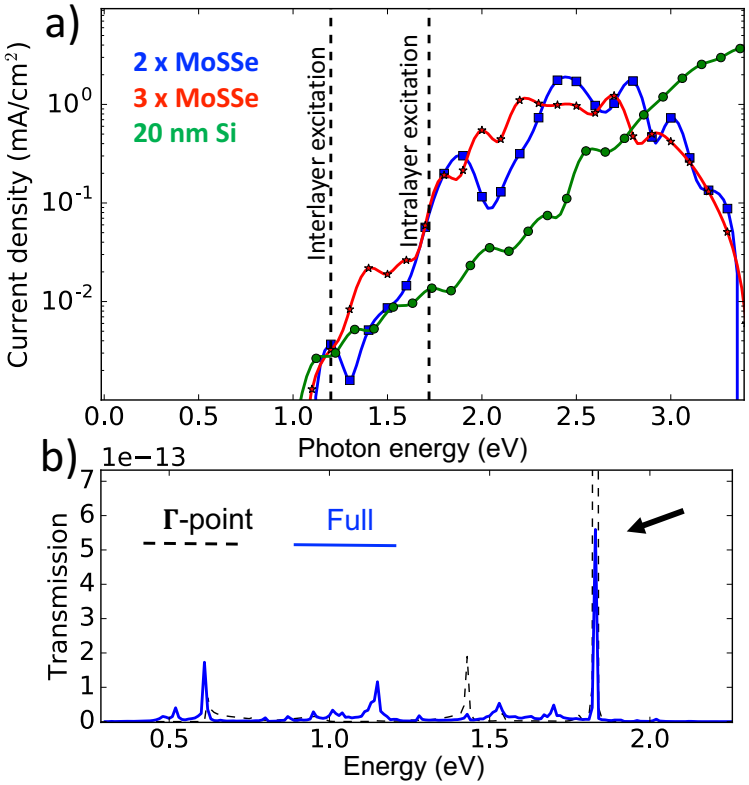

FIGURE 6.7: a) Photocurrent density[144] as a function of photon energy for the trilayer structure shown in Fig. 6.6. The current was at each energy weighted by the flux of the solar AM1.5 reference spectrum[128]. b) Photon mediated transmission as a function of energy for the 2.5 eV photon. The full k-averaged transmission shows a dominant peak at 1.83 eV which is traced back to the cp-channel in a region around the Γ-point as illustrated by the Γ-point transmission. Taken from Paper 7.

gate voltage making it nearly dispersionless, thus creating a new cp-channel replacing the previous one. This highlights how it is possible to tune the cp-transport properties heavily using a gate.

The cp-photocurrent is plotted in Fig. 6.7a for a bilayer and trilayer of Janus MoSSe and compared to the photocurrent of the 19.6 nm silicon *p-n* junction from the previous chapter. The cp-photocurrent was calculated using Eq. (5.13), but with modified photon mediated transmissions where $\alpha = LB, RT$, $\beta = LB, RT$, and $\mathbf{A}_{LB/TR} = \mathbf{G}\mathbf{\Gamma}_{LB/TR}\mathbf{G}^{\dagger}$. We see in Fig. 6.7a that the ultrathin (0.5-1 nm) cp *p-n* junction in the Janus MoSSe devices generates a higher photocurrent than the 19.6 nm thick silicon device over a broad range of the photon energies found in sunlight (see Fig. 5.1)[6]. As such Janus MoSSe shows great promise for PV applications. Interestingly we see that the cp-photocurrent is nearly independent of the thickness of the MoSSe stack; the increased absorption of light due to an additional layer of Janus MoSSe comes with a reduction in transmission from the top to the bottom layer, resulting in little change of the cp-photocurrent. To improve the photocurrent one could instead stack several bilayer Janus MoSSe devices separated e.g. by hBN layers. We notice in Fig. 6.7a a cp-photocurrent coming from photon energies below the calculated 1.72 eV band

[6]The photocurrent of the silicon *p-n* junction was calculated including EPC. For the Janus MoSSe devices we do not include EPC.

gap of monolayer Janus MoSSe. These contributions come from interlayer excitations where an electron-hole pair is created in different layers of the device. As such, multilayer Janus MoSSe devices generate a photocurrent in the same energy range as silicon even though the optical band gap of Janus MoSSe is $\sim 0.6\,\text{eV}$ higher.

In Fig. 6.7b we show the full (k-point averaged) and Γ-point photon mediated cp-transmission $\mathcal{T}^-$ as a function of energy for $\hbar\omega = 2.5\,\text{eV}$ ($\mathcal{T}^+$ is zero at this photon energy). We see that the highest transmission is found for an energy of 1.83 eV, which is the final state energy of an excitation starting from the cp-channel at the Γ-point. The Γ-point transmission in Fig. 6.7b confirms that this transmission comes from the cp-channel. We therefore conclude that the cp-photocurrent is dominated by transmission through the the cp-channel.

At photon energies above 2.5 eV the cp-photocurrent starts to fall of in both Janus MoSSe devices. This can be explained by considering the trilayer Janus MoSSe band structure in Fig. 6.3a. Starting from the cp-channel energy (point B in Fig. 6.3a), for photons with energies above 2.5 eV, one enters a regime where no final-state bands are available in the n-type bottom layer electrode (green lines). As such the dominating contribution to the cp-photocurrent is suppressed and the photocurrent is reduced. At photon energies above 3 eV $\mathcal{T}^+$ becomes nonzero and a competing cp-photocurrent contribution going in the opposite direction is introduced, as electrons can be excited from the bottom (n-type) Janus MoSSe layer to the top (p-type) layer. For photon energies above 3.2 eV the cp-channel photocurrent contribution changes direction and the photocurrent quickly falls of and eventually changes sign (not shown in Fig. 6.7a). This peculiar behavior is not critical for PV applications since the sunlight photon flux at these high energies is minimal (see Fig. 5.1). We note that such effects can only be captured using transport calculations since the absorption spectrum, which is often calculated using first principles, is not directional. According to our result, combining thin-film silicon solar cells with few layer Janus MoSSe could improve the broad spectrum absorption of light. A few layers of Janus MoSSe could e.g. be fabricated on the backside of a thin-film silicon solar cell to combat the problem of weak absorption due to the indirect transition.

6.6 Summary

In this chapter we have investigated three new device concepts based on the built-in cross plane dipole of 2D Janus MoSSe: An unprecedented homogeneous dipole doping effect for graphene stacked on top and below Janus MoSSe layers, the use of graphene electrodes to avoid suppression of the built-in cross plane dipole, and gate-tunable cross plane channels dominating transport and the photocurrent response.

6.6.1 Outlook

We focused in this chapter on the Janus material MoSSe due to its recent discovery. However, candidate materials with similar properties can be found in databases of emerging 2D materials based on first principles stability calculations[142]. For instance the materials Janus CrSSe and Janus ZrSSe should both be thermally and dynamically stable and have band gaps of 0.5 eV and 0.8 eV, respectively. Furthermore, the synthesis process outlined in Fig. 6.1 opens up for possible future nanostructuring of Janus MoSSe by e.g. covering parts of the initial MoS_2 layer (with hBN

or graphene) during the plasma stripping, or during selenization, to leave areas of MoS_2 or the metallic MoSH. Such nanostructuring combined with stacking could lead to a plethora of new interesting devices as seen previously for other 2D materials[5, 150, 151].

Chapter 7

Calibrating TCAD simulations with confined DFT bandstructure

In previous chapters we have presented and investigated first principles methods to improve TCAD modeling. In chapter 3 we took a multiscale approach, describing critical parts of the device from first principles, and using the effective mass model to describe the electronic structure of the separate materials of the device. In continuum models like the effective mass model, the parameters are most commonly fitted to reproduce a material band structure in the bulk. However sometimes the materials used are themselves not bulk-like, like for instance in nanowires or slabs. In such nanoscaled systems, the electrons are confined by the device geometry and the confinement changes the band structure of the electrons. Therefore, the values of the effective mass and non-parabolicity parameters determined from first principles calculations of a bulk system, often cannot be used to construct an accurate description of the confined device. Furthermore it can be very difficult, costly, and sometimes impossible, to obtain reliable experimental data for such parameters for relevant device geometries.

In this chapter we present an automated approach to sorting a band structure of a confined system obtained from first principles according to ladders of subbands. The results serve as a proof of concept for the matching procedure used to sort the bands. The chapter accounts for the method described in the patent application in Appendix B. Using the macroscopic symmetry of the states resulting from an effective mass model we can identify bands in the DFT band structure that are subbands of bulk states occurring due to confinement. These ladders can subsequently be fitted to obtain parameters giving an accurate description of the confined DFT band structure.

7.1 The band structure of confined systems

In a system confined along one, two or three dimensions, i.e. a slab, a nanowire or a quantum dot, only quantized values of wave vectors k_n are allowed in the confined direction. Under the assumption of infinite potential walls in the confined directions the allowed wave vectors are $k_n = n\pi/W$ where W is the width of the potential well and $n = 1, 2, 3....$

If we consider a square nanowire confined along the x and y directions, inserting these quantized wave vectors into the expression for the band structure given by the

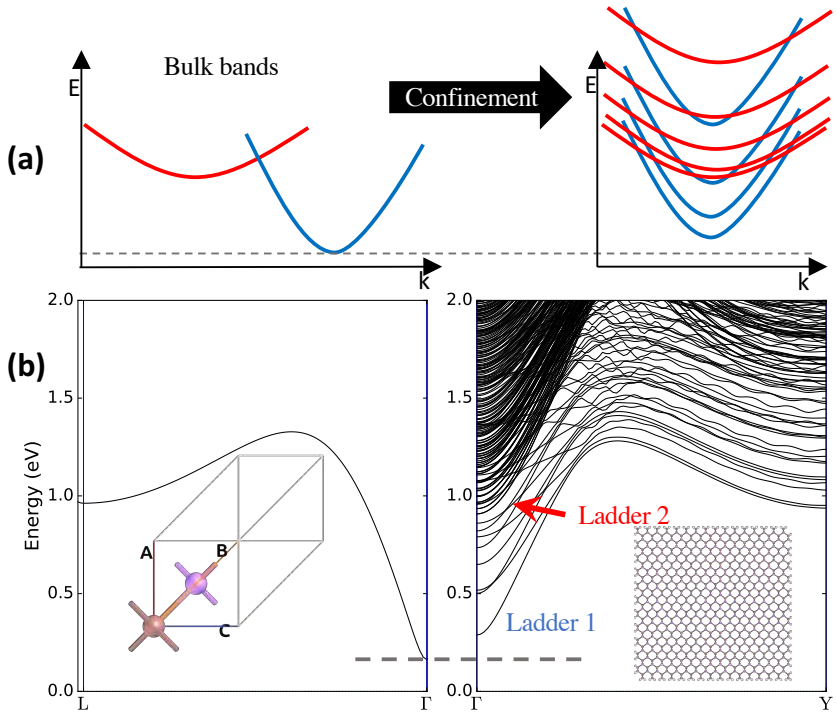

FIGURE 7.1: a) Sketch showing the effects of confinement on the semiconductor band structure. b) Left: InAs bulk band structure as calculated uing DFT. Right: Band structure of a 7x7 nm square [110] InAs nanowire.

anisotropic parabolic effective mass model Eq. (2.5) yields

$$\epsilon_{n_x,n_y}(k_z) = \frac{\hbar^2 n_x^2 \pi^2}{2m_x^* W^2} + \frac{\hbar^2 n_y^2 \pi^2}{2m_y^* W^2} + \frac{\hbar^2 k_z^2}{2m_z^*}, \tag{7.1}$$

where we have defined the bulk conduction band minimum energy as zero. The effects of confinement seen in the above equation are illustrated in Fig. 7.1a. The band gap is increased by

$$\Delta E_{gap} = \frac{\hbar^2 \pi^2}{2m_x^* W^2} + \frac{\hbar^2 \pi^2}{2m_y^* W^2} \tag{7.2}$$

and subbands emerge for each parabola in the bulk band structure forming band *ladders*.

Fig. 7.1b shows the effect of confinement in a real DFT calculation of bulk InAs (left) and a 7 nm nanowire of InAs (right). We see the increase in CBM energy due to the confinement, and two separate ladders of subbands (labeled in the figure).
The parabolic effective mass model only describes the InAs band structure well in the close vicinity of the minimum, and the subband energies are not captured properly. Including non-parabolicity in the transport direction through the parameter α in the following way

$$\epsilon_{nk}^{\alpha}(1 + \alpha\epsilon_{nk}^{\alpha}) = \epsilon_{nk}, \tag{7.3}$$

the description of the bulk band structure is greatly improved. Furthermore the dispersion of the lowest subband in the confined band structure can also be captured approximately. The description of higher lying subbands is also improved if the non-parabolicity is included in all directions[152]. An improved description of the bands can also be obtained using full zone $k \cdot p$ models, at a reasonable computational cost[153–155]. These model are however still typically fitted to the bulk band structure and as such have their limitations for ultrascaled systems.

The description of the confined band structure in Fig. 7.1b could be further improved by fitting an effective mass solution (or a $k \cdot p$ model) of the confined system directly to the subband ladders in the DFT band structure of the confined system. However in order to facilitate such a fitting procedure one must first find a method to identify and separate the ladders of subbands in the complex myriad of DFT bands. We have developed and implemented in QuantumATK[4] such a method based on the macroscopic symmetry of the Kohn-Sham wavefunction of the DFT calculation.

7.2 Description of the multiband fitting approach

In Fig. 7.2a we outline the work flow of generating an effective mass model for a nanoscaled system, with DFT level accuracy of the band structure. We use the example of a 4.5 nm [110] SiNW transistor device using a wrap around gate[1]. A DFT model of the confined SiNW is setup and solved (step 1)[2]. An effective mass model using the confinement potential obtained from DFT, is then setup and solved to generate the effective mass wavefunctions $\tilde{\psi}_m$ of the confined system (step 2). Here the indices n_x, n_y have been collected into a single subband index $m = 0, 1, 2, 3...$ Using the macroscopic symmetry of these effective mass wavefunctions the DFT band structure of the SiNW is sorted into ladders of subbands (step 3).

Finally the confined effective mass model is fitted to the ladders of the DFT band structure (step 4). Since setting up the DFT and effective mass models is straight forward, the main development of the work flow outlined above is the sorting of the DFT SiNW band structure in step 3. In the following section we account for the algorithm as we implemented it in the QuantumATK software.

7.3 Sorting algorithm

The sorting algorithm is illustrated in Fig. 7.2b. The input of the algorithm is the energies and wavefunctions from the DFT model and effective mass model of the confined system denoted E_n, ψ_n, $\tilde{E}_m$ and $\tilde{\psi}_m$ respectively. The first step of the algorithm is to select the lowest energy conduction band n_0 of the DFT band structure which has not yet been matched; for the first iteration this is simply the lowest energy conduction band. The second step is to select the lowest energy effective mass subband $m = 0$. These two bands are now matched to each other.

The objective of the algorithm is to match all of the remaining relevant DFT bands to

[1] We consider only the conduction band although a similar procedure could be performed for the valence bands.

[2] Throughout this chapter we used hydrogen to passivate the semiconductor surfaces. For InAs we use pseudo-hydrogen[156].

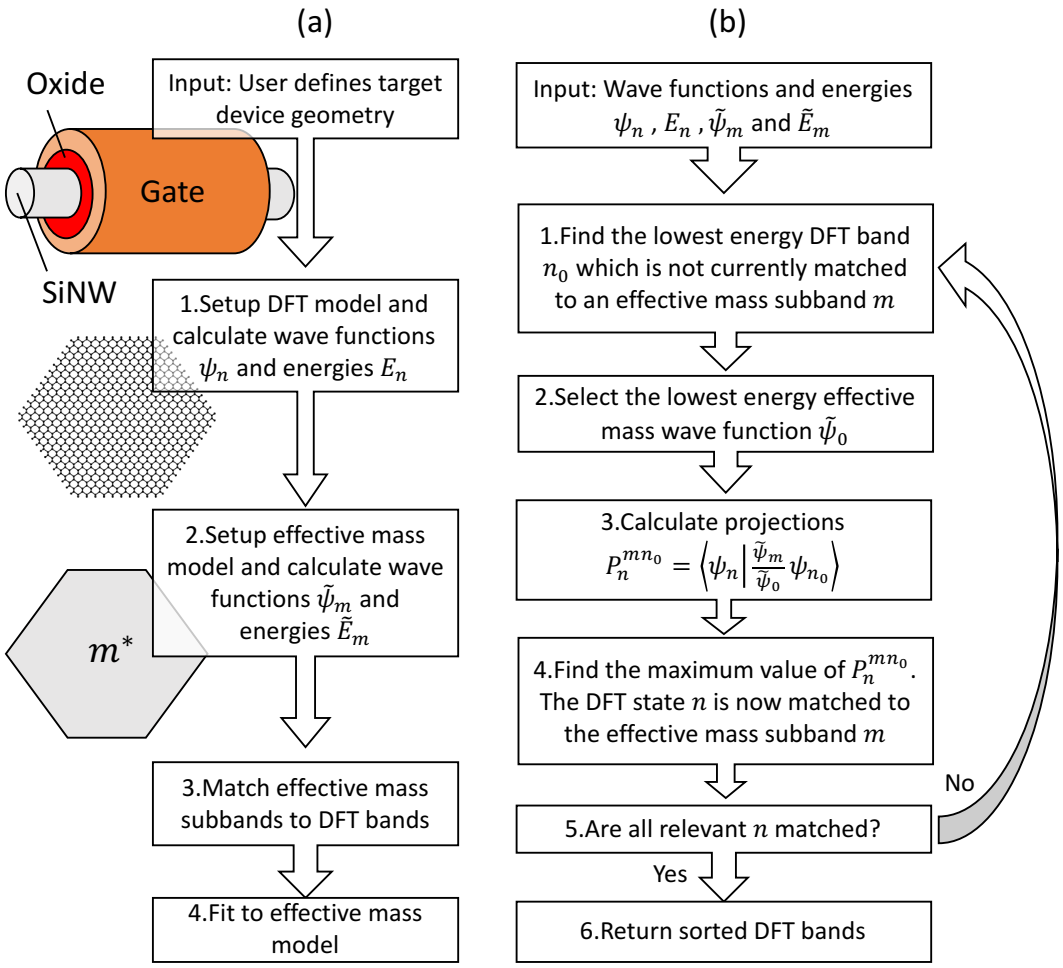

FIGURE 7.2: a) Suggested work flow of an approach to calibrating TCAD tools based on the effective mass model with DFT calculations in confined systems. b) Algorithm used to sort the DFT band structure of a confined system into ladders of subbands.

effective mass subbands[3]. For this purpose, a projector function $P_n^{mn_0}$ is introduced in step three. The projector function is used to identify the DFT wavefunction ψ_{n_0} which has the same relative change to ψ_{n_0} that the effective mass wavefunction $\tilde{\psi}_m$ has to $\tilde{\psi}_0$, thus, the aim is to find the DFT wavefunction that best fulfills the equation

$$\frac{\psi_n}{\psi_{n_0}} \approx \frac{\tilde{\psi}_m}{\tilde{\psi}_0}. \tag{7.4}$$

We therefore construct a trial wavefunction $\psi_{nm}^{trial} = \tilde{\phi}_m \psi_{n_0}$ where $\tilde{\phi}_m = \frac{\tilde{\psi}_m}{\tilde{\psi}_0}$. Such a trial wavefunction will have the same local atomic behavior as ψ_{n_0}, but the macroscopic behavior of the effective mass wavefunction $\tilde{\psi}_m$.

The projector function constitutes the projection of this trial function onto all the DFT wavefunctions

$$P_n^{mn_0} = \left\langle \psi_n | \psi_{mn_0}^{trial} \right\rangle. \tag{7.5}$$

[3]The relevant bands, are those within a chosen energy range above the CBM

The values of the projector function indicates how much the DFT wavefunction resembles the trial function, and thus how well it fulfills Eq. (7.4). In step four the DFT states n with the highest projector function value $P_n^{mn_0}$ are matched to the effective mass subband m as subbands of n_0. The next step is to check if all relevant DFT states n have been matched. If they have, the sorting is completed and the list of subbands in the DFT band structure is returned. If not the algorithm returns to step one and the lowest energy conduction band which has not yet been matched is assumed to be the lowest subband of a new ladder in the DFT band structure. The algorithm continuous until all relevant DFT bands n are matched to effective mass subband m as the subbands of a DFT ladder with lowest energy subband n_0. This procedure is carried out at each k-point in the vicinity of the conduction band minima to generate a sorted band structure.

At certain k-points, the lowest energy DFT band n_0 of a ladder may intersect with another band in the band structure. To keep track of n_0 we therefore choose n_0, at a given k-point denoted by k_1, to be the band n with the highest projection $\langle \psi_n(k_1) | \psi_{n_0}(k_{\min}) \rangle$ where $k_{\min}$ is the k-point at the valley minimum.

7.3.1 Effective mass model

An important part of the sorting algorithm is the effective mass model used for the matching procedure. In this section we account for the effective mass model as we implemented it in the QuantumATK software.

As introduced in chapter 2, the effective mass model is an approximation to the electronic structure close to a conduction band minima. In it, the electronic bands are approximated as parabolic in all directions. As such for the anisotropic effective mass model, the single particle time-independent Schrödinger equation can be written as[157, 158]

$$-\frac{\hbar^2}{2}\left(\frac{1}{m_x^*}\frac{\partial^2}{\partial x^2}+\frac{1}{m_y^*}\frac{\partial^2}{\partial y^2}+\frac{1}{m_z^*}\frac{\partial^2}{\partial z^2}+V(\mathbf{r})\right)\psi_m(\mathbf{r}) = E_m\psi_m(\mathbf{r}), \tag{7.6}$$

where $V(\mathbf{r})$ is the potential energy and we have chosen our coordinate system (x, y, z) along the principal axis of a constant-energy ellipsoid of the semiconductor.

If we consider now a regular real-space grid of (N_x, N_y, N_z) nodes denoted by the subscripts i, j and l respectively, the finite difference approximation for Eq. (7.6) expressed for node $[i, j, l]$ is given by[159]

$$\begin{aligned}
&-\frac{\hbar^2}{2m_x^* a_x^2}[\tilde{\psi}_{i+1,j,l}+\tilde{\psi}_{i-1,j,l}-2\tilde{\psi}_{i,j,l}]-\frac{\hbar^2}{2m_y^* a_y^2}[\tilde{\psi}_{i,j+1,l}+\tilde{\psi}_{i,j-1,l}-2\tilde{\psi}_{i,j,l}] \\
&-\frac{\hbar^2}{2m_z^* a_z^2}[\tilde{\psi}_{i,j,l+1}+\tilde{\psi}_{i,j,l-1}-2\tilde{\psi}_{i,j,l}]+[V_{i,j,l}-E]\tilde{\psi}_{i,j,l}=0,
\end{aligned} \tag{7.7}$$

where we recognize the coupling terms in the x, y and z directions given by

$$t_x = -\frac{\hbar^2}{2m_x^* a_x^2}, \quad t_y = -\frac{\hbar^2}{2m_y^* a_y^2}, \quad t_z = -\frac{\hbar^2}{2m_z^* a_z^2}, \tag{7.8}$$

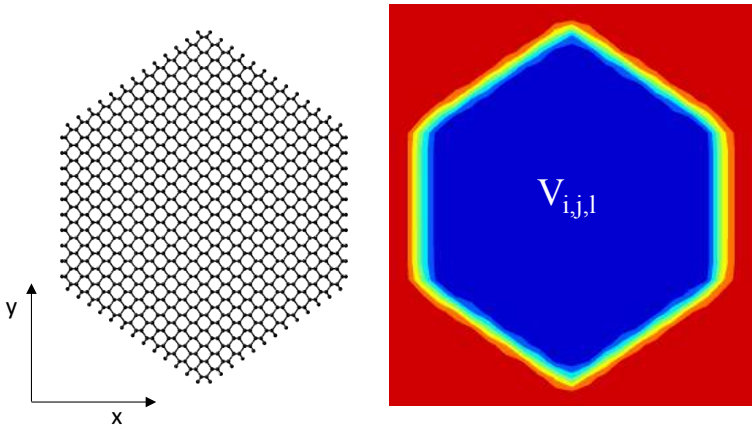

FIGURE 7.3: Silicon nanowire system cross section together with the confinement potential extracted from the DFT calculation and used to setup the effective mass model.

and the onsite potential of each node $\epsilon_{i,j,l} = V_{i,j,l} - E$. To accurately model the confinement potential shape, we use the effective potential from the DFT calculation as $V(x,y,z)$ when setting up the effective mass model. To remove the atomic-scale variations of the effective potential we use a box average. The resulting $V_{x,y,z}$ of the SiNW as defined on the regular grid of the effective mass model is shown in Fig. 7.3 together with the cross section of the SiNW[4]. We see that the confinement potential accurately describes the shape of the nanowire. The number of grid points in each confined direction are chosen by the user and effects the precision with which the confinement potential is reproduced. The effective masses used for the sorting algorithm, could be the bulk effective masses as obtained from experiments or DFT calculations on the bulk system[5].

7.3.2 Results

In Fig. 7.4 we show the effective mass model wavefunctions $\tilde{\psi}_m$ and related functions $\tilde{\phi}_m$ obtained using the confinement potential shown in Fig. 7.3. We see the first and second subbands of the effective mass model have the expected wavefunction symmetry for the quantum particle in a potential well.

For the two ladders $n = 0, 1$ at the Γ-point in the DFT band structure of the SiNW we show in Fig. 7.4 the DFT wavefunctions ψ_{nm} of the three lowest subbands $m = 0, 1, 2$ identified using the matching procedure described in this section. We see clearly the atomic-scale symmetry of the DFT wavefunctions and how it is shared amongst the subbands of a specific ladder. We also see how the macroscopic symmetry of the subbands are identical to those of the effective mass model states, and seemingly unrelated to the atomic-scale symmetry of each ladder. One can imagine looking at the wavefunctions in Fig. 7.4 how calculating for example the trial function $\psi_{01}^{\text{trial}} = \psi_{00}\tilde{\phi}_1$, would result in a wavefunction very similar to ψ_{01}. This is exactly the behavior we are taking advantage of in our algorithm.

[4]For the SiNW we used GGA-1/2 with the SG15-low basis set and 1x1x11 k-points to evaluate the electronic structure.

[5]In our calculations we chose $m_x^* = m_y^* = m_z^* = 0.5$, for the effective mass model used in the sorting algorithm. The real-space grid was chosen so that nodes were separated by ~ 4 Å in all directions.

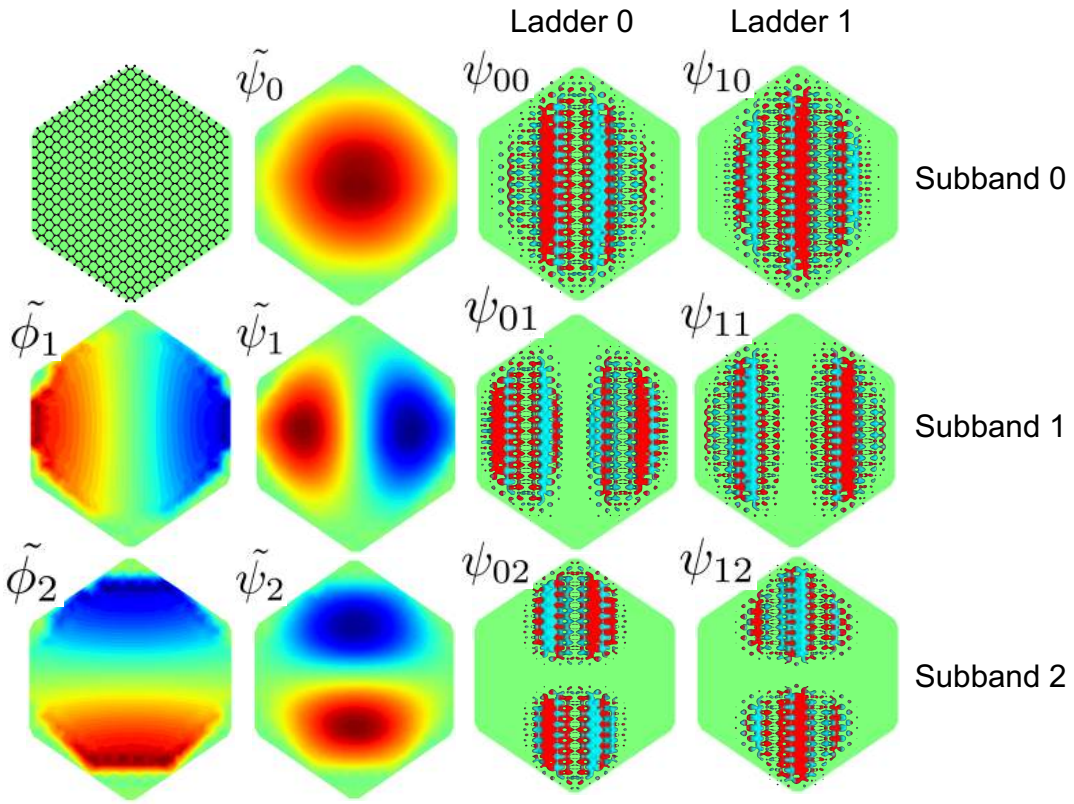

FIGURE 7.4: Silicon nanowire system cross section together with the eigenstates of the three lowest energy subbands of the generated effective mass model labeled $\tilde{\psi}_m$. To the left are the function $\tilde{\phi}_m$ used to setup the trial function in the sorting algorithm. To the right are the blochstates of the corresponding matched subbands of the DFT calculation labeled ψ_{nm} where n denoted the ladder and m denotes the subband.

The identified ladders in the electronic DFT band structure of the SiNW are shown in Fig. 7.5a. The black lines are the electronic bands obtained from DFT. The blue and red lines indicate the subbands of the identified ladders at the two minima in the SiNW band structure. Notice how the sorting algorithm keeps track of the matched bands even as bands cross in the band structure. The three lowest energy matched bands at the Γ-point are the states with the wavefunctions shown in Fig. 7.4. We see in Fig. 7.5a that the matching procedure works also for the conduction band minima with non-zero wave vector. It is clear from Fig. 7.5a that for each minima two nearly degenerate ladders are found.

7.3.3 Checking the quality of the match

During the matching procedure false matches can occur. A false match is when the wavefunction with the highest value of the projecter P_n^{m,n_0} is not the subband m of ladder n which was searched for. It is therefore crucial to have a value indicating the quality of a given match. The value of the projector function can be a good indicator of the quality of the projection. However, in cases were for example the DFT wavefunctions vary rapidly at the atomic-scale or when the shape of the confinement potential is particularly complex, all of the projections may be of low value, making

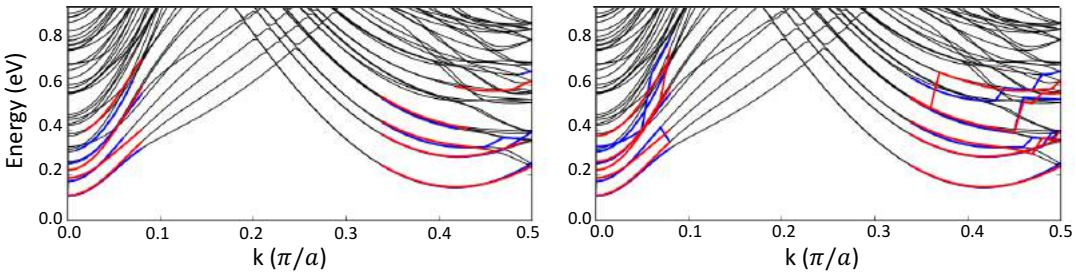

FIGURE 7.5: a) DFT band structure of the 4.5 [110] SiNW system(solid black lines), together with the sorted ladders of subbands (red and blue lines) near the conduction band valleys. Red and blue marks separate ladders. b) Same plot without invoking a tolerance for the qualities of the matches obtained during the sorting algorithm.

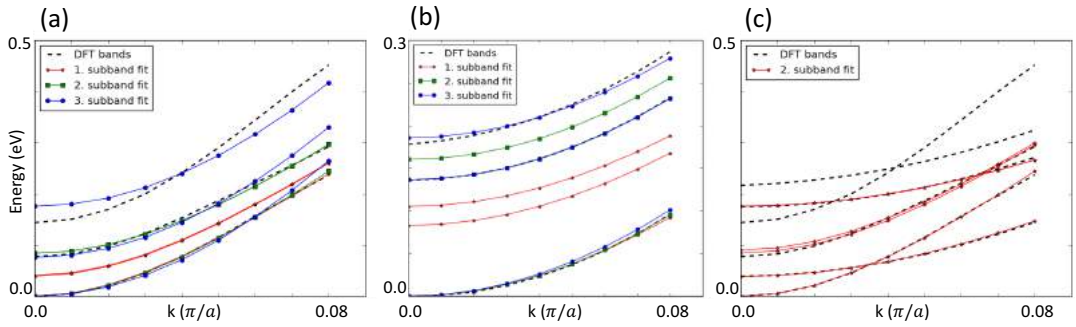

FIGURE 7.6: a) The three lowest energy bands near the Γ point in the DFT band structure of the 4.5 [110] SiNW system(dashed black), together with the corresponding band structure of effective mass models fitted to one (red), two (blue), or three (green) of the DFT subbands shown. b) Same fits to the off-Γ valley. c) Effective mass bands (red) obtained by fitting to the two lowest energy subbands of both valleys at the same time, together with the DFT band structure (dashed black).

it hard to find any good matches. We therefore use instead the ratio between the second best and the best projection obtained, which is a number in the range between 0 and 1. A value close to zero indicates a match of high confidence.

As described above the algorithm identifies new ladders via unmatched bands. As such it is necessary to specify a tolerance for the quality of the matches at the beginning of the matching algorithm.

In Fig. 7.5b we show the conduction bands of the SiNW with identified ladders before invoking minimum tolerance for the quality of matches. We see that some of the identified bands are discontinuous before demanding a certain quality of the matches. After specifying a tolerance of error we see in Fig. 7.5a that the discontinuities are removed and the identified bands follow the expected dispersion[6].

[6]The specified ratio tolerance of 0.4 means that the highest projector function value should be at least 2.5 times larger than the second highest value.

7.4 Fitting to the sorted bands

Having successfully sorted the DFT band structure into ladders of subbands, we can now move on to the final step of the work flow shown in Fig. 7.2a and fit the effective mass TCAD model to the DFT subband ladders. As a proof of concept we here fit the bands of the simple effective mass model outlined in section 7.3.1 with an added non-parabolicity term from Eq. (7.3) to the extracted DFT ladders.

For this purpose we use least-squares fitting to minimize the expression

$$\beta_n = \sum_{m,i} w_m (\tilde{E}_m(k_i) - E_{nm}(k_i))^2 \tag{7.9}$$

where $E_{nm}(k_i)$ are the matched DFT subbands of a specific ladder n evaluated at k-points k_i and w_m are weights with value between 0 and 1.

Fig. 7.6a shows the obtained fit for a ladder at the Γ-point of the 4.5 nm SiNW together with the matched DFT subbands (dashed black line). The red solid line is the effective mass model band structure obtained by fitting only to the lowest energy subband i.e. $w_0 = 1$ and $w_m = 0$ for all $m > 0$. We see, as expected, that the lowest energy subband of the effective mass model fits nicely to the lowest energy subband of the DFT band structure, but subbands 1 and 2 are not well described. Interestingly subbands 1 and 2 of the effective mass model are degenerate and only slightly higher in energy than the lowest energy subband. This could be problematic since it leads to erroneous DOS close to the CBM, which impacts the transport properties. The green line in Fig. 7.6a is the effective mass model band structure obtained by using $w_0 = w_1 = 1$ and $w_m = 0$ for all $m > 1$. As expected the two lowest subbands of the DFT ladder are well described with the obtained effective mass model. The obtained subbands of the fitted effective mass model with $m = 1$ and $m = 2$ are once again degenerate. The effective mass model used to obtain the bands illustrated by blue lines in Fig. 7.6a was fitted with $w_0 = w_1 = w_2 = 1$ and $w_m = 0$ for all $m > 2$. The effective mass description of the third subband is improved, however the fit to the lowest subband is not as good as with the previous models. We hereby see that fitting more bands comes with the price of lower accuracy for each individual band. Fig. 7.6b show the same plots, but for a DFT ladder at the minima away from the Γ-point. Here the obtained $m = 1$ and $m = 2$ subband are never degenerate, but otherwise the fits behave qualitatively the same as for the Γ-point valley.

7.5 Results and discussion

Fitting the DFT ladders at both valleys in the SiNW band structure at the same time, and fitting also the the difference in energy between the valleys, we obtain the effective mass bands shown in Fig. 7.6c (red line)[7]. We observe from Fig. 7.6c that we can get a fair representation of the DFT band structure including higher energy subbands using a simple effective mass model, as we did here. With this fitted effective mass model it is now possible to perform transistor level transport simulation cheaply. The calculated anisotropic effective masses and non-parabolicity parameters are listed in Table 7.1.

To illustrate that the sorting algorithm is not system specific and can be used to

[7] For this fit we used $w_0 = w_1 = 1$ and $w_m = 0$ for $m > 1$.

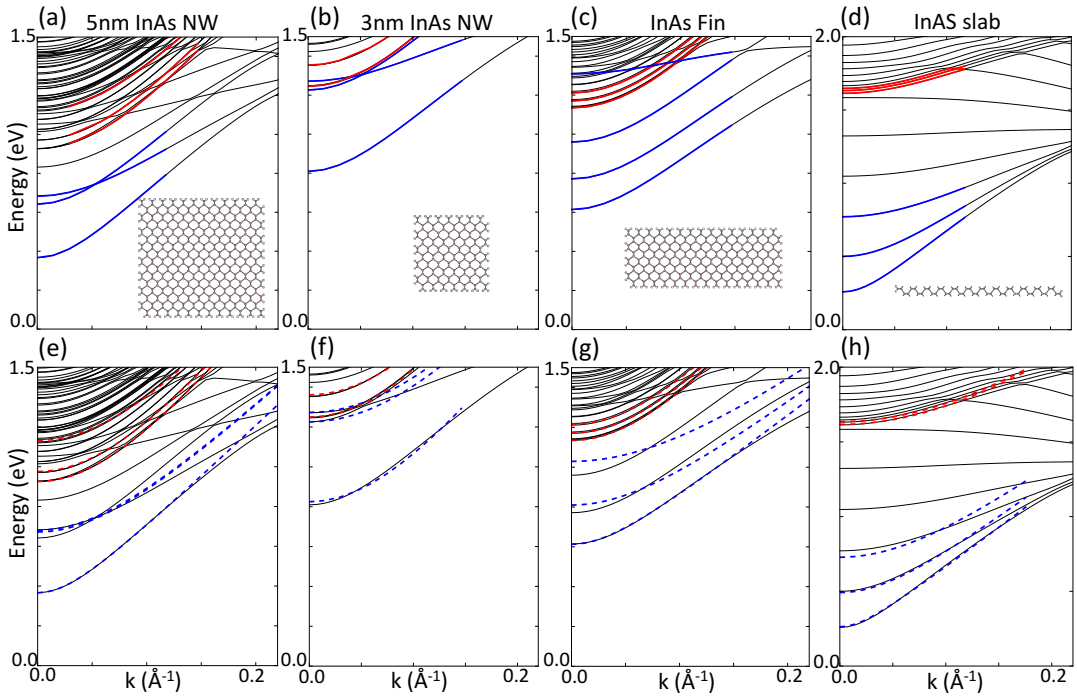

FIGURE 7.7: Results of the sorting algorithm (a-d) and subsequent fitting (e-h) of an effective mass model to the band structure of various confined InAs systems. The solid black lines plot the DFT band structure of the systems shown in the insets, the solid red and blue lines in (a-d) plot the sorted ladders of subbands obtained from the sorting algorithm, the dashed red and blue lines in (e-h) plot the bands obtained from the effective mass model fitted to the ladders. The result in (a) and (e) are for a 5x5 nm square InAs nanowire. The result in (b) and (f) are for a 3x3 nm square InAs nanowire. The result in (c) and (g) are for a 2.5x6.5 nm InAs Fin. The result in (d) and (h) are for a 7.3 nm InAs slab.

Valley	m_x^* (m_0)	m_y^* (m_0)	m_z^* (m_0)	α (eV^{-1})
Γ	0.44	0.39	0.11	2.33
Off-Γ	0.32	0.32	0.35	1.12

TABLE 7.1: Effective masses and non-parabolicity parameters calculated for the two valleys in the 4.5 nm SiNW band structure.

generate effective mass models for many confined systems we show in Fig. 7.7a-d the result of the band sorting applied to confined InAs structures[8]. We see that the sorting is equally successful for wires of different sizes and geometries, and for slabs.

In Fig. 7.7e-h we show how all of the indentified DFT ladders can be fitted to effective mass models.[9] In the 5 nm InAs nanowire band structure (Fig. 7.7a) we see that the two subbands of the ladder indicated by blue lines intersect. We also see that our effective mass model fails to describe this intersection (see Fig. 7.7e). This

[8]For the InAs systems we used meta-GGA with a c-parameter of 0.91 and 1x1x9 k-points to evaluate the electronic structure.

[9]We used here the same settings as for the SiNW sorting run. The effective mass model was fitted to the three lowest subbands. The non-parabolicity parameter was kept fixed to the bulk value of 3.13 eV^{-1}

is due to the assumption going into Eq. (7.6) that our coordinate system falls along the principal axis of a constant-energy ellipsoid of the semiconductor, which results in only having three effective masses (m_x^*, m_y^*, m_z^*). A more general description includes cross terms ($m_{xy}^*, m_{yz}^*, m_{xz}^*$) and the effective mass becomes a 3x3 tensor[157, 159]. The calculated anisotropic effective masses for the systems shown in Fig. 7.7a-d are listed in Table 7.2. We note that the extracted effective masses for the small 3 nm nanowire differs the most from the calculated bulk effective mass ($0.023m_0$).

System	m_x^* (m_0)	m_y^* (m_0)	m_z^* (m_0)
5.0x5.0 nm InAs-NW	0.034	0.026	0.037
3.0x3.0 nm InAs-NW	0.049	0.028	0.041
2.5x6.5 nm InAs-Fin	0.025	0.022	0.022
7.3 nm InAs-slab		0.032	0.035

TABLE 7.2: Effective masses calculated for first ladder in the Γ-valley of the systems shown in Fig. 7.7a-d.

7.6 Summary

We have presented an automated approach to sorting the DFT band structure into ladders of subbands created due to confinement. This sorting enables the direct fitting of effective mass models to the DFT band structure of nanoscaled systems including the confinement subbands. Implementing in the QuantumATK software a simple effective mass model solved on a real-space grid, we illustrate how such a fitting can be done and how the resulting effective mass bands follow those of the first principles DFT calculation in many different confined systems.

Chapter 8

Summary

Technology computer aided design (TCAD) tools are important in the design of new devices and circuits to support the miniaturization of electronics. TCAD tools are used in optimization at the circuit level with compact models calculating the behavior of massive networks of logic devices and interconnects. At the device level models like drift-diffusion (DD) and the Boltzmann transport equation (BTE) adopting a continuum description of the considered materials are used to benchmark device performance. These models are based on input parameters typically extracted experimentally or from first principles calculations on bulk materials at the atomic level. The interpretation of TCAD simulations benefits greatly from the interplay between these different levels of abstraction. However, while the connection between the circuit level and device level is well established, atomic level calculations are still mostly being used to extract basic parameters like effective masses from bulk materials. With the continued downscaling of electronics, these bulk parameters are becoming less and less useful.

This thesis focuses on the connection between first principles atomic scale calculations and the device level models. Various novel methods to extract parameters for device level simulation tools are developed and benchmarked against existing methods and experimental measurements. We also go beyond parameter extraction and benchmark the performance of ultrascaled electronic devices directly from atomic scale calculations. First principles transport calculations are carried out using density functional theory (DFT) combined with nonequilibrium Green's functions (NEGF). In DFT-NEGF calculations one considers semi-infinite "electrodes" at either side of an interacting device region. This setup is ideal for the study of interfaces since it allows for the construction of a single interface between two bulk crystals. Taking advantage of this, we carried out a multiscale study of the promising CZTS(e) thin-film solar cell including, in device level simulations of the full solar cell, details of the CZTS(e)/CdS interface extracted from first principles. We found that the low efficiency seen in CZTSe solar cells could be explained from a large conduction band offset between CZTSe and CdS serving as a blockade for electron transport. For CZTS we discover a narrowing of the band gap near the CZTS/CdS interface leading to open-circuit voltage loss and low efficiency. This new knowledge allows us to suggest methods to improve efficiency in CZTS(e) thin-film solar cells.

We then develop a novel memory efficient approach to calculating the phonon-limited mobility using molecular dynamics (MD) simulation together with DFT-NEGF transmission calculations. We compare the calculated mobilities to state-of-the-art first principles calculations and experiments for one-, two-, and three-dimensional, metallic and semiconducting systems with good agreement over several orders of magnitude.

Another main result of the thesis is the calculation of the total current of a thin-film silicon solar cell including, at the same time, light-matter interactions and electron-phonon coupling from first principles. Using special thermal displacements (STD), we calculate the thermally averaged current over a silicon *p-n* junction under sunlight illumination. The temperature and intensity dependent open-circuit voltage is successfully compared to experimental values.

Furthermore we have found that the cross plane (cp) transport properties of stacked two-dimensional (2D) Janus MoSSe are dominated by a gate-tunable cp-channel with negligible inplane dispersion, but high delocalization in the cp-direction. This new exciting material exhibits a stackable built-in cp-dipole permitting the creation of an atomically thin *p-n* junction through stacking of layers. The cp-dipole is found to dope graphene homogeneously *p* and *n* type, when graphene is deposited on both sides of Janus MoSSe. The induced carrier density far exceeds typical values obtained using backgates or molecular doping. We find that the photocurrent generated by two atomically thin ($\sim$0.5 nm) layers of Janus MoSSe generates a higher photocurrent than $\sim$20 nanometers of silicon over a broad spectrum of sun light. Interestingly we also find that the photocurrent changes direction at a certain wavelength of incoming light.

Lastly we develop an automated approach to sorting the DFT bandstructure of confined systems into separate ladders of subbands, which can then be fitted directly to effective mass models used in device level TCAD tools. We apply the sorting method to various confined systems of silicon and InAs to highlight the robustness of the method.

8.1 Outlook

Several future theoretical studies on the subjects presented in this thesis could potentially be of interest, here we list a few. It would be interesting to study the effect of the $2\mathrm{Cd}_{\mathrm{Cu}} + \mathrm{Cd}_{\mathrm{Zn}} + \mathrm{Cd}_{\mathrm{Sn}}$ point defect on the band gap of CZTS compared to CZTSe, to see whether a band gap narrowing occurs only for CZTS as indicated by the interface calculation in chapter 3. Including additional interesting effects such as dopant/defect scattering or amorphous materials when calculating the mobility using the MD-Landauer approach, in order to quantify the comparative impact of these effects, and the interplay between them could be of much interest. Calculating the photocurrent including EPC for thin-film solar cell based on the recently discovered perovskite absorbers would be interesting, since EPC is thought to be a crucial part of explaining the high efficiencies obtained. Knowledge gained from these calculations could lead to information useful for improving the efficiency even further. Nanostructuring 2D Janus MoSSe using e.g. Janus MoSH as interconnects

and including layers of MoS_2 with no dipole, could potentially lead to many interesting new devices. The theoretical study of such devices is an interesting prospect. Finally, the fitting of effective masses in TCAD tools to the sorted DFT bands of confined systems obtained in chapter 7 and subsequent device level transport calculations would be of interest, to see the impact of describing the confinement in more detail.

Bibliography

[1] G. A. Armstrong and C. K. Maiti, *Technology Computer Aided Design for Si, SiGe and GaAs Integrated Circuits* (The Institution of Engineering and Technology, London. United Kingdom, Jan. 2018), pp. 1–444.

[2] Y.-C. Wu and Y.-R. Jhan, *3D TCAD Simulation for CMOS Nanoeletronic Devices* (Springer Singapore, 2018).

[3] M. Brandbyge, J.-L. Mozos, P. Ordejón, J. Taylor, and K. Stokbro, "Density-functional method for nonequilibrium electron transport", Phys. Rev. B **65**, 165401 (2002).

[4] Atomistix Toolkit version 2018.06, Synopsys QuantumWise A/S.

[5] A. K. Geim and I. V. Grigorieva, "Van der Waals heterostructures", Nature **499**, 419 (2013).

[6] G. E. Moore, "Cramming more components onto integrated circuits", Electronics **38**, 114 (1965).

[7] G. E. Moore, "Progress in digital integrated electronics", International Electron Devices Meeting IEEE, 11–13 (1975).

[8] *The Future of Audio Engineering*, https://tapeop.com/interviews/100/the-future/, Accessed: August 2018.

[9] *How Much Does It Cost To Deliver Topsoil, Dirt, Sand, Mulch Or Rock?*, https://www.homeadvisor.com/cost/landscape/deliver-soil-mulch-or-rocks/, Accessed: July 2018.

[10] *International technology roadmap for semiconductors 2015 edition*, http://www.itrs2.net/itrs-reports.html, Accessed: July 2018.

[11] *Intel's 22-nm Trigate Transistors Exposed*, https://semimd.com/chipworks/2012/04/, Accessed: July 2018.

[12] *International Technology Roadmap for Photovoltaic (ITRPV) Results 2017*, tech. rep. (VDMA Photovoltaic Equipment, 2018).

[13] S. Philipps and W. Warmuth, *Photovoltaics Report*, tech. rep. (Fraunhofer Institute for Solar Energy Systems, ISE, 2017).

[14] "The interface is still the device.", Nature materials **11**, 91 (2012).

[15] A. Sanchez-Soares, C. O'Donnell, and J. C. Greer, "Electronic structure tuning via surface modification in semimetallic nanowires", Phys. Rev. B **94**, 235442 (2016).

[16] A. M. Ionescu, "Tunnel field-effect transistors as energy-efficient electronic switches", Nature **479**, 329 (2011).

[17] *Inelastic Electron Spectroscopy of an H2 molecule placed between 1D Au chains*, https://docs.quantumwise.com/tutorials/inelastic_electron_spectrometry_au_h2_au/inelastic_electron_spectrometry_au_h2_au.html, Accessed: August 2018.

[18] P. Hohenberg and W. Kohn, "Inhomogeneous Electron Gas", Phys. Rev. **136**, B864–B871 (1964).

[19]J Kohanoff, *Electronic Structure Calculations for Solids and Molecules* (Cambridge University Press, 2006).

[20]W. Kohn and L. J. Sham, "Self-Consistent Equations Including Exchange and Correlation Effects", Phys. Rev. **140**, A1133–A1138 (1965).

[21]K. T. Butler, J. M. Frost, J. M. Skelton, K. L. Svane, and A. Walsh, "Computational materials design of crystalline solids", Chem. Soc. Rev. **45**, 6138–6146 (2016).

[22]J. M. Soler, E. Artacho, J. D. Gale, A. García, J. Junquera, P. Ordejón, and D. Sánchez-Portal, "The SIESTA method for ab initio order- N materials simulation", Journal of Physics: Condensed Matter **14**, 2745 (2002).

[23]Y. Xue, S. Datta, and M. A. Ratner, "First-principles based matrix Green's function approach to molecular electronic devices: general formalism", Chemical Physics **281**, 151 –170 (2002).

[24]A. Pecchia and A. D. Carlo, "Atomistic theory of transport in organic and inorganic nanostructures", Reports on Progress in Physics **67**, 1497 (2004).

[25]M. P. L. Sancho, J. M. L. Sancho, J. M. L. Sancho, and J Rubio, "Highly convergent schemes for the calculation of bulk and surface Green functions", Journal of Physics F: Metal Physics **15**, 851 (1985).

[26]Y. Meir and N. S. Wingreen, "Landauer formula for the current through an interacting electron region", Phys. Rev. Lett. **68**, 2512–2515 (1992).

[27]H. Haug and A.-P. Jauho, *Quantum Kinetics in Transport and Optics of Semiconductors* (Springer-Verlag, 1996).

[28]L. V. Keldysh, "Diagram technique for nonequilibrium processes", Sov. Phys. JETP **20**, 1018 (1965).

[29]R. A. Craig, "Perturbation expansion for real-time Green's functions", J. Math. Phys. **9**, 605 (1968).

[30]P. Danielewicz, "Quantum theory of nonequilibrium processes, I", Ann. Phys. **152**, 239 (1984).

[31]T. Gunst, T. Markussen, K. Stokbro, and M. Brandbyge, "First-principles method for electron-phonon coupling and electron mobility: Applications to two-dimensional materials", Phys. Rev. B **93**, 035414 (2016).

[32]G. J. Ackland, M. C. Warren, and S. J. Clark, "Practical methods in ab initio lattice dynamics", J. Phys. Condens. Matter **9**, 7861 (1997).

[33]K. Kunc and R. M. Martin, "Ab initio force constants of GaAs: A new approach to calculation of phonons and dielectric properties", Phys. Rev. Lett. **48**, 406–409 (1982).

[34]T. Frederiksen, M. Paulsson, M. Brandbyge, and A.-P. Jauho, "Inelastic transport theory from first principles: Methodology and application to nanoscale devices", Phys. Rev. B **75**, 205413 (2007).

[35]J.-T. Lü, R. B. Christensen, G. Foti, T. Frederiksen, T. Gunst, and M. Brandbyge, "Efficient calculation of inelastic vibration signals in electron transport: Beyond the wide-band approximation", Phys. Rev. B **89**, 081405 (2014).

[36]M. Zacharias, C. E. Patrick, and F. Giustino, "Stochastic approach to phonon-assisted optical absorption", Phys. Rev. Lett. **115**, 177401 (2015).

[37] A. Pecchia, M. Gheorghe, A. D. Carlo, and P. Lugli, "Modulation of the electronic transport properties of carbon nanotubes with adsorbed molecules", Synthetic Metals **138**, Organic Materials for Device Applications. Proceedings of Symposium F, E-MRS Spring Meeting 2002, June 18-21, 2002, Strasbourg, France, 89 –93 (2003).

[38] Y. Liu, Z. Yuan, R. J. H. Wesselink, A. A. Starikov, M. van Schilfgaarde, and P. J. Kelly, "Direct method for calculating temperature-dependent transport properties", Phys. Rev. B **91**, 220405 (2015).

[39] J. Li, G. Speyer, and O. F. Sankey, "Conduction switching of photochromic molecules", Phys. Rev. Lett. **93**, 248302 (2004).

[40] D. Q. Andrews, R. P. Van Duyne, and M. A. Ratner, "Stochastic modulation in molecular electronic transport junctions: Molecular dynamics coupled with charge transport calculations", Nano Lett. **8**, 1120–1126 (2008).

[41] M. Paulsson, C. Krag, T. Frederiksen, and M. Brandbyge, "Conductance of alkanedithiol single-molecule junctions: A molecular dynamics study", Nano Lett. **9**, 117–121 (2008).

[42] G. C. Solomon, D. Q. Andrews, R. H. Goldsmith, T. Hansen, M. R. Wasielewski, R. P. Van Duyne, and M. A. Ratner, "Quantum interference in acyclic systems: Conductance of cross-conjugated molecules", Journal of the American Chemical Society **130**, 17301–17308 (2008).

[43] M. Zacharias and F. Giustino, "One-shot calculation of temperature-dependent optical spectra and phonon-induced band-gap renormalization", Phys. Rev. B **94**, 075125 (2016).

[44] M Burgelman, P Nollet, and S Degrave, "Modelling polycrystalline semiconductor solar cells", Thin Solid Films **361-362**, 527–532 (2000).

[45] D. Stradi, U. Martinez, A. Blom, M. Brandbyge, and K. Stokbro, "General atomistic approach for modeling metal-semiconductor interfaces using density functional theory and nonequilibrium Green's function", Physical Review B **93**, 155302 (2016).

[46] G. Margaritondo, *Electronic structure of semiconductor heterojunctions* (Kluwer Academic Publishers, 1988).

[47] E. Moulin, U. W. Paetzold, H. Siekmann, J. Worbs, A. Bauer, and R. Carius, "Study of thin-film silicon solar cell back reflectors and potential of detached reflectors", Energy Procedia **10**, European Materials Research Society Conference, 106 –110 (2011).

[48] A. Ingenito, J. C. O. Lizcano, S. L. Luxembourg, R. Santbergen, A. Weeber, O. Isabella, and M. Zeman, "Optimized back Reflectors for Rear Diffused c-Si Solar Cells", Energy Procedia **55**, Proceedings of the 4th International Conference on Crystalline Silicon Photovoltaics (SiliconPV 2014), 94 –100 (2014).

[49] V. M. Fthenakis, "Life cycle impact analysis of cadmium in CdTe PV production", Renewable and Sustainable Energy Reviews **8**, 303 –334 (2004).

[50] M. Woodhouse, A. Goodrich, R. Margolis, T. James, R. Dhere, T. Gessert, T. Barnes, R. Eggert, and D. Albin, "Perspectives on the pathways for cadmium telluride photovoltaic module manufacturers to address expected increases in the price for tellurium", Solar Energy Materials and Solar Cells **115**, 199 –212 (2013).

[51] A. Polman, M. Knight, E. C. Garnett, B. Ehrler, and W. C. Sinke, "Photovoltaic materials: Present efficiencies and future challenges", Science **352**, aad4424 (2016).

[52]Y. S. Lee, T. Gershon, O. Gunawan, T. K. Todorov, T. Gokmen, Y. Virgus, and S. Guha, "Cu_2ZnSnS_4 Thin-Film Solar Cells by Thermal Co-evaporation with 11.6% Efficiency and Improved Minority Carrier Diffusion Length", Advanced Energy Materials **5**, 1401372 (2015).

[53]W. Wang, M. T. Winkler, O. Gunawan, T. Gokmen, T. K. Todorov, Y. Zhu, and D. B. Mitzi, "Device Characteristics of CZTSSe Thin-Film Solar Cells with 12.6% Efficiency", Advanced Energy Materials **4**, 1301465 (2013).

[54]S. Chen, A. Walsh, J.-H. Yang, X. G. Gong, L. Sun, P.-X. Yang, J.-H. Chu, and S.-H. Wei, "Compositional dependence of structural and electronic properties of $Cu_2ZnSn(S,Se)_4$ alloys for thin film solar cells", Physical Review B **83**, 125201 (2011).

[55]S. Siebentritt, "Why are kesterite solar cells not 20% efficient?", Thin Solid Films **535**, 1–4 (2013).

[56]A. Polizzotti, I. L. Repins, R. Noufi, S.-H. Wei, and D. B. Mitzi, "The state and future prospects of kesterite photovoltaics", Energy & Environmental Science **6**, 3171–3182 (2013).

[57]X. Liu, Y. Feng, H. Cui, F. Liu, X. Hao, G. Conibeer, D. B. Mitzi, and M. Green, "The current status and future prospects of kesterite solar cells: A brief review", Progress in Photovoltaics: Research and Applications (2016) 10.1002/pip.2741.

[58]C. Tavernier, F. G. Pereira, O. Nier, D. Rideau, F. Monsieur, G. Torrente, M. Haond, H. Jaouen, O. Noblanc, Y. M. Niquet, M. Jaud, F. Triozon, M. Casse, J. Lacord, and J. C. Barbe, "TCAD modeling challenges for 14nm FullyDepleted SOI technology performance assessment", in 2015 International Conference on Simulation of Semiconductor Processes and Devices (SISPAD) (2015), pp. 4–7.

[59]O. Nier, D. Rideau, Y. M. Niquet, F. Monsieur, V. H. Nguyen, F. Triozon, A. Cros, R. Clerc, J. C. Barbé, P. Palestri, D. Esseni, I. Duchemin, L. Smith, L. Silvestri, F. Nallet, C. Tavernier, H. Jaouen, and L. Selmi, "Multi-scale strategy for high-k/metal-gate UTBB-FDSOI devices modeling with emphasis on back bias impact on mobility", Journal of Computational Electronics **12**, 675–684 (2013).

[60]Y. Hinuma, A. Grüneis, G. Kresse, and F. Oba, "Band alignment of semiconductors from density-functional theory and many-body perturbation theory", Physical Review B **90**, 155405 (2014).

[61]S.-H. Wei and A. Zunger, "Calculated natural band offsets of all II–VI and III–V semiconductors: Chemical trends and the role of cation d orbitals", Applied Physics Letters **72**, 2011 (1998).

[62]A. Alkauskas, P. Broqvist, F. Devynck, and A. Pasquarello, "Band Offsets at Semiconductor-Oxide Interfaces from Hybrid Density-Functional Calculations", Physical Review Letters **101**, 106802 (2008).

[63]Y.-H. Li, A. Walsh, S. Chen, W.-J. Yin, J.-H. Yang, J. Li, J. L. F. Da Silva, X. G. Gong, and S.-H. Wei, "Revised ab initio natural band offsets of all group IV, II-VI, and III-V semiconductors", Applied Physics Letters **94**, 212109 (2009).

[64]V. I. Anisimov, J. Zaanen, and O. K. Andersen, "Band theory and Mott insulators: Hubbard U instead of Stoner I", Physical Review B **44**, 943–954 (1991).

[65]J. Paier, R. Asahi, A. Nagoya, and G. Kresse, "Cu_2ZnSnS_4 as a potential photovoltaic material: A hybrid Hartree-Fock density functional theory study", Phys. Rev. B **79**, 115126 (2009).

[66]S. Tajima, R. Asahi, D. Isheim, D. N. Seidman, T. Itoh, M. Hasegawa, and K. Ohishi, "Atom-probe tomographic study of interfaces of Cu_2ZnSnS_4 photovoltaic cells", Applied Physics Letters **105**, 093901 (2014).

[67]F. Liu, C. Yan, J. Huang, K. Sun, F. Zhou, J. A. Stride, M. A. Green, and X. Hao, "Nanoscale Microstructure and Chemistry of Cu_2ZnSnS_4 /CdS Interface in Kesterite Cu_2ZnSnS_4 Solar Cells", Advanced Energy Materials **6**, 1600706 (2016).

[68]R. Haight, A. Barkhouse, O. Gunawan, B. Shin, M. Copel, M. Hopstaken, and D. B. Mitzi, "Band alignment at the $Cu_2ZnSn(S_xSe_{1-x})_4$ /CdS interface", Applied Physics Letters **98**, 253502 (2011).

[69]J. Li, M. Wei, Q. Du, W. Liu, G. Jiang, and C. Zhu, "The band alignment at CdS/ Cu_2ZnSnS_4 heterojunction interface", Surface and Interface Analysis **45**, 682–684 (2013).

[70]T. Kato, H. Hiroi, N. Sakai, and H. Sugimoto, "Buffer/Absorber Interface Study on Cu_2ZnSnS_4 and $Cu_2ZnSnSe_4$ Based Solar Cells: Band Alignment and Its Impact on the Solar Cell Performance", in 28th European Photovoltaic Solar Energy Conference and Exhibition (2013), pp. 2125–2127.

[71]B. Shin, O. Gunawan, Y. Zhu, N. A. Bojarczuk, S. J. Chey, and S. Guha, "Thin film solar cell with 8.4% power conversion efficiency using an earth-abundant Cu_2ZnSnS_4 absorber", Progress in Photovoltaics: Research and Applications **21**, 72–76 (2013).

[72]K. Sun, C. Yan, F. Liu, J. Huang, F. Zhou, J. A. Stride, M. Green, and X. Hao, "Over 9% Efficient Kesterite Cu_2ZnSnS_4 Solar Cell Fabricated by Using $Zn_{1-x}Cd_xS$ Buffer Layer", Advanced Energy Materials **6**, 1600046 (2016).

[73]S. Tajima, T. Itoh, H. Hazama, K. Ohishi, and R. Asahi, "Improvement of the open-circuit voltage of Cu_2ZnSnS_4 solar cells using a two-layer structure", Applied Physics Express **8**, 082302 (2015).

[74]T. Minemoto, T. Matsui, H. Takakura, Y. Hamakawa, T. Negami, Y. Hashimoto, T. Uenoyama, and M. Kitagawa, "Theoretical analysis of the effect of conduction band offset of window/CIS layers on performance of CIS solar cells using device simulation", Solar Energy Materials and Solar Cells **67**, 83–88 (2001).

[75]M. Gloeckler and J. Sites, "Efficiency limitations for wide-band-gap chalcopyrite solar cells", Thin Solid Films **480-481**, 241–245 (2005).

[76]C. J. Hages, N. J. Carter, R. Agrawal, and T. Unold, "Generalized current-voltage analysis and efficiency limitations in non-ideal solar cells: Case of $Cu_2ZnSn(S_xSe_{1-x})_4$ and $Cu_2Zn(Sn_yGe_{1-y})(S_xSe_{1-x})_4$", Journal of Applied Physics **115**, 234504 (2014).

[77]A. Redinger, M. Mousel, M. H. Wolter, N. Valle, and S. Siebentritt, "Influence of S/Se ratio on series resistance and on dominant recombination pathway in $Cu_2ZnSn(SSe)_4$ thin film solar cells", Thin Solid Films **535**, 291–295 (2013).

[78]K. Wang, O. Gunawan, T. Todorov, B. Shin, S. J. Chey, N. A. Bojarczuk, D. Mitzi, and S. Guha, "Thermally evaporated Cu_2ZnSnS_4 solar cells", Applied Physics Letters **97**, 143508 (2010).

[79]T. Ericson, J. J. Scragg, A. Hultqvist, J. T. Watjen, P. Szaniawski, T. Torndahl, and C. Platzer-Björkman, "Zn(O, S) Buffer Layers and Thickness Variations of CdS Buffer for Cu_2ZnSnS_4 Solar Cells", IEEE Journal of Photovoltaics **4**, 465–469 (2014).

[80]C. Platzer-Björkman, C. Frisk, J. K. Larsen, T. Ericson, S.-Y. Li, J. J. S. Scragg, J. Keller, F. Larsson, and T. Törndahl, "Reduced interface recombination in Cu_2ZnSnS_4 solar cells with atomic layer deposition $Zn_{1-x}Sn_xOy$ buffer layers", Applied Physics Letters **107**, 243904 (2015).

[81]S. Tajima, K. Kataoka, N. Takahashi, Y. Kimoto, T. Fukano, M. Hasegawa, and H. Hazama, "Direct measurement of band offset at the interface between CdS and Cu_2ZnSnS_4 using hard X-ray photoelectron spectroscopy", Applied Physics Letters **103**, 243906 (2013).

[82]M. Baer, B.-A. Schubert, B. Marsen, R. G. Wilks, S. Pookpanratana, M. Blum, S. Krause, T. Unold, W. Yang, L. Weinhardt, C. Heske, and H.-W. Schock, "Cliff-like conduction band offset and KCN-induced recombination barrier enhancement at the CdS/Cu_2ZnSnS_4 thin-film solar cell heterojunction", Applied Physics Letters **99**, 222105 (2011).

[83]C. Yan, F. Liu, N. Song, B. K. Ng, J. A. Stride, A. Tadich, and X. Hao, "Band alignments of different buffer layers (CdS, Zn(O,S), and In_2S_3) on Cu_2ZnSnS_4", Applied Physics Letters **104**, 173901 (2014).

[84]J. Li, Q. Du, W. Liu, G. Jiang, X. Feng, W. Zhang, J. Zhu, and C. Zhu, "The band offset at CdS/Cu_2ZnSnS_4 heterojunction interface", Electronic Materials Letters **8**, 365–367 (2012).

[85]A Santoni, F Biccari, C Malerba, M Valentini, R Chierchia, and A Mittiga, "Valence band offset at the CdS/Cu_2ZnSnS_4 interface probed by x-ray photoelectron spectroscopy", Journal of Physics D: Applied Physics **46**, 175101 (2013).

[86]S. Huang, W. Luo, and Z. Zou, "Band positions and photoelectrochemical properties of Cu_2ZnSnS_4 thin films by the ultrasonic spray pyrolysis method", en, Journal of Physics D: Applied Physics **46**, 235108 (2013).

[87]H. Du, M. J. Romero, I. Repins, G. Teeter, R. Noufi, and M. M. Al-Jassim, "Nanoscale measurements of the surface photovoltage in $Cu(In, Ga)Se_2$, Cu_2ZnSnS_4, and $Cu_2ZnSnSe_4$ thin films: The role of the surface electronics on the efficiency of solar cells", in 2011 37th IEEE Photovoltaic Specialists Conference (2011), pp. 001983–001986.

[88]M. Salvador, S. M. Vorpahl, H. Xin, W. Williamson, G. Shao, D. U. Karatay, H. W. Hillhouse, and D. S. Ginger, "Nanoscale Surface Potential Variation Correlates with Local S/Se Ratio in Solution-Processed CZTSSe Solar Cells", Nano Letters **14**, 6926–6930 (2014).

[89]A.-Y. Lu, H. Zhu, J. Xiao, C.-P. Chuu, Y. Han, M.-H. Chiu, C.-C. Cheng, C.-W. Yang, K.-H. Wei, Y. Yang, Y. Wang, D. Sokaras, D. Nordlund, P. Yang, D. A. Muller, M.-Y. Chou, X. Zhang, and L.-J. Li, "Janus monolayers of transition metal dichalcogenides", en, Nature Nanotechnology **12**, 744–749 (2017).

[90]J. Zhang, S. Jia, I. Kholmanov, L. Dong, D. Er, W. Chen, H. Guo, Z. Jin, V. B. Shenoy, L. Shi, and J. Lou, "Janus Monolayer Transition-Metal Dichalcogenides", ACS Nano **11**, 8192–8198 (2017).

[91]Z. Guan, S. Ni, and S. Hu, "Tunable Electronic and Optical Properties of Monolayer and Multilayer Janus MoSSe as a Photocatalyst for Solar Water Splitting: A First-Principles Study", The Journal of Physical Chemistry C **122**, 6209–6216 (2018).

[92]Y. Ji, M. Yang, H. Lin, T. Hou, L. Wang, Y. Li, and S.-T. Lee, "Janus Structures of Transition Metal Dichalcogenides as the Heterojunction Photocatalysts for Water Splitting", en, The Journal of Physical Chemistry C **122**, 3123–3129 (2018).

[93]X. Ma, X. Wu, H. Wang, and Y. Wang, "A Janus MoSSe monolayer: a potential wide solar-spectrum water-splitting photocatalyst with a low carrier recombination rate", en, J. Mater. Chem. A **6**, 2295–2301 (2018).

[94]C. Persson, "Electronic and optical properties of Cu_2ZnSnS_4 and $Cu_2ZnSnSe_4$", Journal of Applied Physics **107**, 053710 (2010).

[95]S. Chen, A. Walsh, X.-G. Gong, and S.-H. Wei, "Classification of Lattice Defects in the Kesterite Cu_2ZnSnS_4 and $Cu_2ZnSnSe_4$ Earth-Abundant Solar Cell Absorbers", Advanced Materials **25**, 1522–1539 (2013).

[96]N. Sakai, H. Hiroi, and H. Sugimoto, "Development of Cd-free buffer layer for Cu_2ZnSnS_4 thin-film solar cells", in 2011 37th IEEE Photovoltaic Specialists Conference (2011), pp. 003654–003657.

[97]E. H. Hwang and S. Das Sarma, "Acoustic phonon scattering limited carrier mobility in two-dimensional extrinsic graphene", Phys. Rev. B **77**, 115449 (2008).

[98]S. Chen, X. G. Gong, A. Walsh, and S.-H. Wei, "Crystal and electronic band structure of Cu_2ZnSnX_4 (X=S and Se) photovoltaic absorbers: First-principles insights", Applied Physics Letters **94**, 041903 (2009).

[99]K. Kaasbjerg, K. S. Thygesen, and K. W. Jacobsen, "Unraveling the acoustic electron-phonon interaction in graphene", Phys. Rev. B **85**, 165440 (2012).

[100]K. M. Borysenko, J. T. Mullen, E. A. Barry, S. Paul, Y. G. Semenov, J. M. Zavada, M. B. Nardelli, and K. W. Kim, "First-principles analysis of electron-phonon interactions in graphene", Phys. Rev. B **81**, 121412 (2010).

[101]O. D. Restrepo, K. E. Krymowski, J. Goldberger, and W. Windl, "A first principles method to simulate electron mobilities in 2d materials", en, New J. Phys. **16**, 105009 (2014).

[102]C.-H. Park, N. Bonini, T. Sohier, G. Samsonidze, B. Kozinsky, M. Calandra, F. Mauri, and N. Marzari, "Electron Phonon Interactions and the Intrinsic Electrical Resistivity of Graphene", Nano Lett. **14**, 1113–1119 (2014).

[103]J.-A. Yan, W. Y. Ruan, and M. Y. Chou, "Electron-phonon interactions for optical-phonon modes in few-layer graphene: First-principles calculations", Phys. Rev. B **79**, 115443 (2009).

[104]M. Brandbyge, M. R. Sørensen, and K. W. Jacobsen, "Conductance eigenchannels in nanocontacts", Phys. Rev. B **56**, 14956–14959 (1997).

[105]M. Dreher, F. Pauly, J. Heurich, J. C. Cuevas, E. Scheer, and P. Nielaba, "Structure and conductance histogram of atomic-sized Au contacts", Phys. Rev. B **72**, 075435 (2005).

[106]A. Pecchia, M. Gheorghe, A. Di Carlo, P. Lugli, T. A. Niehaus, T. Frauenheim, and R. Scholz, "Role of thermal vibrations in molecular wire conduction", Phys. Rev. B **68**, 235321 (2003).

[107]A. Franceschetti, "First-principles calculations of the temperature dependence of the band gap of Si nanocrystals", Phys. Rev. B **76**, 161301 (2007).

[108]Y.-M. Niquet, V.-H. Nguyen, F. Triozon, I. Duchemin, O. Nier, and D. Rideau, "Quantum calculations of the carrier mobility: Methodology, Matthiessen's rule, and comparison with semi-classical approaches", Journal of Applied Physics **115**, 054512 (2014).

[109]P. Erhart and K. Albe, "Analytical potential for atomistic simulations of silicon, carbon, and silicon carbide", Phys. Rev. B **71**, 035211 (2005).

[110]J. Schneider, J. Hamaekers, S. T. Chill, S. Smidstrup, J. Bulin, R. Thesen, A. Blom, and K. Stokbro, "ATK-ForceField: a new generation molecular dynamics software package", Modelling and Simulation in Materials Science and Engineering **25**, 085007 (2017).

[111]T. Markussen, R. Rurali, A.-P. Jauho, and M. Brandbyge, "Scaling theory put into practice: first-principles modeling of transport in doped silicon nanowires", Phys. Rev. Lett. **99**, 076803 (2007).

[112]C. Canali, C. Jacoboni, F. Nava, G. Ottaviani, and A. Alberigi-Quaranta, "Electron drift velocity in silicon", Phys. Rev. B **12**, 2265–2284 (1975).

[113]W. Zhang, C. Delerue, Y.-M. Niquet, G. Allan, and E. Wang, "Atomistic modeling of electron-phonon coupling and transport properties in *n*-type [110] silicon nanowires", Phys. Rev. B **82**, 115319 (2010).

[114]H. W. Sheng, M. J. Kramer, A. Cadien, T. Fujita, and M. W. Chen, "Highly optimized embedded-atom-method potentials for fourteen fcc metals", Phys. Rev. B **83**, 134118 (2011).

[115]D. R. Lide, *Handbook of chemistry and physics, 75th edition* (New York: CRC Press, 1997).

[116]M. Machón, S. Reich, H. Telg, J. Maultzsch, P. Ordejón, and C. Thomsen, "Strength of radial breathing mode in single-walled carbon nanotubes", Phys. Rev. B **71**, 035416 (2005).

[117]K. Hannewald and P. A. Bobbert, "Anisotropy effects in phonon-assisted charge-carrier transport in organic molecular crystals", Phys. Rev. B **69**, 075212 (2004).

[118]F. Ortmann, F. Bechstedt, and K. Hannewald, "Theory of charge transport in organic crystals: Beyond Holstein's small-polaron model", Phys. Rev. B **79**, 235206 (2009).

[119]M. Bernardi and J. C. Grossman, "Computer Calculations across Time and Length Scales in Photovoltaic Solar Cells", Energy Environ. Sci. (2016) 10.1039/C6EE01010E.

[120]N. Cavassilas, M. Bescond, H. Mera, and M. Lannoo, "One-shot current conserving quantum transport modeling of phonon scattering in n-type double-gate field-effect-transistors", Applied Physics Letters **102**, 013508 (2013).

[121]M. Bescond, C. Li, H. Mera, N. Cavassilas, and M. Lannoo, "Modeling of phonon scattering in n-type nanowire transistors using one-shot analytic continuation technique", Journal of Applied Physics **114**, 153712 (2013).

[122]H. Mera, M. Lannoo, N. Cavassilas, and M. Bescond, "Nanoscale device modeling using a conserving analytic continuation technique", Phys. Rev. B **88**, 075147 (2013).

[123]J. Noffsinger, E. Kioupakis, C. G. Van de Walle, S. G. Louie, and M. L. Cohen, "Phonon-assisted optical absorption in silicon from first principles", Phys. Rev. Lett. **108**, 167402 (2012).

[124]J. Chen, Y. Hu, and H. Guo, "First-principles analysis of photocurrent in graphene *pn* junctions", Phys. Rev. B **85**, 155441 (2012).

[125]L. Zhang, K. Gong, J. Chen, L. Liu, Y. Zhu, D. Xiao, and H. Guo, "Generation and transport of valley-polarized current in transition-metal dichalcogenides", Phys. Rev. B **90**, 195428 (2014).

[126]L. E. Henrickson, "Nonequilibrium photocurrent modeling in resonant tunneling photodetectors", J. Appl. Phys. **91**, 6273–6281 (2002).

[127]J. Tersoff, "Empirical interatomic potential for silicon with improved elastic properties", Phys. Rev. B **38**, 9902–9905 (1988).

[128]ASTM, "Standard Tables for Reference Solar Spectral Irradiances : Direct Normal and Hemispherical on 37° Tilted Surface", Astm **03**, 1–21 (2013).

[129]L. G. Ferreira, M. Marques, and L. K. Teles, "Slater half-occupation technique revisited: the LDA-1/2 and GGA-1/2 approaches for atomic ionization energies and band gaps in semiconductors", AIP Advances **1**, 032119 (2011).

[130]M. Levinshtein, S. Rumyantsev, and M. Shur, *Handbook series on semiconductor parameters. vol.1* (World Scientific, 1996).

[131]P. Würfel, *Physics of solar cells* (Wiley-VCH Verlag GmbH & Co. KGaA, Wenheim, 2005).

[132]B. J. Huang, P. E. Yang, Y. P. Lin, B. Y. Lin, H. J. Chen, R. C. Lai, and J. S. Cheng, "Solar cell junction temperature measurement of PV module", Solar Energy **85**, 388 –392 (2011).

[133]P. Löper, D. Pysch, A. Richter, M. Hermle, S. Janz, M. Zacharias, and S. W. Glunz, "Analysis of the temperature dependence of the open-circuit voltage", Energy Procedia **27**, 135 –142 (2012).

[134]S. Chander, A. Purohit, A. Sharma, S. P. Nehra, and M. S. Dhaka, "A study on photovoltaic parameters of mono-crystalline silicon solar cell with cell temperature", Energy Reports **1**, 104 –109 (2015).

[135]J. Yang, X. Wen, H. Xia, R. Sheng, Q. Ma, J. Kim, P. Tapping, T. Harada, T. W. Kee, F. Huang, Y.-B. Cheng, M. Green, A. Ho-Baillie, S. Huang, S. Shrestha, R. Patterson, and G. Conibeer, "Acoustic-optical phonon up-conversion and hot-phonon bottleneck in lead-halide perovskites", Nat. Comm. **8**, 14120 (2017).

[136]H. Kim, J. Hunger, E. Cánovas, M. Karakus, Z. Mics, M. Grechko, D. Turchinovich, S. H. Parekh, and M. Bonn, "Direct observation of mode-specific phonon-band gap coupling in methylammonium lead halide perovskites", Nat. Comm. **8**, 687 (2017).

[137]A. D. Wright, C. Verdi, R. L. Milot, G. E. Eperon, M. A. Pérez-Osorio, H. J. Snaith, F. Giustino, M. B. Johnston, and L. M. Herz, "Electron-phonon coupling in hybrid lead halide perovskites", Nat. Comm. **7**, 11755 (2016).

[138]P.-A. Mante, C. C. Stoumpos, M. G. Kanatzidis, and A. Yartsev, "Electron-acoustic phonon coupling in single crystal $CH_3NH_3PbI_3$ perovskites revealed by coherent acoustic phonons", Nat. Comm. **8**, 14398 (2017).

[139]K. S. Novoselov, A. K. Geim, S. V. Morozov, D. Jiang, Y. Zhang, S. V. Dubonos, I. V. Grigorieva, and A. A. Firsov, "Electric field effect in atomically thin carbon films", Science **306**, 666–669 (2004).

[140]D. Y. Qiu, F. H. da Jornada, and S. G. Louie, "Environmental Screening Effects in 2d Materials: Renormalization of the Bandgap, Electronic Structure, and Optical Spectra of Few-Layer Black Phosphorus", Nano Lett. **17**, 4706–4712 (2017).

[141]T. Gunst, K. Kaasbjerg, and M. Brandbyge, "Flexural-Phonon Scattering Induced by Electrostatic Gating in Graphene", Phys. Rev. Lett. **118**, 046601 (2017).

[142]F. A. Rasmussen and K. S. Thygesen, "Computational 2d Materials Database: Electronic Structure of Transition-Metal Dichalcogenides and Oxides", J. Phys. Chem. C **119**, 13169–13183 (2015).

[143]S. Smidstrup, D. Stradi, J. Wellendorff, P. A. Khomyakov, U. G. Vej-Hansen, M.-E. Lee, T. Ghosh, E. Jónsson, H. Jónsson, and K. Stokbro, "First-principles Green's-function method for surface calculations: A pseudopotential localized basis set approach", Phys. Rev. B **96**, 195309 (2017).

[144]The current was scaled by the electrode cross-sectional area (width times the effective layer thickness $h \approx 7.5$Å).

[145]T. O. Wehling, K. S. Novoselov, S. V. Morozov, E. E. Vdovin, M. I. Katsnelson, A. K. Geim, and A. I. Lichtenstein, "Molecular Doping of Graphene", Nano Lett. **8**, 173–177 (2008).

[146]L. Wang, I. Meric, P. Y. Huang, Q. Gao, Y. Gao, H. Tran, T. Taniguchi, K. Watanabe, L. M. Campos, D. A. Muller, J. Guo, P. Kim, J. Hone, K. L. Shepard, and C. R. Dean, "One-Dimensional Electrical Contact to a Two-Dimensional Material", Science **342**, 614–617 (2013).

[147]A. Das, S. Pisana, B. Chakraborty, S. Piscanec, S. K. Saha, U. V. Waghmare, K. S. Novoselov, H. R. Krishnamurthy, A. K. Geim, A. C. Ferrari, and A. K. Sood, "Monitoring dopants by Raman scattering in an electrochemically top-gated graphene transistor", Nature Nanotechnology **3**, 210–215 (2008).

[148]D. K. Efetov and P. Kim, "Controlling Electron-Phonon Interactions in Graphene at Ultrahigh Carrier Densities", Phys. Rev. Lett. **105**, 256805 (2010).

[149]S. Grover, A. Joshi, A. Tulapurkar, and M. M. Deshmukh, "Abrupt p-n junction using ionic gating at zero-bias in bilayer graphene", Scientific Reports **7**, 3336 (2017).

[150]T. G. Pedersen, C. Flindt, J. Pedersen, N. A. Mortensen, A.-P. Jauho, and K. Pedersen, "Graphene Antidot Lattices: Designed Defects and Spin Qubits", Phys. Rev. Lett. **100**, 136804 (2008).

[151]T. G. Pedersen, C. Flindt, J. Pedersen, A.-P. Jauho, N. A. Mortensen, and K. Pedersen, "Optical properties of graphene antidot lattices", Phys. Rev. B **77**, 245431 (2008).

[152]G. Mugny, F. Triozon, J. Li, Y.-M. Niquet, G. Hiblot, D. Rideau, and C. Delerue, "Band structure of III-V thin films: An atomistic study of non-parabolic effects in confinement direction", in EUROSOI-ULIS 2015: 2015 Joint International EUROSOI Workshop and International Conference on Ultimate Integration on Silicon (2015), pp. 301–304.

[153]D. Rideau, M. Feraille, M. Michaillat, Y. Niquet, C. Tavernier, and H. Jaouen, "On the validity of the effective mass approximation and the Luttinger k.p model in fully depleted SOI MOSFETs", Solid-State Electronics **53**, 452 –461 (2009).

[154]G. Mugny, D. Rideau, F. Triozon, Y.-M. Niquet, C. Kriso, F. G. Pereira, D. Garetto, C. Tavernier, and C. Delerue, "Full-zone $k \cdot p$ parametrization for III-As materials", in 2015 International Conference on Simulation of Semiconductor Processes and Devices (SISPAD) (2015), pp. 28–31.

[155]D. Rideau, M. Feraille, L. Ciampolini, M. Minondo, C. Tavernier, H. Jaouen, and A. Ghetti, "Strained Si, Ge, and $Si_{1-x}Ge_x$ alloys modeled with a first-principles-optimized full-zone $k \cdot p$ method", Phys. Rev. B **74**, 195208 (2006).

[156]J. Li and L.-W. Wang, "Band-structure-corrected local density approximation study of semiconductor quantum dots and wires", Phys. Rev. B **72**, 125325 (2005).

[157]F. Stern and W. E. Howard, "Properties of semiconductor surface inversion layers in the electric quantum limit", Phys. Rev. **163**, 816–835 (1967).

[158]R. Yukawa, K. Ozawa, S. Yamamoto, R.-Y. Liu, and I. Matsuda, "Anisotropic effective mass approximation model to calculate multiple subband structures at wide-gap semiconductor surfaces: Application to accumulation layers of $SrTiO_3$ and ZnO", Surface Science **641**, 224 –230 (2015).

[159]M. Bescond, N. Cavassilas, and M. Lannoo, "Effective-mass approach for n-type semiconductor nanowire MOSFETs arbitrarily oriented", Nanotechnology **18**, 255201 (2007).

[160]L. Lindsay and D. A. Broido, "Optimized Tersoff and Brenner empirical potential parameters for lattice dynamics and phonon thermal transport in carbon nanotubes and graphene", Phys. Rev. B **81**, 205441 (2010).

Appendix A

Boltzmann transport equation calculation parameters

This appendix lists the paramters used for the BTE calculations performed in chapter 4.

A.1 Silicon nanowire

The BTE calculation for the SiNW system was performed using Tersoff potentials for the phonons[109]. Hamiltonian derivatives were calculated using 11 repetitions along the transport direction of the unit-cell. Only the lowest conduction band is included in the EPC calculation and we used 150 k-points in the range $[0, 0.05]\pi/a$ and 100 q-points in the range $[-0.2, 0.2]\pi/a$ where a is the lattice vector of the unit-cell. For the mobility calculation we used an energy broadening 3 meV for the δ function.

A.2 Bulk silicon

The BTE calculation for the bulk silicon system was performed using DFT for the phonons. Hamiltonian derivatives were calculated using (7,7,7) repetitions of the silicon unit-cell. Only the lowest conduction band valley is included in the EPC calculation and we sample the BZ locally corresponding to a $99x99x99$ Monkhorst-Pack grid. For intravalley scattering the phonon BZ is sampled using a $25x25x25$ grid where in a region around the Γ point given by $|q| < 0.075\pi/a$. This sampling is then shifted to account for intervalley scattering.

A.3 (8,0) carbon nanotube

For the semiconducting CNT we used optimized Tersoff potentials for the phonons[160]. Hamiltonian derivatives were calculated using 5 repetitions along the transport direction of the unit-cell. Only the lowest conduction band is included in the EPC calculation and we used 41 k-points in the range $[-0.07, 0.07]\pi/a$ and 41 q-points in the range $[-0.28, 0.28]\pi/a$ where a is the lattice vector of the unit-cell. For the mobility calculation we used an energy broadening 3 meV for the δ function. The chemical potential was shifted to 0.3 eV above the intrinsic Fermi level

A.4 (4,4) carbon nanotube

For the metallic CNT we used optimized Tersoff potentials for the phonons[160]. Hamiltonian derivatives were calculated using 3 repetitions along the transport direction of the unit-cell. Only the conduction bands at the Fermi level are included in the EPC calculation and we used 80 k-points in the range $[0.30, 0.46\pi/a$ and 400 q-points in the range $[-0.5, 0.5]\pi/a$ where a is the lattice vector of the unit-cell. For the mobility calculation we used an energy broadening 3 meV for the δ function. The chemical potential was shifted to 0.2 eV above the intrinsic Fermi level

Appendix B

Publications

Paper 1

Semiconductor band alignment from first principles: A new nonequilibrium Green's function method applied to the CZTSe/CdS interface for photovoltaics

Mattias Palsgaard, Andrea Crovetto, Tue Gunst, Troels Markussen, Ole Hansen, Kurt Stokbro, and Mads Brandbyge

2016 International Conference on Simulation of Semiconductor Processes and Devices (SISPAD), pp. 377–380

Simulation of Semiconductor Processes and Devices 2016
Edited by E. Bär, J. Lorenz, and P. Pichler

Semiconductor band alignment from first principles: a new nonequilibrium Green's function method applied to the CZTSe/CdS interface for photovoltaics.

Mattias L. N. Palsgaard*†, Andrea Crovetto†, Tue Gunst†, Troels Markussen*, Ole Hansen†, Kurt Stokbro*
and Mads Brandbyge†
†Center for Nanostructured Graphene (CNG), Department of Micro- and Nanotechnology (DTU Nanotech)
*Quantumwise A/S, Fruebjergvej 3, Postbox 4, DK-2100 Copenhagen, Denmark

***Abstract*—In this paper we present a method to obtain the band offset of semiconductor heterointerfaces from Density Functional Theory together with the nonequilibrium Green's function method. Band alignment and detailed properties of the interface between $Cu_2ZnSnSe_4$ and CdS are extracted directly from first principles simulations. The interface is important for photovoltaics applications where in particular the band offsets are important for efficiency. The band bending pose a problem for accurate atomistic simulations of band offsets due to its long range. Here we investigate two different methods for dealing with band bending directly. One involves doping the materials to induce a shorter screening length. The other method is to apply a voltage bias across the interface to correct for the band bending. The calculated band offsets agree well with previous experimental and theoretical studies and, interestingly, the offset is seen to depend on whether or not the interface is under flat-band conditions.**

I. Introduction

Semiconductor heterointerfaces play an increasingly important role in optical and electronic devices due to miniaturization and to the pervasive trend of introducing new materials to tailor the desired device properties [1]. In particular, the valence- and conduction band offsets (VBO and CBO) at the interface affect the transport properties and recombination rates at the interface [2].

Methods to obtain VBO and CBO from first principles have been recently reviewed [3]. Among them, an explicit interface modeling method inspired by the photoemission measurement has gained significant popularity due to its excellent agreement with experimental data [4]–[6]. In this method, the energy positions of the valence bands of materials A and B are first calculated separately in the two unstrained bulk materials with respect to a reference energy unique to each bulk calculation (for example, the position of a core level). Then, an explicit interface calculation is employed to align the two valence band positions to a common energy reference, which can be a core level or the averaged local potential.

Conversely, we propose a method where the band alignment can be obtained directly from the interface supercell calculation containing both materials using Density Functional Theory (DFT) together with Nonequilibrium Green's functions (NEGF). In this way it is further possible to extract information about the atomic properties of the interface such as defects and tunneling of states over the interface and study transport phenomena. Similar methods have been used previously to study Schottky barriers [7].

To demonstrate this method, we have selected the CZTSe-CdS interface as a case study. $Cu_2ZnSnSe_4$ (CZTSe, band gap 1.0 eV), Cu_2ZnSnS_4 (CZTS, band gap 1.5 eV) and their alloy $Cu_2ZnSnS_xSe_{4-x}$ (CZTSSe, tunable band gap 1.0-1.5 eV) are promising p-type semiconductors for thin-film photovoltaics. To indicate all three materials in general terms we use the notation CZTS(e). In solar cell devices, their n-type heterojunction partner is typically CdS, with which the best conversion efficiencies reported so far have been achieved [8], [9]. A schematic band diagram is shown in Fig. 1(a).

As noted in a number of review papers [10]–[12], loss mechanisms at the CZTS(e)/CdS interface are believed to be one of the reasons why laboratory-scale CZTS(e) solar cells still lag far behind their theoretical maximum efficiency. To emphasize the potentially dramatic consequences of an unfavorable band alignment of the CZTSe/CdS interface on solar cell efficiency, we have carried out a device-level simulation (Fig. 1(b)). There, we have swept the electron affinity of CZTSe to recreate different hypothetical band alignments, according to Anderson's rule [2]. The results are shown in Fig. 1(b). A type I alignment, or conduction band "spike" with a height between +0.1 eV and +0.4 eV (Fig. 1) is found to be optimal, in agreement with similar studies on other solar cell heterointerfaces [13], [14].

Despite the importance of the offset values in device performance, only few reports of calculated band alignments are available in the literature and mostly with focus on CZTS. Only one report could be found on CZTSe [15]. To the best of our knowledge, only the photoemission-inspired calculation method [4] has been reported for any CZTS(e)/CdS interface [15]. The actual band alignment at the CZTS-CdS interface is still disputed, with experimental and theoretical offsets scat-

978-1-5090-0818-6/16/$31.00

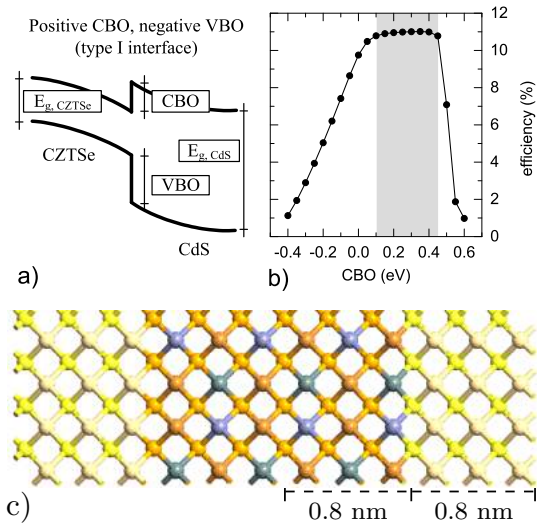

Figure 1: a) Schematic illustration of the sign conventions and symbols used for the band alignment problem. The signs of the CBO and VBO are referred to the lower band gap semiconductor, so that a positive CBO means that the CdS conduction band lies above the CZTSe conduction band. Assuming a negative VBO, a positive (negative) CBO results in a type I (II) interface, also known as conduction band spike (cliff). $E_{\mathrm{g,CZTSe}}$ and $E_{\mathrm{g,CdS}}$ are the band gaps of CZTSe and CdS respectively. b) Simulated CZTSe/CdS heterojunction solar cell efficiency as a function of the conduction band offset. The shaded region is the optimal CBO range for achieving maximum efficiency. c) Periodic supercell containing the (100)/(100) interface of CZTS and CdS, dimensioned as in previously reported calculations [15].

tered in a broad energy range -0.34 eV to +0.45 eV. However, the few existing studies for the CZTSe-CdS interface are in rather good agreement: Different photoemission experiments have measured +0.48 eV [16], +0.34 eV [17], and +0.3 eV offsets [18], while a theoretical study has calculated a +0.34 eV offset [15]. This provides a benchmark for our proposed method and allows adding new information to an interface in which the band alignment is relatively well established.

II. Computational Details

The preliminary device-level simulation was performed numerically with the finite-element method as implemented in the thin-film solar cell simulation software SCAPS [19] on a standard CZTSe/CdS/ZnO device structure. The material parameters were taken from various literature sources [20], [21]. The CBO between CZTSe and CdS was swept from -0.4 eV to +0.6 eV by sweeping the electron affinity of CZTS while maintaining the flat band conditions at the contacts.

All first-principles calculations in this study were performed with the ATK DFT software [22] using a double zeta polarized LCAO basis set [23], [24]. The combination of DFT with NEGF enables a device setup with semi-infinite electrodes on each side of the interface.

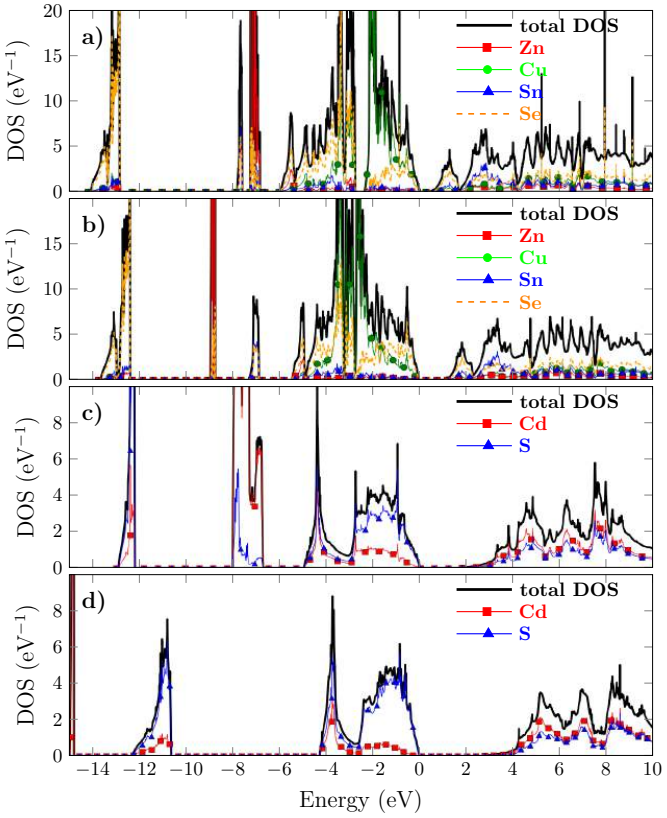

Figure 2: Total and projected density of states of bulk CZTSe calculated with GGA (a) and GGA + U (b) and for bulk CdS calculated with GGA (c) and GGA + U (d).

It is well known that the bandgaps of CZTSe and CdS are poorly reproduced with the conventional local density approximation (LDA) or generalized gradient approximation (GGA) approach to the exchange-correlation potential in DFT calculations [15]. We use the semi-empirical Hubbard correction where an additional energy term of the form

$$E_U = \frac{1}{2}\sum_{\mu} U_\mu \left(n_\mu - n_\mu^2\right) \tag{1}$$

where n_μ is the projection onto an atomic shell and U is chosen to reproduce the experimental bandgap in the bulk unit cell of either material, is added to the usual GGA-PBE exchange-correlation functional. This method is a computationally cheap way to correct for the self interaction of localized electrons in strongly correlated systems [25]. In Fig. 2, we compare density of states (DOS) of bulk CZTSe calculated with and without the Hubbard correction term. As expected the bandgaps are opened and the valence bands of d-like character for Zn and Cd are downshifted in energy. This is very similar to the effects seen when using the G_0W_0(HSE) approach on CZTS [26] indicating a high degree of self interaction error in these systems. Previous theoretical studies [15] have been performed on interface supercells with up to 3 unit cells of either material. This means that dimensions only up to a few nm in the direction perpendicular to the interface plane have been used

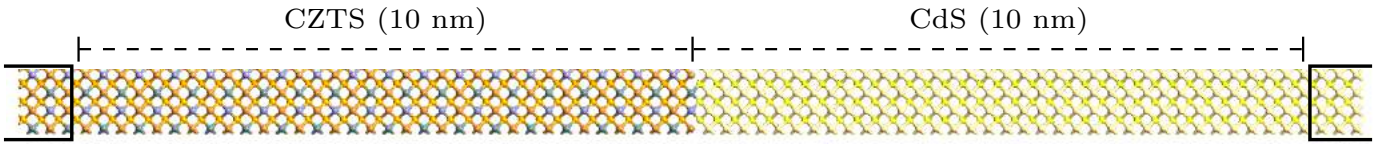

Figure 3: Structure used to simulate the 100/100 interface of CZTSe (left) and CdS (right). The supercell is more than five times larger than that used in previous work [15].

(Fig. 1). Furthermore these calculations were performed using periodic boundary conditions (PBC) in all directions resulting in interfaces separated by less than 2 nm as shown in Fig. 1.

Instead, in this work we employed a supercell that is 20 nm in length (Fig. 3) and semi-infinite boundary conditions in the direction perpendicular to the interface plane, as allowed by the DFT-NEGF approach. This assures that bulk-like conditions are met on either side. This approach can be justified as the thickness of each layer of material in real devices is tens of nm for CdS and hundreds of nm for CZTSe, so semi-infinite boundary conditions give a better description of the situation than PBC's [7]. The supercells employed in the calculation are periodic along the interface using 5x3 k-points. In the electrodes of the device a 3x5x100 k-point grid is used. K-points were chosen so that the total energy of the bulk materials was converged to within 0.5 meV. Several interfaces can be constructed with different surface geometries and formation energies. Here we consider the CZTSe(100)/CdS(100) interface, which has relatively low strain of ∼2.5%. GGA + U is known to overestimate lattice parameters for CZTS(e), we therefore keep the experimental lattice parameter for CZTSe. When setting up the interface the CdS bulk crystal is strained to fit that of CZTSe.

All relaxation where performed until interatomic force where below 0.02 eV/Å. Calculations of the local density of states (LDOS) in the device were performed using 11x11 k-points. Using this scheme we can for the first time study directly the effect of the interface on the band-alignment and transport properties in this system.

III. Results

Fig. 4(a) shows the LDOS and the local potential across the intrinsic (non-doped) interface. We see a clear spike-like CBO in agreement with previous theoretical and experimental studies [15], [16]. The potential shows a residual slope towards the electrodes indicating that the screening is not contained within the supercell. Nevertheless, the CBO obtained with this method (∼0.3eV) is in good agreement with experimental data measured under equilibrium conditions [17], [18]. To address the problem of the residual slope in the potential, one can reduce the screening length by doping both materials. Our simulations include doping by adding a complementary charge to the atomic sites. Fig. 4(b) shows the LDOS and local potential across the interface where a p-type (n-type) charge density of 10^{18} cm^{-3} unit charges are added to CZTSe (CdS). Adding the charge removes the residual slope of the potential, however it also dramatically changes the electronic structure of

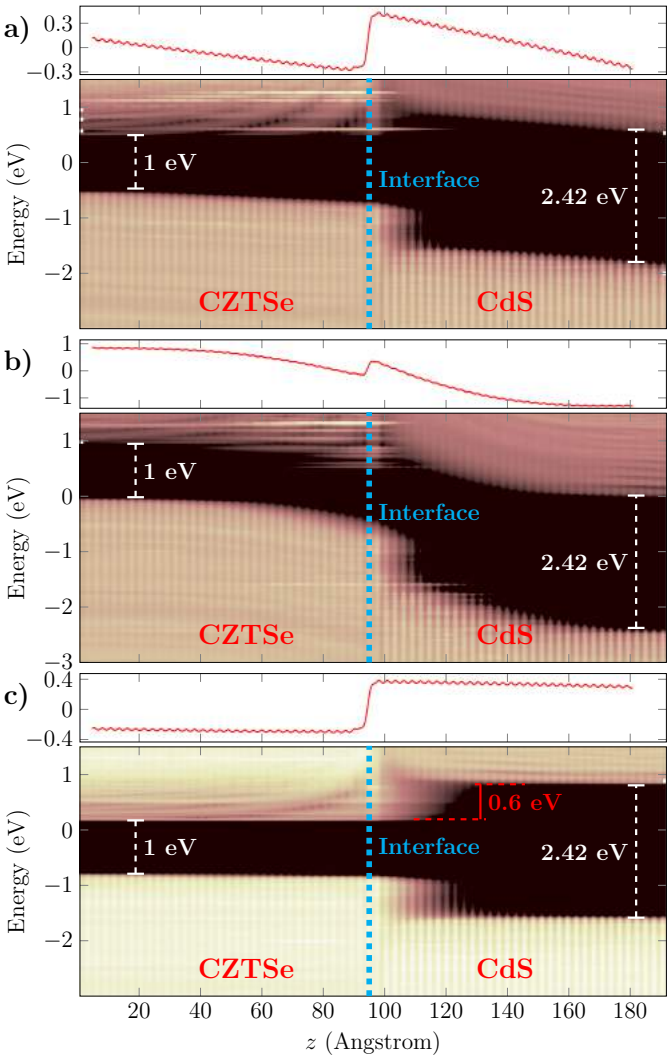

Figure 4: The local potential (top) and local density of states (bottom) of the CZTSe/CdS interface resolved along the direction perpendicular to the interface surface. (a) equilibrium conditions with zero bias and zero doping; (b) equilibrium conditions with zero bias and 10^{18} cm^{-3} doping density; (c) non-equilibrium conditions with an applied forward bias to achieve flat-band conditions and zero doping.

the interface. Further, it must be emphasized that the amount of charge needed here to contain the screening within the cell is very large compared to the real doping density of CZTSe, which is on the order of 10^{15}–10^{16} cm^{-3} [8]. In

fact, the experimental screening length of CZTSe (equivalent to the depletion region width in a p-n^+ junction device) is about 20 times larger than the width of the CZTSe layer in our supercell and consequently several hundred times larger than previous theoretical studies [8], [15]. To handle weakly screened materials, i.e. with band bending occurring over more than a few nm, we apply a small forward bias in the device simulations. Fig. 4(c) shows the LDOS and potential across such a system. Clearly we have in this way achieved flat band conditions on both sides of the device and at the same time removed the residual slope of the local potential. Such a calculation is only possible due to the device setup we have used here. The obtained CBO is +0.6 eV which agrees nicely with the only reported measurement done under flat-band conditions [16]. Note that the CBO is larger in the flat-band case than in the case of equilibrium band bending, which was also the case in experimental studies [16]–[18]. Finally in the LDOS for the undoped and doped systems at equilibrium, Fig. 4(a) and Fig. 4(b) respectively, localized states appear inside the gaps of either material. Localized states can have a crucial impact on the performance of any electronic device by e.g. increasing the recombination rate. They may also lead to errors in experimental measurements of band offsets due to lack of sufficient resolution to distinguish an interface state from its nearest bulk band. These states can be addressed directly in the device method as opposed to bulk supercell simulations. In particular, we note that the CBO in the doped system (Fig. 4(b)) is strongly influenced by the presence of localized states.

IV. Conclusion

We have successfully analyzed the electronic structure of the interface between CdS and $Cu_2ZnSnSe_4$ using first principles calculations. This interface is of particular interest for the photovoltaics community. The conduction band offset across the interface has been identified as a bottleneck for efficiency of a promising thin-film solar cell device, using device simulations. From DFT-NEGF calculations a CBO of $+0.6$ eV is found under flat-band conditions imposed by applying a forward bias over the interface to correct for band-bending. The results agree reasonably well with experiments under equilibrium and flat-band conditions.

Acknowledgment

This work is partly funded by the Innovation Fund Denmark (IFD) under File No. 5016-00102.

References

[1] "The interface is still the device." *Nature materials*, vol. 11, no. 2, p. 91, mar 2012.

[2] G. Margaritondo, *Electronic structure of semiconductor heterojunctions*. Kluwer Academic Publishers.

[3] Y. Hinuma, A. Grüneis, G. Kresse, and F. Oba, "Band alignment of semiconductors from density-functional theory and many-body perturbation theory," *Physical Review B*, vol. 90, no. 15, p. 155405, oct 2014.

[4] S.-H. Wei and A. Zunger, "Calculated natural band offsets of all II–VI and III–V semiconductors: Chemical trends and the role of cation d orbitals," *Applied Physics Letters*, vol. 72, no. 16, p. 2011, apr 1998.

[5] A. Alkauskas, P. Broqvist, F. Devynck, and A. Pasquarello, "Band Offsets at Semiconductor-Oxide Interfaces from Hybrid Density-Functional Calculations," *Physical Review Letters*, vol. 101, no. 10, p. 106802, sep 2008.

[6] Y.-H. Li, A. Walsh, S. Chen, W.-J. Yin, J.-H. Yang, J. Li, J. L. F. Da Silva, X. G. Gong, and S.-H. Wei, "Revised ab initio natural band offsets of all group IV, II-VI, and III-V semiconductors," *Applied Physics Letters*, vol. 94, no. 21, p. 212109, may 2009.

[7] D. Stradi, U. Martinez, A. Blom, M. Brandbyge, and K. Stokbro, "General atomistic approach for modeling metal-semiconductor interfaces using density functional theory and nonequilibrium green's function," *Phys. Rev. B*, vol. 93, p. 155302, Apr 2016.

[8] Y. S. Lee, T. Gershon, O. Gunawan, T. K. Todorov, T. Gokmen, Y. Virgus, and S. Guha, "$Cu_2ZnSnSe_4$ Thin-Film Solar Cells by Thermal Co-evaporation with 11.6% Efficiency and Improved Minority Carrier Diffusion Length," *Advanced Energy Materials*, vol. 5, no. 7, p. 1401372, apr 2015.

[9] W. Wang, M. T. Winkler, O. Gunawan, T. Gokmen, T. K. Todorov, Y. Zhu, and D. B. Mitzi, "Device Characteristics of CZTSSe Thin-Film Solar Cells with 12.6% Efficiency," *Advanced Energy Materials*, vol. 4, no. 7, p. 1301465, nov 2013.

[10] S. Siebentritt, "Why are kesterite solar cells not 20% efficient?" *Thin Solid Films*, vol. 535, pp. 1–4, 2013.

[11] A. Polizzotti, I. L. Repins, R. Noufi, S.-H. Wei, and D. B. Mitzi, "The state and future prospects of kesterite photovoltaics," *Energy & Environmental Science*, vol. 6, no. 11, pp. 3171–3182, oct 2013.

[12] X. Liu, Y. Feng, H. Cui, F. Liu, X. Hao, G. Conibeer, D. B. Mitzi, and M. Green, "The current status and future prospects of kesterite solar cells: a brief review," *Progress in Photovoltaics: Research and Applications*, jan 2016.

[13] T. Minemoto, T. Matsui, H. Takakura, Y. Hamakawa, T. Negami, Y. Hashimoto, T. Uenoyama, and M. Kitagawa, "Theoretical analysis of the effect of conduction band offset of window/CIS layers on performance of CIS solar cells using device simulation," *Solar Energy Materials and Solar Cells*, vol. 67, no. 1, pp. 83–88, 2001.

[14] M. Gloeckler and J. Sites, "Efficiency limitations for wide-band-gap chalcopyrite solar cells," *Thin Solid Films*, vol. 480-481, pp. 241–245, jun 2005.

[15] S. Chen, A. Walsh, J.-H. Yang, X. G. Gong, L. Sun, P.-X. Yang, J.-H. Chu, and S.-H. Wei, "Compositional dependence of structural and electronic properties of $Cu_2ZnSn(S,Se)_4$ alloys for thin film solar cells," *Physical Review B*, vol. 83, no. 12, p. 125201, mar 2011.

[16] R. Haight, A. Barkhouse, O. Gunawan, B. Shin, M. Copel, M. Hopstaken, and D. B. Mitzi, "Band alignment at the $Cu_2ZnSn(S_xSe_{1-x})_4$/CdS interface," *Applied Physics Letters*, vol. 98, no. 25, p. 253502, jun 2011.

[17] J. Li, M. Wei, Q. Du, W. Liu, G. Jiang, and C. Zhu, "The band alignment at CdS/$Cu_2ZnSnSe_4$ heterojunction interface," *Surface and Interface Analysis*, vol. 45, no. 2, pp. 682–684, feb 2013.

[18] T. Kato, H. Hiroi, N. Sakai, and H. Sugimoto, "Buffer/Absorber Interface Study on Cu_2ZnSnS_4 and $Cu_2ZnSnSe_4$ Based Solar Cells: Band Alignment and Its Impact on the Solar Cell Performance." *28th European Photovoltaic Solar Energy Conference*, pp. 2125–2127, sep 2013.

[19] M. Burgelman, P. Nollet, and S. Degrave, "Modelling polycrystalline semiconductor solar cells," *Thin Solid Films*, vol. 361-362, pp. 527–532, feb 2000.

[20] M. Gloeckler, "Device physics of Cu(In,Ga)Se2 thin-film solar cells," PhD thesis, Colorado State University, 2005.

[21] K. Ito, *Copper Zinc Tin Sulfide-Based Thin-Film Solar Cells*. Wiley, 2015.

[22] Atomistix ToolKit version 2015.0, QuantumWise A/S.

[23] J. M. Soler, E. Artacho, J. D. Gale, A. García, J. Junquera, P. Ordejón, and D. Sánchez-Portal, "The siesta method for ab initio order- n materials simulation," *Journal of Physics: Condensed Matter*, vol. 14, no. 11, p. 2745, 2002.

[24] M. Brandbyge, J.-L. Mozos, P. Ordejón, J. Taylor, and K. Stokbro, "Density-functional method for nonequilibrium electron transport," *Phys. Rev. B*, vol. 65, p. 165401, Mar 2002.

[25] V. I. Anisimov, J. Zaanen, and O. K. Andersen, "Band theory and Mott insulators: Hubbard U instead of Stoner I," *Physical Review B*, vol. 44, no. 3, pp. 943–954, jul 1991.

[26] J. Paier, R. Asahi, A. Nagoya, and G. Kresse, "Cu_2ZnSnS_4 as a potential photovoltaic material: A hybrid hartree-fock density functional theory study," *Phys. Rev. B*, vol. 79, p. 115126, Mar 2009.

Paper 2

Interface band gap narrowing behind open circuit voltage losses in Cu_2ZnSnS_4 solar cells

Andrea Crovetto, *Mattias Palsgaard*, Tue Gunst, Troels Markussen, Kurt Stokbro, Mads Brandbyge, and Ole Hansen

Applied Physics Letters. **110**, 083903, (2017)

Interface band gap narrowing behind open circuit voltage losses in Cu_2ZnSnS_4 solar cells

Andrea Crovetto,[1,a)] Mattias L. N. Palsgaard,[1,2,b)] Tue Gunst,[1] Troels Markussen,[2] Kurt Stokbro,[2] Mads Brandbyge,[1] and Ole Hansen[1,3]
[1]*DTU Nanotech, Technical University of Denmark, DK-2800 Kgs. Lyngby, Denmark*
[2]*QuantumWise A/S, DK-2100 Copenhagen, Denmark*
[3]*V-SUSTAIN, Villum Center for the Science of Sustainable Fuels and Chemicals, Technical University of Denmark, DK-2800 Kgs. Lyngby, Denmark*

(Received 11 January 2017; accepted 6 February 2017; published online 22 February 2017)

We present evidence that bandgap narrowing at the heterointerface may be a major cause of the large open circuit voltage deficit of Cu_2ZnSnS_4/CdS solar cells. Bandgap narrowing is caused by surface states that extend the Cu_2ZnSnS_4 valence band into the forbidden gap. Those surface states are consistently found in Cu_2ZnSnS_4, but not in $Cu_2ZnSnSe_4$, by first-principles calculations. They do not simply arise from defects at surfaces but are an intrinsic feature of Cu_2ZnSnS_4 surfaces. By including those states in a device model, the outcome of previously published temperature-dependent open circuit voltage measurements on Cu_2ZnSnS_4 solar cells can be reproduced quantitatively without necessarily assuming a cliff-like conduction band offset with the CdS buffer layer. Our first-principles calculations indicate that Zn-based alternative buffer layers are advantageous due to the ability of Zn to passivate those surface states. Focusing future research on Zn-based buffers is expected to significantly improve the open circuit voltage and efficiency of pure-sulfide Cu_2ZnSnS_4 solar cells. *Published by AIP Publishing.* [http://dx.doi.org/10.1063/1.4976830]

Even though Cu_2ZnSnS_4 (CZTS) solar cells could be a sustainable solution to the increasing global energy demand, they are still plagued by a low open circuit voltage compared to their Shockley-Queisser limit, which has so far prevented them from reaching a sufficiently high efficiency for commercialization.[1] In this work, we show evidence of an interface mechanism limiting the open circuit voltage, and we demonstrate that this mechanism can be overcome by choosing a particular class of materials as interface partners of CZTS.

Knowledge of the "recombination energy deficit" $\Delta\phi$, i.e., the difference between the bandgap of the absorber and the activation energy (ϕ) of the main recombination path, can help identify where the limiting mechanism is located. $\Delta\phi$ can be estimated by a temperature-dependent open circuit voltage measurement.[2] If $\Delta\phi > 0$, recombining electrons and holes are separated by an energy distance that is smaller than the absorber bandgap. Here, there is a significant difference between CZTS and its selenide equivalent $Cu_2ZnSnSe_4$ (CZTSe). State-of-the-art CZTSe solar cells are limited by bulk recombination because measured $\Delta\phi$ values correspond roughly to the depth of the bulk tail states of CZTSe, from which carriers recombine.[2] Conversely, in state-of-the-art CZTS solar cells, $\Delta\phi$ is around 0.4 eV,[3–5] even though the depth of the CZTS bulk tail states is only 0.1–0.2 eV lower than the bandgap.[6,7] Such a mismatch implies that the energy distance between recombining electrons and holes is further reduced somewhere in the solar cell. A popular hypothesis is that the interface between CZTS and its usual heterojunction partner CdS (or "buffer layer") features a cliff-like conduction band offset (CBO). In such a scenario, the energy distance between recombining electrons on the CdS side and holes on the CZTS side is reduced by an amount equal to the CBO. However, even though many reports of a cliff-like CBO exist for devices with efficiency below 5%, all band alignment measurements on CZTS/CdS solar cells with efficiency above 7% yielded a spike-like or nearly flat CBO[8–11] (Fig. S1, supplementary material). Therefore, we conclude that a large cliff-like CBO may exist in some lower-performance CZTS/CdS solar cells but not in the best reported CZTS/CdS solar cells.

In an attempt to identify another mechanism that may contribute to the large $\Delta\phi$ value, we performed first-principles electronic structure calculations on the CZTS(100)/CdS(100) and CZTSe(100)/CdS(100) interfaces. The calculations were based on a density functional theory-nonequilibrium Green's function approach (DFT-NEGF) within the generalized gradient approximation (GGA-PBE) as implemented in the Atomistix ToolKit,[12] similarly to a previous publication.[13] A semi-empirical Hubbard energy term was added to the GGA-PBE exchange-correlation potential to correct for self-interaction of localized d-orbitals and yield accurate bandgaps (DFT + U approach). All calculations were performed with a double-zeta-polarized basis set based on a linear combination of atomic orbitals (LCAO). Atomic positions of the CZTS(e) were relaxed keeping the experimental lattice parameters. For CdS, we relaxed the atomic positions until all forces were below 0.02 eV/Å in a cell strained to fit that of CZTS(e) in the directions parallel to the interface. The lattice parameter perpendicular to the interface was relaxed until the stress was below 0.005 eV/Å^3. The choice of (100)/(100) interface orientation can be justified based on transmission electron microscopy results, which consistently show a (100)-oriented

[a)]Electronic mail: ancro@nanotech.dtu.dk
[b)]Electronic mail: mattias.palsgaard@quantumwise.com

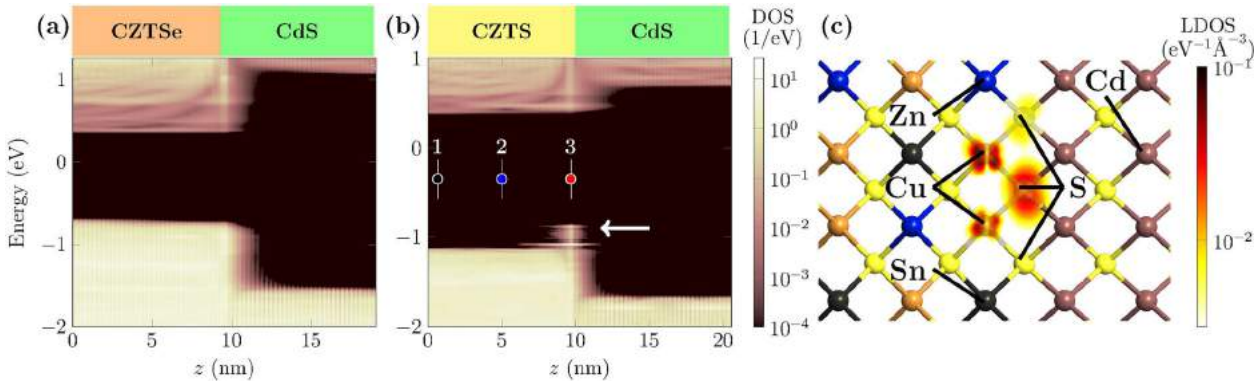

FIG. 1. Local density of states of (a) the CZTSe/CdS interface and (b) the CZTS/CdS interface resolved along the direction perpendicular to the interface plane. (c) Spatially resolved DOS of the localized states at the CZTS/CdS interface. The DOS at a single energy, marked by the arrow in (b), is plotted in the figure.

CZTS/CdS epitaxial interface.[14,15] This also justifies modeling the CZTS/CdS interface as epitaxial in our calculation. For the bulk calculations of CZTS (CdS), we used a $5 \times 5 \times 3$ ($5 \times 5 \times 5$) Monkhorst-Pack **k**-point grid. For the interface calculations (density of states (DOS) calculations), we used 5×3 (21×21) transverse **k**-points. As explained in a previous publication,[13] a forward voltage bias was applied across the supercell to remove residual slopes of the local potential near the electrodes. For an appropriate magnitude of the applied voltage, flat-band conditions are achieved. To justify this approach, we emphasize that: (i) the electrostatic potential drop at the junction (band bending) occurs over a much larger length scale than the supercell length;[4,6,16] thus, to a first order approximation, the bands can be assumed to be flat within the calculated region; (ii) the optimal working point of the solar cell device is indeed close to flat-band conditions (forward bias).

Figs. 1(a) and 1(b) show the calculated density of states (DOS) close to the band edges in the interface region for the two material pairs. The resulting CBOs are +0.2 eV for the CZTS/CdS interface and +0.6 eV for the CZTSe/CdS interface. Besides the differences in band alignment, we note that localized interface states are present at the CZTS/CdS interface but are absent at the CZTSe/CdS interface.

The existence of the localized states results essentially in an extension of the valence band up to 0.2–0.3 eV above the original valence band maximum (VBM) of CZTS (Fig. 2(a)). By repeating the calculation using different computational techniques and modeling assumptions, we have verified that the presence of the localized states (and their absence at the CZTSe/CdS interface) is not an artifact of the calculation. This is shown in the supplementary material. In a separate calculation on a S-terminated CZTS/vacuum interface ("surface calculation"), localized states above the VBM of CZTS were also observed (Figs. S6 and S7, supplementary material). This suggests that the states are due to dangling bonds at the CZTS surface that are not satisfactorily passivated by a CdS buffer layer. In fact, the states are highly localized on Cu sites in the first cationic layer of CZTS and on their neighboring S atoms in the interface anionic layer (Fig. 1(c)). Since the valence band of CZTS originates from Cu and S states,[13,17] this explains why those localized states affect the valence band but not the conduction band. Interestingly, there exists some experimental evidence of the presence of electrically active surface states in CZTS and their absence from CZTSe, as predicted by our calculation. A surface photovoltage measurement by scanning tunneling microscopy[18] revealed that, in CZTSe, the photocurrent scaled linearly with optical excitation intensity, whereas in CZTS, the photocurrent saturated quickly. The authors concluded that this was due to the predominance of surface states in the CZTS response but not in the CZTSe response. In another study, a work function measurement on CZTSSe surfaces with inhomogeneous S/(S + Se) content revealed that the Fermi level position in areas with higher S content did not match the theoretical expectation based on the band edge positions of ideal bulk materials.[19]

The identification of localized states at the CZTS/CdS interface can help explain why state-of-the-art CZTS/CdS solar cells still have a large $\Delta\phi$ even in the case of an optimal band alignment with CdS. To demonstrate this quantitatively, we incorporate the first-principles calculation results into a model for device-level simulation. The simulation of a CZTS/CdS/ZnO solar cell was carried out with the finite element method as implemented in the software SCAPS.[20] Device parameters are listed in Table S1, supplementary material.

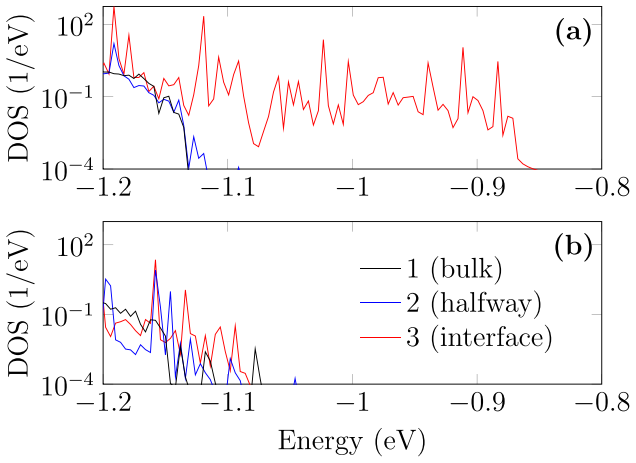

FIG. 2. Local density of states close to the VBM at the three positions indicated in Fig. 1(b) for the case of: (a) the CZTS/CdS interface and (b) the CZTS/ZnS interface.

Besides the inclusion of the localized states, the device model has two important features. The first is the small spike-like band alignment between CZTS and CdS, consistent with state-of-the-art CZTS/CdS solar cells (Fig. S1, supplementary material). The second is the distinction between an optical bandgap of 1.5 eV and a transport bandgap of 1.35 eV. This simulation approach has been suggested before[21] to model the mismatch between the bandgap of the extended states and the bandgap from which bulk recombination occurs (which includes the tail states due to bulk fluctuations in the CZTS band edges). 0.15 eV is a typical depth for the tail states of high-quality CZTS.[6,7]

The interface states are included in the device model as follows. According to the first-principles calculations, the states have a similar DOS to the valence band of bulk CZTS up to 0.2–0.3 eV above the original VBM (Fig. 2(a)) and are only present in an interface region that extends less than 5 nm into CZTS (Fig. 1(b)). Therefore, the interface states are modeled as a 0.2 eV upward shift in the valence band over a 5 nm region at the interface rather than a valence band tail or a single defect level within the gap. This is equivalent to narrowing the interface bandgap on the CZTS side of the junction, which means that the energy barrier for recombination is reduced (by 0.2 eV) at the interface, much like the case of a cliff-like CBO with CdS. The other material parameters of this interface region are kept identical to a baseline CZTS device without interface states that we simulated for comparison.

The near-interface band diagram of the simulated device is shown in Fig. 3(a). In a device with interface states, the interface hole density increases by three orders of magnitude compared to the baseline device, up to a range that is comparable to the electron density (Fig. 3(b)). This is a crucial effect that implies a higher Shockley-Read-Hall interface recombination rate, because the latter increases with increasing electron and hole densities, and is maximized when the two densities equal each other.[22] To verify that this device model is compatible with real CZTS/CdS solar cells, we use our device model to simulate a temperature-dependent open circuit voltage measurement from which ϕ is usually extracted experimentally (Fig. 3(c)). Open circuit voltages are obtained by simulating the current-voltage (JV) curve of the solar cell under AM1.5 illumination at different simulated temperatures (Fig. S9, supplementary material). For the baseline case without interface states, extrapolation of the open circuit voltage to 0 K yields 1.34 V. This matches the value of the bulk transport bandgap (1.35 eV) defined in our model, and it means that such a baseline device is not limited by interface recombination. In the solar cell with interface states, the open circuit voltage extrapolates to 1.11 V, which matches the value of the transport gap minus 0.2 eV narrowing at the interface as defined for the interface region (1.15 eV). The corresponding recombination energy deficit is 0.39 eV, which fits very well the recombination energy deficits of 0.3 eV, 0.4 eV, and 0.4 eV found experimentally in the highest-efficiency CZTS/CdS solar cells.[3–5] As long as the simulated device is dominated by interface recombination, the simulated value of the recombination energy deficit is robust with respect to changes in various device parameters, including defect characteristics.

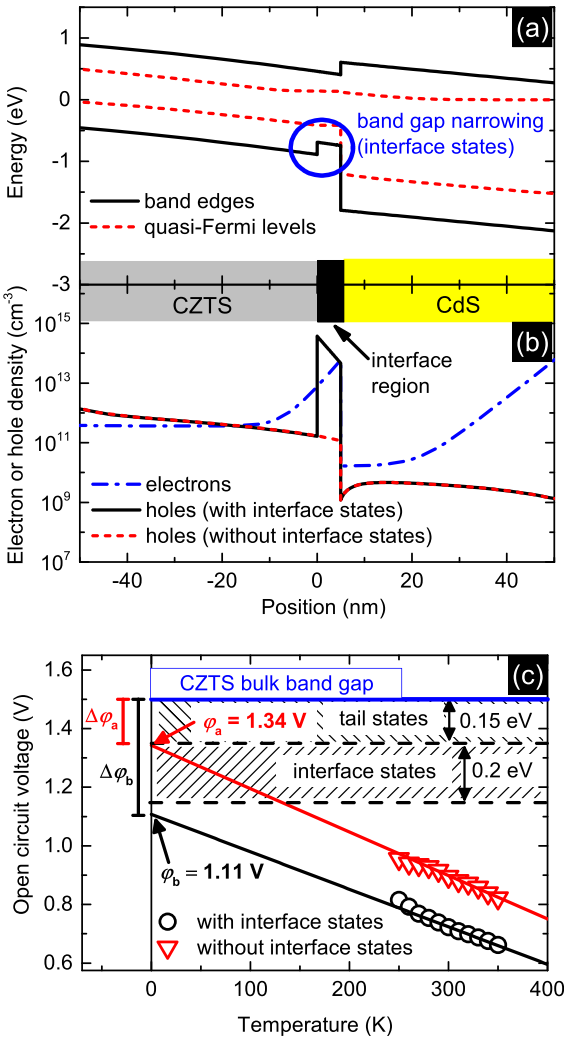

FIG. 3. Simulated properties of the interface region of a CZTS/CdS solar cell under AM1.5 illumination, with the inclusion of localized states at the interface. (a) Band diagram and corresponding quasi-Fermi levels for electrons and holes. (b) Electron and hole density in the same region. The hole density increases significantly when interface states are added, whereas the electron density is the same in both scenarios. (c) Simulated open circuit voltage of CZTS/CdS solar cells as a function of temperature. The linearly extrapolated 0 K intercept of the data yields the activation energy of the dominant recombination path.

Such findings demonstrate that narrowing of the interface bandgap through an upward shift of the CZTS valence band can explain existing temperature-dependent open circuit voltage measurements just as well as a cliff-like CBO does. They also imply that optimal passivation of the interface states can result in a considerable enhancement of the open circuit voltage. This interesting prospect may be practically realized by replacing CdS with an appropriate passivation material. The question is which material would work. Here, we limit our analysis to a (100)/(100) interface with a metal chalcogenide (MX, where M is the metal and X is the chalcogen) with a cubic or tetragonal structure. The interfacial cationic layer of such a material breaks the bulk crystal structure of CZTS by introducing a layer of $2M_{Cu} + M_{Zn} + M_{Sn}$ point defects. Therefore, one strategy could be to search for a metal whose related defect complex does not form states within the bandgap of CZTS. If one chooses M = Zn,

the defect complex reduces to just $2Zn_{Cu} + Zn_{Sn}$. The effect of this particular defect complex on the electronic properties of CZTS has been investigated before.[23] The result was that the $2Zn_{Cu} + Zn_{Sn}$ complex does not narrow the bandgap of CZTS. Therefore, one may expect a Zn chalcogenide material (such as ZnS) to remove the interface states.

To test this hypothesis, we repeated our CZTS interface calculation replacing CdS with ZnS (the computational methods involving ZnS are the same as for CdS). Strikingly, Fig. 2(b) shows that no interface states are present anymore within the resolution of the calculation. This indicates that the ideal situation of a CZTS interface without bandgap narrowing could be achieved by the replacement of CdS by a Zn chalcogenide, with a corresponding shift of the dominant recombination path from the interface to the bulk. Our results provide a clear explanation of why open circuit voltage improvement due to interface modification has so far been achieved experimentally by Zn-based alternative buffers $Zn_{1-x}Sn_xO_x$,[7] (Zn,Cd)S,[16] and another unspecified Zn-based buffer.[24] $Zn_{1-x}Sn_xO_x$ has also been the only material able to reduce $\Delta\phi$ from the typical 0.3–0.4 eV down to 0.16 eV,[7] which corresponds roughly to the depth of CZTS bulk tail states.

To conclude, we have shown that the interface bandgap of CZTS/CdS solar cells is narrowed by localized states that shift the valence band maximum of CZTS to a higher energy. The same effect does not occur at the CZTSe/CdS interface. This phenomenon can explain why interface recombination is always observed to dominate in CZTS solar cells but not in CZTSe solar cells—a fact that has so far been attributed to differences in the conduction band alignment of the two materials with the CdS buffer layer. Zn-based chalcogenides can effectively passivate CZTS surfaces by removing the localized states. This can explain why Zn-based alternative buffer layers have so far outperformed other buffer layer materials, thus giving a clear recipe for future improvement.

See supplementary material for a review of the band alignment between CZTS and CdS; confirmation of the interface bandgap narrowing phenomenon by alternative methods; atomic structures used to calculate electronic properties; spatial density of states of a calculated CZTS/ZnS interface; a table with all parameters used in device simulation; and simulated current-voltage curves.

This work was supported by the Danish Council for Strategic Research, VILLUM Fonden (Grant No. 9455) and the Innovation Fund Denmark (File No. 5016-00102).

[1]A. Polman, M. Knight, E. C. Garnett, B. Ehrler, and W. C. Sinke, Science **352**, aad4424 (2016).
[2]A. Redinger, M. Mousel, M. H. Wolter, N. Valle, and S. Siebentritt, Thin Solid Films **535**, 291 (2013).
[3]K. Wang, O. Gunawan, T. Todorov, B. Shin, S. J. Chey, N. A. Bojarczuk, D. Mitzi, and S. Guha, Appl. Phys. Lett. **97**, 143508 (2010).
[4]S. Tajima, T. Itoh, H. Hazama, K. Ohishi, and R. Asahi, Appl. Phys. Express **8**, 082302 (2015).
[5]T. Ericson, J. J. Scragg, A. Hultqvist, J. T. Watjen, P. Szaniawski, T. Torndahl, and C. Platzer-Björkman, IEEE J. Photovoltaics **4**, 465 (2014).
[6]B. Shin, O. Gunawan, Y. Zhu, N. A. Bojarczuk, S. J. Chey, and S. Guha, Prog. Photovolt. Res. Appl. **21**, 72 (2013).
[7]C. Platzer-Björkman, C. Frisk, J. K. Larsen, T. Ericson, S.-Y. Li, J. J. S. Scragg, J. Keller, F. Larsson, and T. Törndahl, Appl. Phys. Lett. **107**, 243904 (2015).
[8]R. Haight, A. Barkhouse, O. Gunawan, B. Shin, M. Copel, M. Hopstaken, and D. B. Mitzi, Appl. Phys. Lett. **98**, 253502 (2011).
[9]S. Tajima, K. Kataoka, N. Takahashi, Y. Kimoto, T. Fukano, M. Hasegawa, and H. Hazama, Appl. Phys. Lett. **103**, 243906 (2013).
[10]T. Kato, H. Hiroi, N. Sakai, and H. Sugimoto, in *28th European Photovoltaic Solar Energy Conference and Exhibition* (WIP, 2013), pp. 2125–2127.
[11]N. Terada, S. Yoshimoto, K. Chochi, T. Fukuyama, M. Mitsunaga, H. Tampo, H. Shibata, K. Matsubara, S. Niki, N. Sakai, T. Katou, and H. Sugimoto, Thin Solid Films **582**, 166 (2015).
[12]Atomistix ToolKit Version 2015.0 (QuantumWise A/S, 2015).
[13]M. Palsgaard, A. Crovetto, T. Gunst, T. Markussen, O. Hansen, K. Stokbro, and M. Brandbyge, in *2016 International Conference on Simulation of Semiconductor Processes and Devices (SISPAD)* (IEEE, Nuremberg, Germany, 2016), pp. 377–380.
[14]S. Tajima, R. Asahi, D. Isheim, D. N. Seidman, T. Itoh, M. Hasegawa, and K. Ohishi, Appl. Phys. Lett. **105**, 093901 (2014).
[15]F. Liu, C. Yan, J. Huang, K. Sun, F. Zhou, J. A. Stride, M. A. Green, and X. Hao, Adv. Energy Mater. **6**, 1600706 (2016).
[16]K. Sun, C. Yan, F. Liu, J. Huang, F. Zhou, J. A. Stride, M. Green, and X. Hao, Adv. Energy Mater. **6**, 1600046 (2016).
[17]C. Persson, J. Appl. Phys. **107**, 053710 (2010).
[18]H. Du, M. J. Romero, I. Repins, G. Teeter, R. Noufi, and M. M. Al-Jassim, in *2011 37th IEEE Photovoltaic Specialists Conference* (IEEE, 2011), pp. 001983–001986.
[19]M. Salvador, S. M. Vorpahl, H. Xin, W. Williamson, G. Shao, D. U. Karatay, H. W. Hillhouse, and D. S. Ginger, Nano Lett. **14**, 6926 (2014).
[20]M. Burgelman, P. Nollet, and S. Degrave, Thin Solid Films **361–362**, 527 (2000).
[21]C. Frisk, T. Ericson, S. Y. Li, P. Szaniawski, J. Olsson, and C. Platzer-Björkman, Sol. Energy Mater. Sol. Cells **144**, 364 (2016).
[22]C.-T. Sah, R. Noyce, and W. Shockley, Proc. IRE **45**, 1228 (1957).
[23]S. Chen, A. Walsh, X.-G. Gong, and S.-H. Wei, Adv. Mater. **25**, 1522 (2013).
[24]N. Sakai, H. Hiroi, and H. Sugimoto, in *2011 37th IEEE Photovoltaic Specialists Conference* (IEEE, 2011), pp. 003654–003657.

Paper 3

Electron-phonon scattering from Green's function transport combined with molecular dynamics: Applications to mobility predictions

Troels Markussen, *Mattias Palsgaard*, Daniele Stradi, Tue Gunst, Mads Brandbyge, and Kurt Stokbro

Physical Review B **95**, 245210 (2017)

Electron-phonon scattering from Green's function transport combined with molecular dynamics: Applications to mobility predictions

Troels Markussen,[1,*] Mattias Palsgaard,[1,2] Daniele Stradi,[1] Tue Gunst,[2] Mads Brandbyge,[2] and Kurt Stokbro[1]

[1]*QuantumWise A/S, Fruebjergvej 3, Postbox 4, DK-2100 Copenhagen, Denmark*

[2]*Department of Micro- and Nanotechnology (DTU Nanotech), Center for Nanostructured Graphene (CNG), Technical University of Denmark, DK-2800 Kgs. Lyngby, Denmark*

(Received 10 January 2017; published 23 June 2017)

We present a conceptually simple method for treating electron-phonon scattering and phonon limited mobilities. By combining Green's function based transport calculations and molecular dynamics, we obtain a temperature dependent transmission from which we evaluate the mobility. We validate our approach by comparing to mobilities and conductivities obtained by the Boltzmann transport equation for different bulk and one-dimensional systems. For bulk silicon and gold we compare against experimental values. We discuss limitations and advantages of each of the computational approaches.

DOI: 10.1103/PhysRevB.95.245210

I. INTRODUCTION

The continued down-scaling of electronic devices and interconnects calls for accurate simulation models which incorporates the effects of quantum confinement of both electrons and phonons, surface effects, strain, etc. It is increasingly difficult to describe all such effects with continuum models, which are typically parametrized to fit bulk materials. Atomistic models, on the other hand, can describe many of the important effects. Density functional theory (DFT) is particularly important in this respect since it is a first-principles method which doesn't need to be fitted to a particular device, while it is computationally possible to study systems with several thousands of atoms.

Electron-phonon coupling (EPC) plays a central role in the performance of most electronic devices. Several recent studies have studied EPC in bulk materials by calculating the EPC from first principles and using the Boltzmann transport equation (BTE) for evaluating the electron mobility and conductivity [1–8]. Bulk calculations of EPC can, however, be rather demanding as one needs to integrate the coupling over both electron and phonon wave vectors (**k** and **q** space). Moreover, EPC in amorphous materials can only be calculated approximately with the BTE approach.

Atomistic modeling of electronic devices is typically carried out using nonequilibrium Green's function (NEGF) theory in combination with either DFT [9] or tight-binding methods [10,11]. EPC can be rigorously included in NEGF using perturbation theory. However, the resulting equations are numerically very challenging and approximations need to be applied. Approximate methods include lowest order expansions of the inelastic current [12,13] or approximations to the EPC self-energy [10,14].

With few exceptions [15], most of EPC with both the BTE and within NEGF assumes that the phonons can be described within the harmonic approximation, since addition of anharmonic effects significantly increases the computational burden. However, at room temperatures and above there will be anharmonic contributions to the phonons for many materials. Molecular dynamics (MD) simulations, on the other hand, inherently includes anharmonic effects without extra computational requirements.

Previous works have used MD simulations in combination with standard Landauer transmission calculations. This has primarily been done in order to sample different configurations of, e.g., a molecule in contact with two metallic electrodes [16–19], metallic point contacts [20,21], and carbon nanotubes [22]. A single study used MD simulations to actually probe the energy dependent EPC [23]. MD simulations have also been successfully applied in combination with DFT calculations to calculate the temperature dependent band structure of bulk and nanocrystals of silicon [24]. Recently, Liu *et al.* [25] used a very similar approach to successfully obtain mean free paths and resistivities in bulk metals. Along the same lines, Zacharias *et al.* [26] have recently used stochastic displacements of the atoms to calculate the temperature dependent optical absorption in silicon.

In this work, we develop a MD-Landauer approach for calculating the temperature dependent mobility and conductivity. In a device geometry with a central region coupled to two electrodes, we perform MD simulations in a certain part of the central region. When increasing the length of the MD region we obtain a length dependent resistance. From the slope of the linearly increasing resistance vs length curve we obtain the resistivity and eventually the mobility. Further computational details will be provided below.

We apply the method to various systems covering metals and semiconductors as well as one-, two-, and three-dimensional systems. In order to validate our approach we compare the mobilities obtained from the MD-Landauer approach with results obtained from the BTE for the same systems. In general we find that the two approaches give similar results. Our BTE approach has been described in a previous work [8]. Here we further validate the BTE method by comparing the obtained temperature dependent electron mobilities of bulk silicon with experimental values. All calculations have been performed with the Atomistix ToolKit (ATK) [27].

The paper is organized as follows. In Sec. II we first describe general details of our computational methods. The

*troels.markussen@quantumwise.com

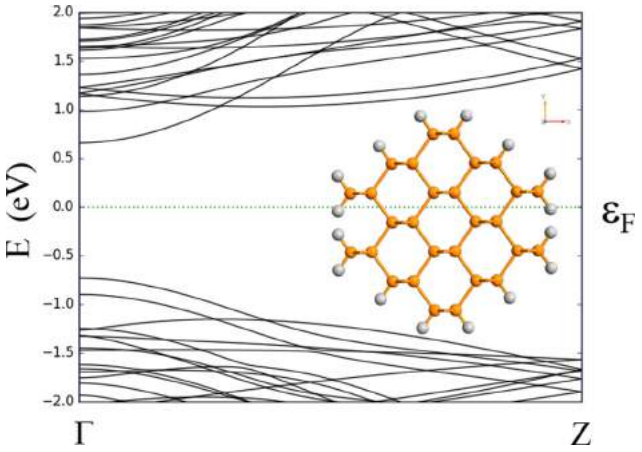

FIG. 1. Electronic band structure of the SiNW. The inset shows a cross sectional view of the SiNW.

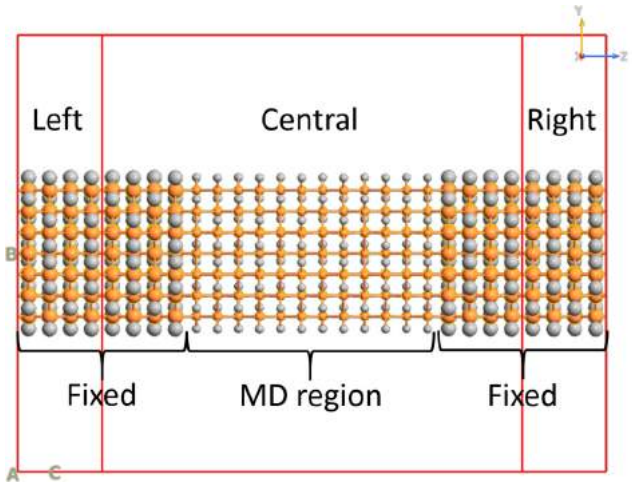

FIG. 2. Device setup for the MD-Landauer approach. A central region is coupled to two semi-infinite electrodes (left and right). Initially the wire is periodic in the z direction. An MD simulation is performed for the atoms in the middle part of the central region (MD region), while the electrodes as well as the first electrode copy on either side of the central region are kept fixed at their equilibrium positions. The fixed atoms are drawn as larger spheres.

MD-Landauer method is detailed in Sec. II A, where we also show results for a silicon nanowire. In Sec. II B we present results for bulk silicon and compare against experimental mobilities, while results for a gold nanowire and bulk gold is presented in Secs. II C and II D. We discuss advantages and weaknesses of the two methods in Sec. III and summarize our findings in Sec. IV.

II. METHODS AND RESULTS

All results presented in this paper are obtained with ATK [27]. The electronic structure, band energies, Hamiltonians, and derivative of Hamiltonians are calculated from density functional theory (DFT) within the local density approximation (LDA) for the exchange-correlation functional [28]. For the gold nanowires, we additionally compare properties obtained by density functional tight binding [29].

Phonon energies and polarization vectors have been calculated from either DFT or from classical force field potentials [30] (details will be provided for each studied system). In the case of MD simulations we only use the classical potentials.

Our implementation of the electron-phonon coupling and BTE has been documented and verified in Ref. [8] for various two-dimensional systems.

A. MD-Landauer approach

In this section we present the details in our MD-Landauer approach for treating electron-phonon scattering. We will illustrate the method by showing calculations for the 1.5 nm [110] silicon nanowire (SiNW). A similar procedure is used for the other systems presented below.

Figure 1 shows the electronic band structure for the SiNW. The conduction band minimum is 0.66 eV above the Fermi energy (at 0.0 eV in the plot). The next conduction band is 0.32 eV higher in energy and for electron transport close to the conduction band minimum (CBM) it is sufficient to include the lowest conduction band.

We now consider a device configuration where a central region is coupled to two semi-infinite electrodes (left and right) as shown in Fig. 2. The atomic positions in the electrodes are kept at their equilibrium positions and so are the first copy of the electrodes inside the central region. In the middle part of the central region, called *MD region* in Fig. 2, the atoms are allowed to move according to a molecular dynamics simulation. For all the calculations presented in this paper, the MD simulations are performed using classical potentials which make the calculations very efficient [30]. For the SiNW and bulk Si MD calculations we apply a Tersoff potential [31]. For both the SiNW and Au nanowires we have compared the results from BTE using phonons calculated with DFT with phonons from classical calculations and found the obtained results qualitatively agree, thus justifying the use of classical potentials. We note that the MD approach does not displace atoms along a single phonon mode at a time. Hereby, the predictability of the MD-Landauer approach does not rely on the accurate description of a single phonon mode but rather the full configuration space including anharmonic effects.

When the MD simulation is equilibrated we take a snapshot of the atomic configuration and calculate the electronic transmission function using DFT. This step first involves a self-consistent DFT-NEGF calculation of the device configuration and subsequently a calculation of the Landauer transmission function using a standard Green's function method:

$$\mathcal{T}(E,\mathbf{x}\{T\}) = \mathrm{Tr}[\mathbf{G}^r(E,\mathbf{x}\{T\})\Gamma_L(E)\mathbf{G}^a(E,\mathbf{x}\{T\})\Gamma_R(E)], \tag{1}$$

where $\mathbf{G}^r = [E\mathbf{S}(\mathbf{x}\{T\}) - \mathbf{H}(\mathbf{x}\{T\}) - \Sigma_L(E) - \Sigma_R(E)]^{-1}$ is the retarded Green's function in the central region described by the Hamiltonian $\mathbf{H}(\mathbf{x}\{T\})$ and overlap $\mathbf{S}(\mathbf{x}\{T\})$ matrices. The Hamiltonian and overlap matrices depend explicitly on the random displacements of the atoms ($\mathbf{x}$), which in turn depend on the temperature used in the MD calculation, as well as on the random initial velocities used in the MD simulations. Due to this randomness, we need to perform

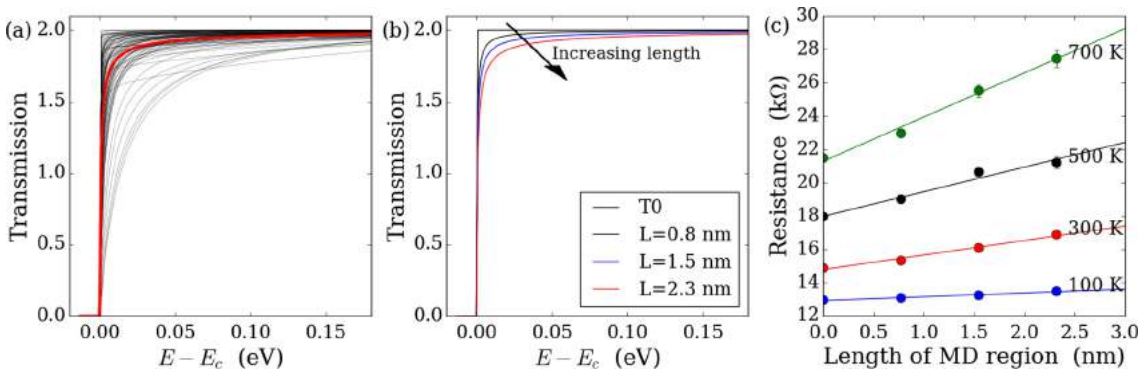

FIG. 3. (a) Transmission functions from different MD simulations (thin black lines) together with the average transmission (thick red). The length of the MD region is 2.3 nm and the temperature is 100 K. The average transmission functions at three different lengths are shown in panel (b). Panel (c) shows the resistance vs length of the MD region for the SiNW at 100 K.

several MD simulations in order to obtain a good sample averaging. The coupling to the semi-infinite left and right electrodes is taken into account through the self-energies $\Sigma_{L,R}(E)$, whose imaginary part gives the coupling matrices $\Gamma_{L,R}(E) = -2\,\mathrm{Im}[\Sigma_L(E)]$. All transmission functions are calculated at zero bias. Figure 3(a) shows the results of 100 individual MD + Landauer transmissions (thin black lines) as well as the average transmission function (thick red). Each MD calculation is started with a Maxwell-Boltzmann distribution of the velocities corresponding to the target temperature. We use a Langevin thermostat [32] with a time step of 1 fs. After an equilibration time of 5 ps we take a snapshot of the configuration and calculate the electronic transmission spectrum with DFT-NEGF. Since the MD calculations are very fast, we simply restart the MD calculations for each sample. Due to the random initial velocities, each MD simulation will result in different configurations after the same equilibration time.

This procedure is repeated at different lengths of the MD region, $\mathcal{L}$, with average transmissions shown in Fig. 3(b). From the average transmission $\langle \mathcal{T}_{\mathcal{L}}(E,T)\rangle$ we obtain the length and temperature dependent conductance from the Landauer formula

$$G(\mathcal{L},T) = \frac{2e^2}{h}\int \langle \mathcal{T}_{\mathcal{L}}(E,T)\rangle \left(-\frac{\partial f(E,\mu,T)}{\partial E}\right) dE, \quad (2)$$

where $f(E,\mu,T) = (e^{(E-\mu)/k_BT}+1)^{-1}$ is the Fermi-Dirac distribution function at chemical potential μ. We allow ourself to freely adjust the chemical potential without explicitly taking doping effects into account. Notice that the average transmission $\langle \mathcal{T}_{\mathcal{L}}(E,T)\rangle$ only depends on the energy and temperature, when averaged properly. The remaining effect of randomness is represented by error bars in the plots of resistance and mobility presented below.

Figure 3(c) shows the resistance $R(\mathcal{L},T) = 1/G(\mathcal{L},T)$ vs length of the MD region. The points show the average resistance, and the error bars show the standard deviations of the average resistance. We observe that the resistance increases linearly with length showing that the resistance is ohmic. The linear fit to the averaged data is written as

$$R(\mathcal{L},T) = R_c + \rho_{1D}(T)\mathcal{L}, \quad (3)$$

thus defining a one-dimensional resistivity, $\rho_{1D}(T)$, which depends on temperature, but not on wire length. R_c is the length independent contact resistance. Note that the one-dimensional resistivity has units of Ω/m, whereas a usual bulk resistivity is measured in units of Ω m. In order to convert the one-dimensional conductivity to a bulk quantity we must multiply with the wire cross sectional area A, i.e., $\rho_{\mathrm{bulk}} = \rho_{1D}\cdot A$. When performing the sample averaging, the resistance increases linearly all the way down to zero length of the MD region, and the resistivity is rather insensitive to the exact range. In particular, for one-dimensional systems, one should be aware that a too long MD region could lead to electron localization with an exponentially increasing resistance [33]. For all the systems studied here, we have checked that the length of the MD region is shorter than the localization length. By rewriting Eq. (3) as [33]

$$R(\mathcal{L},T) = R_c(1+\mathcal{L}/\lambda), \quad (4)$$

we obtain a measure of the mean free path, $\lambda = R_c/\rho_{1D}$. Since the localization length is always longer than λ we can assure that the studied systems are not in the localization regime. The room temperature mean free path for the SiNW obtained from Fig. 3(c) is $\lambda = 17$ nm.

In order to calculate the mobility we need to determine the carrier density. From a separate calculation of the density of states, $D(E)$, of the bulk wire (evaluated at the equilibrium atomic structure) we calculate the carrier density per unit area

$$\tilde{n} = \frac{n}{A} = \int_{E_g}^{\infty} f(E,E_F,T)D(E)dE, \quad (5)$$

where we use the middle of the band gap, E_g, as the lower integration limit in the case of electron mobilities. In the case of holes, we should integrate from $-\infty$ to E_g and replace $f \to 1-f$. We finally calculate the mobility as

$$\mu = \frac{1}{q\,n\,\rho_{\mathrm{bulk}}} = \frac{1}{q\,\tilde{n}\,\rho_{1D}}. \quad (6)$$

Notice that the final expression for the mobility does not depend on the wire cross sectional area.

The resulting mobilities obtained with the MD-Landauer method are shown in Fig. 4 together with results obtained from the BTE. In the same figure we also show electron mobilities

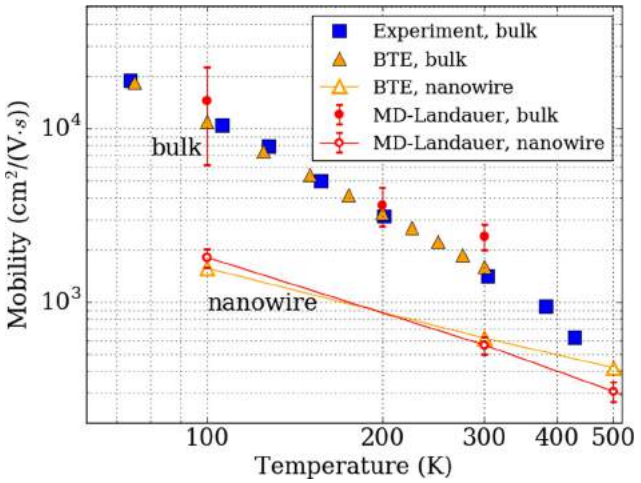

FIG. 4. Phonon limited mobility vs temperature for the SiNW (open markers with lines) and bulk silicon (filled markers) calculated with BTE and with the MD-Landauer approach. The error bars for the MD-Landauer results indicate the standard deviations on the calculated mobilities. Experimental values for bulk silicon [34] are shown for comparison (blue dots).

for bulk silicon obtained from BTE and MD-Landauer together with experimental values.

For the BTE calculations electrons are calculated using DFT with local density approximation (LDA) exchange-correlation functional and double-ζ-polarized (DZP) basis set. Hamiltonian derivatives are calculated using supercells repeated 11 times along the [110] direction. The phonons are calculated using classical potentials. When calculating the EPC we include only the lowest conduction band and use 150 k points in the range $[0,0.05]\pi/a$, with a being the unit cell length of the nanowire. All phonons are included and we use 100 q points in the range $[-0.2,0.2]\pi/a$. When calculating the mobility an energy broadening of 3 meV is used for the approximate δ function in the Fermi's golden rule expression of the phonon mediated transition rate between states.

For the bulk silicon calculations, we evaluate the mobility at a doping level of 1×10^{18} cm^{-3}. However, since we do not explicitly include the dopant atoms in the calculations, the calculated mobility is essentially independent of doping level. We first notice that the two computational methods give almost the same temperature dependent mobility. Second, we observe that the mobility of the SiNW is almost an order of magnitude smaller than the bulk values. More details about the bulk silicon calculations are presented below. The reduction of the mobility in nanowires is in good agreement with previous theoretical studies based on tight-binding models [35].

The reduced mobility in the nanowire can be traced back to the increased EPC in nanowires due to (i) reduced complexity in fulfilling the selection rules for energy and momentum matching due to band folding and (ii) localization and mixing of corresponding bulk phonon modes. Scattering from surface modes is found to be insignificant. The origin of the scattering is directly available from the BTE through the scattering rate with individual phonon modes (not shown). However, in the MD-Landauer approach part of this information is lost. On the other hand, it does not require one to store the scattering rate for all k, q, and phonon mode indices. Being more memory efficient the MD-Landauer approach may therefore be more appealing as a design tool for complex systems with many degrees of freedom and for bulk systems that can be very memory demanding due to the large number of k, q, and phonon mode combinations needed.

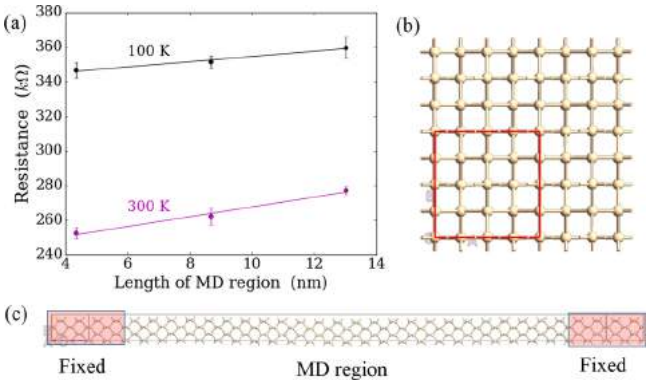

FIG. 5. (a) Length dependent resistance of bulk silicon at temperatures 100 K and 300 K. Panel (b) shows the cross section of the calculation cell (red box) while the device configuration is shown in (c). The length of the MD region is 13 nm.

B. Bulk silicon

We next consider the phonon limited electron mobility in bulk silicon.

We performed MD-Landauer calculation for bulk silicon at temperatures 100 K, 200 K, and 300 K. The bulk silicon MD-Landauer calculations were performed on a 2×2 supercell with the transport in the [100] direction, as shown in Figs. 5(b) and 5(c), with the length of the MD region varying from 4 to 13 nm. We performed 20 different MD simulations in order to get averaged transmissions. The effective doping is 1×10^{18} cm^{-3} as for the SiNW. The bulk silicon device has periodic boundary conditions in the x and y directions. For the self-consistent calculations we use an 11×11 transverse k-point sampling, while the transmission spectra were averaged with a 21×21 transverse k-point sampling. Figure 5(a) shows average resistances vs length of MD region for temperatures 100 K (top curve) and 300 K (bottom curve). From the slope of the linear fits, we obtain the mobility as explained above. The error bars indicate the standard deviations on the average resistances. The room temperature mean free path is $\lambda = 76$ nm.

For the BTE calculations, both phonons and electrons are calculated using DFT. The dynamical matrix and Hamiltonian derivatives are calculated from supercells constructed as a (7,7,7) repetition of the primitive silicon unit cell (686 atoms). For the electron-phonon and mobility calculations we only consider a single conduction band valley and sample the electronic Brillouin zone (BZ) in a local region around that valley with a sampling corresponding to a $99 \times 99 \times 99$ Monkhorst-Pack mesh. The phonon BZ is sampled with a $25 \times 25 \times 25$ mesh in a region around the Γ point for intravalley scattering, with $|q| < 0.075\pi/a$ with a being the silicon lattice constant. A similar, but shifted sampling is used

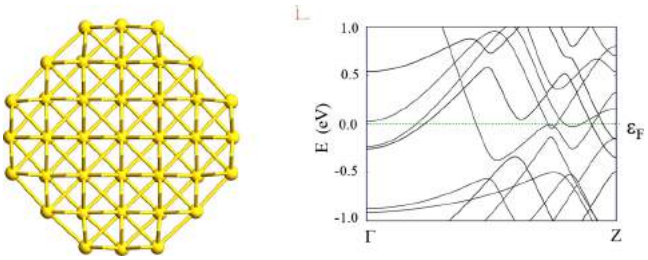

FIG. 6. Cross section of the Au NW (left) and electronic band structure (right). The diameter of the wire is approximately 1 nm.

for intervalley scattering. All six phonon modes are included in the calculation.

In Fig. 4 we show the calculated electron mobility vs temperature together with experimental data [34]. It is evident that the BTE calculations reproduce the experimental data very well over the whole temperature interval. In addition to the BTE and experimental results, we also show the MD-Landauer results at temperatures 100 K, 200 K, and 300 K. It is encouraging that the MD-Landauer method gives mobility values in close agreement with the BTE and experimental results.

C. Au nanowire

We now continue to study metallic systems. The first system we consider is a thin gold nanowire with a diameter of 1.3 nm. A cross sectional view is shown in Fig. 6 (left) together with the electronic band structure calculated with a single-ζ-polarized basis set.

For the gold NW we have in addition to DFT performed calculations with a density functional tight binding (DFTB) description of the electrons [29]. For the BTE we have used phonons calculated from either DFT or from the embedded atom model (EAM) [36]. The MD simulations are only performed with EAM. In Table I we compare the nanowire resistivities obtained with the various methods (BTE or MD-Landauer) and how the parameters are calculated. The top row shows results from BTE with both electrons and phonons obtained with DFT. The following rows show results where the phonons are described with EAM and the electrons either with DFT or DFTB. There is an overall good agreement between the two methods and the different parameters. It is computationally much more expensive to calculate the phonons from DFT than with the classical EAM. It is thus encouraging to see that the phonons seem to be accurately enough described with the

TABLE I. Resistivities of the Au nanowire at 300 K calculated in different ways. For reference, the experimental resistivity of bulk gold is 2.44×10^{-8} Ω m at room temperature.

Method	Parameters	ρ ($\times 10^{-8}$ Ω m)
BTE	(DFT)	5.6
BTE	(EAM+DFT)	4.6
BTE	(EAM+DFTB)	3.8
MD-Landauer	(EAM+DFT)	7.1
MD-Landauer	(EAM+DFTB)	7.5

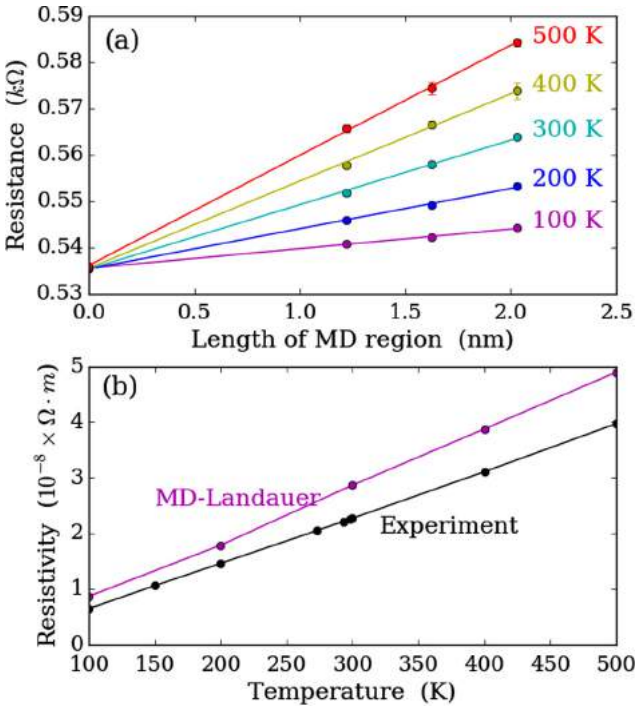

FIG. 7. Length dependent resistance at different temperatures (a) and temperature dependent resistivity (b). The resistivity is calculated for bulk Au with the MD-Landauer method. All results in this figure are obtained with EAM for the phonons/MD and DFTB for the electronic parts. The black points show experimental results [38].

EAM. This is true even though the EAM phonon energies are up to 30% lower in energy than the DFT phonon energies.

In accordance with the silicon results, we find that the BTE and MD-Landauer methods give similar results for the resistivity, within a factor of two difference.

D. Au bulk

We now continue to study bulk gold in order to illustrate that our MD-Landauer approach also can be applied to bulk metallic systems, which were also studied in Ref. [25] with a similar approach. For bulk calculations we set up a device with a cross section of 0.82×0.82 nm^2 corresponding to a 5×5 repetition of the Au unit cell, when the transport is along the [001] direction. We have verified that using 3×3 and 4×4 repetitions gives essentially the same results. When calculating the transmission through the bulk system, we average over 6×6 transverse **k** points. The MD simulations are performed with the EAM and the electronic structure and transmission function is calculated with DFTB. We have verified for a single temperature (300 K) that calculating the electronic properties with DFT gives essentially the same resistivity.

Figure 7(a) shows the resistance vs length of MD region for increasing temperatures. At all temperatures the resistance increases linearly with length and the resistivity is thus well defined. The room temperature mean free path is $\lambda =$ 38 nm, in close agreement to recently estimated values [37]. Panel (b) shows the calculated temperature dependent resistivity of bulk gold together with experimental values [38]. The

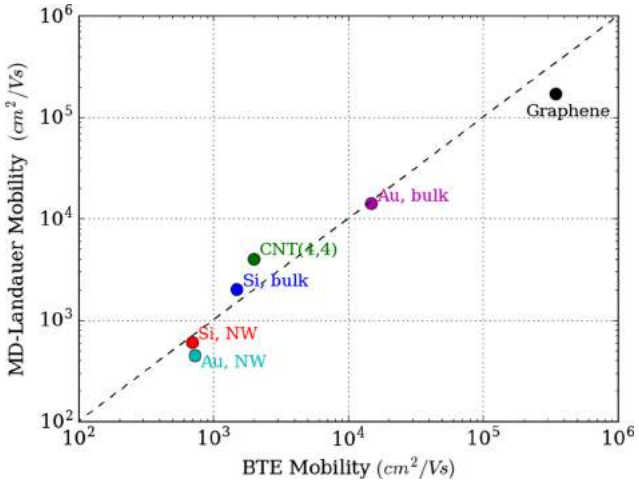

FIG. 8. Comparison of room temperature (300 K) mobilities calculated with BTE and with the MD-Landauer approach.

MD-Landauer method gives bulk gold resistivities which are in very good agreement with the experimental results with about 30% difference.

III. DISCUSSION

From the results presented above it is evident that the BTE and the MD-Landauer method provide similar estimates for the phonon limited mobility in a variety of materials. To further illustrate this, we compare in Fig. 8 room temperature mobilities for a number of systems [graphene, (4,4)-CNT, bulk silicon, silicon nanowire, bulk gold, and a gold nanowire]. Some of the calculations have been detailed above, while the others are obtained in similar ways. All the calculations have been performed with DFT describing the electron transmission function. The figure illustrates that although the two calculation methods show deviations on a quantitative level within a factor of 2–3, they generally predict the same mobility trends over more than two orders of magnitude. Both methods have their advantages and limitations. We will now discuss and compare various aspects of the two methods as they are implemented in ATK.

The BTE is the most rigorous and theoretically well founded of the two methods, but it relies on several assumptions. (i) It is clearly an assumption that the Boltzmann transport equation is an adequate description. This implies that any quantum interference effects are neglected, and any renormalization of the electronic band energies or eigenstates are not included. The effect of lowering the band gap in semiconductors at increasing temperatures is thus not included in the BTE approach, while the band gap reduction is included in the MD-Landauer method [24]. (ii) It is further assumed that the EPC can be described with first order perturbation theory through Fermi's golden rule. All scattering processes include a single phonon. Also, the construction of the perturbed Hamiltonian assumes that the screening is linear such that a change in Hamiltonian from a sum of single atom displacements is the same as the change in Hamiltonian from the summed displacements. This has known limitations for, e.g., polar materials where the long-wavelength Fröhlich interaction is not correctly included [39]. Note that this is not a limitation in the BTE approach, but rather the way we calculate the electron-phonon coupling from finite displacements of individual atoms. (iii) The phonons are assumed to be described within the harmonic approximation. This means that anharmonic phonon-phonon couplings are not included. With these assumptions the BTE rigorously describes the scattering processes taking correctly into account the finite energy difference from initial to final electron states under absorption or emission of a phonon. The phonon occupation is also correctly described by a Bose-Einstein distribution.

The MD-Landauer method is not as well theoretically founded as the BTE. However, from the Born-Oppenheimer approximation we can argue that the electronic motion is much faster than the nuclear ones. If we are considering a finite and short MD region, an incoming electron passing through the MD region essentially experiences a fixed potential landscape setup by the atoms in their instantaneous positions. A similar potential landscape giving similar resistivities can be obtained from a system with randomly displaced atomic positions [40]. However, this requires a calibration of the amplitude of the random displacements for a given temperature, while the MD simulations inherently include this information and further provide a more physical description of the atomic displacements. Nevertheless, the MD-Landauer method does not correctly include finite energy transfer between the electronic and phonon systems, and assisted processes, where, e.g., an electron absorbs a phonon to reach a higher lying final state, are not included. We note that a similar neglect of energy transfer has been used for simulation of inelastic tunneling spectroscopy of vibrations in molecular junctions [41,42] and in the simulation of temperature dependent optical absorption [26]. An advantage with the MD-Landauer approach is that it is not limited to first order perturbation theory. Given the perturbation in the Hamiltonian that is caused by the displaced atoms, the Green's function is solved exactly. Also, contrary to the way we calculate the EPC for the BTE approach, the MD-Landauer method does not assume the linear screening discussed above, and long wavelength Fröhlich scattering will thus be included, provided the length of the MD region is long enough. The MD simulations naturally include anharmonic effects, which might be important at temperatures above the Debye temperature for the respective material. In the low temperature limit, the MD simulations will on the other hand not be correct since the phonon modes are occupied according to a Boltzmann distribution rather than the Bose-Einstein distribution implying that zero-point motions are not included.

In terms of applications, the two approaches also have different advantages and shortcomings. For bulk materials the BTE requires that both $\mathbf{k}$ and $\mathbf{q}$ are sampled on fine grids, resulting in a six-dimensional sampling, which is demanding computationally as well as memorywise. In the MD-Landauer approach one should only converge the transverse $\mathbf{k}$-point sampling for the transmission calculation in bulk systems. In addition to this, the cross sectional size of the unit cell must be converged. One also needs to converge the sample averaging over different MD snapshots.

A clear advantage of the BTE approach is that it is relatively easy to obtain mobilities at many different temperatures. For

the BTE calculations, the most time-consuming part is the calculations of the electron-phonon coupling matrix elements, which are temperature independent. The subsequent mobility calculations for different temperatures are computationally relatively inexpensive. For the MD-Landauer method, all calculations need to be redone for every temperature.

For device calculations, inclusion of EPC leads to a very substantial complication of the calculations, when treated with NEGF [10,12,14]. The MD-Landauer method could, on the other hand, be included in device calculations without significant extra computational load. This potential application of the MD-Landauer approach will be pursued in future works.

Finally, the MD-Landauer approach is also applicable for studying EPC in amorphous systems, for which the BTE cannot be used since the electronic band structure is not well defined. Inclusion of other scattering mechanisms such as defect scattering or grain-boundary scattering is likewise relatively easy to include in the MD-Landauer approach.

IV. CONCLUSION

We have introduced a conceptually simple approach based on molecular dynamics (MD) and the Landauer transmission for calculating phonon-limited mobilities and resistivities. The results obtained with the MD-Landauer method are compared with values obtained from the Boltzmann transport equation (BTE). For several one-dimensional as well as bulk systems the results from the two methods are in good agreement with each other as well as with available experimental results. Our first-principles calculations further support the conclusion of enhanced electron-phonon coupling in nanowires previously indicated by tight-binding simulations. Advantages and shortcomings of the two methods were discussed. The MD-Landauer approach is a memory-efficient and computationally appealing alternative with a predictive power at the level of state-of-the-art BTE solvers for studying EPC in bulk and nanoscale systems.

ACKNOWLEDGMENTS

The authors acknowledges support from Innovation Fund Denmark, grant Nano-Scale Design Tools for the Semiconductor Industry (79-2013-1) and from the European Commissions Seventh Framework Programme (FP7/20072013), Grant Agreement IIIV-MOS Project No. 619326. The Center for Nanostructured Graphene (CNG) is sponsored by the Danish Research Foundation, Project No. DNRF103.

[1] E. H. Hwang and S. D. Sarma, Phys. Rev. B **77**, 115449 (2008).
[2] J. H. Chen, C. Jang, M. Ishigami, S. Xiao, W. G. Cullen, E. D. Williams, and M. S. Fuhrer, Solid State Commun. **149**, 1080 (2009).
[3] K. Kaasbjerg, K. S. Thygesen, and K. W. Jacobsen, Phys. Rev. B **85**, 165440 (2012).
[4] K. M. Borysenko, J. T. Mullen, E. A. Barry, S. Paul, Y. G. Semenov, J. M. Zavada, M. B. Nardelli, and K. W. Kim, Phys. Rev. B **81**, 121412 (2010).
[5] O. D. Restrepo, K. E. Krymowski, J. Goldberger, and W. Windl, New J. Phys. **16**, 105009 (2014).
[6] C.-H. Park, N. Bonini, T. Sohier, G. Samsonidze, B. Kozinsky, M. Calandra, F. Mauri, and N. Marzari, Nano Lett. **14**, 1113 (2014).
[7] J.-A. Yan, W. Y. Ruan, and M. Y. Chou, Phys. Rev. B **79**, 115443 (2009).
[8] T. Gunst, T. Markussen, K. Stokbro, and M. Brandbyge, Phys. Rev. B **93**, 035414 (2016).
[9] M. Brandbyge, J.-L. Mozos, P. Ordejón, J. Taylor, and K. Stokbro, Phys. Rev. B **65**, 165401 (2002).
[10] M. Luisier and G. Klimeck, Phys. Rev. B **80**, 155430 (2009).
[11] K. Stokbro, D. E. Petersen, S. Smidstrup, A. Blom, M. Ipsen, and K. Kaasbjerg, Phys. Rev. B **82**, 075420 (2010).
[12] T. Frederiksen, M. Paulsson, M. Brandbyge, and A.-P. Jauho, Phys. Rev. B **75**, 205413 (2007).
[13] J.-T. Lü, R. B. Christensen, G. Foti, T. Frederiksen, T. Gunst, and M. Brandbyge, Phys. Rev. B **89**, 081405 (2014).
[14] R. Rhyner and M. Luisier, Phys. Rev. B **89**, 235311 (2014).
[15] R. Rhyner and M. Luisier, Appl. Phys. Lett. **105**, 062113 (2014).
[16] J. Li, G. Speyer, and O. F. Sankey, Phys. Rev. Lett. **93**, 248302 (2004).
[17] D. Q. Andrews, R. P. Van Duyne, and M. A. Ratner, Nano Lett. **8**, 1120 (2008).
[18] M. Paulsson, C. Krag, T. Frederiksen, and M. Brandbyge, Nano Lett. **9**, 117 (2008).
[19] G. C. Solomon, D. Q. Andrews, R. H. Goldsmith, T. Hansen, M. R. Wasielewski, R. P. Van Duyne, and M. A. Ratner, J. Am. Chem. Soc. **130**, 17301 (2008).
[20] M. Brandbyge, M. R. Sørensen, and K. W. Jacobsen, Phys. Rev. B **56**, 14956 (1997).
[21] M. Dreher, F. Pauly, J. Heurich, J. C. Cuevas, E. Scheer, and P. Nielaba, Phys. Rev. B **72**, 075435 (2005).
[22] A. Pecchia, M. Gheorghe, A. D. Carlo, and P. Lugli, Synth. Met. **138**, 89 (2003).
[23] A. Pecchia, M. Gheorghe, A. D. Carlo, P. Lugli, T. A. Niehaus, T. Frauenheim, and R. Scholz, Phys. Rev. B **68**, 235321 (2003).
[24] A. Franceschetti, Phys. Rev. B **76**, 161301 (2007).
[25] Y. Liu, Z. Yuan, R. J. H. Wesselink, A. A. Starikov, M. van Schilfgaarde, and P. J. Kelly, Phys. Rev. B **91**, 220405 (2015).
[26] M. Zacharias, C. E. Patrick, and F. Giustino, Phys. Rev. Lett. **115**, 177401 (2015).
[27] Atomistix ToolKit, version 2016, QuantumWise A/S.
[28] J. P. Perdew and A. Zunger, Phys. Rev. B **23**, 5048 (1981).
[29] V. M. P. Koskinen, Comput. Mater. Sci. **47**, 237 (2009).
[30] J. Schneider, J. Hamaekers, S. T. Chill, S. Smidstrup, J. Bulin, R. Thesen, A. Blom, and K. Stokbro, arXiv:1701.02495v1.
[31] P. Erhart and K. Albe, Phys. Rev. B **71**, 035211 (2005).
[32] N. Goga, A. J. Rzepiela, A. H. de Vries, S. J. Marrink, and H. J. C. Berendsen, J. Chem. Theory Comput. **8**, 3637 (2012).
[33] T. Markussen, R. Rurali, A.-P. Jauho, and M. Brandbyge, Phys. Rev. Lett. **99**, 076803 (2007).
[34] C. Canali, C. Jacoboni, F. Nava, G. Ottaviani, and A. Alberigi-Quaranta, Phys. Rev. B **12**, 2265 (1975).
[35] W. Zhang, C. Delerue, Y.-M. Niquet, G. Allan, and E. Wang, Phys. Rev. B **82**, 115319 (2010).

[36] H. W. Sheng, M. J. Kramer, A. Cadien, T. Fujita, and M. W. Chen, Phys. Rev. B **83**, 134118 (2011).
[37] D. Gall, J. Appl. Phys. **119**, 085101 (2016).
[38] D. R. Lide, *Handbook of Chemistry and Physics*, 75th ed. (CRC Press, New York, 1997).
[39] J.-J. Zhou and M. Bernardi, Phys. Rev. B **94**, 201201 (2016).
[40] We have performed calculations on bulk Au with randomly displaced atoms. The magnitude R of the displacement is calibrated for a given temperature from the formula $E(R) - E(0) = \frac{3N}{2} k_B T$, where $E(R)$ is the total energy of the system with each atom displaced by a random amount $r \in [-R/2, R/2]$ in each Cartesian direction. $E(0)$ is the total energy of the equilibrium structure and N is the number of atoms. In doing so, the calculated room temperature resistivity is about 30% lower than the one calculated with the MD displaced atoms.
[41] A. Troisi and M. A. Ratner, J. Chem. Phys. **125**, 214709 (2006).
[42] A. Troisi and M. A. Ratner, Nano Lett. **6**, 1784 (2006).

Paper 4

First-principles electron transport with phonon coupling: Large scale at low cost

Tue Gunst, Troels Markussen, *Mattias Palsgaard*, Kurt Stokbro, and Mads Brandbyge

Physical Review B **96**, 161404(R) (2017)

PHYSICAL REVIEW B **96**, 161404(R) (2017)

First-principles electron transport with phonon coupling: Large scale at low cost

Tue Gunst,[1,*] Troels Markussen,[2] Mattias L. N. Palsgaard,[2] Kurt Stokbro,[2] and Mads Brandbyge[1]

[1]*Department of Micro- and Nanotechnology (DTU Nanotech), Center for Nanostructured Graphene (CNG), Technical University of Denmark, DK-2800 Kgs. Lyngby, Denmark*

[2]*QuantumWise A/S, Fruebjergvej 3, Postbox 4, DK-2100 Copenhagen, Denmark*

(Received 28 June 2017; published 11 October 2017)

Phonon-assisted tunneling plays a crucial role for electronic device performance and even more so with future size down-scaling. We show how one can include this effect in large-scale first-principles calculations using a single "special thermal displacement" (STD) of the atomic coordinates at almost the same cost as elastic transport calculations, by extending the recent method of Zacharias *et al.* [Phys. Rev. B **94**, 075125 (2016)] to the important case of Landauer conductance. We apply the method to ultrascaled silicon devices and demonstrate the importance of phonon-assisted band-to-band and source-to-drain tunneling. In a diode the phonons lead to a rectification ratio suppression in good agreement with experiments, while in an ultrathin body transistor the phonons increase off currents by four orders of magnitude, and the subthreshold swing by a factor of 4, in agreement with perturbation theory.

DOI: 10.1103/PhysRevB.96.161404

Introduction. Electron-phonon inelastic scattering is one of the major challenges for emerging high-performance ultrascaled devices, from the viewpoint of both experiments and device simulations [1]. Semiclassical device simulations fail to describe quantum tunneling, while atomistic quantum simulations often are too time-consuming to treat phonon scattering accurately. Reducing the computational cost of inelastic, compared to elastic, device simulations has therefore been an important and unsolved challenge for decades since the first ultrascaled transistors emerged. In the extreme limit of molecular-scale devices there are accurate first-principles methods for inelastic processes available [2–13], while in the opposite bulk continuum limit, deformation potentials (DPs) are extracted for Boltzmann transport equations (BTEs) that accurately describe low bias transport [14–17]. However, in between these two regimes efficient computational methods are missing. One approach is to apply the continuum DP, despite the fact that electron-phonon coupling (EPC) is known to change significantly in nanostructured devices [18–20] and in an electrostatic environment [21]. Alternatively, it is possible to perform atomistic tight-binding calculations with coarse diagonal self-energy approximations at an extensive computational cost [22,23]. Modern computers are unable to include EPC from first-principles beyond the molecular scale, while the understanding and design of emerging ultrascaled devices calls for atomistic simulations with an accurate description of EPC for thousands of atoms including quantum confinement, strain, and surface effects.

Stochastic sampling of lattice fluctuations, through molecular dynamics [24–30] (MD) and Monte Carlo [31–33], has previously been used to estimate the variation of the Landauer conductance or dielectric function with temperature. Key motivations in these developments are the conceptual simplicity and computer memory efficiency compared to perturbation theory (PT). The MD is able to capture anharmonic effects, but is limited to the classical high-temperature regime for systems with light atoms, neglecting zero-point motion and low-temperature freeze-out of phonons [31–34]. However, the computational cost of sampling all atomic displacements in the configuration space introduces yet a system-size-scaling cost which remains an obstacle in all these methods.

Recently, Zacharias and Giustino [35] showed that the stochastic sampling of configurations can be replaced by a *single* optimal supercell configuration for band gap renormalization and phonon-assisted optical absorption. Inspired by the work of Zacharias and Giustino, we present in this Rapid Communication a "special thermal displacement" (STD) method based on nonequilibrium Green's functions (NEGFs). The STD method is able to deterministically handle EPC in systems with thousands of atoms with a computational burden equivalent to that of elastic transport. This extends the capability of computer simulations to handle nanometer-scaled devices. The method applies to systems with a high degree of repetition of the same basic unit cell since it relies on cancellations of errors between degenerate phonon modes. Often good force fields exist in such systems, while the electron-phonon coupling is less well described. We therefore combine phonons obtained by a force field with the EPC evaluated from density functional theory (DFT). We target systems which have a bulklike representation of vibrations (nonlocalized), which is the case for a large selection of technologically important devices. As key examples, we study the properties of bulk silicon, the performance of silicon-based rectifiers, and double-gated metal-oxide-semiconductor field-effect transistors (MOSFETs). We demonstrate how EPC can be studied by first-principles calculations for systems with thousands of atoms using modest computer resources, while yielding results consistent with PT for smaller systems. This makes the STD method a promising nanoscale design tool for predicting trends in realistic nanodevices under working conditions.

Finite temperature phonon-assisted tunneling. The starting point is to consider the adiabatic limit of slowly moving atoms where we consider the parametric dependence of the

*tue.gunst@nanotech.dtu.dk

retarded device Green's function, $\mathbf{G}^r(E,\{\mathbf{u}_\lambda\})$, on the nuclear displacements, $\mathbf{u}_\lambda(T,V)$. The thermally averaged current is given by [36]

$$I(V,T) = \frac{2e}{h}\int dE\langle\mathcal{T}(E,T)\rangle[f_L - f_R],$$
$$\langle\mathcal{T}(E,T)\rangle = \Pi_\lambda \int du_\lambda \frac{\exp\left(-u_\lambda^2/2\sigma_\lambda^2\right)}{\sqrt{2\pi}\sigma_\lambda}\mathcal{T}(E,\{\mathbf{u}_\lambda\}), \tag{1}$$

where $\mathcal{T}(E,\{\mathbf{u}_\lambda\}) = \mathrm{Tr}[\Gamma_L\mathbf{G}^r(\{\mathbf{u}_\lambda\})\Gamma_R\mathbf{G}^a(\{\mathbf{u}_\lambda\})]$, Γ_α are the electrode coupling matrices, and f_α the Fermi function at the chemical potential of lead α. The phonon modes are labeled by λ with frequency ω_λ, eigenmode vector $\mathbf{e}_\lambda$, and characteristic length, l_λ. The Gaussian width σ is related to the mean-square displacement $\langle\mathbf{u}_\lambda^2\rangle = l_\lambda^2[2n_B(T)+1] = \sigma_\lambda^2(T)$ at a temperature T. In principle these integrals can be computed directly for small systems by Gaussian quadratures or by Monte Carlo importance sampling to obtain the average over the ensemble of possible atomic positions. However, a single STD, $\mathbf{u}_{\mathrm{STD}}$, is sufficient for large systems with a high repetition of smaller unit cells, defined as

$$\mathbf{u}_{\mathrm{STD}}(T) = \sum_\lambda s_\lambda(-1)^{\lambda-1}\sigma_\lambda(T)\mathbf{e}_\lambda. \tag{2}$$

Here s_λ denotes the sign of the first nonzero element in $\mathbf{e}_\lambda$ enforcing the same choice of "gauge" for the modes. Our equations are in a form similar to the dielectric function of bulk systems considered by Zacharias and Giustino [35,37]. For completeness we repeat the argument [35] stating that the STD configuration gives the correct thermal average for large systems by comparing the Taylor expansion of Eq. (1) around the equilibrium configuration evaluated at the mode displacements,

$$\mathcal{T}(E,\{\mathbf{u}_\lambda\}) = \mathcal{T}_0(E) + \sum_\lambda \frac{\partial\mathcal{T}(E,\{\mathbf{u}_\lambda\})}{\partial\mathbf{u}_\lambda}\mathbf{u}_\lambda + \frac{1}{2}\sum_\lambda \frac{\partial^2\mathcal{T}(E,\{\mathbf{u}_\lambda\})}{\partial\mathbf{u}_\lambda^2}\mathbf{u}_\lambda^2 + \mathcal{O}(\sigma^3),$$
$$\langle\mathcal{T}(E,T)\rangle = \mathcal{T}_0(E) + \frac{1}{2}\sum_\lambda \sigma_\lambda^2(T)\frac{\partial^2\mathcal{T}(E,\{\mathbf{u}_\lambda\})}{\partial\mathbf{u}_\lambda^2} + \mathcal{O}(\sigma^4) \tag{3}$$

to the Taylor expansion around the STD configuration $\mathbf{u}_{\mathrm{STD}}$ evaluated at zero:

$$\mathcal{T}_{\mathrm{STD}}(E,T) = \mathcal{T}_0(E) - \sum_\lambda \frac{\partial\mathcal{T}(E,\{\mathbf{u}_\lambda\})}{\partial\mathbf{u}_\lambda}s_\lambda(-1)^{\lambda-1}\sigma_\lambda(T) + \frac{1}{2}\sum_{\lambda\lambda'} \frac{\partial^2\mathcal{T}(E,\{\mathbf{u}_\lambda\})}{\partial\mathbf{u}_\lambda\partial\mathbf{u}_{\lambda'}}s_\lambda s_{\lambda'}(-1)^{\lambda+\lambda'-2}\sigma_\lambda \times(T)\sigma_{\lambda'}(T) + \mathcal{O}(\sigma^3). \tag{4}$$

The two successive terms, in the sum of the first-order part of Eq. (4), cancel each other since for large systems the two phonon modes λ and $\lambda+1$ are near degenerate resulting in an equivalent electron-phonon coupling and transmission derivatives. The second-order term in Eq. (4) is finite only for $\lambda = \lambda'$ and specifically λ and $\lambda+1$ terms once again have opposite signs. Hereby the STD expression Eq. (4) approaches the direct result Eq. (3) for $N\to\infty$. According to Ref. [35] the accuracy can be controlled not only by system size but also by configurational averaging over configurations with a systematically flipped sign in a subset of the mode displacements in Eq. (2). Unlike PT, which relies on a series truncation at the lowest $\mathcal{O}(\sigma^2)\sim\mathcal{O}(u^2)$, the STD expression holds to all orders in σ_λ. This is consistent with the adiabatic assumption of large displacements and low velocities. The current in Eq. (1) evaluated from the STD, Eq. (2), provides a simple model treating phonon-assisted tunneling and temperature-dependent EPC renormalization of the electronic structure on an equal footing. The STD approximates the correct thermal average, $\langle\mathcal{T}(E,T)\rangle \approx \mathcal{T}(E,\mathbf{u}_{\mathrm{STD}}(T))$, of the Landauer conductance, and resembles the special quasirandom structures (SQS) used to model infinite random alloys [38]. The phonon occupations could include a contribution, in addition to the thermal n_B, from finite bias heating. This would pave the way for current-saturation and heating modeling in nanoscale devices in the future.

Silicon n-i-n junction device. We now turn to device characteristics including EPC [39]. Figure 1 presents full quantum device simulations including EPC for a two-dimensional Si *n-i-n* double-gated MOSFET with 10 nm gate length. Decreasing the gate voltage the device goes from an on state where the current originates from thermionic emission to an off state where the current is determined by source-to-drain tunneling through the barrier. Comparing the interacting STD-Landauer result with the elastic calculation shows that the on current is almost unchanged by phonon scattering [Fig. 1(b)]. The on current reaches a value of $\sim$10 A/m even with phonon scattering at 300 K. However, phonon-assisted tunneling is found to increase the off-state current by four orders of magnitude. Consequently, we extract a significant subthreshold swing (S) degradation from $S\approx$ 97 mV/dec to $S\approx$ 375 mV/dec at 300 K. Existing device simulations on silicon FETs have not reported any significant phonon-assisted S degradation, most likely because they either neglect quantum tunneling, or are based on deformation potentials (corresponding to a purely imaginary and diagonal self-energy in the NEGF formalism) and effective-mass or tight-binding approximations [40–43]. A single study found a significant increase in the subthreshold current in silicon nanowires (SiNWs) partly traced back to the renormalization (self-energy real part), however, still within deformation potential approximations [44]. In Fig. 1(d) we illustrate the temperature-dependent broadening and shift of the density of states that effectively modifies the barrier thickness and phonon-assisted tunneling rates from electron states with s/d-type orbital character through evanescent p-type states in the intrinsic barrier region. Since elastic tunneling is suppressed by the orbital symmetry, we find that the off current is highly sensitive to temperature and significantly increased by EPC at finite temperature.

These results agree with quantum PT, as implemented in the lowest order expansion (LOE) method [2,45]. The LOE calculation essentially requires evaluation of the transition rates between scattering states for each phonon mode one

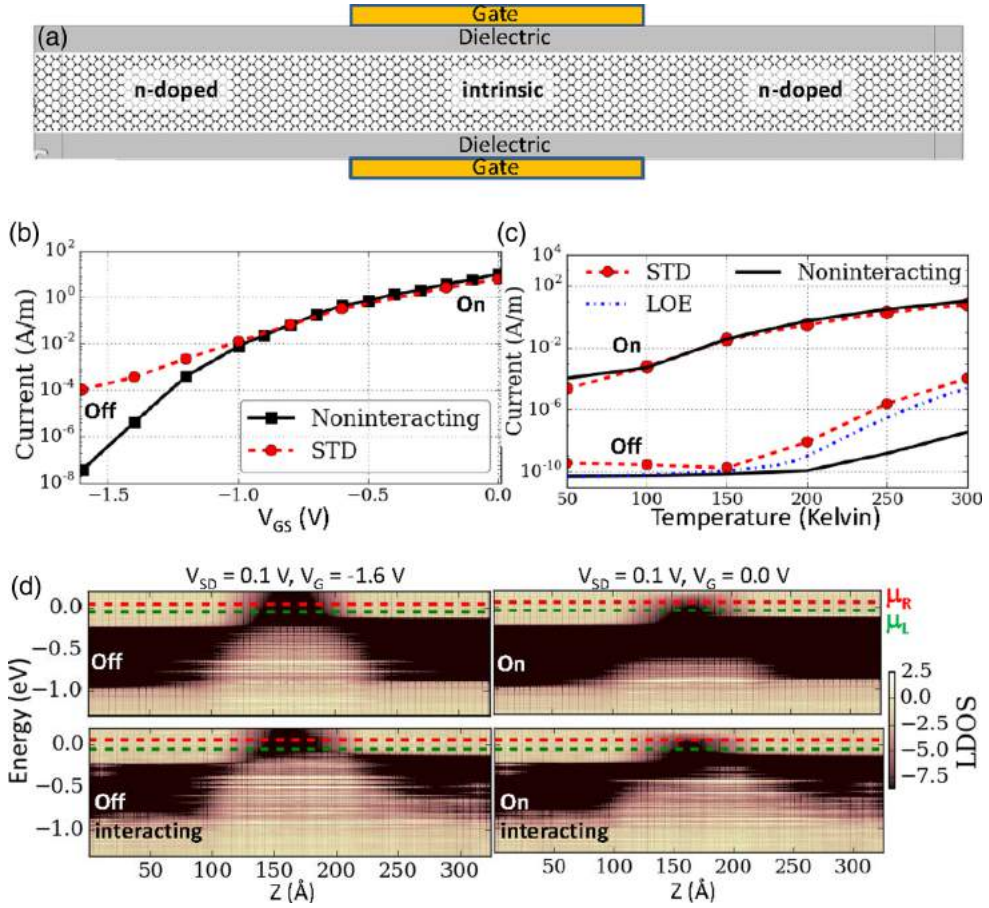

FIG. 1. (a) Silicon *n-i-n* junction tunneling device with a source and drain doping of 1.0×10^{21} cm^{-3}, length of 33 nm, and ∼2000 atoms. (b) Current versus gate voltage, V_G, for a source-drain voltage $V_{SD} = 0.1$ V and at 300 K. (c) Current at $V_G = -1.6$ V (on) and $V_G = 0$ V (off) as a function of temperature for $V_{SD} = 0.1$ V. (d) Tunneling barrier dependence on V_G and temperature illustrated by the local device density of states (LDOS). Regions of low (high) LDOS are shown in dark (bright) color illustrating the forbidden (permitted) bands along the device. Finite temperature electron-phonon coupling increases the off-state current hereby degrading the device performance.

by one. This makes a full LOE calculation computationally more expensive by a factor of at least 6000 from the number of phonon modes present in the device. This is a tremendous task and to achieve this for a single gate value we employ several computational approximations [36]. In Fig. 1(c), we show the temperature dependence of the on and off currents and validate the STD-Landauer result with the computational expensive LOE calculation for the off state. Importantly, we obtain an excellent match between the LOE and the STD-Landauer method. The temperature dependence of the current shows that phonon-assisted tunneling is frozen out below 150 K. Similarly, other simulations have found that phonon broadening of single impurity levels in SiNWs suppress current saturation above 150 K [46]. In conclusion, phonon-assisted tunneling is found to play a major role for leakage currents in ultrathin-body transistors at room temperature.

Silicon rectifiers. Next we show that finite temperature EPC does not only increase source-to-drain tunneling, but also significantly increases the band-to-band tunneling in *p-n* junctions. In Fig. 2 we consider transport in a short (6.5 nm) and a long (19.6 nm) silicon *p-n* junction [7,47,48] with transport in the [100] crystal direction.

Figures 2(c) and 2(d) show the modification of the IV characteristics due to EPC in the short (long) rectifier. To demonstrate the validity of the STD-Landauer method, we start by comparing the IV curves obtained with that from a PT(LOE) calculation [2,45]. Again, the PT calculation is computationally more expensive by a factor of at least 150 from the number of modes in the device. Nevertheless, we obtain an almost perfect match between the two in Fig. 2(c).

One challenge for DFT simulations of silicon devices is the fact that the screening length is often longer than system sizes reachable by PT calculations. This is illustrated by the local density of states (LDOS) in Figs. 2(e) and 2(f) which show how the typical *p-n* junction potential profile emerges when increasing the device length. As shown in Fig. 2(f), the STD-Landauer approach enables large-scale device simulations including EPC that secures converged screening potentials. In addition, we also see that EPC gives rise to significant changes in the LDOS of the device that highlights the importance of EPC in device characterization. Device performance is measured by its ability to have a high forward current, I_{ON}, and a low reverse leakage current, I_{OFF}. The I_{ON}/I_{OFF} figure of merit is reduced from 2×10^8 to 4 at ±0.5 V and 6×10^9 to 5×10^2 at ±0.6 V due to EPC. The reverse current

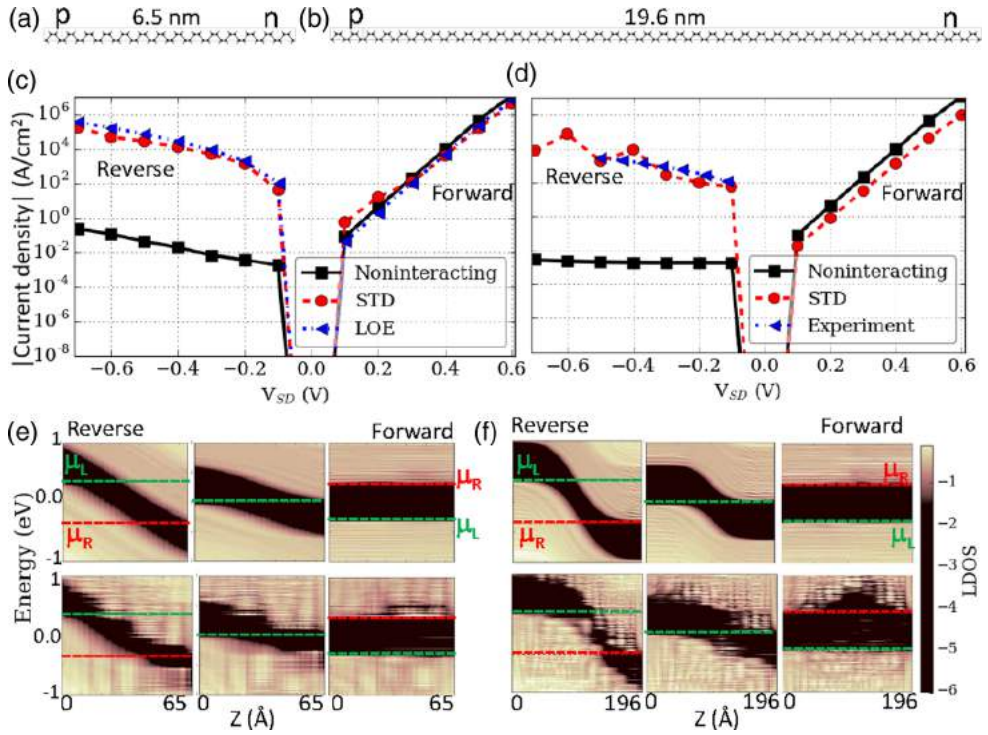

FIG. 2. Silicon *p-n* junction devices with doping values of $\pm 2 \times 10^{19}$ cm^{-3}. Device characteristics are compared between a short [(a),(c)] and long [(b),(d)] rectifier. The short device permits comparison with perturbation theory (LOE) while the screening is not fully enclosed within the device as shown by the local density of states (e). In both short and long devices the LDOS is strongly renormalized at 300 K [(e),(f) (lower panels)] and the reverse leakage currents are increased by six orders of magnitude. Experimental off current in (d) from Ref. [47] for a slightly asymmetrically doped SiNW at the Esaki onset.

still saturates, but at a much higher value. Hereby the low bias performance in terms of the rectification ratio is ruined demonstrating how the EPC can have a detrimental impact on the rectification ratio, and consequently a higher power is needed for efficient rectification.

The STD-Landauer result shows an increasing off current due to phonon excitation when increasing the temperature to 300 K. Recent experiments performed by Schmid *et al.* [47] on *pn* junctions made from silicon nanowires with a diameter of 60 nm report on several key features that match our findings. Their experiments at different temperatures underline the pivotal role played by phonons in the device characteristics. They explore a range of dopings going from normal to Esaki diode characteristics. At room temperature and at the lowest doping corresponding to the onset of Esaki characteristics, they find a maximum off-current density of 10^3 A/cm^2 at a reverse bias of -0.5 V. Our device is at a doping level just before the onset of Esaki characteristics, where Fermi levels are still inside the gap [cf. Fig. 2(f)]. The doping onset of the Esaki regime serves as a good point of reference since it is independent of the band gap value. In agreement with the experiments, we estimate $I_{OFF}(-0.5\text{ V}) \approx 10^3$ A/cm^2 and also find $I_{ON}/I_{OFF} < 1$ below ± 0.5 V, while the noninteracting ballistic result is off by roughly six orders of magnitude. In addition, the

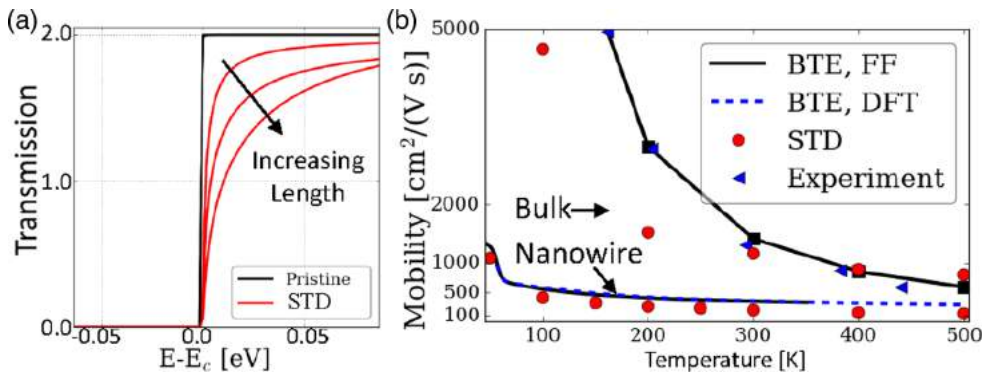

FIG. 3. STD-Landauer mobilities. (a) Transmission for the pristine and STD configurations for three different lengths of a 1.3-nm-diameter silicon nanowire. (b) Mobilities of a silicon nanowire and bulk silicon. STD result is compared to BTE as well as experimental data from Ref. [49] and force-field (FF) phonons for bulk and nanowire, respectively.

experiment shows a strong temperature dependence of the off current indicating an increased probability for transmission across the junction consistent with the additional transport channels opened by EPC in our simulations. Unlike the ballistic noninteracting case, we find that I_{OFF} increases with bias [Fig. 2(d)]. This is traced back to an increased window for inelastic transmission across the device that scales with the bias window. Again, this trend fits with the experiments performed by Schmid *et al.* [47]

Carrier mobilities. Carrier mobilities limited by EPC is an important performance indicator of materials. Finally, we show that the STD-Landauer approach has a predictive power at the level of state-of-the-art BTE solvers [14] based on the full first-principles EPC, and that both methods are in excellent agreement with available experimental results. In Fig. 3, we present mobilities obtained from the STD-Landauer device model. The resistance $R(\mathcal{L},T) = 1/G(\mathcal{L},T) = R_c + \rho_{1D}(T)\mathcal{L}$ increases linearly with length, $\mathcal{L}$, of the dynamic region in the Ohmic regime. In Fig. 3(a) we show the transmissions at 300 K for increasing device lengths. From this we extract a one-dimensional resistivity, $\rho_{1D}(T)$, which depends on temperature but not on wire length, and the contact resistance, R_c. From the density of states, $D(E)$, and carrier density, $\tilde{n} = \int_{E_g}^{\infty} f(E - E_F,T)D(E)dE$, we can obtain a mobility $\mu = \frac{1}{q\tilde{n}\rho_{1D}}$. The obtained values for bulk silicon compares well with both experimental values as well as BTE results from room temperature. The STD-Landauer result includes multiphonon effects and assumes the correct quantum occupations where optical modes are frozen out at low temperatures. The adiabatic assumption neglects, however, the frequency in single-phonon emission for modes with a high frequency which may explain part of the discrepancy at low temperature. Our first-principles calculations further support the conclusion of enhanced electron-phonon coupling in nanowires [19,24,50]. In addition, we compare the results obtained with both force-field and DFT phonons for the SiNW giving almost the exact same values. The predictability of the STD-Landauer approach in general does not rely on an accurate description of a single-phonon mode but rather the full configuration space. Hereby force fields become even more relevant for device simulations.

Conclusions. We have presented how a single STD together with a Landauer conductance calculation enables nanometer-scale nonequilibrium device simulations including phonon-assisted tunneling and temperature renormalization from first principles. Our results are in excellent agreement with both experiments and state-of-the-art perturbation theory calculations and underline the key role played by phonon-assisted band-to-band and source-to-drain tunneling in the performance of ultrascaled silicon rectifiers and transistors. Tunneling from electron states with s/d character through evanescent p-type states in the transistor barrier may put a limit to the performance of sub-10-nm devices and the length scale where elastic and classical device simulations are reliable. Importantly, the STD-Landauer approach is far more memory and computational efficient making it appealing as an atomistic design tool in electronics. The STD method evaluates phonon coupling under operating conditions and in the future it may open up the possibility for efficient modeling of current-induced heating by letting the phonon occupations depend on the applied bias voltage.

Acknowledgments. The authors acknowledge support from Innovation Fund Denmark through Grant No. 79-2013-1 and the Quantum Innovation Center (QUBIZ). C.N.G. is sponsored by the Danish National Research Foundation, Project No. DNRF103.

[1] A. M. Ionescu and H. Riel, Nature (London) **479**, 329 (2011).
[2] J.-T. Lü, R. B. Christensen, G. Foti, T. Frederiksen, T. Gunst, and M. Brandbyge, Phys. Rev. B **89**, 081405 (2014).
[3] T. Frederiksen, M. Paulsson, M. Brandbyge, and A.-P. Jauho, Phys. Rev. B **75**, 205413 (2007).
[4] Y. Lee, M. Lannoo, N. Cavassilas, M. Luisier, and M. Bescond, Phys. Rev. B **93**, 205411 (2016).
[5] H. Mera, T. G. Pedersen, and B. K. Nikolić, Phys. Rev. B **94**, 165429 (2016).
[6] Y. Lee, M. Bescond, N. Cavassilas, D. Logoteta, L. Raymond, M. Lannoo, and M. Luisier, Phys. Rev. B **95**, 201412 (2017).
[7] W. Vandenberghe, B. Sorée, W. Magnus, and M. V. Fischetti, J. Appl. Phys. **109**, 124503 (2011).
[8] Y.-M. Niquet, V.-H. Nguyen, F. Triozon, I. Duchemin, O. Nier, and D. Rideau, J. Appl. Phys. **115**, 054512 (2014).
[9] J. Jiang, M. Kula, W. Lu, and Y. Luo, Nano Lett. **5**, 1551 (2005).
[10] A. Troisi and M. A. Ratner, Nano Lett. **6**, 1784 (2006).
[11] M. Galperin, M. A. Ratner, and A. Nitzan, J. Phys.: Condens. Matter **19**, 103201 (2007).
[12] A. Gustafsson, H. Ueba, and M. Paulsson, Phys. Rev. B **90**, 165413 (2014).
[13] A. Troisi, M. A. Ratner, and A. Nitzan, J. Chem. Phys. **118**, 6072 (2003).
[14] T. Gunst, T. Markussen, K. Stokbro, and M. Brandbyge, Phys. Rev. B **93**, 035414 (2016).
[15] E. H. Hwang and S. Das Sarma, Phys. Rev. B **77**, 115449 (2008).
[16] F. Giustino, Rev. Mod. Phys. **89**, 015003 (2017).
[17] M. V. Fischetti and S. E. Laux, J. Appl. Phys. **80**, 2234 (1996).
[18] D. Bozyigit, N. Yazdani, M. Yarema, O. Yarema, W. M. M. Lin, S. Volk, K. Vuttivorakulchai, M. Luisier, F. Juranyi, and V. Wood, Nature (London) **531**, 618 (2016).
[19] W. Zhang, C. Delerue, Y.-M. Niquet, G. Allan, and E. Wang, Phys. Rev. B **82**, 115319 (2010).
[20] G. Mil'nikov and N. Mori, J Comput. Electron. **15**, 1179 (2016).
[21] T. Gunst, K. Kaasbjerg, and M. Brandbyge, Phys. Rev. Lett. **118**, 046601 (2017).
[22] M. Luisier and G. Klimeck, Phys. Rev. B **80**, 155430 (2009).
[23] R. Rhyner and M. Luisier, Phys. Rev. B **89**, 235311 (2014).
[24] T. Markussen, M. Palsgaard, D. Stradi, T. Gunst, M. Brandbyge, and K. Stokbro, Phys. Rev. B **95**, 245210 (2017).
[25] Y. Liu, Z. Yuan, R. J. H. Wesselink, A. A. Starikov, M. van Schilfgaarde, and P. J. Kelly, Phys. Rev. B **91**, 220405 (2015).

[26] J. Li, G. Speyer, and O. F. Sankey, Phys. Rev. Lett. **93**, 248302 (2004).
[27] D. Q. Andrews, R. P. Van Duyne, and M. A. Ratner, Nano Lett. **8**, 1120 (2008).
[28] M. Paulsson, C. Krag, T. Frederiksen, and M. Brandbyge, Nano Lett. **9**, 117 (2009).
[29] G. C. Solomon, D. Q. Andrews, R. H. Goldsmith, T. Hansen, M. R. Wasielewski, R. P. Van Duyne, and M. A. Ratner, J. Am. Chem. Soc. **130**, 17301 (2008).
[30] M. Dreher, F. Pauly, J. Heurich, J. C. Cuevas, E. Scheer, and P. Nielaba, Phys. Rev. B **72**, 075435 (2005).
[31] M. Zacharias, C. E. Patrick, and F. Giustino, Phys. Rev. Lett. **115**, 177401 (2015).
[32] B. Monserrat, Phys. Rev. B **93**, 014302 (2016).
[33] A. Pecchia, M. Gheorghe, A. Di Carlo, P. Lugli, T. A. Niehaus, T. Frauenheim, and R. Scholz, Phys. Rev. B **68**, 235321 (2003).
[34] S. Poncé, Y. Gillet, J. L. Janssen, A. Marini, M. Verstraete, and X. Gonze, J. Chem. Phys. **143**, 102813 (2015).
[35] M. Zacharias and F. Giustino, Phys. Rev. B **94**, 075125 (2016).
[36] See Supplemental Material at http://link.aps.org/supplemental/10.1103/PhysRevB.96.161404 for detailed information on the DFT-NEGF modeling, a derivation of Eq. (1), and additional Refs. [51–55].
[37] Originally Zacharias *et al.* termed their method one-shot. Here we extend it to the case of transport where one-shot is usually used for non-self-consistent current-conserving approximations, minimizing iterations between the electron and phonon equations. One-shot methods still require many DFT calculations to obtain the full EPC. The method used in this work is one-shot and in addition only requires a single DFT calculation for the STD and is therefore much more efficient than bare one-shot methods.
[38] S.-H. Wei, L. G. Ferreira, J. E. Bernard, and A. Zunger, Phys. Rev. B **42**, 9622 (1990).
[39] Atomistix ToolKit, version 2016, QuantumWise A/S. Computational settings are in the Supplemental Material.
[40] N. Cavassilas, M. Bescond, H. Mera, and M. Lannoo, Appl. Phys. Lett. **102**, 013508 (2013).
[41] N. Mori, H. Takeda, and H. Minari, J. Comput. Electron. **7**, 268 (2008).
[42] A. Svizhenko and M. P. Anantram, IEEE Trans. Electron Devices **50**, 1459 (2003).
[43] S. O. Koswatta, S. J. Koester, and W. Haensch, IEEE Trans. Electron Devices **57**, 3222 (2010).
[44] R. Valin, M. Aldegunde, A. Martinez, and J. R. Barker, J. Appl. Phys. **116**, 084507 (2014).
[45] T. Gunst, T. Markussen, K. Stokbro, and M. Brandbyge, Phys. Rev. B **93**, 245415 (2016).
[46] M. Bescond, H. Carrillo-Nuñez, S. Berrada, N. Cavassilas, and M. Lannoo, Solid-State Electron. **122**, 1 (2016).
[47] H. Schmid, C. Bessire, M. T. Björk, A. Schenk, and H. Riel, Nano Lett. **12**, 699 (2012).
[48] R. Rhyner, M. Luisier, and A. Schenk, *Proceedings of International Conference on Simulation of Semiconductor Processes and Devices (SISPAD 2012)* (Denver, CO, 2012), pp. 55–58.
[49] C. Jacoboni, C. Canali, G. Ottaviani, and A. Alberigi Quaranta, Solid-State Electron. **20**, 77 (1977).
[50] One can also extract the mean free path, $l_{mfp} = R_c/\rho_{1D}$, from the length-dependent resistance $R(\mathcal{L},T) = R_c(T)[1 + \mathcal{L}/l_{mfp}(T)]$. For the SiNW we obtain a room-temperature mean free path of 3.1 nm.
[51] M. Brandbyge, J.-L. Mozos, P. Ordejón, J. Taylor, and K. Stokbro, Phys. Rev. B **65**, 165401 (2002).
[52] D. Stradi, U. Martinez, A. Blom, M. Brandbyge, and K. Stokbro, Phys. Rev. B **93**, 155302 (2016).
[53] J. Tersoff, Phys. Rev. B **38**, 9902 (1988).
[54] R. Feynman, *Statistical Mechanics: A Set of Lectures*, 1st ed. (Avalon Publishing, New York, 1998).
[55] C. E. Patrick and F. Giustino, J. Phys.: Condens. Matter **26**, 365503 (2014).

Paper 5

New approaches for first-principles modelling of inelastic transport in nanoscale semiconductor devices with thousands of atoms

Tue Gunst, Mads Brandbyge, *Mattias Palsgaard*, Troels Markussen, and Kurt Stokbro

2017 International Conference on Simulation of Semiconductor Processes and Devices (SISPAD), pp. 13-16

New approaches for first-principles modelling of inelastic transport in nanoscale semiconductor devices with thousands of atoms

Tue Gunst*, Mads Brandbyge*, Mattias Palsgaard*†, Troels Markussen† and Kurt Stokbro†
*DTU Nanotech Center for Nanostructured Graphene (CNG), Technical University of Denmark, DK-2800 Kgs. Lyngby Denmark.
†QuantumWise A/S, Fruebjergvej 3, DK-2100 Copenhagen, Denmark. Email:kurt.stokbro@quantumwise.com

***Abstract*—We present two different methods which both enable large-scale first-principles device simulations including electron-phonon coupling (EPC). The methods are based on Density Functional Theory and Nonequilibrium Greens Functions (DFT-NEGF) calculations of electron transport. The inelastic current is in both methods calculated in a post-processing step to a self consistent DFT calculation. The first method is based on first order perturbation theory in the EPC self-energy within the Lowest Order Expansion (LOE) approximation. The method requires calculation of the first-principles EPC in the device region and it includes the effect of each phonon mode on the current perturbatively. This approach is made practical by calculating the EPC of the device region using a smaller periodic reference system. In addition, the phonon modes are assembled into a small number of energy intervals in which phonon modes are described collectively. The second method involves calculating the electron transmission for a single configuration where the atoms are displaced according to the phonon temperature of the system. Thus, this method has a computational cost equivalent to conventional elastic transport calculations. Both methods have been implemented in the Atomistix ToolKit (ATK) and we apply the methods for calculating the inelastic current in a silicon n-i-n junction and for calculation of phonon limited mobilities of silicon nanowires.**

I. Introduction

As electronic devices approach the nanoscale, accurate modelling often requires that the effect of each individual atom is included in the simulation. First-principles modelling using DFT-NEGF is an attractive approach, since it can accurately describe the atomic-scale details and electronic structure of surfaces, interfaces and different material combinations without the use of any experimental data[1]. However, most studies have so far been limited to simulations of the elastic current, even though EPC is known to play a crucial role in room-temperature performance of many nanoscale devices[2]. The inclusion of EPC into first-principles transport calculations has so far been limited to small molecular systems, due to the high computational cost[3]. In this paper, we present two methods[4] which enable electron transport calculations with EPC at a computational cost similar to that of elastic quantum transport calculations. Both methods are implemented in the Atomistix ToolKit (ATK)[5].

In the first section we present the basic theory behind the methods, and in the second section we compare the methods for calculating the inelastic transport in a 2D n-i-n silicon device and for the phonon limited mobility of a silicon nanowire.

II. Theory

In this section we briefly introduce the methods for calculating the inelastic current for a nanoscale device. We will assume that the device is a two-probe configuration, as illustrated in Fig. 1a. In a two-probe configuration the system is divided into a left electrode, central region and a right electrode. For the left and the right electrode we will describe the system using periodic boundary conditions.

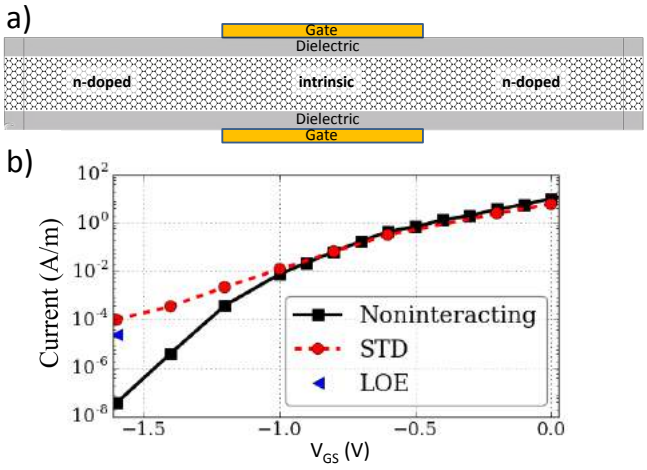

Fig. 1. (a) Silicon n-i-n junction tunneling device with a source and drain doping of 1.0×10^{21} cm^{-3}, length of 33 nm and $\sim$ 2000 atoms. (b) Current versus gate-voltage, V_G, for a source-drain voltage V_{SD}=0.1 V and at 300 K. The solid line shows results without EPC (Noninteracting), the red dashed line shows results including EPC in the STD approximation, and the single blue triangle shows results for including EPC in the LOE approximation

In the following subsections we will introduce the two methods. Both methods are post-processing methods, i.e. they use the Hamiltonian from a self-consistent electronic structure calculation of the systems without electron-phonon coupling. The first method use a Special Thermal Displacement (STD) of all atoms at a specific temperature which mimics the thermal fluctuations of the configuration. The inelastic current can be obtained by calculating a single elastic transmission spectrum for this STD configuration[4]. The second method is based

on lowest order perturbation theory in the electron-phonon coupling self-energies using the Lowest Order Expansion (LOE)[6].

A. The STD method

The STD method is conceptually related to the Special Quasi-Random Structure (SQS) method for describing Random Alloys. In the SQS method a single geometry is used to represent a random alloy, the geometry is selected to give the same physical property as the average value obtained for a random distribution of structures[7]. In the STD method a single configuration is selected which have the same physical property as the average value obtained for a thermal distribution of structures[4], [8]. In Ref. [9] we showed that the average transmission from a thermal distribution of configurations accurately describes the inelastic electron transmission spectrum due to electron-phonon scattering at this temperature. In the STD method the average is replaced with a single representative geometry. To calculate the STD we need the Dynamical matrix (D) of the central region of the system. A first-principles calculation of the full Dynamical Matrix can be very time consuming, however, for most systems a good approximation can be obtained by using a force-field, or in the case of a repeated two-probe system by repeating D calculated for the left electrode.

To obtain the STD we first need to calculate the phonon eigenspectrum using the Dynamical matrix of the central region. The phonon modes are labeled by λ with frequency ω_λ, eigenmode vector $\mathbf{e}_\lambda$, and characteristic length, l_λ. The STD is then given by[4]

$$\mathbf{u}_{STD}(T) = \sum_\lambda s_\lambda (-1)^{\lambda-1} \sigma_\lambda(T) \mathbf{e}_\lambda \tag{1}$$

Here s_λ denotes the sign of the first non-zero element in $\mathbf{e}_\lambda$ enforcing the same choice of "gauge" for the modes. The Gaussian width σ is related to the mean square displacement $\langle \mathbf{u}_\lambda^2 \rangle = l_\lambda^2 (2n_B(T)+1) = \sigma_\lambda^2(T)$ at a temperature T, where n_B is the Bose-Einstein distribution.

The 'trick' in the STD method is the use of opposite phases for phonons with similar frequencies, in this way phonon-phonon correlation functions average to zero and the transmission spectrum of the STD configuration becomes similar to a thermal average of single phonon excitations.

The final step in the STD method is to calculate the self-consistent Hamiltonian of the displaced system, and use that to calculate a normal electron transmission spectrum. Thus, the computation effort for the inelastic transmission is for the STD method similar to elastic transmission.

B. The LOE method

The LOE method for the inelastic current calculation is based on perturbation theory in the first Born approximation. Besides the Hamiltonian and the Dynamical matrix of the central region (as needed in the STD method) it requires knowledge of the Hamiltonian derivative with respect to the atomic positions in the central region, $\nabla H(r)$.

The first-principles calculations of $\nabla H(r)$ can be prohibitive for a large system. The system in Fig. 1a is what we will call a "Repeated Two-probe system". In such a system the atomic configuration of the central region can be generated by repeating the left electrode along the transport direction. For a repeated two-probe system $\nabla H(r)$ can be obtained to a good approximation from the $\nabla H(r)$ of the left electrode.

From t$\nabla H(r)$ of the central region we can get the electron-phonon matrix element in reciprocal space[10].

$$\begin{aligned} M^{\mu\nu}_{\lambda,\mathbf{k},\mathbf{q}} &= \sum_{mn} e^{i\mathbf{k}\cdot(\mathbf{R}_n-\mathbf{R}_m)-i\mathbf{q}\cdot\mathbf{R}_m} \\ &\quad \times \langle \phi_\nu \mathbf{R}_m | \mathbf{v}_{\mathbf{q},\lambda} \cdot \nabla H_0(r) | \phi_\mu \, \mathbf{R}_n \rangle, \end{aligned} \tag{2}$$

where the (mn)-sum runs over repeated unit cells in the super cell calculation of the hamiltonian derivatives[10], and the subscript 0 indicates that the derivatives are only calculated for atoms in the unit cell with index 0. $|\phi_\mu \, \mathbf{R}_n\rangle$ represent the μ'th LCAO basis orbital in the unit cell displaced from the reference cell by the lattice vector $\mathbf{R}_n$.

Following ref. [6] we obtain inelastic transmission functions, which are symmetric in the applied bias and account for a finite transfer of momentum, $\mathcal{T}^{ems/abs}_{\lambda,\mathbf{k},\mathbf{q}}(\epsilon) =$

$$\begin{aligned} &\mathrm{Tr}\left[M^\lambda \tilde{A}_L^{\mathbf{k}+\mathbf{q}}(\pm) M^\lambda A_R^{\mathbf{k}}(\mp)\right] \\ &+\mathrm{Im}\Big\{\mathrm{Tr}\left[M^\lambda A_R^{\mathbf{k}+\mathbf{q}}(\pm)\Gamma_L^{\mathbf{k}+\mathbf{q}}(\pm) G^{\mathbf{k}+\mathbf{q}}(\pm) M^\lambda A_R^{\mathbf{k}}(\mp)\right] \\ &\quad + \mathrm{Tr}\left[M^\lambda A_R^{\mathbf{k}+\mathbf{q}}(\mp)\Gamma_L^{\mathbf{k}+\mathbf{q}}(\mp) G^{\mathbf{k}+\mathbf{q}}(\mp) M^\lambda A_L^{\mathbf{k}}(\pm)\right]\Big\} \end{aligned} \tag{3}$$

where we use the short hand notation $A_L^{\mathbf{k}}\left(\epsilon \pm \frac{\hbar\omega_\lambda}{2}\right) = A_L^{\mathbf{k}}(\pm)$. In the first line we have $\tilde{A}_L^{\mathbf{k}+\mathbf{q}} = \left(G^{\mathbf{k}+\mathbf{q}}\right)^\dagger \Gamma_L^{\mathbf{k}+\mathbf{q}} G^{\mathbf{k}+\mathbf{q}}$, whereas the other spectral functions are defined as $A_L^{\mathbf{k}+\mathbf{q}} = G^{\mathbf{k}+\mathbf{q}}\Gamma_L^{\mathbf{k}+\mathbf{q}}\left(G^{\mathbf{k}+\mathbf{q}}\right)^\dagger$. We finally evaluate the current following [2] as

$$\begin{aligned} I(V) = -\frac{2e}{hN_\mathbf{k}N_\mathbf{q}} \sum_{\lambda,\mathbf{k},\mathbf{q}} &\int_{-\infty}^{\infty} d\epsilon [\mathcal{T}^{ems}_{\lambda,\mathbf{k},\mathbf{q}}(\epsilon) F^{ems}_{\lambda,\mathbf{q}}(\epsilon) \\ &+\mathcal{T}^{abs}_{\lambda,\mathbf{k},\mathbf{q}}(\epsilon) F^{abs}_{\lambda,\mathbf{q}}(\epsilon)], \end{aligned} \tag{4}$$

where $N_\mathbf{k}$ and $N_\mathbf{q}$ are the numbers of $\mathbf{k}$ and $\mathbf{q}$-points and where the energy- and mode depended prefactors are

$$\begin{aligned} F^{ems}_{\lambda,\mathbf{q}}(\epsilon) &= n_F(\epsilon-\mu_L)[1-n_F(\epsilon-\mu_R+\hbar\omega_{\lambda,\mathbf{q}})][n_B(\hbar\omega_{\lambda,\mathbf{q}})+1] \\ &\quad -n_F(\epsilon-\mu_R-\hbar\omega_{\lambda,\mathbf{q}})[1-n_F(\epsilon-\mu_L)]n_B(\hbar\omega_{\lambda,\mathbf{q}}) \\ F^{abs}_{\lambda,\mathbf{q}}(\epsilon) &= n_F(\epsilon-\mu_L)[1-n_F(\epsilon-\mu_R-\hbar\omega_{\lambda,\mathbf{q}})]n_B(\hbar\omega_{\lambda,\mathbf{q}}) \\ &\quad -n_F(\epsilon-\mu_R+\hbar\omega_{\lambda,\mathbf{q}})[1-n_F(\epsilon-\mu_L)][n_B(\hbar\omega_{\lambda,\mathbf{q}})+1], \end{aligned}$$

where $n_F(\epsilon) = 1/(e^{\epsilon/k_BT}+1)$ and $n_B(\hbar\omega) = 1/(e^{\hbar\omega/k_BT}-1)$ are the Fermi-Dirac and Bose-Einstein distribution functions respectively.

In calculating the inelastic current we formally have a sum over all the phonon modes. In order to reduce the computational burden, we perform a summation of the phonon modes in energy intervals to form new effective phonon modes. We typically use intervals of 10 meV length, i.e $[0, 0.01]$ eV, $[0.01, 0.02]$eV, etc. Similar approximations are commonly used in other codes[11]. The sum over modes in Eq. (4) and related

equations above is thus replaced by a sum over phonon energy intervals using the redefined phonon modes. Otherwise the formulas remain the same.

III. Results

In the following we compare the methods for the inelastic transport in a nanoscale 2-d silicon n-i-n device and the phonon limited mobility of a silicon nanowire.

A. n-i-n junction

The first system we investigate is a 2-d Silicon n-i-n junction, as illustrated in Fig. 1a. The system is confined in the vertical direction with a thickness of 2 nm and the surfaces are passivated with Hydrogen atoms. The out-of-plane direction is periodic, and the horizontal direction is the transport direction. The device is surrounded by a 1 nm dielectrics with $\epsilon = 4$ and controlled through a gate electrode. The device is intrinsic between the gate electrodes, and n-doped ($1.0 \times 10^{21}\,\mathrm{cm}^{-3}$) outside the gate.

For the DFT-NEGF calculation we use the ATK package[5]. We use the Local Density Approximation (LDA) for the exchange-correlation functional. The Si and H atoms are described by normconserving pseudopotentials and the electronic structure described by a spd basis set (9 orbital per atom). To describe the periodic direction we use 9 k-points for the SCF calculation and 51 k-points for the transport calculation. The dielectric and gate electrode are described at the continuum level within the poisson equation for the Hartree potential. The method for doping is described in Ref. [12]. The elastic transport at an electronic temperature of 300K is shown with the black solid line in Fig. 1b.

The next step is to include EPC using the STD approximation. To this end we need the Dynamical matrix which we calculate numerically from a classical potential[13]. Using the dynamical matrix we calculate the STD at 300K and perform a SCF calculation for the resulting geometry. From the SCF Hamiltonian we calculate the transmission and the resulting current for different gate biases. The result is shown with the dashed red line in Fig. 1b. We see that the EPC has only little effect for the on-current, however, the off-current is increased by 4 orders of magnitude and the subthreshold swing is degraded from 97 mV/dec to 375 mV/dec.

To check if this result is correct we perform a LOE calculation for the off-current. For this calculation we need the EPC matrix element. Since the system is a repeated two probe device, we only need to calculate the EPC for the left electrode and repeat it to get the EPC of the central region. We can now calculate the inelastic current in the LOE approximation. The LOE calculation is more time consuming and we have only calculated a single point for the off-current. As seen from Fig. 1b the LOE and STD approximations are in excellent agreement. Since the two approaches are very different, it shows that the different approximations for including EPC are valid.

Existing device simulations on silicon FETs have not reported any significant phonon-assisted tunneling. We believe that this is most likely because they either neglect quantum-tunneling, or are based on deformations potentials (corresponding to a purely imaginary and diagonal self-energy in the NEGF formalism) and effective-mass or tight-binding approximations[14], [15], [16], [17]. Thus, our new first principles calculations with a complete description of the EPC are the most accurate description to date of a nanoscale FET. The main error source in the calculation is the use of DFT-LDA which severely underestimates the band gap of Si (0.66 eV in our calculation). We are presently investigating the use of LDA+1/2[18] which reproduces the bandgap of Si (1.18 eV). Preliminary results show that an increased bandgap slightly reduce the phonon assisted tunneling but the main conclusions are the same.

B. Silicon nanowire

In a recent paper[9], we calculated the phonon limited mobility of nanowires using a full first-principles calculations combined with the Boltzmann Transport Equations (BTE)[10] and also from a Molecular Dynamics (MD) Landauer approach. In the MD-Landauer approach an ensemble of configurations are obtained from MD trajectories at the given temperature, and then the transmission spectrum is averaged over this ensemble to obtain an inelastic transmission spectrum[10]. The mobility is obtained through the length dependence of the conductance, i.e. transmission calculations for typically 3 different system lengths are used to calculate the mobility. The STD method can also be considered as a "one-shot" MD-Landauer approach, instead of using an ensemble of configurations, we use a single configuration with the same average atom-atom correlations as the MD ensemble. In the following we will compare the BTE and MD methods with the LOE and STD methods.

The system we consider is a silicon nanowire, illustrated in Fig. 2a. It has a diameter of 1.5nm and is oriented along the (100) direction. The surfaces are passivated with hydrogen. For the MD, STD and LOE methods we consider 3 different lenghts, 5, 10 and 15 nm. Other computational details are similar to the n-i-n study.

Fig. 2b shows the resulting mobilities. The BTE result serves as a good point of reference since it is the most conventional approach. We see that the STD results closely follow the BTE data, proving the validity of the approach. The MD results shows a higher mobility than the STD results and the discrepancy is increased for decreasing temperature. We expect that this is due to the use of classical MD which neglect zero-point motion. The zero-point motion is included in both the BTE and STD calculations. The LOE result gives slightly to high values at low temperatures. For a one-dimensional system the transmission near the band edge is more sensitive towards perturbations due to the van Hove singularity in the density of states. In this limit, one may observe strong modifications of the current beyond lowest order perturbation theory. Recently, several papers have developed an analytic continuation approach that enables a renormalization of the LOE result so that it gives results equivalent to the self-

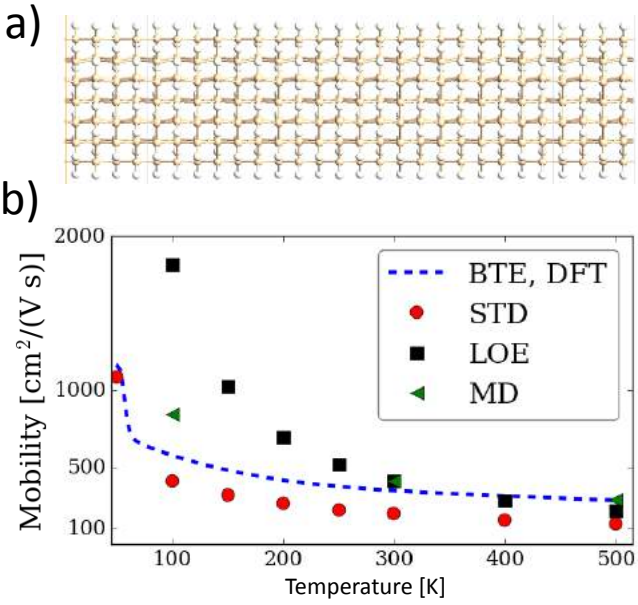

Fig. 2. a) Geometry of the silicon nanowire used for the mobility calculation. b) Mobility as function of temperature for the BTE, STD, MD and LOE methods.

consistent Born approximation[14]. Here we employ the lowest order analytic continuation approach for the nanowire due to its simplicity. While the LOE includes EPC as a perturbation to the current, MD and STD directly evaluates the inelastic current at displaced atomic positions. In general, all four methods gives results that agree from room temperature and above.

IV. Conclusion

We have presented two methods which enable computational efficient first principles transport calculations including EPC. Most efficient and promising is the STD method. This method uses an additional elastic transport calculation for a displaced configuration to provide the effect of EPC, and thereby allows for including EPC at essentially the same cost as elastic quantum transport calculations. We presented results for the electrical properties of a silicon 2D-FET and mobility of a silicon nanowire. The results illustrated the accuracy of the approach.

Acknowledgment

The authors acknowledge support from Innovation Fund Denmark through Grant No. 79-2013-1 and the Quantum Innovation Center (QUBIZ). CNG is sponsored by the Danish National Research Foundation, project No. DNRF103.

References

[1] M. Brandbyge, J.-L. Mozos, P. Ordejón, J. Taylor, and K. Stokbro, "Density-functional method for nonequilibrium electron transport," *Phys. Rev. B*, vol. 65, no. 16, p. 165401, mar 2002.

[2] W. Vandenberghe, B. Sorée, W. Magnus, and M. V. Fischetti, "Generalized phonon-assisted zener tunneling in indirect semiconductors with non-uniform electric fields: A rigorous approach," *Journal of Applied Physics*, vol. 109, no. 12, p. 124503, 2011.

[3] T. Frederiksen, M. Paulsson, M. Brandbyge, and A.-P. Jauho, "Inelastic transport theory from first principles: Methodology and application to nanoscale devices," *Physical Review B*, vol. 75, no. 20, p. 205413, 2007.

[4] T. Gunst, T. Markussen, M. Palsgaard, K. Stokbro, and M. Brandbyge, *Submitted*, 2017.

[5] "Atomistix ToolKit version 2017.3," quantumWise A/S (www.quantumwise.com).

[6] J.-T. Lü, R. B. Christensen, G. Foti, T. Frederiksen, T. Gunst, and M. Brandbyge, "Efficient calculation of inelastic vibration signals in electron transport: Beyond the wide-band approximation," *Physical Review B*, vol. 89, no. 8, p. 081405, 2014.

[7] A. Zunger, S.-H. Wei, L. Ferreira, and J. E. Bernard, "Special quasirandom structures," *Physical Review Letters*, vol. 65, no. 3, p. 353, 1990.

[8] M. Zacharias and F. Giustino, "One-shot calculation of temperature-dependent optical spectra and phonon-induced band-gap renormalization," *Phys. Rev. B*, vol. 94, no. 7, p. 075125, Aug. 2016. [Online]. Available: http://link.aps.org/doi/10.1103/PhysRevB.94.075125

[9] T. Markussen, M. Palsgaard, D. Stradi, T. Gunst, M. Brandbyge, and K. Stokbro, "Electron-phonon scattering from green's function transport combined with molecular dynamics: Applications to mobility predictions," *Phys. Rev. B*, vol. 95, p. 245210, 2017.

[10] T. Gunst, T. Markussen, K. Stokbro, and M. Brandbyge, "First-principles method for electron-phonon coupling and electron mobility: Applications to two-dimensional materials," *Physical Review B*, vol. 93, no. 3, p. 035414, 2016.

[11] M. Luisier and G. Klimeck, "Atomistic full-band simulations of silicon nanowire transistors: Effects of electron-phonon scattering," *Physical Review B*, vol. 80, no. 15, p. 155430, 2009.

[12] D. Stradi, U. Martinez, A. Blom, M. Brandbyge, and K. Stokbro, *Phys. Rev. B*, vol. 93, p. 155302, 2016.

[13] J. Tersoff, "Empirical interatomic potential for silicon with improved elastic properties," *Physical Review B*, vol. 38, no. 14, p. 9902, 1988.

[14] N. Cavassilas, M. Bescond, H. Mera, and M. Lannoo, "One-shot current conserving quantum transport modeling of phonon scattering in n-type double-gate field-effect-transistors," *Applied Physics Letters*, vol. 102, no. 1, p. 013508, Jan. 2013. [Online]. Available: http://scitation.aip.org.globalproxy.cvt.dk/content/aip/journal/apl/102/1/10.1063/1.4775

[15] N. Mori, H. Takeda, and H. Minari, "Effects of phonon scattering on electron transport in double-gate MOSFETs," *J Comput Electron*, vol. 7, no. 3, pp. 268–271, Sep. 2008. [Online]. Available: https://link-springer-com.proxy.findit.dtu.dk/article/10.1007/s10825-008-0199-1

[16] A. Svizhenko and M. P. Anantram, "Role of scattering in nanotransistors," *IEEE Transactions on Electron Devices*, vol. 50, no. 6, pp. 1459–1466, Jun. 2003.

[17] S. O. Koswatta, S. J. Koester, and W. Haensch, "On the Possibility of Obtaining MOSFET-Like Performance and Sub-60-mV/dec Swing in 1-D Broken-Gap Tunnel Transistors," *IEEE Transactions on Electron Devices*, vol. 57, no. 12, pp. 3222–3230, Dec. 2010.

[18] L. G. Ferreira, M. Marques, and L. K. Teles, "Approximation to density functional theory for the calculation of band gaps of semiconductors," *Physical Review B*, vol. 78, no. 12, p. 125116, 2008.

Paper 6

Efficient First-Principles Calculation of Phonon-Assisted Photocurrent in Large-Scale Solar-Cell Devices

Mattias Palsgaard, Troels Markussen, Tue Gunst, Mads Brandbyge, and Kurt Stokbro

Physical Review Applied **10**, 014026 (2017)

Editors' Suggestion

Efficient First-Principles Calculation of Phonon-Assisted Photocurrent in Large-Scale Solar-Cell Devices

Mattias Palsgaard,[1,2,*] Troels Markussen,[1] Tue Gunst,[2] Mads Brandbyge,[2] and Kurt Stokbro[1]

[1] *Synopsys-QuantumWise A/S, Fruebjergvej 3, Postbox 4, DK-2100 Copenhagen, Denmark*

[2] *Department of Micro- and Nanotechnology (DTU Nanotech), Center for Nanostructured Graphene (CNG), Technical University of Denmark, DK-2800 Kgs. Lyngby, Denmark*

(Received 21 December 2017; revised manuscript received 20 April 2018; published 25 July 2018)

We present a straightforward and computationally cheap method to obtain the phonon-assisted photocurrent in large-scale devices from first-principles transport calculations. The photocurrent is calculated using the nonequilibrium Green's function with light-matter interaction from the first-order Born approximation, while electron-phonon coupling (EPC) is included through special thermal displacements. We apply the method to a silicon solar-cell device and demonstrate the impact of including EPC in order to properly describe the current due to the indirect band-to-band transitions. The first-principles results are successfully compared to experimental measurements of the temperature and light-intensity dependence of the open-circuit voltage of a silicon photovoltaic module. Our calculations illustrate the pivotal role played by EPC in photocurrent modeling to avoid underestimation of the open-circuit voltage, short-circuit current, and maximum power. This work represents a recipe for computational characterization of future photovoltaic devices including the combined effects of light-matter interaction, phonon-assisted tunneling, and the device potential at finite bias from the level of first-principles simulations.

DOI: 10.1103/PhysRevApplied.10.014026

I. INTRODUCTION

Photovoltaics (PV) represents a promising technology as a replacement for the burning of fossil fuels. In the past couple of decades, many promising thin-film absorber materials have been discovered, all of them with unique strengths and weaknesses. CdTe and copper indium gallium selenide [CIGS, $CuIn_{(1-x)}Ga_{(x)}Se_2$] can produce high efficiencies, but include rare and toxic elements, while copper zinc tin sulfide (CZTS, Cu_2ZnSnS_4) includes only nontoxic earth-abundant elements, but suffers from low efficiency and open-circuit voltage (V_{OC}) [1–4]. Clearly, there is still room for the discovery of new materials to improve on the cost-efficiency relationship. The field of computational material science has seen massive progression, and as a result the difference between the system size and complexity attainable in simulations and experiments is becoming smaller every day. Recently, a review was published on the design of new materials using first-principles calculations [5]. Here, it is stressed how the abundance of candidate materials together with the lack of efficient devices highlight the need for efficient predictive device calculations. Continuum models are used extensively in the field of PV to extract benchmark parameters from measurements on devices and to predict the performance of new device geometries [6]. It is difficult to include important effects such as confinement of electrons and phonons, surface effects, and strain in the continuum models. These effects can, however, be captured using atomistic models based on density-functional theory (DFT). DFT combined with the nonequilibrium Green's function (NEGF) formalism [7–9] has, for example, previously been used to improve a continuum-model study of transport through the interface between CZTS and the buffer material CdS, which is important for CZTS solar-cell efficiency [10,11]. In spite of the influx of new thin-film-based PV cells, silicon remains the market leader and about 90% of PV cells are still based on silicon, where large modules with high efficiency and stability can be produced [1].

Silicon has an indirect band gap and as such, in order to conserve momentum, absorption of a photon below the fundamental direct gap energy must be accompanied by the absorption or emission of a phonon. A number of recent studies also show that EPC plays a key role in the outstanding performance of PV cells based on direct-band-gap perovskites [12–15].

*mlnp@nanotech.dtu.dk

The study of phonon-assisted photon absorption from first principles is notoriously difficult as it involves a double sum over fine grids of **k** points and complex two-excitation processes. Therefore state-of-the-art DFT calculations of phonon-assisted absorption have so far been limited to bulk crystals where the supercell contains only a few atoms [16–18], while empirical models have been used for studies of realistic devices [19]. Recently, Zacharias and Giustino [18] introduced a very efficient method for including phonon-induced absorption processes using a single supercell calculation in which the atoms are displaced away from their equilibrium positions. We recently adopted this special-thermal-displacement (STD) approach to study electron transport in silicon systems with over 1000 atoms, including electron-phonon coupling within the DFT NEGF formalism [20].

In this paper we apply STD to calculations of the first-order photocurrent in a 19.6-nm silicon *p-n* junction from DFT NEGF. In this way we are able to capture the phonon-assisted absorption over the indirect band gap of silicon and study directly the effect of temperature on the performance of the device. In the following section, we summarize the methodology used to calculate the photocurrent using the first-order Born approximation and the inclusion of EPC through the STD approach. Exhaustive derivations of the important equations can be found in previous publications [18,20–23].

II. METHOD

We calculate the photocurrent as a first-order perturbation to the electronic system caused by the interaction with a weak electromagnetic field. The electron-photon interaction is given by the Hamiltonian

$$H' = \frac{e}{m_0}\mathbf{A}\cdot\mathbf{P}, \tag{1}$$

where **A** is the vector potential and **P** is the momentum operator. For a single-mode monochromatic light source, we have [21]:

$$\mathbf{A} = \mathbf{e}\left(\frac{\hbar\sqrt{\tilde{\mu}_r\tilde{\epsilon}_r}}{2N\omega\tilde{\epsilon}c}F\right)^{1/2}(be^{-i\omega t} + b^\dagger e^{i\omega t}), \tag{2}$$

where $\tilde{\mu}_r$ is the relative permeability, $\tilde{\epsilon}_r$ is the relative permittivity, $\tilde{\epsilon}$ is the permittivity, ω is the frequency of the light, F is the photon flux, N is the number of photons, $b^\dagger$ and b are the bosonic creation and annihilation operators, and **e** is a unit vector giving the polarization of the light.

Using the standard Meir-Wingreen formula [24] and including only first-order terms in F, we arrive at an expression similar to Fermi's golden rule for the current into the left (L) and right (R) leads due to absorption of photons [23,25]:

$$I_\alpha = \frac{e}{h}\int_{-\infty}^{\infty}\sum_{\beta=L,R}[1-f_\alpha(E)]f_\beta(E-\hbar\omega)T^-_{\alpha,\beta}(E) - f_\alpha(E)[1-f_\beta(E+\hbar\omega)]T^+_{\alpha,\beta}(E)dE, \tag{3}$$

$$T^-_{\alpha,\beta}(E) = N\,\mathrm{Tr}\{M^\dagger\tilde{A}_\alpha(E)MA_\beta(E-\hbar\omega)\}, \tag{4}$$

$$T^+_{\alpha,\beta}(E) = N\,\mathrm{Tr}\{M\tilde{A}_\alpha(E)M^\dagger A_\beta(E+\hbar\omega)\}, \tag{5}$$

where $\alpha \in L, R$, f_α is the Fermi-Dirac distribution function of lead α, $A_\alpha = G\Gamma_\alpha G^\dagger$ is the spectral function of lead α, $\tilde{A}_\alpha = G^\dagger\Gamma_\alpha G$ is the time-reversed spectral function of lead α, and the electron-photon coupling matrix is

$$M_{ml} = \frac{e}{m_0}\left(\frac{\hbar\sqrt{\tilde{\mu}_r\tilde{\epsilon}_r}}{2N\omega\tilde{\epsilon}c}F\right)^{1/2}\mathbf{e}\cdot\mathbf{P}_{ml}. \tag{6}$$

The total photocurrent is then calculated as $I_{\mathrm{ph}} = I_L - I_R$. The retarded G and advanced $G^\dagger$ Green's functions, the spectral broadening of the leads Γ_α, and the momentum operator **P** are calculated self-consistently from DFT NEGF simulations of the silicon *p-n* junction device.

The temperature-dependent EPC is included through a single displacement of the atomic positions according to [18,20]

$$\mathbf{u}_{\mathrm{STD}}(T) = \sum_\lambda(-1)^{\lambda-1}\sigma_\lambda(T)\mathbf{e}_\lambda, \tag{7}$$

where $\mathbf{e}_\lambda$ is the eigenvector of phonon mode λ and the Gaussian width σ is given by

$$\sigma_\lambda(T) = l_\lambda\sqrt{2n_\lambda(T)+1}, \tag{8}$$

where $n_\lambda(T)$ and $l_\lambda = \sqrt{\hbar/2M_p\Omega_\lambda}$ are the Bose-Einstein occupation and vibrational characteristic length of mode λ with frequency Ω_λ. Phonon modes are obtained using a supercell method [26–28]. The configuration displaced according to Eq. (7) gives the correct thermal average of the Landauer conductance and the optical absorption for sufficiently large systems with many repetitions of the same unit cell [18,20].

In summary the total current at bias V and temperature T is calculated as follows:

$$I(V,T) = I_0[V,\mathbf{u}_{\mathrm{STD}}(T)] + I_{\mathrm{ph}}[V,\mathbf{u}_{\mathrm{STD}}(T)], \tag{9}$$

where I_0 is the dark current coming from the applied bias. By displacing the atomic coordinates once according

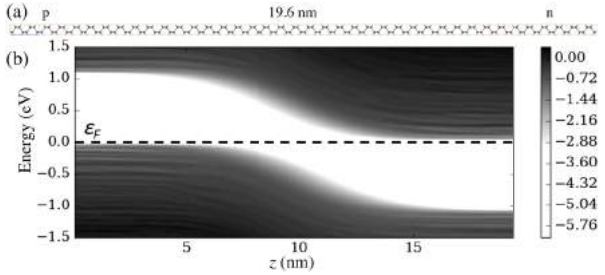

FIG. 1. (a) Structure and cell used in the calculation of the 19.6-nm silicon *p-n* junction, with $n = 2 \times 10^{19}$ cm^{-3}. (b) Local density of states along the transport direction of the silicon *p-n* junction on a logarithmic scale.

to Eq. (7), calculating, and adding the two current contributions, we get the current under illumination of a single frequency of light. To calculate the total current under sunlight illumination, we integrate the current over frequency with the flux F given by the AM1.5 reference spectrum. All DFT NEGF calculations in this study were performed using the ATK DFT software [29–31], with the SG15-low basis set and 11×11 (21×21) **k** points in the electronic structure (transport) calculations. DFT within the local-density approximation (LDA) or the generalized-gradient approximation (GGA) to the exchange-correlation potential is known to underestimate the band gaps in semiconductors. In order to overcome this band-gap problem, we used the GGA+1/2 exchange-correlation method [32], which yields accurate band structures for a wide range of materials with the same computational effort as normal GGA calculations. With these parameters we obtain an indirect band gap of 1.135 eV for pristine silicon (neglecting zero-point motion). All phonon calculations were performed using Tersoff potentials [33,34]. Electronic doping was included by adding a charge fixed at the position of every silicon atom in the structure, as in previous work [35]. The DFT electronic structure under applied bias was calculated self-consistently using the standard NEGF approach [31].

III. RESULTS AND DISCUSSION

Figure 1(a) shows the considered 19.6-nm silicon *p-n* junction with transport along the [100] direction. The related local density of states is shown in Fig. 1(b) and we can see the typical *p-n* profile along the device, with flat bands near the electrode indicating converged screening potentials [20,35]. Furthermore, we see that the calculated band gap is very close to the one observed in experiments on silicon [36].

In Fig. 2(a) we compare the photocurrent density calculated for a pristine silicon (neglecting zero-point motion) *p-n* junction with that of a 300-K STD structure for $F = 1/\text{Å}^2$ s. The dashed lines indicate the energies of the indirect ($E_g^{\text{indirect}} = 1.135$ eV) and direct ($E_g^{\text{direct}} = 2.853$ eV) band gaps of the bulk silicon structure using the same calculational settings. First, we see that the obtained band gap agrees well with the experimental value (1.12 eV) [36], verifying our use of the GGA+1/2 exchange-correlation method. Second, we see that the inclusion of EPC through the STD results in an increase in photocurrent from the indirect transition of about two orders of magnitude. The photocurrent as a function of photon energy at 300 K compares well to previous calculations of the absorption coefficients in bulk silicon, where EPC was included in the same way [18]. Temperature effects on the electronic structure are included in the STD method, and indeed we see a finite photocurrent at photon energies below the bulk band gap corresponding to a reduction in the band gap with temperature. In addition to the finite-temperature renormalization of the band gap, we obtain the actual photocurrent of the transport setup assisted by band-to-band tunneling and including the device potential at finite bias. Unlike calculations on bulk silicon, we see here a small finite contribution to the photocurrent coming from the indirect transition even without EPC. This we trace back to symmetry breaking by the ultrathin *p-n* junction and the resulting device potential along the [100] direction. This current contribution is analyzed in more detail in the Supplemental Material [37]. In simulations based on the bulk-silicon band structure, such transitions

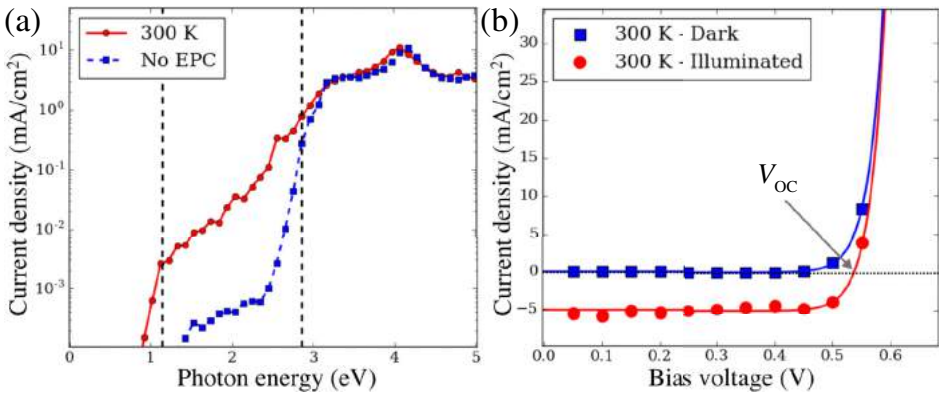

FIG. 2. (a) Calculated photocurrent density for the pristine (blue dashed) and STD displaced (red solid) system, where $F = 1/\text{Å}^2$ s and $V = 50$ mV. (b) Calculated room-temperature current density as a function of voltage for the silicon *p-n* junction in the dark ($F = 0$) and under illumination.

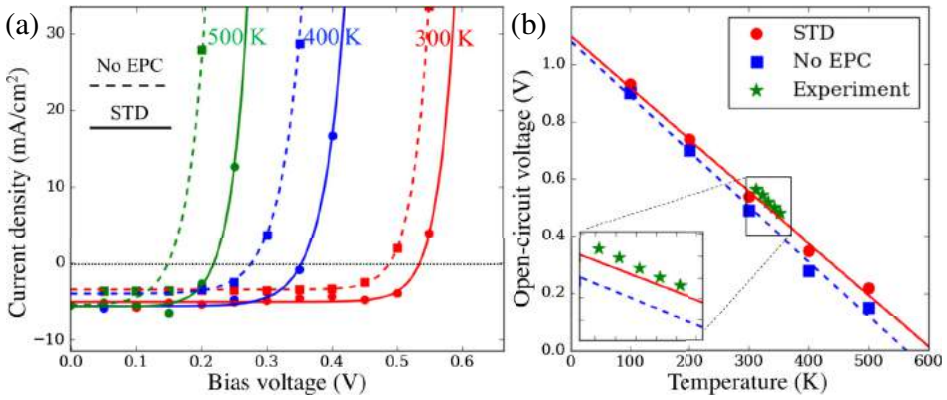

FIG. 3. (a) Calculated *I-V* curves with (solid) and without (dashed) EPC for different temperatures. (b) Calculated open-circuit voltage as a function of temperature with linear fits. The green star markers are experimental measurements from [40]. The inset shows a close-up near the experimental measurements. In all calculations and experimental values shown in this figure, a light intensity of 1 sun was used.

would be prohibited by the opposite symmetry of conductance and valence states if not assisted by phonons. This follows from the selection rule due to momentum conservation, which is a consequence of translational symmetry. However, in a *p-n* junction, the system is not translationally invariant in the transport direction, and hence the momentum in the transport direction is not a conserved quantity. The effects of phonon-assisted tunneling, temperature renormalization, and the device potential are all seen to play an important role in the quantitative photocurrent device characteristics. Regarding below-gap transitions, a similar result was seen previously when studying theoretically the phonon-assisted tunneling into graphene in a scanning-tunneling-spectroscopy setup [38]. Here a finite but strongly suppressed tunneling into the Dirac point of graphene is seen even below the threshold voltage of the phonon opening the inelastic channel. In order to generate an *I-V* curve, we need to calculate the total photocurrent under sunlight illumination. To that end we used the AM1.5 reference spectrum and integrated the spectral current densities for a certain applied bias.

The *I-V* curve of the silicon *p-n* junction is shown in Fig. 2(b), with and without the addition of photocurrent. A least-squares fit of the calculated data points to the usual expression for the current of a diode under illumination $I = I_{\mathrm{ph}} + I_0[\exp(qV/nk_BT) - 1]$ is added. The result looks very much like what is expected [39], with a photocurrent being a nearly constant contribution at all applied biases. The applied bias voltage where the illuminated *I-V* curve crosses the zero-current-density line and no current is generated is known as the open-circuit voltage (V_{OC}) and is a measurable parameter used to benchmark solar-cell performance. For crystalline-silicon PV cells, the open-circuit voltage is known to be in the range 0.55–0.60 V [40–42] at room temperature, in good agreement with the 0.54 V obtained from our calculation. The short-circuit current, obtained at zero applied bias, varies a lot depending on the quality and device geometry of the measured solar cell, making a direct comparison with our results difficult. The obtained 5 mA cm^{-2} is, however, aligned with typical values published in the literature [41,42].

To analyze the direct impact of EPC on the device, we plot in Fig. 3(a) the *I-V* curve under illumination for the perfectly symmetric (noninteracting) silicon system together with that of the system where atomic positions are displaced according to STD [Eq. (7)] for different temperatures. Without EPC the short-circuit current density is underestimated by about 25%. Importantly, the open-circuit voltage is significantly underestimated without EPC and one obtains $V_{\mathrm{OC}} = 0.49$ V at 300 K. The open-circuit voltage of a PV device is an important performance indicator that defines its quality and is typically very well controlled, so a ∼10% loss at room temperature

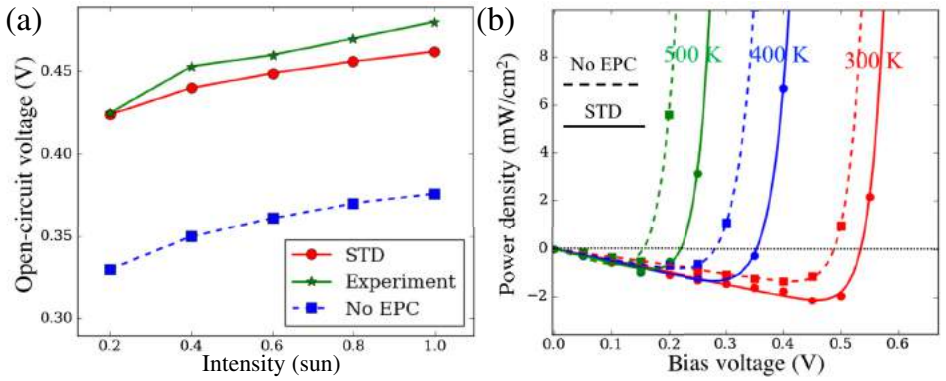

FIG. 4. (a) Open-circuit voltage as a function of light intensity at 352 K. The calculated results including EPC were extrapolated from the fitted line in Fig. 3(b), since we did not perform calculations at the exact temperature measured in [40]. (b) Calculated power density as a function of applied voltage with (solid) and without (dashed) EPC for different temperatures.

is substantial. This highlights the importance of including phonon effects in device calculations of indirect semiconductor PV devices.

We will now analyze the temperature dependence of the device characteristics, which can often be extracted from experiments. The short-circuit current is largely constant while the open-circuit voltage is degraded for higher temperatures, due to the increased probability of carriers tunneling through the *p-n* junction via electron-phonon scattering events at bias voltages below the band gap. In the case with no EPC, the increased current at higher temperatures comes only from the temperature dependence of the Fermi-Dirac distribution. Comparing with the results where EPC is ignored (dashed lines), we see that the open-circuit voltage is systematically underestimated and that the error is larger at high temperature. It is not surprising that the inclusion of EPC is more important at higher temperatures where the phonon population is higher. The short-circuit current is also constant for the case without EPC, but it is too low at all temperatures. Using the results shown in Fig. 3(a), we can extract the open-circuit voltage, which is often measured in experiments on solar-cell devices, as a function of temperature. The open-circuit voltage as a function of temperature with and without the inclusion of EPC is shown in Fig. 3(b). A linear fit was performed on both data sets using least-squares fitting, and the best fit was plotted alongside the data points. For both cases, we get the expected linear temperature dependence. The open-circuit voltage extrapolated to the $T = 0$ K point is often used in experiments to extract the activation energy of the dominant recombination path. Here we get 1.1 V $\pm$ 0.025 V with EPC and 1.08 V $\pm$ 0.029 V without EPC, both slightly below our calculated band gap. In Fig. 3(b) we also compare the calculated results with experiments carried out by Huang *et al.* [40], where the open-circuit voltage of a crystalline-silicon PV module was measured under simulated solar irradiation while controlling the cell temperature. The calculated results including EPC agree nicely with the experimental measurements. The calculated open-circuit voltages without the inclusion of EPC are much lower than the experimental values at all temperatures. Experimental measurements of V_{OC} performed at temperatures in the range 100–300 K under 1.1 sun illumination [41] also agree nicely with the values calculated including EPC (not shown).

Lastly, we will analyze the trends with light intensity. In Fig. 4(a) we show the calculated open-circuit voltage for different intensities of the light source at a temperature of 352 K and compare with experimental values from Huang *et al.* [40]. Again we see that the results where EPC is included through STD agree nicely with experimental measurements. The best agreement is seen at 0.2 sun, which is to be expected given the assumption of a weak field going into Eq. (1). On the other hand, the open-circuit voltages calculated while neglecting EPC do not agree with the experimental values. In fact, even the results calculated at 1 sun are below the experimental values, where only an intensity of 0.2 sun is used. This underlines the pivotal role played by EPC in PV devices. Figure 4(b) shows the generated power density for the *p-n* junction with and without the inclusion of EPC. We see that the maximum power and maximum power point are both underestimated in the case without EPC.

IV. CONCLUSION

We have presented a computationally cheap method to calculate the phonon-assisted photocurrent in large-scale devices from first principles. Previous studies of phonon-assisted optical absorption using state-of-the-art methods have been limited to bulk systems of high symmetry, where only a handful of atoms are considered due to the computational cost. Here we study a 19.6-nm-long silicon *p-n* junction under working conditions with an applied bias. The calculated current density as a function of photon energy is similar in shape to the temperature-renormalized bulk optical absorption of silicon calculated in previous studies using a similar description of EPC [18]. Our results agree nicely with experiments both for values of the open-circuit voltages and for trends in how they scale, with temperature and light intensity. The phonon interaction has a significant impact on the device characteristics, highlighting the need for photocurrent transport calculations including phonon coupling when considering devices using indirect semiconductors as the absorber material. The combination of device simulations with photon coupling as well as phonon coupling, through special thermal displacements, offers an appealing way forward in the difficult problems of combined light-matter interaction, phonon-assisted tunneling, temperature renormalization, and the nonequilibrium device potential in quantitative first-principles simulations.

ACKNOWLEDGMENTS

This work is partly funded by the Innovation Fund Denmark (IFD) under File No. 5016-00102. We thank Andrea Crovetto and Urs Aeberhard for their input on this work.

[1] S. Philipps and W. Warmuth, Photovoltaics Report, Tech. Rep. (Fraunhofer Institute for Solar Energy Systems, ISE, 2017).

[2] V. M. Fthenakis, Life cycle impact analysis of cadmium in CdTe PV production, Renew. Sustain. Energy Rev. **8**, 303 (2004).

[3] M. Woodhouse, A. Goodrich, R. Margolis, T. James, R. Dhere, T. Gessert, T. Barnes, R. Eggert, and D. Albin, Perspectives on the pathways for cadmium telluride photovoltaic module manufacturers to address expected increases

in the price for tellurium, Sol. Energy Mater. Sol. Cells **115**, 199 (2013).
[4] A. Polman, M. Knight, E. C. Garnett, B. Ehrler, and W. C. Sinke, Photovoltaic materials: Present efficiencies and future challenges, Science **352**, aad4424 (2016).
[5] K. T. Butler, J. M. Frost, J. M. Skelton, K. L. Svane, and A. Walsh, Computational materials design of crystalline solids, Chem. Soc. Rev. **45**, 6138 (2016).
[6] M. Burgelman, P. Nollet, and S. Degrave, Modelling polycrystalline semiconductor solar cells, Thin Solid Films **361-362**, 527 (2000).
[7] L. V. Keldysh, Diagram technique for nonequilibrium processes, Sov. Phys. JETP **20**, 1018 (1965).
[8] R. A. Craig, Perturbation expansion for real-time Green's functions, J. Math. Phys. **9**, 605 (1968).
[9] P. Danielewicz, Quantum theory of nonequilibrium processes, I, Ann. Phys. **152**, 239 (1984).
[10] A. Crovetto, M. L. N. Palsgaard, T. Gunst, T. Markussen, K. Stokbro, M. Brandbyge, and O. Hansen, Interface band gap narrowing behind open circuit voltage losses in Cu_2ZnSnS_4 solar cells, Appl. Phys. Lett. **110**, 083903 (2017).
[11] M. L. N. Palsgaard, A. Crovetto, T. Gunst, T. Markussen, O. Hansen, K. Stokbro, and M. Brandbyge, Semiconductor band alignment from first principles: A new nonequilibrium Green's function method applied to the CZTSe/CdS interface for photovoltaics, in *SISPAD 2016* (2016), pp. 377–380.
[12] J. Yang, X. Wen, H. Xia, R. Sheng, Q. Ma, J. Kim, P. Tapping, T. Harada, T. W. Kee, F. Huang, Y.-B. Cheng, M. Green, A. Ho-Baillie, S. Huang, S. Shrestha, R. Patterson, and G. Conibeer, Acoustic-optical phonon up-conversion and hot-phonon bottleneck in lead-halide perovskites, Nat. Commun. **8**, 14120 (2017).
[13] H. Kim, J. Hunger, E. Cánovas, M. Karakus, Z. Mics, M. Grechko, D. Turchinovich, S. H. Parekh, and M. Bonn, Direct observation of mode-specific phonon-band gap coupling in methylammonium lead halide perovskites, Nat. Commun. **8**, 687 (2017).
[14] A. D. Wright, C. Verdi, R. L. Milot, G. E. Eperon, M. A. Pérez-Osorio, H. J. Snaith, F. Giustino, M. B. Johnston, L. M. Herz, Electron-phonon coupling in hybrid lead halide perovskites, Nat. Commun. **7**, 11755 (2016).
[15] P.-A. Mante, C. C. Stoumpos, M. G. Kanatzidis, and A. Yartsev, Electron-acoustic phonon coupling in single crystal $CH_3NH_3PbI_3$ perovskites revealed by coherent acoustic phonons, Nat. Commun. **8**, 14398 (2017).
[16] J. Noffsinger, E. Kioupakis, C. G. Van de Walle, S. G. Louie, and M. L. Cohen, Phonon-Assisted Optical Absorption in Silicon from First Principles, Phys. Rev. Lett. **108**, 167402 (2012).
[17] M. Zacharias, C. E. Patrick, and F. Giustino, Stochastic Approach to Phonon-Assisted Optical Absorption, Phys. Rev. Lett. **115**, 177401 (2015).
[18] M. Zacharias and F. Giustino, One-shot calculation of temperature-dependent optical spectra and phonon-induced band-gap renormalization, Phys. Rev. B **94**, 075125 (2016).
[19] U. Aeberhard, Quantum-kinetic theory of photocurrent generation via direct and phonon-mediated optical transitions, Phys. Rev. B **84**, 035454 (2011).
[20] T. Gunst, T. Markussen, M. L. N. Palsgaard, K. Stokbro, and M. Brandbyge, First-principles electron transport with phonon coupling: Large scale at low cost, Phys. Rev. B **96**, 161404 (2017).
[21] L. E. Henrickson, Nonequilibrium photocurrent modeling in resonant tunneling photodetectors, J. Appl. Phys. **91**, 6273 (2002).
[22] L. Zhang, K. Gong, J. Chen, L. Liu, Y. Zhu, D. Xiao, and H. Guo, Generation and transport of valley-polarized current in transition-metal dichalcogenides, Phys. Rev. B **90**, 195428 (2014).
[23] J. Chen, Y. Hu, and H. Guo, First-principles analysis of photocurrent in graphene *pn* junctions, Phys. Rev. B **85**, 155441 (2012).
[24] Y. Meir and N. S. Wingreen, Landauer Formula for the Current Through an Interacting Electron Region, Phys. Rev. Lett. **68**, 2512 (1992).
[25] C. Rivas, R. Lake, G. Klimeck, W. R. Frensley, M. V. Fischetti, P. E. Thompson, S. L. Rommel, and P. R. Berger, Full-band simulation of indirect phonon assisted tunneling in a silicon tunnel diode with delta-doped contacts, Appl. Phys. Lett. **78**, 814 (2001).
[26] T. Gunst, T. Markussen, K. Stokbro, and M. Brandbyge, First-principles method for electron-phonon coupling and electron mobility: Applications to two-dimensional materials, Phys. Rev. B **93**, 035414 (2016).
[27] G. J. Ackland, M. C. Warren, and S. J. Clark, Practical methods in *ab initio* lattice dynamics, J. Phys. Condens. Matter **9**, 7861 (1997).
[28] K. Kunc and R. M. Martin, *Ab initio* Force Constants of GaAs: A New Approach to Calculation of Phonons and Dielectric Properties, Phys. Rev. Lett. **48**, 406 (1982).
[29] Atomistix ToolKit version 2017.1, Synopsys-QuantumWise A/S.
[30] J. M. Soler, E. Artacho, J. D. Gale, A. García, J. Junquera, P. Ordejón, and D. Sánchez-Portal, The SIESTA method for *ab initio* order-*N* materials simulation, J. Phys.: Condens. Matter **14**, 2745 (2002).
[31] M. Brandbyge, J.-L. Mozos, P. Ordejón, J. Taylor, and K. Stokbro, Density-functional method for nonequilibrium electron transport, Phys. Rev. B **65**, 165401 (2002).
[32] L. G. Ferreira, M. Marques, and L. K. Teles, Approximation to density functional theory for the calculation of band gaps of semiconductors, Phys. Rev. B **78**, 125116 (2008).
[33] J. Tersoff, Empirical interatomic potential for silicon with improved elastic properties, Phys. Rev. B **38**, 9902 (1988).
[34] J. Schneider, J. Hamaekers, S. T. Chill, S. Smidstrup, J. Bulin, R. Thesen, A. Blom, and K. Stokbro, ATK-forcefield: A new generation molecular dynamics software package, Modell. Simul. Mater. Sci. Eng. **25**, 085007 (2017).
[35] D. Stradi, U. Martinez, A. Blom, M. Brandbyge, and K. Stokbro, General atomistic approach for modeling metal-semiconductor interfaces using density functional theory and nonequilibrium Green's function, Phys. Rev. B **93**, 155302 (2016).
[36] M. Levinshtein, S. Rumyantsev, and M. Shur, *Handbook Series on Semiconductor Parameters* (World Scientific, Singapore, 1996), Vol. 1.

[37] See Supplemental Material at http://link.aps.org/supplemental/10.1103/PhysRevApplied.10.014026 for [convergence of the STD photocurrent with *p*-*n* junction size and an extended discussion about photocurrent contributions coming from photons with energies below the direct band gap of silicon.].

[38] M. L. N. Palsgaard, N. P. Andersen, and M. Brandbyge, Unravelling the role of inelastic tunneling into pristine and defected graphene, Phys. Rev. B **91**, 121403 (2015).

[39] P. Würfel, *Physics Today* (Wiley-VCH Verlag GmbH & Co. KGaA, Weinheim, 2005).

[40] B. J. Huang, P. E. Yang, Y. P. Lin, B. Y. Lin, H. J. Chen, R. C. Lai, and J. S. Cheng, Solar cell junction temperature measurement of PV module, Sol. Energy **85**, 388 (2011).

[41] P. Löper, D. Pysch, A. Richter, M. Hermle, S. Janz, M. Zacharias, and S. W. Glunz, Analysis of the temperature dependence of the open-circuit voltage, Energy Procedia **27**, 135 (2012).

[42] S. Chander, A. Purohit, A. Sharma, S. P. Nehra, and M. S. Dhaka, A study on photovoltaic parameters of monocrystalline silicon solar cell with cell temperature, Energy Rep. **1**, 104 (2015).

Paper 7

Stacked Janus device concepts: abrupt pn-junctions and cross-plane channels

Mattias Palsgaard, Tue Gunst, Troels Markussen, Kristian Sommer Thygesen, and Mads Brandbyge

Submitted to Nanoletters

Stacked Janus device concepts: abrupt pn-junctions and cross-plane channels

Mattias Palsgaard,[*,†,‡,¶] Tue Gunst,[*,‡,¶] Troels Markussen,[†] Kristian Sommer Thygesen,[§,¶] and Mads Brandbyge[‡,¶]

†*Synopsys-QuantumWise, Fruebjergvej 3, Postbox 4, DK-2100 Copenhagen, Denmark*

‡*Department of Micro- and Nanotechnology (DTU Nanotech), Technical University of Denmark, DK-2800 Kgs. Lyngby, Denmark*

¶*Center for Nanostructured Graphene (CNG)*

§*Department of Physics, Center for Atomic-scale Materials Design, Technical University of Denmark, DK-2800 Kgs. Lyngby, Denmark*

E-mail: mlnp@nanotech.dtu.dk; tue.gunst@nanotech.dtu.dk

Abstract

Janus transition metal dichalcogenides with a built-in structural cross-plane (cp) asymmetry have recently emerged as a new class of 2D materials with a large cp dipole. Using first principles calculations, and a tailored transport method, we demonstrate that stacking graphene and MoSSe Janus structures result in record high homogeneous doping of graphene and abrupt, atomic-thin, cross-plane *pn*-junctions. We show how graphene, in contrast to metals, can act as electrodes to Janus stacks without screening the cp dipole, and predict a large photo-current response dominated by a cp transport channel in a few-layer stacked device. The photo-current is above that of a corresponding thin-film silicon device illustrating the great potential of Janus stacks f.ex. in photovoltaic devices.

Controlling the built-in or environmental planar symmetry of two-dimensional materials paves the way for a next level of rich 2D physics phenomena. One promising example is the emerging Janus transition metal dichalcogenides (TMD's), such as MoSSe, where a strong planar asymmetry, due to different atomic species on each side, generates a large dipole across the plane.[1,2] Other recent relevant examples include how the stacking environment of 2D materials can be used to tune properties like the optical gap,[3] mobility,[4] interlayer excitons[5,6] and local doping.[7,8] One key focus has so far been to find TMD's with different band gaps.[9] However, the properties of Janus MoSSe are far more interesting than an expected band gap in between the two out-of-plane symmetric parents (MoS_2 and $MoSe_2$).

While structural stability[10] and the potential usefulness of MoSSe for solar water splitting[11–13] and band gap engineering[14] have been examined previously, device properties and the interaction of the Janus dipole with other stacking materials and electrodes have not been discussed so far. Here we show how stacking graphene and Janus structures gives a route to record high homogeneous doping of graphene in abrupt *pn*-junctions. In addition, semi-metallic leads such as graphene, are needed to avoid the dipole cancellation due to the screening that occurs in metallic contacting. Such effects are crucial to address for the potential application of Janus structures in devices. Finally, we provide for the first time estimates of the photo-current generated in device configurations. Harvesting solar energy through photovoltaics (PV) represents a promising technology as a replacement for burning fossil fuels and the potential of Janus TMD's as a new alternative or constituent in PV devices in the future is discussed. We calculate the ballistic single-particle charge transfer with a transport method tailored to stacked Janus and Janus-graphene devices, neglecting excitonic effects. Computational details are described in the Methods section.

Monolayer Janus MoSSe. The origin of the out-of-plane asymmetry and the resulting Janus dipole mechanism is illustrated in Fig. 1 for a monolayer MoSSe system. A layer of Mo is sandwiched in between a layer of S and Se atoms on each side. From the calculated bandstructure in Fig. 1(a) we find a direct band gap, located at the K and K'-points, with a

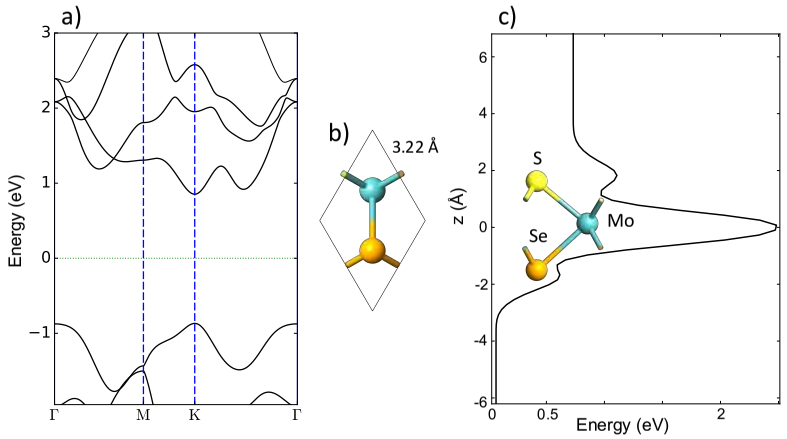

Figure 1: Janus dipole mechanism. a) Bandstructure and b) Top view of the unit cell of monolayer Janus MoSSe. c) Electrostatic difference potential averaged in the plane of monolayer MoSSe plotted as a function of the cross-plane (cp) position, z.

value of 1.72 eV which corresponds nicely to the 1.77 eV optical band gap previously reported for Janus MoSSe.[1,13,15]

In Fig.1(c) we show the electrostatic difference potential averaged over the xy-plane as a function of the z-position. This clearly illustrates the built-in cp dipole field with a potential difference of 0.66 eV between the two sides. Previous studies discuss the structural asymmetry and a large out-of-plane piezoelectric polarization of Janus materials.[1,16] A simple explanation of the cp dipole field, observed in Fig. 1(c), can be found in the fact that S and Se atoms have slightly different electronegativity, which for a full layer gives a large difference in work-function between the two surfaces and induces a dipole across the slab. We employ Neumann boundary conditions at the vacuum boundaries when solving the Poisson equation[4,17] allowing for self-consistent calculations of the surface dipole field.

Stacked Janus MoSSe. By stacking multiple Janus MoSSe layers on top of each other it is possible to stack the dipoles of the individual layers and obtain an atomically thin

pn-junction across the multilayer system. We demonstrate this by projecting the bands on each layer in a trilayer Janus MoSSe system in Fig. 2(a). The bands are colored according

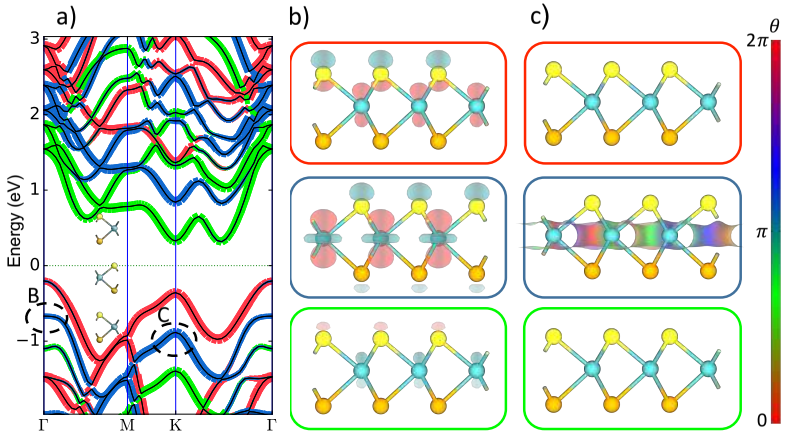

Figure 2: a) Bandstructure of trilayer Janus MoSSe projected onto the seperate layers. The structure is shown in the inset. Line thickness and the color red, blue and green lines represents projections on the top, middle and bottom layers, respectively. b) Cross-plane channel: Bloch state isosurface of the Γ-point state highlighted by point B in a). c) In-plane channel: Bloch state isosurface of the K-point state highlighted by point C in a). The color shows the phase of the wavefunction.

to the projection on each of the three layers, with the bottom layer having a Se surface and the top layer has a S surface. Clearly, the top (red) layer with the S-terminated surface is more *p*-like and the bottom (green) layer with the Se-terminated surface is *n*-like and added layers each obtain bands shifted by ∼0.5 eV. This trend applies for 1-3 layers until the 4th layer is added, where the conduction band minimum and valence band maximum intersect the Fermi level and a *pn*-junction is obtained. Adding additional layers to the stack does not increase the dipole due to charge transfer between the top and bottom layers. In addition, we find that stacked Janus MoSSe gets an indirect band gap as the valence band maximum shifts from the K, K'-points to the Γ-point. However, rather than discussing this

in terms of a decreasing band gap, we focus on the fact here that stacking Janus layers is a way of obtaining atomically thin *pn*-junctions inherently through the Janus dipole effect. This is interesting for the potential applications in e.g. photodiodes, which we will return to after a discussion about how to contact such a Janus surface induced dipole *pn*-junction and identifying possibly photo-current active channels.

Photo-current active channels through the *pn*-junction will have a high degree of spatial distribution across the different layers. This is not the case for the highly-dispersive valence bands near the K-valley (marked C in Fig. 2(a)). Looking at the valence band in Fig. 2(a) near the Γ-point (marked B), we find a state that has a low in-plane dispersion but is delocalized in the cp-direction (the blue line projected band is thinner at the Γ-point as compared to the K-point due to contributions from all three layers). We highlight this through Fig. 2(b) showing the isosurface of the Bloch state located near the Γ-point that illustrates the spread across the slab of this state. In Fig. 2(c) we show the corresponding valence band state at the K-point (also highlighted in 2(a)) with the same isovalue. In contrast to the Γ-point state, the K-point state is an in-plane channel; it is highly localized in the middle MoSSe monolayer showing no delocalization in the cp-direction.

While the valence states in the K-valley are merely a superposition of states localized in each layer, illustrated in Fig. 2(c), this is not the case for the Γ-valleys - a point so far overlooked in the literature. The three states originating from different layers at the Γ-point are dissimilar and the one originating from the middle MoSSe layer is the most spread out. We conclude that the state shown in Fig. 2(b) is a cp-channel distributed across all layers of the system. Due to the low in-plane dispersion it exhibits a molecular orbital-like character. Contrary to a usual in-plane transport mechanism such low-dispersive bands can therefore be a good indication of cp-transport activity. This cp-channel will be dominating the large photo-current response, as shown below.

Another interesting point that has not been discussed previously is the difference in effective masses (inverse curvature) of the valence bands around the Γ-point. From Fig. 2(a)

we see that the effective mass of the valence bands around the Γ-point increases significantly for the second layer and changes sign for the third layer. This change is caused by the cp-field between the layers and can be reversed by creating an external field in the opposite direction of the built-in dipole using e.g. gates of opposite polarity above and below the structure. We therefore make a conjecture that the photo-current active band will be highly tunable by external gating. We will explicitly show that is this indeed the case when discussing the device simulations.

Stacked Janus MoSSe and Graphene. Next we discuss the concept of Janus dipole doping of graphene and show how graphene can be used as electrodes for Janus MoSSe devices. Stacked systems are illustrated in Fig. 3(a,b). The stacking of dipoles, shown in the multilayer MoSSe structures, creates a unique opportunity for creating atomically thin *pn*-junctions in the cp-direction for harvesting of solar energy. To facilitate such a device, connections to metallic leads are necessary. However simply adding bulk metal leads to the top and bottom layers would completely screen the built-in dipole ruining the *pn*-junction as shown in the Supporting Information (Fig. S1-S4). This screening could turn out to be a major challenge for exploiting the built-in cp-dipole and the unique properties of Janus materials. We expect semi-metallic 2D materials to screen the cp-field less efficiently and have therefore examined the effect of adding graphene monolayers to the top and bottom of multilayer MoSSe.

In Fig. 3(c) we show the projected bandstructure of three layers of MoSSe with graphene (leads) added to the top and bottom of the structure as shown in Fig. 3(b). A hexagonal supercell of graphene on top of MoSSe (shown in Fig. 3(a)) was obtained with four and seven repetitions of the MoSSe and graphene unit cells, respectively. A compressive strain of ∼1% is added to graphene in this supercell. We chose to strain only graphene since we are interested in the details of the MoSSe electronic structure while graphene is simply used as a lead.[18–20] Importantly, we see from Fig. 3(c) that while some screening of the cp-dipole occurs, it mostly survives. As indicated in the bandstructure the difference in energy between

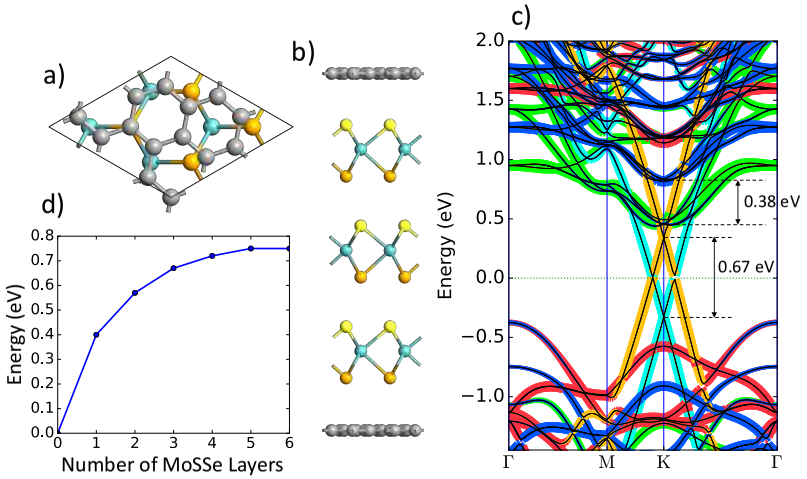

Figure 3: a) Top view of 2D hexagonal supercell of graphene-MoSSe stack. b) Side view of trilayer MoSSe sandwiched between graphene. c) Projected bandstructure of trilayer Janus MoSSe with graphene added on top and at the bottom. Red, blue and green lines represents projections on to the first, second and third MoSSe layer, respectively. d) Energy-shift between the two graphene Dirac-points for varying number of Janus layers.

the states localized on adjacent MoSSe layers is reduced from 0.51 eV to 0.38 eV as a result of screening effects when adding graphene on either side. Graphene is therefore promising as electronic leads to Janus MoSSe preserving the dipole effect.

Interestingly the graphene layers are strongly doped n- and p-type on the top and bottom respectively, in fact the charge neutrality point in the graphene sheets are separated by 0.67 eV by the intense field created by the three layer MoSSe structure. The concept of Janus dipole doping is summarized is Fig. 3(d). The doping effect increases up to a 0.8 eV separation of the charge neutrality points for six layers of MoSSe which is a very high homogeneous doping of graphene. This effect could be used to effectively dope graphene in a non-intrusive way where no dopant atoms need to be implanted in the pristine graphene sheet and the doping can be controlled by the number of stacked MoSSe layers used. The maximal Fermi-

level shift of 0.8 eV in Fig. 3(d) corresponds to a carrier density of $1 \times 10^{13}\,\mathrm{cm}^{-2}$. This falls in between typical doping values of a few times $10^{12}\,\mathrm{cm}^{-2}$, e.g. achieved with molecular doping[21] or backgates,[22] and the ultrahigh carrier densities of $\sim 10^{14}\,\mathrm{cm}^{-2}$ obtained by electrolytic gating.[23,24] Stacked Janus-graphene structures hereby give a promising route to abrupt pn-junctions, something that has previously required complex double-gated configurations,[25] with a homogeneity exceeding that of electrolytic or ionic gating and with the outer layers (graphene or Janus) being accessible due to the internal Janus-doping. Next we will discuss the potential optoelectronic applications of Janus materials and the transport model used.

Transport model of stacked devices. In Fig. 4(a) we illustrate the envisioned device consisting of MoSSe sandwiched between two graphene electrodes. Even for a monolayer of Janus MoSSe we see in Fig. 4(b) that a remarkable 0.4 eV shift in energy occurs between the graphene sheets which are separated by less than 1 nm while the MoSSe bandstructure remains intact. In order to check that a current can be injected from the doped graphene layers through Janus MoSSe, we calculate the cp-transmission from the Landauer-Büttiker expression

$$T_{cp} = \mathrm{Tr}\{\Gamma_{LB} G \Gamma_{RT} G^{\dagger}\} \tag{1}$$

where G is the retarded Green's function of the device and $\Gamma_{LB/RT}$ is the broadening coming from the left bottom and right top graphene leads respectively, as shown in Fig. 4(a). To obtain $\Gamma_{LB/RT}$ the full Γ_L and Γ_R matrices for the leads indicated in Fig. 4(a) were calculated recursively using the DFT-NEGF code provided by the QuantumATK software.[27] Subsequently $\Gamma_{L/R}$ was projected onto $\Gamma_{LB/RT}$ parts by removing indices of the full matrices related to the other layers (Supporting Information, Fig. S5). In this way cp-transport is considered with the transport direction still inside the plane. Fig. 4(c) shows $T_{cp}(E)$ for the monolayer MoSSe system with monolayer graphene leads on either side. Clearly transmission channels are available and a high transmission is seen for a bias window above the MoSSe

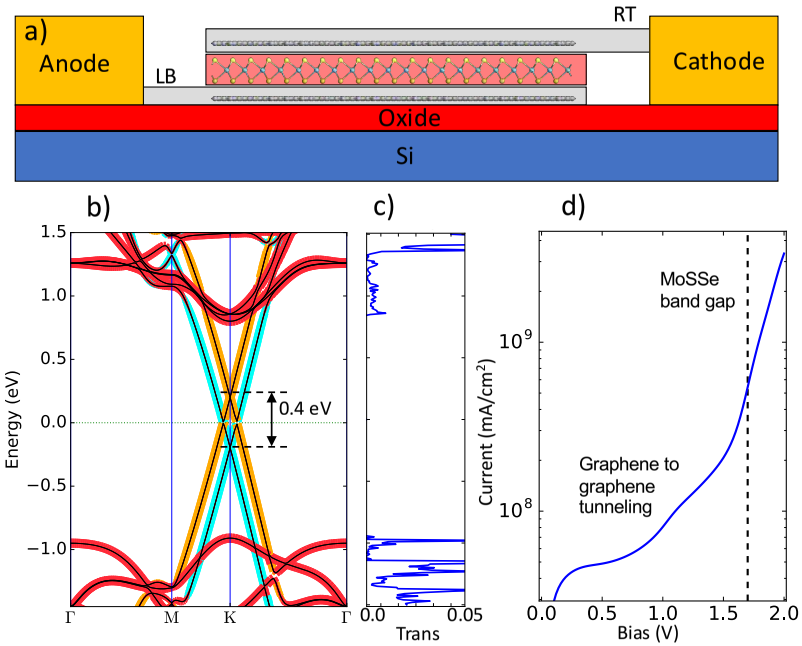

Figure 4: a) Envisioned device with graphene and Janus stacks to avoid dipole cancellation and achieve an abrupt *pn*-junction. b) Projected bandstructure of monolayer Janus MoSSe with graphene on top and at the bottom. Red line represents projection on the MoSSe, yellow and cyan lines projection onto the top and bottom graphene layer, respectively. c) Electron transmission from the left bottom graphene electrode to the right top graphene electrode. d) IV-characteristics[26] of the graphene-Janus stacked device at 300 K. The current is evaluated from the zero bias transmission function.

gap where states are available in all three monolayers. A very small transmission directly from one graphene layer to the other is also seen at the Fermi level, where the graphene cones intersect. We consequently find a low bias regime with a direct graphene-graphene tunneling current and a high bias regime with bulk Janus transport in the IV-characteristics shown in Fig. 4(d).

Janus MoSSe device photo-current. Next we consider the electron transmission and

photogenerated current for a three layer MoSSe device, Fig. 5(a). Since we have shown how

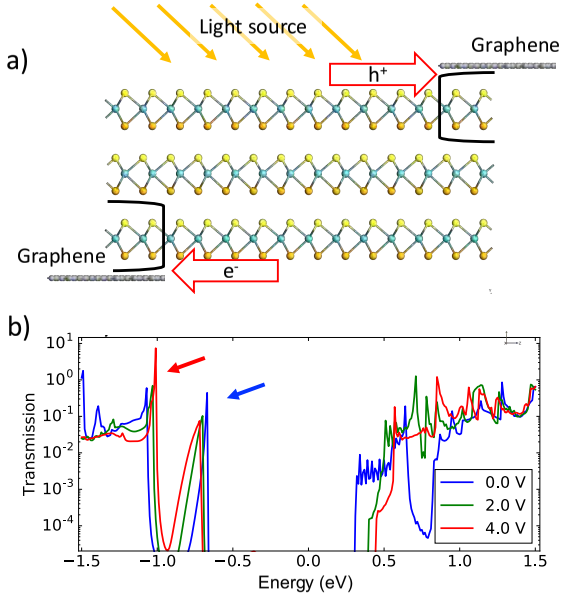

Figure 5: a) Trilayer Janus MoSSe device structure used to calculate transmission from the top to the bottom layer. b) Out-of-plane transmission for different values of the gate voltage illustrating the tunability of the cp-channel.

screening of the cp-dipole can be avoided by semi-metallic graphene leads, we imagine a device where MoSSe is directly exposed to light and the connection to graphene is made further away from photo-active area (or is considered transparent as compared to the full stack). In this case, we can consider transport directly from the top left to the bottom right MoSSe layer, as illustrated in Fig. 5(a), which makes the calculations computationally feasible. In order to examine the tunability of the photo-responsive cp-channel we included two metallic gates separated by 40 Å above and below the three layer structure. A voltage of positive/negative polarity was applied to the top/bottom gate to control a field in the

opposite direction of the built-in dipole field of the MoSSe. In this device, the dipole field creates a *pn*-junction in the cp-direction that is capable of separating holes and electrons into the top and bottom layers, hereby generating a photocurrent between the layers. The physical transport mechanism is interlayer tunneling via the cp-channel discussed previously.

The cp Landauer-Büttiker transmission (1) is shown in Fig. 5(b) for three different values of the gate voltage. First we see a clear peak in the transmission at -0.67 eV for the system without applied gate voltage (indicated by a blue arrow) which is due to the cp-channel. The delocalization of the cp-channel across the MoSSe layer enables it to carry the cp-current effectively. Furthermore, the almost dispersion-less bands of the cp-channel, shown in Fig. 2(a), leads to a sharply peaked van Hove-like transmission. It is possible to tune the dispersion of the band by applying the gate voltage to creates an electrical field opposite to the built-in field. We observe how the peak is broadened due to the increased band dispersion and resulting decrease in density of states for the cp-channel. Furthermore, as the gate voltage is increased another sharp transmission peak emerges at lower energy (indicated by a red arrow). This peak is related to the Γ-point valence state, shown in Fig. 2(a). The increased gate voltage tunes the effective mass of this band making it nearly dispersion-less in the plane, and create a new cp-channel (red arrow) replacing the previous one (blue arrow). This shows how it is possible to tune the in-plane effective mass and the cp-transport properties substantially with a gate voltage.

In Fig. 6(a) we plot the photo-excited cp-current for a two and three layer Janus-MoSSe device compared to that calculated for a 20 nm thick silicon *pn*-junction.[29,30] Interestingly, the extremely thin (0.5-1 nm) Janus photo-devices generates a current above that of the 20-40 times thicker silicon device considered, which underlines the great potential of Janus materials in thin-film photodiodes. Comparing the two and three layer MoSSe photo-currents, we see that the generated photo-current is almost independent of the thickness: the absorption of photons is improved by adding an additional Janus-MoSSe layer while the tunneling transmission is reduced at the larger distance from the top to the bottom layer. These

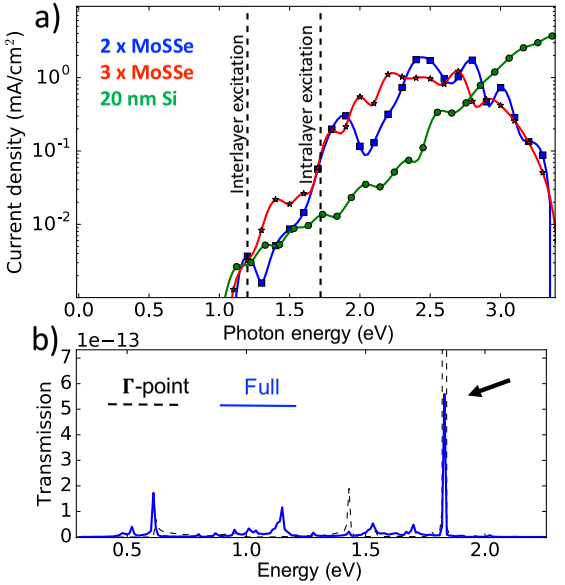

Figure 6: a) Photocurrent density[26] as a function of photon energy for the three layer structure shown in Fig. 5(a). The current was at each energy weighted by the flux of the solar AM1.5 reference spectrum.[28] b) Photon mediated transmission as a function of energy for the 2.5 eV photon. The full k-averaged transmission shows a dominant peak at 1.83 eV which is traced back to the cp-channel in a region around the Γ-point as illustrated by the Γ-point transmission.

two mechanisms almost cancel each other, and we find that there is only a small difference between the photo-excited cp-current for two and three layers of Janus-MoSSe.

We notice that for both Janus-devices there is a significant contribution to the current from photons with energies below the 1.72 eV gap of monolayer Janus-MoSSe (as indicated by the vertical dashed lines in Fig. 6(a)). This current originates from interlayer excitations where the conduction band and valence band are in different Janus layers, effectively reducing the transport gap of the Janus-MoSSe device.

The origin of the large photo-current is illustrated in Fig. 6(b), showing the photon-

mediated transmission for photons with an energy of $\hbar\omega$ =2.5 eV. The highest transmission (indicated by an arrow in Fig. 6(b)) is located at an energy of 1.83 eV, which is the final state energy of an excitation starting from the Γ-point cp-channel shown in Fig. 2(b) (further highlighted by the Γ-point transmission, which illustrates that the dominant peak can be traced back to a region in the vicinity of the Γ-point). This clearly shows that the cp-photocurrent in multilayer Janus-MoSSe is dominated by the cp-channel. Furthermore, we notice that at photon energies above 2.5 eV the photo-current starts to fall off. While this high energy region is less relevant in the context of solar cell applications it is still interesting to explain this somewhat unusual behavior. Starting at the cp-channel energy, point B in Fig. 2(a) we see that for energies photon above 2.5 eV one enters a regime where there are no bands in the opposite layer. Hereby, the cp-current is reduced and eventually the current starts to run in the opposite direction. This behavior is only captured by transport calculations which can account for the current direction of the generated electrons.

Finally, we point out the potential use of 2D Janus TMD's in tandem structures. Combining for instance a few MoSSe Janus layers with silicon thin-films could increase the broad spectrum absorption of light, especially in the low energy regime where silicon absorbs weakly. We chose in this study to focus on MoSSe due to its recent experimental realization. However, with recent efforts to create databases of emerging 2D materials[9] it is possible to identify other Janus candidates that has a lower band gap and a similar expected dipole effect. For instance we notice that CrSSe and ZrSSe has a band gap of approximately 0.5 eV and 0.8 eV, respectively, while certain bulk materials with a large dipole effect like BiTeI should be exfoliable. This underlines some of the prospects in studying new Janus materials to increase device performance and how Janus materials could play an important role as alternatives or constituents in PV devices in the future.

Conclusion. In summary, we have employed first principles calculations and a tailored transport method to demonstrate three new concepts rooted in the built-in structural out-of-plane asymmetry of novel 2D Janus materials: The Janus dipole doping effect, the Janus-

graphene electrode stacks for avoided dipole cancellation, and the Janus cross-plane channels dominating the photo-current response. It was illustrated how the Janus dipole doping allows one to achieve so far unprecedented homogeneous doping levels of graphene in abrupt, atomic-thin, *pn*-junctions. In particular, the graphene leads are crucial for device applications of Janus materials due to the dipole cancellation with conventional metallic electrodes. Among many possible applications of Janus stacks we focused on the photo-voltaic properties, and showed how Janus cross-plane channels gives rise to a photo-current exceeding that of thin-film silicon devices.

Methods

All results presented in this paper are obtained using the QuantumATK software.[27] Electronic structure calculations are calculated using Density Functional Theory (DFT) with a double zeta polarized LCAO basis set and (51x51) k-points. Local Density Approximation (LDA) is used for the exchange-correlation potential. In the out-of-plane direction over 30 Å of vacuum is included and Neumann conditions are employed at the boundary. Transport calculations are performed with the usual DFT-NEGF approach[31] using 301 k-points in the transverse direction. We chose a lattice parameter (3.22Å) and interlayer distance (3.14Å) as calculated previously.[13] Atomic coordinates were relaxed until all interatomic forces were below 0.02 eV/Å. Guan et al.[13] found $A'B$ stacking order to have the lowest binding energy for bilayer Janus MoSSe unlike the conventional TMD's that all exhibit AA' stacking. However since the difference in binding energy between AA' and $A'B$ is only 2 meV both configurations are likely to be found in experiments. We therefore choose to study AA' stacking which allows for straightforward comparison with previous studies of devices using other TMD's.

As derived in previous studies[29,32–34] the first order correction to the current into lead

$\alpha = TL/BR$ due to absorption of N photons with frequency ω is given by

$$\begin{aligned} I_\alpha =& \frac{e}{h}\int_{-\infty}^{\infty}\sum_{\beta=L,R}[1-f_\alpha(E)]f_\beta(E-\hbar\omega)T^-_{\alpha,\beta}(E) \\ & - f_\alpha(E)[1-f_\beta(E+\hbar\omega)]T^+_{\alpha,\beta}(E)dE, \end{aligned} \tag{2}$$

$$T^-_{\alpha,\beta}(E) = N\mathrm{Tr}\{\Gamma_\alpha(E)G(E)MA_\beta(E-\hbar\omega)M^\dagger G^\dagger(E)\}, \tag{3}$$

$$T^+_{\alpha,\beta}(E) = N\mathrm{Tr}\{\Gamma_\alpha(E)G(E)M^\dagger A_\beta(E+\hbar\omega)MG^\dagger(E)\} \tag{4}$$

where f_α is the Fermi Dirac distribution function of lead α, $A_\alpha = G\Gamma_\alpha G^\dagger$ is the spectral function of lead α, G and $G^\dagger$ are the retarded and advanced Green's functions and M the electron-photon coupling matrix given by

$$M_{ml} = \frac{e}{m_0}\left(\frac{\hbar\sqrt{\tilde{\mu}_r\tilde{\epsilon}_r}}{2N\omega\tilde{\epsilon}c}F\right)^{\frac{1}{2}}\mathbf{e}\cdot\mathbf{p}_{ml}. \tag{5}$$

where $\tilde{\epsilon}, \tilde{\epsilon}_r$ and $\tilde{\mu}_r$ are the isotropic, homogenous permittivity, relative permittivity and relative permeability respectively, F is the photon flux and $\mathbf{p}$ is the momentum operator. We take $\tilde{\mu}_r = 1$. For the dielectric constant of MoSSe we have taken the average in-plane value of the MoS_2 and $MoSe_2$ parent TMD's.[35]

Associated content

Supporting Information. Details on screening from metallic leads, the projection of the lead coupling matrices and the length dependence of the current.

Acknowledgement

This work is partly funded by the Innovation Fund Denmark (IFD) under File No. 5016-00102, and the Lundbeck foundation (No. R95-A10510). The Center for Nanostructured Graphene (CNG) is sponsored by the Danish Research Foundation, Project DNRF103.

References

(1) Lu, A.-Y. et al. *Nature Nanotechnology* **2017**, *12*, 744–749.

(2) Zhang, J.; Jia, S.; Kholmanov, I.; Dong, L.; Er, D.; Chen, W.; Guo, H.; Jin, Z.; Shenoy, V. B.; Shi, L.; Lou, J. *ACS Nano* **2017**, *11*, 8192–8198.

(3) Qiu, D. Y.; da Jornada, F. H.; Louie, S. G. *Nano Lett.* **2017**, *17*, 4706–4712.

(4) Gunst, T.; Kaasbjerg, K.; Brandbyge, M. *Phys. Rev. Lett.* **2017**, *118*, 046601.

(5) Rivera, P.; Yu, H.; Seyler, K. L.; Wilson, N. P.; Yao, W.; Xu, X. *Nature Nanotechnology* **2018**, 1.

(6) Kunstmann, J.; Mooshammer, F.; Nagler, P.; Chaves, A.; Stein, F.; Paradiso, N.; Plechinger, G.; Strunk, C.; Schüller, C.; Seifert, G.; Reichman, D. R.; Korn, T. *Nature Physics* **2018**, *14*, 801–805.

(7) Gong, Y.; Yuan, H.; Wu, C.-L.; Tang, P.; Yang, S.-Z.; Yang, A.; Li, G.; Liu, B.; Groep, J. v. d.; Brongersma, M. L.; Chisholm, M. F.; Zhang, S.-C.; Zhou, W.; Cui, Y. *Nature Nanotechnology* **2018**, *13*, 294–299.

(8) Chen, J.-W. et al. *Nature Communications* **2018**, *9*, 3143.

(9) Rasmussen, F. A.; Thygesen, K. S. *J. Phys. Chem. C* **2015**, *119*, 13169–13183.

(10) Cheng, Y. C.; Zhu, Z. Y.; Tahir, M.; Schwingenschlögl, U. *EPL* **2013**, *102*, 57001.

(11) Ji, Y.; Yang, M.; Lin, H.; Hou, T.; Wang, L.; Li, Y.; Lee, S.-T. *The Journal of Physical Chemistry C* **2018**, *122*, 3123–3129.

(12) Ma, X.; Wu, X.; Wang, H.; Wang, Y. *J. Mater. Chem. A* **2018**, *6*, 2295–2301.

(13) Guan, Z.; Ni, S.; Hu, S. *The Journal of Physical Chemistry C* **2018**,

(14) Wen, Y.-N.; Xia, M.-G.; Zhang, S.-L. *Computational Materials Science* **2018**, *152*, 20–27.

(15) That the band gap almost exactly matches the optical band gap is fortuitous and a consequence of the cancelation between the missing self-energy effects in the band structure and excitonic effects in the 2D semiconductors.

(16) Dong, L.; Lou, J.; Shenoy, V. B. *ACS Nano* **2017**, *11*, 8242–8248.

(17) Smidstrup, S.; Stradi, D.; Wellendorff, J.; Khomyakov, P. A.; Vej-Hansen, U. G.; Lee, M.-E.; Ghosh, T.; Jónsson, E.; Jónsson, H.; Stokbro, K. *Phys. Rev. B* **2017**, *96*, 195309.

(18) Gunst, T.; Lü, J.-T.; Hedegård, P.; Brandbyge, M. *Phys. Rev. B* **2013**, *88*, 161401.

(19) Papior, N.; Gunst, T.; Stradi, D.; Brandbyge, M. *Phys. Chem. Chem. Phys.* **2015**, *18*, 1025–1031.

(20) Stradi, D.; Papior, N. R.; Hansen, O.; Brandbyge, M. *Nano Lett.* **2017**, *17*, 2660–2666.

(21) Wehling, T. O.; Novoselov, K. S.; Morozov, S. V.; Vdovin, E. E.; Katsnelson, M. I.; Geim, A. K.; Lichtenstein, A. I. *Nano Lett.* **2008**, *8*, 173–177.

(22) Wang, L.; Meric, I.; Huang, P. Y.; Gao, Q.; Gao, Y.; Tran, H.; Taniguchi, T.; Watanabe, K.; Campos, L. M.; Muller, D. A.; Guo, J.; Kim, P.; Hone, J.; Shepard, K. L.; Dean, C. R. *Science* **2013**, *342*, 614–617.

(23) Das, A.; Pisana, S.; Chakraborty, B.; Piscanec, S.; Saha, S. K.; Waghmare, U. V.; Novoselov, K. S.; Krishnamurthy, H. R.; Geim, A. K.; Ferrari, A. C.; Sood, A. K. *Nature Nanotechnology* **2008**, *3*, 210–215.

(24) Efetov, D. K.; Kim, P. *Phys. Rev. Lett.* **2010**, *105*, 256805.

(25) Grover, S.; Joshi, A.; Tulapurkar, A.; Deshmukh, M. M. *Scientific Reports* **2017**, *7*, 3336.

(26) The current was scaled by the electrode cross-sectional area (width times the effective layer thickness $h \approx$7.5Å).

(27) Atomistix Toolkit version 2018.06, Synopsys QuantumWise A/S.

(28) ASTM, *Astm* **2013**, *03*, 1–21.

(29) Palsgaard, M.; Markussen, T.; Gunst, T.; Brandbyge, M.; Stokbro, K. *Phys. Rev. Applied* **2018**, *10*, 014026.

(30) For the silicon device we have included phonon-assisted processes[36] that generates most of the photo-current due to the indirect band gap. For MoSSe we did not include phonon coupling and the direct transition already gives a significant current. The estimate here then gives a lower limit to the photo-current generated without phonon-assisted processes in MoSSe.

(31) Brandbyge, M.; Mozos, J.-L.; Ordejón, P.; Taylor, J.; Stokbro, K. *Phys. Rev. B* **2002**, *65*, 165401.

(32) Henrickson, L. E. *J. Appl. Phys.* **2002**, *91*, 6273–6281.

(33) Zhang, L.; Gong, K.; Chen, J.; Liu, L.; Zhu, Y.; Xiao, D.; Guo, H. *Phys. Rev. B* **2014**, *90*, 195428.

(34) Chen, J.; Hu, Y.; Guo, H. *Phys. Rev. B* **2012**, *85*, 155441.

(35) Laturia, A.; Put, M. L. V. d.; Vandenberghe, W. G. *npj 2D Materials and Applications* **2018**, *2*, 6.

(36) Gunst, T.; Markussen, T.; Palsgaard, M. L. N.; Stokbro, K.; Brandbyge, M. *Phys. Rev. B* **2017**, *96*, 161404.

Graphical TOC Entry

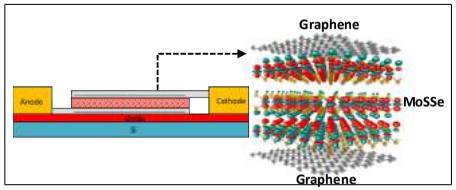

Patent application

Systems and methods for providing approximate electronic-structure models from calculated band structure data

Kurt Stokbro, and *Mattias Palsgaard*

PCT Patent Application No. PCT/EP2016/064628

US 20180129765A1

(19) **United States**

(12) **Patent Application Publication** (10) **Pub. No.: US 2018/0129765 A1**

Stokbro et al. (43) **Pub. Date: May 10, 2018**

(54) **SYSTEMS AND METHODS FOR PROVIDING APPROXIMATE ELECTRONIC-STRUCTURE MODELS FROM CALCULATED BAND STRUCTURE DATA**

(71) Applicant: **Synopsys, Inc.**, Mountain View, CA (US)

(72) Inventors: **Kurt Stokbro**, Farum (DK); **Mattias Palsgaard**, Copenhagen (DK)

(73) Assignee: **Synopsys, Inc.**, Mountain View, CA (US)

(21) Appl. No.: **15/865,076**

(22) Filed: **Jan. 8, 2018**

Related U.S. Application Data

(63) Continuation-in-part of application No. PCT/EP2016/064628, filed on Jun. 23, 2016.

(60) Provisional application No. 62/188,959, filed on Jul. 6, 2015.

Publication Classification

(51) **Int. Cl.**
G06F 17/50 (2006.01)

(52) **U.S. Cl.**
CPC ***G06F 17/5018*** (2013.01); *H01L 29/785* (2013.01); *G06F 2217/02* (2013.01); *G06F 2217/16* (2013.01)

(57) **ABSTRACT**

Computer-aided methods for simulating confined nanodevices are disclosed. In example implementations, atomic-scale model of the nanodevices are generated so that dimensions and materials are specified. Then, band structures which comprise wave functions and Eigen energies are calculated using First Principles Methods (FPM). Effective mass modeled which comprise wave functions and Eigen energies are generated. After that, spatial wave functions of the calculated FPM band structures are mapped to the generated effective mass band structures wave functions by considering global behavior. In response to the mapping, generated effective mass models are fitted to calculated FPM energies so that approximate electronic band structures of the confined nanodevices are modeled. Computer programs for carrying out the methods, data media and computer systems are also disclosed.

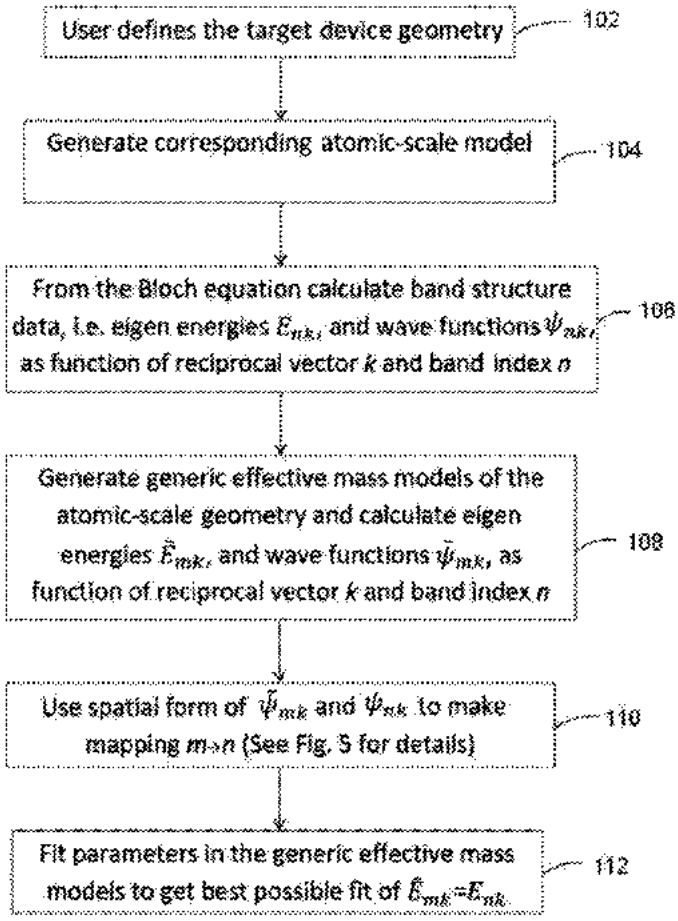

Published by:
DTU Nanotech
Department of Micro- and Nanotechnology
Technical University of Denmark
Ørsteds Plads, building 345C
DK-2800 Kgs. Lyngby